BIOPOLYMER SYNTHESIS
OF
POUROUS CARBON NANOCOMPOSITES

by

Ashleigh Edward Danks

A thesis submitted to the University of Birmingham for the degree of

DOCTOR OF PHILOSOPHY

School of Chemistry

College of Engineering and Physical Sciences

University of Birmingham

April 2017

Word Count: 40,439

ABSTRACT

As the world faces resource management problems such as providing sustainable energy and sourcing rare elements, demand is growing for new materials to help combat these. Biopolymer sol-gel synthesis has the potential to create a wide range of functional materials, in particular from the spontaneous foaming of gelatin and metal nitrates upon drying. If this process can be controlled and expanded to other biopolymers then catalytic systems could be designed for many applications.

The gelatin foaming mechanism was investigated by a variety of techniques including small angle neutron scattering and rheology. The cause of the foaming was attributed to the evaporation of water and the gels ability to stabilise the bubbles formed. Links between the structural properties of the gel and porous carbon have been suggested as a way of predicting and selecting certain morphologies whilst in the liquid state.

Research has also been carried out using microwaves as an alternative to conventional furnaces, this was done to make the synthesis more environmentally friendly. During this research several metal carbides/nitrides were synthesised, including metastable phases.

Using this biopolymer sol-gel synthesis, materials were synthesised and tested as catalysts for methanol steam reforming as an example of possible applications for this research. Both sets of materials showed activity for their respective reactions in line with current literature.

Finally, further optimisation is possible on all aspects of this thesis and future research should be carried out to maximise the potential of this facile and versatile synthesis technique.

ACKNOWLEDGEMENTS

To start I have had the opportunity to travel a great deal for my doctoral studies and receive training and support from a number of institutions. I would like to thank the following professional bodies for allowing to visit or for providing support during my PhD:- EPSRC, EU, RSC, AWM, ISIS, Diamond, ILL, NIMS, DSTL, University of Glasgow, Healan Ingredient.

During my travels and studies I have met many knowledgeable researchers, there are a few in particular I would like to thank for their support. Prof Ya Xu and Prof Yoshio Sakka were my hosts during my extended visits to NIMS and without them I would not have had the opportunity carry out my research there. I thank Dr Brian Pauw and Dr Martin Hollamby for answering my questions and helping, understand my data (SAXS and SANS respectively); I remember them explain SAS on a napkin in the usual pre-beamline pub trip.

A huge thanks is also owed to my supervisor, Dr Zoe Schnepp, who has supported me through my masters and PhD projects. Thank you for giving me the opportunity to experience a wide range of things I would not have done otherwise, such as trips abroad and working with companies.

Thank you to Rosie and Heidi, and others, for battling through the gibberish that I call a thesis draft, without you my examiners would think this thesis was written by a monkey. Thanks to my Greg for being the ChemDraw guru.

I would like to thank my sisters, Edwina and Kassandra for their unwavering support and faith that I could complete my PhD on my timetable. Thank you to Kassandra especially for housing me on and off for the past 10 years.

Finally I would like to thank my colleagues in the Haworth building, especially the fifth floor guys, for the support both academically and socially which has been essential in keeping everyone motivated.

CONTENTS LISTING

TABLE OF CONTENTS

LIST OF FIGURES

LIST OF PAPERS

DIRECTLY RELATED TO THIS RESEARCH

- Thompson, E.; Danks, A. E.; Bourgeois, L.; Schnepp, Z. *Green Chemistry* **2015**, *17*, 551.

- Schnepp, Z.; Danks, A. E.; Hollamby, M. J.; Pauw, B. R.; Murray, C. A.; Tang, C. C. *Chemistry of Materials* **2015**, *27*, 5094.

- Danks, A. E.; Hall, S. R.; Schnepp, Z. *Materials Horizons* **2016**.

- Danks, A. E.; Hollamby, M. J.; Hammouda, B.; Fletcher, D. C.; Johnston-Banks, F.; Rogers, S. E.; Schnepp, Z. *Journal of Materials Chemistry A* **2017**.

INDIRECTLY RELATED

- Yang, Z., A. E. Danks, J. Wang, Y. Zhang, and Z. Schnepp. "Triple Templating of Graphitic Carbon Nitride to Enhance Photocatalytic Properties." *APL Mater.* 4, no. 1 (2016): 015706.

CHAPTER 1

INTRODUCTION

1.1 GENERAL INTRODUCTION

Global challenges such as energy, climate change and clean water have led to a constant demand for more sophisticated materials and this has driven a steady stream of new materials to be developed.[1] Recently making materials with the desired properties is no longer the only concern and thought has be given to the synthesis methods as well. This shift in priorities is largely driven by concerns over human impact on the planet e.g. waste build up and global warming, so making these new materials economically cost effective as well as environmentally friendly is the challenge facing materials chemists. This can be addressed by considering the principles of green chemistry, discussed later.

The main aim of this research is to take a biopolymer sol-gel (BSG) synthesis method and use it to generate a general route to designer catalysts; based on a porous carbon framework with embedded nanoparticles selected depending on the application. The advantage of BSG is that it is possible to integrate the multiple physical and chemical variables into a single synthetic step. The general synthesis is facile and its advantages/ disadvantages will be discussed in Chapter 2, this chapter will also detail a mechanistic study that was carried out to gain a greater understanding of the system and developed strategies to control it. Several catalysts were developed alongside the mechanism study to show the suitability of this to be used in different areas. Microwave synthesis was investigated as a low cost and energy efficient alternative to conventional furnace heating (Chapter 3). A copper : zinc based catalyst for methanol steam reforming (MSR) was synthesised and tested (Chapter 4) and tungsten carbide was synthesised to be either a co-catalyst for environmental remediation of water or used in the hydrogen evolution reaction (Chapter 5). Finally background information is given on the main experimental techniques through this thesis (Appendix E).

This introduction will cover the general concepts and motivations as well as serving to set the scope of this research within wider scientific goals. Whilst the following chapters are set around the central themes they are discrete in their content and so each chapter will have a brief introduction specific to the topic.

1.2 WHAT IS GREEN CHEMISTRY?

The essence of green chemistry is being mindful of the chemicals, synthesis techniques and waste disposal and not just about the materials being produced but also about generating safer chemistry. Green chemistry can be summarised by 12 principles that Paul Anastas and John Warner[2] set out. All 12 principles are important for green synthesis, however only the most relevant ones to this research will be discuss here.

The corner stone of this research is principle 7 - the 'use of renewable feedstocks', by using biopolymers, not only could they offer a renewable source for precursors (i.e. carbon) but they are often a waste product of established industries, e.g. gelatin from the meat industry. This can also be seen as 'preventing waste' which is the first principle. Sustainability is key to any future material as society tries to minimise our impact on the world, to do this we must target renewable and earth abundant sources for precursors. On a related note, although not a green chemistry principle, by using waste products as a feedstock adds value, which is an economical incentive for companies who would otherwise have to pay for disposal of the waste. Gelatin already has many uses in cosmetics, pharmaceuticals and the food industry[3] so it may seem an odd choice for this research, however reports in 2013 stated that the annual consumption of gelatin in these industries is currently less than what can be produced.[4] There have been several papers detailing the possible materials and current research aims to build on this by investigating the fine details of the synthesis.[5,6] There are potential ethical concerns about catalysts based on porcine gelatin on a useful scale, so this work is a starting point to highlight the potential and further work should include using alternatives or raw biomass.[7]

Biopolymers for the most part are water soluble which allows the reaction to take place in an aqueous medium; this makes the whole synthesis safer and by definition less toxic (Principles 3 and 5). The synthesis of these materials are facile and safe, but the products are porous carbons impregnated with nanoparticles so attention must be given to the toxicological properties and potential environmental impact. This was not carried out in this work but as these syntheses are developed further this should form part of the research. Finally, samples are dried and calcined at lower temperatures than one would normally find for a solid state synthesis of carbide (e.g. tungsten carbide can be synthesis at 900 °C under flowing argon rather than the solid state methods which occur at 1100 - 1500 °C.[8,9]

1.3 SOL-GEL

1.3.1 TRADITIONAL SOL-GEL CHEMISTRY

Sol-gel chemistry has been around since the mid-1800s and one of the first examples of ‘traditional’ sol-gel reactions was demonstrated by Ebelmen:[10] when a metal alkoxide was prepared from $SiCl_4$, it started to gel when left exposed to air. He later discovered that this was due to water in the atmosphere hydrolysing the metal alkoxide; this reaction is then followed by condensation and polymerisation. The main disadvantage of this technique is you are limited to elements that form alkoxides[11] and whether you can control the relative rates of the hydrolysis/condensation reactions. So since these early experiments into 'chemie douce'[12] chemists have found many ways to tune these reactions for the desired outcome. This has resulted in periodic reviews of the subject[13-16] which should indicate that this area of research is vast and still very active; this means the various methods could be described at length, however only the areas placing this research in the literature and those that directly relate to it will be discussed.

As mentioned earlier, the origin of sol-gel is from the work of Ebelmen where he discovered a gel forming in his reaction mixture. It is now known that this was the hydrolysis of the silicon alkoxide in the reaction (Reaction 1), the water coming from the atmosphere, and since then a lot of work has been done with silicon chemistry using the tetra-monoalkoxide,[17] silanes[18] and many other silicon compounds. [19,20]

$$Si(OR)_4 + nH_2O \rightarrow Si(OR)_{4-n}(OH)_n + nROH \qquad (1)$$

The electron donating/withdrawing of power of the -OR group versus the incoming -OH on the silicon have a big impact of the relative rates of hydrolysis and condensation. These reactions can be acid or base catalysed to speed up the process. The rates are controlled by the stability of the transition state which is a sum of a number of factors, these will be discussed for acidic catalysed reactions, the opposite is true for basic conditions. A hydrolysis reaction involves replacing an –OR group with a –OH group via a pentavalent transition state (Reaction 2). The second step is the condensation step and it results in a siloxane bond (Reaction 3). The alkaline form of these reactions are shown in Figure 1.2. The order of these steps is what controls the final product, for example in acidic media multiple sequential hydrolysis steps are less favourable (i.e. slower) and so condensation occurs rapidly on terminal silanols; this results in chains that eventually form interconnected gels. Conversely, the faster hydrolysis reactions in basic conditions result in products like $(OH)_3$-Si-$(OH)_3$ before condensation occurs. This means pH can be used to form different shaped networks, low pH will result in cross linked long chains and the high pH will have small agglomerates that eventually network, Figure 1.1.[13]

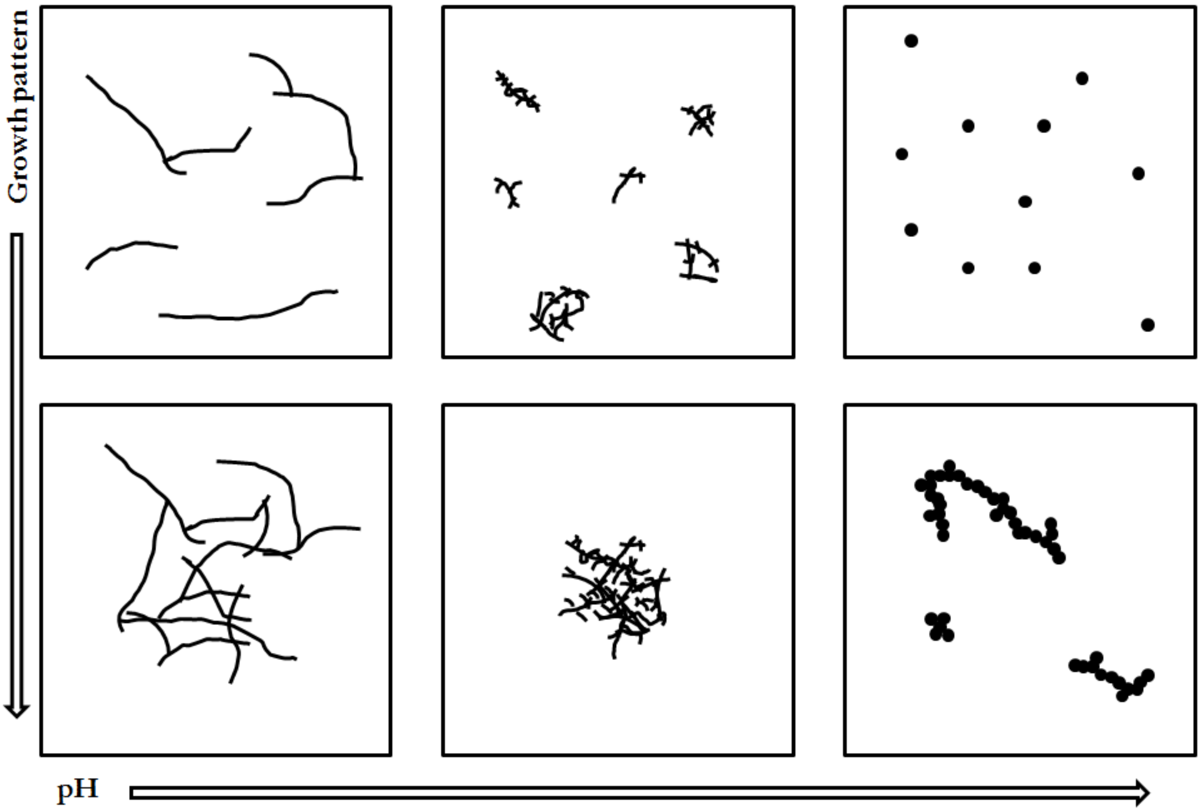

Figure 1.1 Schematic of gel growth patterns with changing pH adapted from ref[15]

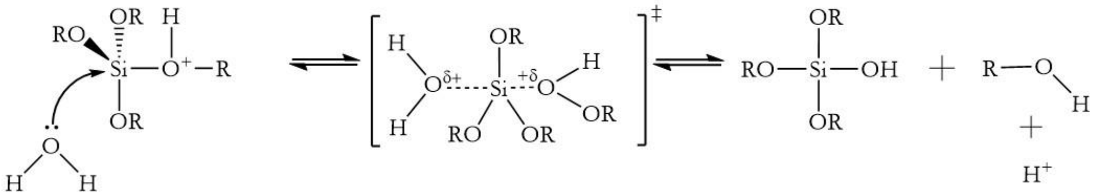

(2)

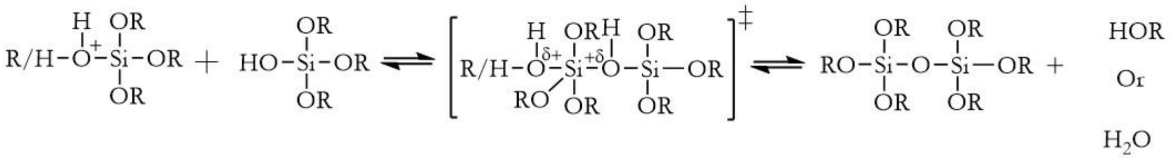

(3)

Despite the difficultly in controlling the reactivity of some alkoxides, traditional sol-gel has also been applied to many other elements in the periodic table[11] with roughly similar reaction pathways. This has allowed, potentially, for a vast array of different possible compounds, however it can be very difficult to make ternary or higher order compounds due to the differing reactivities of the alkoxides. The chances of a successful reaction can be increased by considering the partial charge model,[12] this considers the electronegativity differences, which for most other elements is lower than silicon, and can be used to generate the partial charges on the central metal ions (E.g. in the tetraethoxy compounds, Si +0.32 and Ti +0.63).[15] The higher partial charges on these metals(due to lower electronegativity) favour the nucleophilic attack of the H_2O/OH^- (Reaction 2) in the hydrolysis reaction. It is this that cause many of the problems; 1) Phase separation due to hydrolysis speed; 2) violent reaction with water, so some of these need special handling and safety precautions and the reaction often precipitates ill-defined metal–oxo/hydroxo compounds. It is possible however to perform these reactions by limiting the water content and introducing additives to the system to slow the reaction down. The addition of a chelating ligand (e.g. acetyl acetone(acac))[21] can also be used to further stabilise the compound and slow the reaction down, so by combining all the techniques above it is possible to generate many different compounds. Finally there are many post synthesis treatments which further allow for different types of materials to be made (e.g. spin coating, freeze drying, the use of templates), Figure 1.2.[22-24]

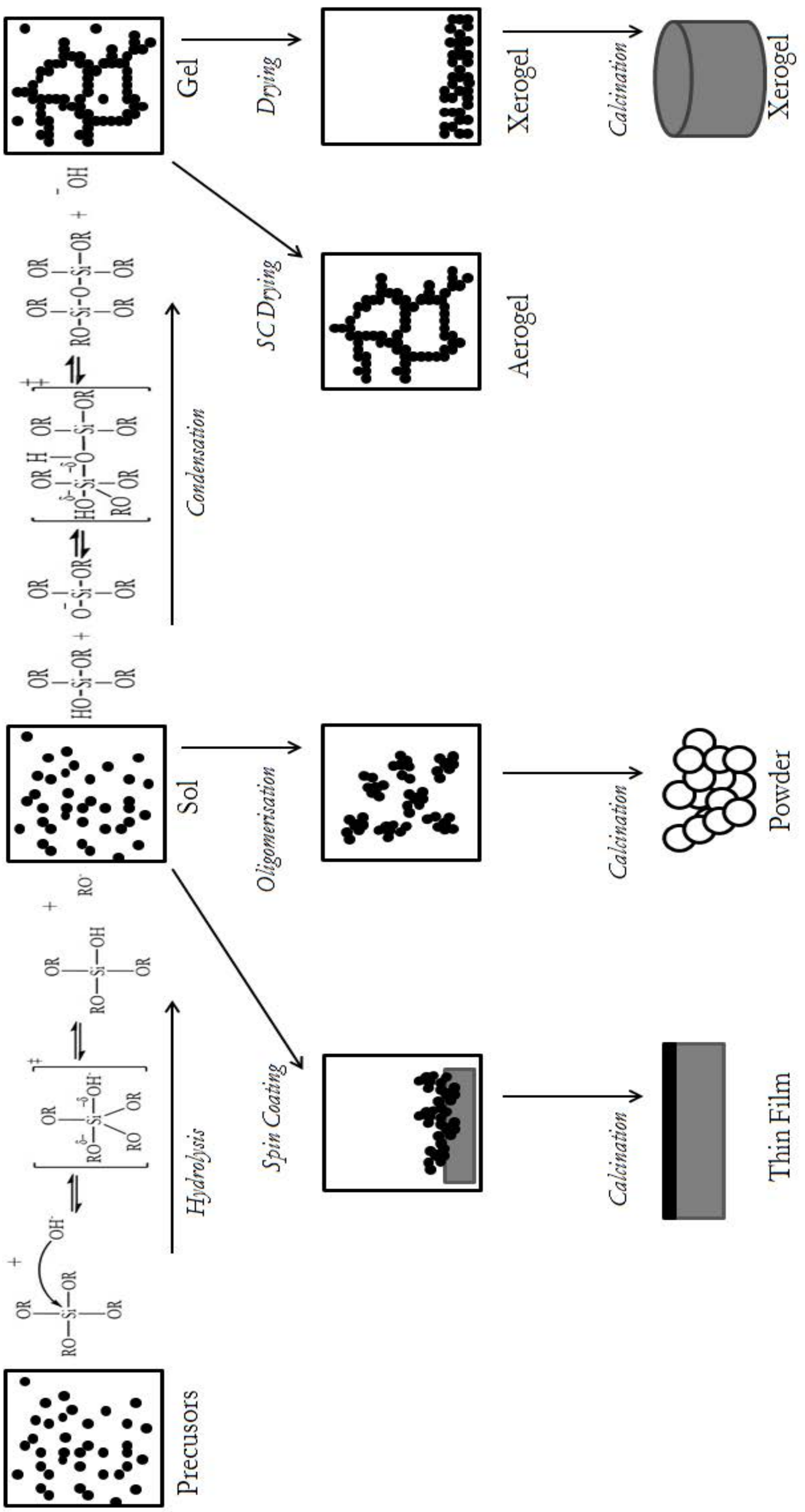

Figure 1.2 Schematic of traditional sol-gel and post-processing

1.3.2 SMALL METAL CHELATOR SOL-GEL

The next step for sol-gel chemistry was then to use multi-dentate ligands which stabilise the individual metal ions and allow for aqueous conditions to be used, there are many different ligands used but by far the most common is citrate followed by EDTA.[25] Citric acid is triprotic and contains three carboxylic acids, all of which are able to dissociate with the addition of a base. These carboxylic acid motifs can be used to enhance cation ion binding, however, it is important to note that pH control is vital in a system with multiple metal species to stop precipitation on any one metal species.[26,27] The chelated metal ions that have chelated to the citrate molecules then have weak intermolecular bonds to nearby neighbours; this can be seen as the 'gel' phase. The citrate sol-gel method is favoured so heavily because of its availability and low cost. The production of metal oxide materials is one major use of this technique especially where there are several metals involved. The organic material may be burnt off long before the final inorganic compounds start to form, however it is instrumental in forming multiple nucleation sites and for maintaining atomic level mixing of all species in the mixture during the early stages of synthesis. As with traditional sol-gel, by changing the synthesis parameters it is possible to form new reaction schemes to produce different outcomes, e.g. by calcining in nitrogen rather than air it becomes possible to maintain some of the initial carbon.

1.3.3 IN-SITU POLYMERISATION SOL-GEL

In the 1960's Pechini took the next step in formalising the network formation replacing the weak intermolecular bonds with covalent ones. Figure 1.3 below shows this was done by chelating metal ions into citrate (A) and using ethylene glycol (B) to polymerise the citrate molecules together (C/D).[28] The benefits of forming a continuous network are that the chelated species are prevented from precipitating out of solution and the final polymer network helps to reduce sintering during heat treatments due to enhanced thermal stability. Also having the metal ions trapped in a rigid network further enacts control over the final product. This technique has been used to synthesise complex ternary and quaternary metal oxide compounds.[29,30] Just like the previous techniques there have been further modifications which have had interesting results, e.g. urea has been used to control the pH as the sample decomposes. More recently, and more interestingly for this research, the Pechini sol-gel method has been used to make transition metal (TM) carbides (e.g. Mo_2C was synthesised using a metal acetate/citrate/ethlene glycol/urea mixture heated to 850 °C).[31] Transition metal carbides are well known for their mechanical properties but these are now being investigated for their catalytic properties, so simple synthesis routes have opened up their potential applications.

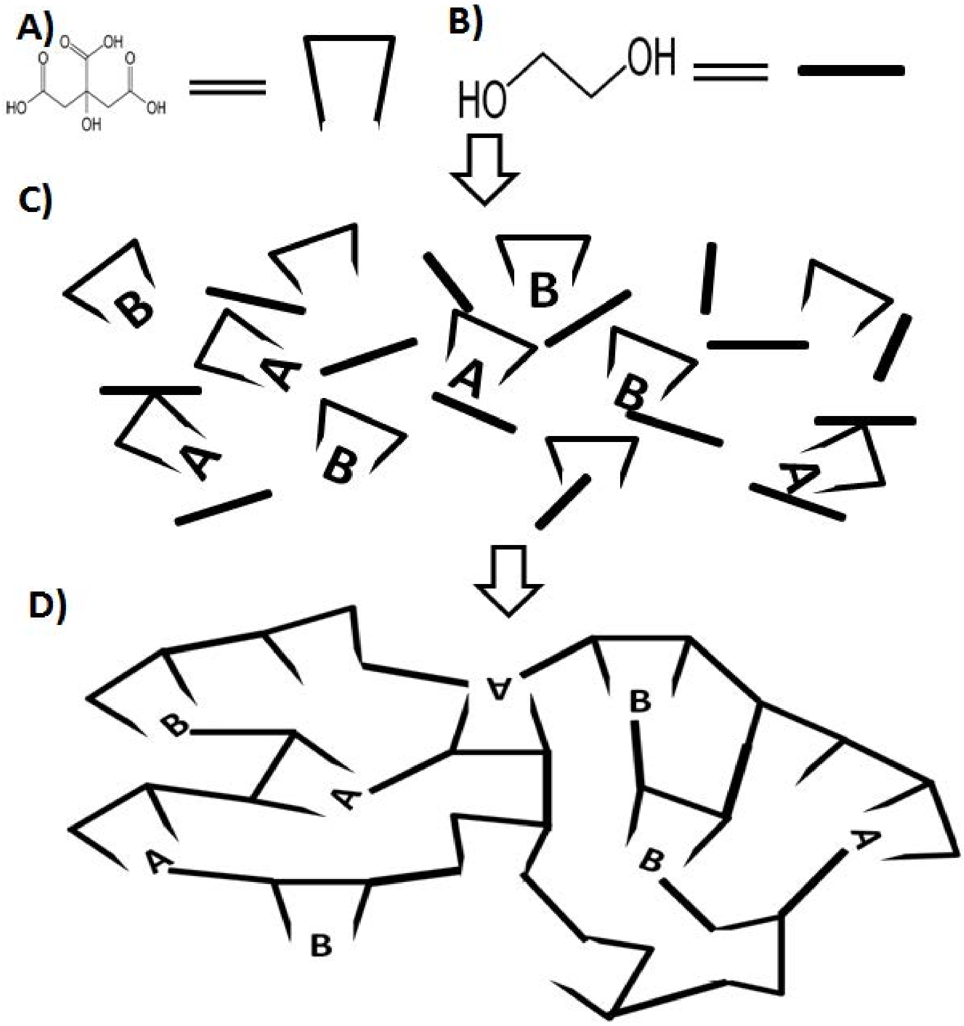

Figure 1.3 Schematic of Pechini synthesis

1.3.4 POLYMER SOL-GEL - SYNTHETIC POLYMERS

After Pechini the final step along this branch in this field was to take pre-formed polymers and use them to sequester metal ions around and along their lengths, homogenising the solution and again ensuring numerous nucleation sites. The early work into this field started with synthetic polymers which were readily available. Other types of sol-gel chemistry had been investigated including microwave and non-aqueous sol-gel syntheses.[32,33]

A popular and well used example is the simple mixing of polyvinyl alcohol (PVA) with metal nitrates to form a gel at relatively low temperatures, this is heated in a furnace either directly or after a drying step.[34] The polymer in these cases can control a number of variables; 1) particle size can be kept very small (25nm)[35] for the same reasons as stated earlier; 2) the homogeneity of the sample can also depend on the polymer, specifically the ratio of metal ion to polymer on the polymer as shown by Liu et al.[36] Many other polymers have been used in sol-gel syntheses including polyethylene glycol (PEG)[37] and polyvinylpyrrolidone (PVP);[38] but the most relevant is the combination of polyacrylonitrile (PAN) and poly(urea-coformaldehyde) methylated resin (PUF) with chromium chloride to create nanoparticulate chromium carbide/nitride on carbon fibres.[39]

1.3.5 POLYMER SOL-GEL - BIOPOLYMERS

The final type of sol-gel to be discussed involves the use of biopolymers, there are a couple definitions for the term 'biopolymer' but in this thesis it shall refer to a macromolecule taken from biomass. Biopolymers are of interest for materials synthesis, especially for their use in sol-gel chemistry because they can easily be extracted from biomass and they are readily available, e.g. the gelatin market is expected to have a 6.75% compound annual growth rate until 2017 to a total of 514 Gt.[4] Across all the biopolymers there is a massive amount of chemical and structural diversity, including self assembly into ordered structures, some of which are very long range and have a high level of ordering. It is these factors, which if they can be incorporated into the final product could lead to new materials that are both structurally and chemically complex. The next sections will detail the chemistry of the biopolymers used in this research, this is by no means a complete list and more information can be found here.[16]

The International Union of Pure and Applied Chemistry (IUPAC) define a colloidal system as a dispersion of one phase in another where, "the molecules or polymolecular particles dispersed in a medium have at least in one direction a dimension roughly between 1 nm and 1 mm".

A biopolymer fits the description of a colloid, set out by IUPAC, by having order that extends for more the 1 nm. Gel formation is triggered by either adding metal ions or cooling as the biopolymers are often dissolved in hot water; cooling therefore causes a conformational change in the biopolymer. Biopolymer sol-gel (BSG) has many benefits in addition to the one already mentioned, there is no need to form the network in situ as it already exists also due to their structural complexity and it is possible to use different biopolymers to form different structures (e.g. fibres or mesoporous structures[40,41]).

1.3.5.1 GENERAL STRUCTURAL INFORMATION

There are a number of similarities between the biopolymers which should be addressed before discussing the specifics of each biopolymer. The main focus of BSG chemistry has been on polysaccharides and polypeptides, the former of which is based on chains of monosaccharide units typically featuring 6-membered pyranose rings and the latter is made up of amino acids. The chains formed in polysaccharides are made through glycosidic bonds which are formed through carbons on the rings and there are two possible configurations α and β, Figure 1.4. The most common linkage, to produce linear polymers, is between carbons 1 and 4 written as $\alpha 1 \rightarrow 4$ or β1→4, respectfully. Polysaccharides can be further categorised as: amide/amines (chitin/chitosan), carboxyls (pectin, alginate), hydroxyls (agar, starch, cellulose) and sulfate (carrageenan), and this is based on their side group functionality.[42]

The chemical diversity in polypeptides comes from the variations in the sequence and quantities of the amino acids that make each one, it is important to remember there are a large number of different amino acids. There are a wide range of different types of biopolymers available but not all of these will be discussed here as they are not relevant to the work presented, the next sections details the biopolymers that were used in this work. As a final point it should be noted that many biomass sources represent a mixture of different biopolymers, such as crystalline fibres and also inorganic compounds.

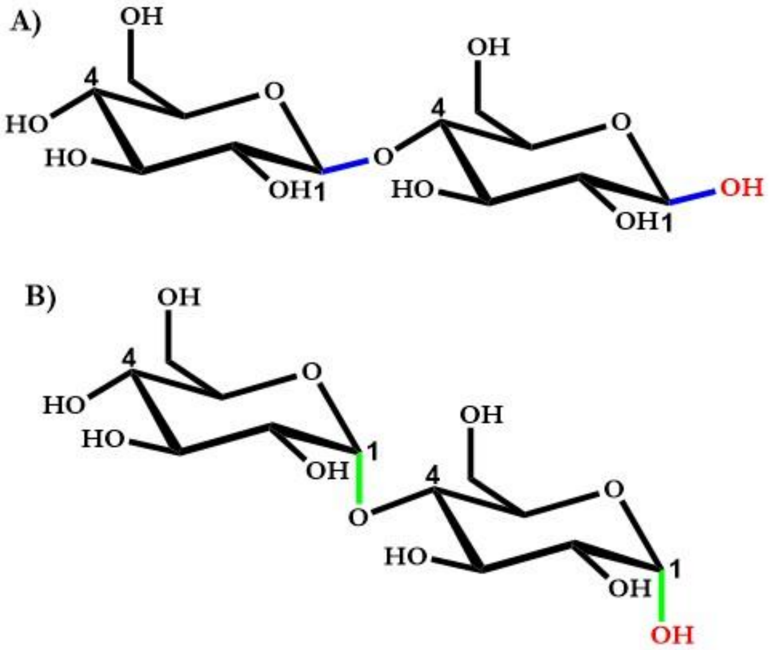

Figure 1.4 A) α and B) β glycosidic linkages

1.3.5.2 GELATIN

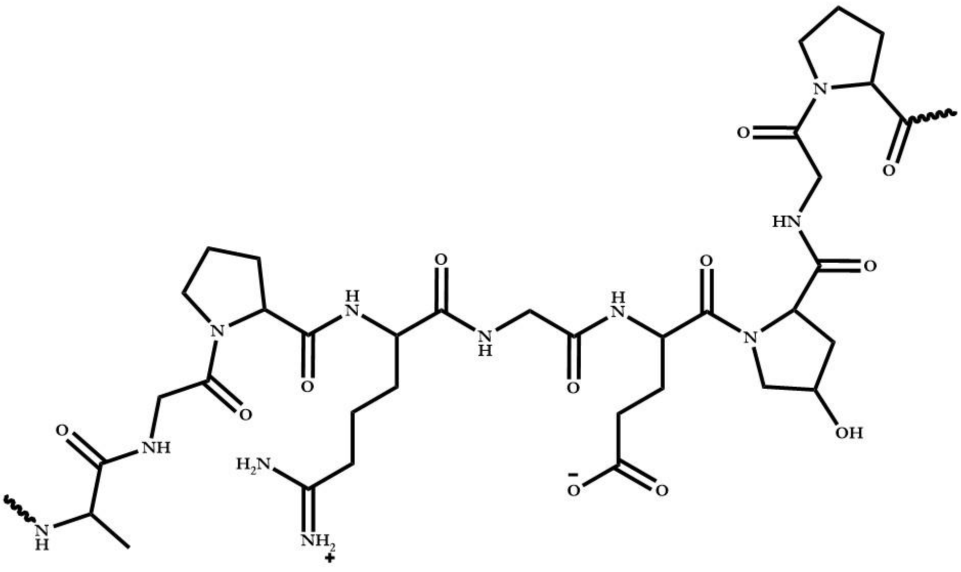

Figure 1.5 Representative structure of gelatin (-Ala-Gly-Pro-Arg-Gly-Glu-4Hyp-Gly-Pro-)

Gelatin is the primary biopolymer used in this thesis; the reasons for this will be explained in Chapter 2.

The exact composition of gelatin is complicated because it depends on how and what it was extracted from, (e.g. bovine gelatins tends to be more linear whereas porcine gelatins are more highly branched) but there are a number of features common to gelatin sources.[43,44] The main source of gelatin is animal skin and bones through hydrolysis of the collagen. Gelatin is extracted under either acidic or basic conditions, this is indicated by the Type A or Type B notation respectively. Being a polypeptide, gelatin is made up of amino acids and as mentioned before it varies on source, etc. but the general composition is 33% glycine, 21% proline and hydroproline, 10% alanine up to a MW of ~100 000, the remainder is made up of other amino acids in much smaller quantities.[45,46]

Making gels with gelatin is extremely easy, dissolving in hot water up to 50 wt%, forming clear/pale yellow solutions. On cooling the solution it sets into a gel, this is due to the polypeptide chains forming right-handed superhelices comprised of 3 left-handed helical strands, the junction zones are rich in proline and hydroxyproline 'monomers'.[47]

1.3.5.3 AGAR

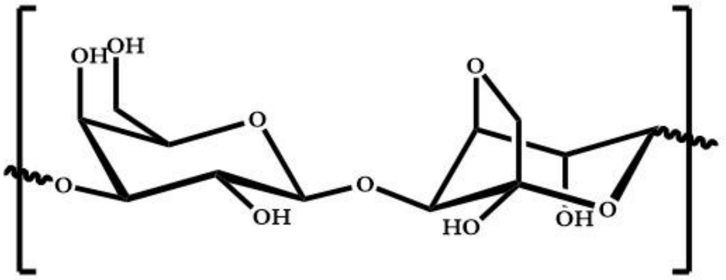

Agarose

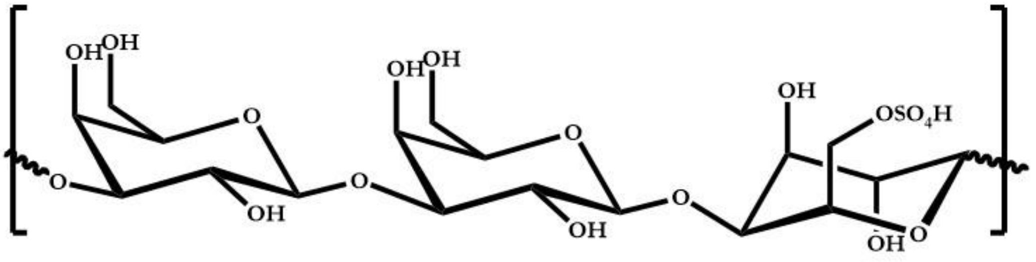

Agaropectin

Figure 1.6 Structure of agar showing both agarose and agaropectin

Agar is obtained from Rhodophycae, this is the same family of red seaweeds that carrageenan is extracted from albeit from different species.[48] This makes them very similar, in fact, chemically the only difference is the lack of sulfate groups in agarose. Structurally there are a number of differences, agar is a mixture of agarose and agaropectin whereas carrageenan is a single polymer based on β(1→3)-D-galactopyranose and α(1→4)-D-galactopyranose units. Sulfates can be on either or both units depending on the type of carrageenan.[49] Agarose has α(1→4)-3,6-anhydro-L-galactopyranose units. Agaropectin is a sulfated and branched polymer with poor metal binding properties.[50]

Agar has enjoyed much success in biomedical applications for growing fungi and bacteria but its use in materials synthesis has been limited; despite this we choose this as a suitable biopolymer for this research because it shares a number of favourable features with our other biopolymers. It has -OH groups for metal binding and readily forms gels at reasonably low temperatures. Another factor that made us consider this biopolymer was the availability of a metal and nitrogen free, i.e. only C, H, O, starting material (unlike Na-alginate).

1.3.5.4 DEXTRAN

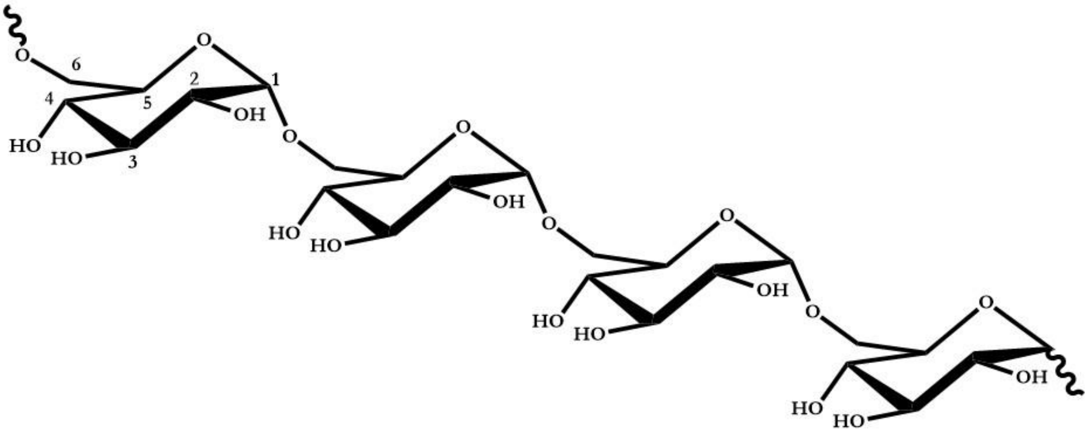

Figure 1.7 Schematic showing the structure of dextran

Dextran is a complex, highly-branched polysaccharide comprised primarily of α(1→6) glycosidically bonded glucans, with α(1→2), α(1→3) and α(1→4) bonded side chains (Figure 1.7). Production of dextran is achieved through enzymatic digestion of sucrose by bacteria such as *Leuconostoc mesenteroides* and the main side groups are hydroxyls, although the polymer also contains reductive aldehyde substituents. The ability of dextran to bind, and if necessary reduce, metal ions over a large range of concentrations is very good and as such is used for producing metallic nano- and microstructures.[51] Another use for the biopolymer is that it is biocompatible, highly soluble and stable making it important in biomedical applications. A final advantage of dextran is the propensity for modification, e.g. an anionic dextran sulfate or carboxymethyl-dextran has enhanced metal binding.[52]

A number of studies have been conducted where the reactions result in a porous material this can be 'sponge-like' metal/metal oxides or even zeolites.[53] Macroporous metals and metal oxides have been prepared though the use of aqueous metal salts (Cu, Ag and Au) and dextran. The mixture formed a viscous liquid that could be shaped into monoliths or drawn out into macroscopic wires, the next step was to dry and then heat in air to 800 °C. Of particular note in the case of gold and silver, the dextran reduced and slowed sintering of the metal ions although presumably some did occur during the final heating process as the polymer burns off.[51] Similarly, a paste containing the necessary nitrates to produce $YBa_2Cu_3O_{7-x}$ can be combined with dextran and calcined at 920 °C to produce sponges of the superconductor.[54] This particular study was extended to carboxylated crosslinked dextran beads (CM-Sephadex®) the result was $YBa_2Cu_3O_{7-x}$ with the same spherical structure, the microstructure consisted of agglomerated nanoparticles.

1.3.5.5 STARCH

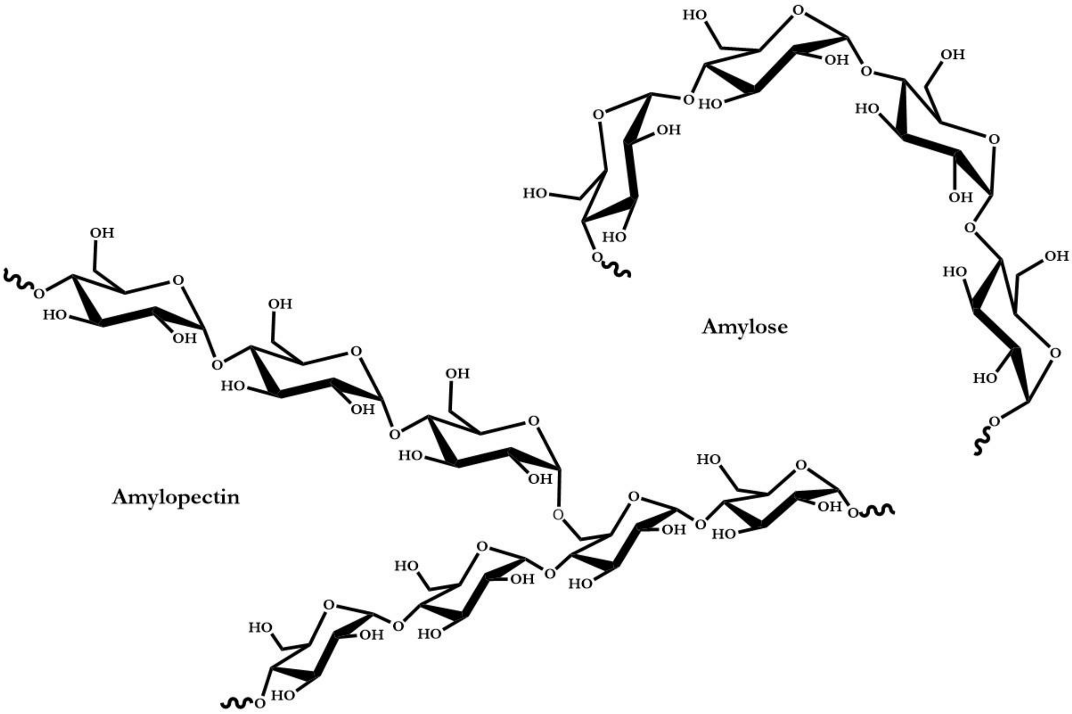

Figure 1.8 Structure of starch showing both amylose and amylopectin

Starch, like agar, is a mixture of two homomers, amylose and amylopectin, in an approximate 1:4 ratio, depending on the species of plant it comes from, this ratio also affects solubility but generally it is not soluble in cold water. Both homomers are formed of α-D-glucose, the difference comes from their glycosidic linkage. Amylose is linear polymer utilising α(1→4) glycosidic links, whereas amylopectin uses α(1→4) glycosidic links with a α(1→6) non-randomly approximately every 30 units and is a complex, highly branched polymer. Like dextran, starch has -OH side group that can be easily modified to change physical properties such as metal binding.

As previously mentioned control over size, polydispersity and purity of nanoparticles is critical to some applications and starch can be used to address some of the problems with traditional synthesis. One such material is doped Ln:YVO_4, used in lamps and displays,[55] and another is the production of 'Thernard's blue' ($Co_xZn_{1-x}Al_2O_4$) and both can be made by simply heating a mixture of aqueous metal salts with starch to form a gel, followed by calcination in air. Starch behaves as both the chelating agent and as the medium to stop sintering in the early stages for heating.[56] Carbides, as well as oxides, can be produced by a starch sol-gel route and due to the tuneable nature of starch it is possible to produce specific structural features in the precursor which are carried fourth to the final product. An example of such is a porous metal carbide, SiC, produced from starch as both the gelling agent and carbon source.[57]

The above discussion of the various types of sol-gel has shown that there are a number of advantages to solution based chemistry over conventional based so called 'solid state' reactions, especially when biopolymers are employed. It is important to note that this does not mean solid state reactions are inferior but the sol-gel is more adaptable in certain situations. Data from this chapter has been published, please find the paper for this work in Appendix F from page 257.

1.4 REFERENCES

(1) Livage, J. *New Journal of Chemistry* **2001**, *25*, 1.

(2) Anastas, P. T.; Warner, J. C. *Green chemistry: theory and practice*; Oxford university press, 2000.

(3) Imeson, A. *Food stabilisers, thickeners and gelling agents*; John Wiley & Sons, 2011.

(4) ltd, N. G. I. *39th Annual Report*, 2014-2015 Revtrieved from http://gelatin.in/uploads/companyfinancials/1848568350-2016-06-02_01-43-31.pdf.

(5) Schnepp, Z.; Wimbush, S. C.; Antonietti, M.; Giordano, C. *Chemistry of Materials* **2010**, *22*, 5340.

(6) Schnepp, Z.; Hall, S. R.; Hollamby, M. J.; Mann, S. *Green Chemistry* **2011**, *13*, 272.

(7) Thompson, E.; Danks, A. E.; Bourgeois, L.; Schnepp, Z. *Green Chemistry* **2015**, *17*, 551.

(8) Kuo, C. L.; Carl, M. D.; Google Patents: 1950.

(9) Schwarzkopf, P.; Kieffer, R.; Benesousky, F. *Refractory hard metals: borides, carbides, nitrides and silicides*; Macmillan, 1953.

(10) Ebelmen *Justus Liebigs Annalen der Chemie* **1846**, *57*, 319.

(11) Mehrotra, R. C. *Journal of Non-Crystalline Solids* **1988**, *100*, 1.

(12) Livage, J.; Henry, M.; Sanchez, C. *Progress in Solid State Chemistry* **1988**, *18*, 259.

(13) Kakihana, M. *J Sol-Gel Sci Technol* **1996**, *6*, 7.

(14) Flory, P. J. *Faraday Discussions of the Chemical Society* **1974**, *57*, 7.

(15) Cushing, B. L.; Kolesnichenko, V. L.; O'Connor, C. J. *Chemical Reviews* **2004**, *104*, 3893.

(16) Danks, A. E.; Hall, S. R.; Schnepp, Z. *Materials Horizons* **2016**.

(17) Brinker, C. J.; Scherer, G. W. *Sol-gel science: the physics and chemistry of sol-gel processing*; Academic press, 2013.

(18) Que, W.; Sun, Z.; Zhou, Y.; Lam, Y. L.; Chan, Y. C.; Kam, C. H. *Thin Solid Films* **2000**, *359*, 177.

(19) Green, W. H.; Le, K. P.; Grey, J.; Au, T. T.; Sailor, M. J. *Science* **1997**, *276*, 1826.

(20) Gill, I.; Ballesteros, A. *Journal of the American Chemical Society* **1998**, *120*, 8587.

(21) Changrong, X.; Huaqiang, C.; Hong, W.; Guangyao, M.; Dingkun, P. *Journal of membrane science* **1999**, *162*, 181.

(22) Sui, R.; Charpentier, P. *Chemical Reviews* **2012**, *112*, 3057.

(23) Pasquarelli, R. M.; Ginley, D. S.; O'Hayre, R. *Chemical Society Reviews* **2011**, *40*, 5406.

(24) Liu, Y.; Goebl, J.; Yin, Y. *Chemical Society Reviews* **2013**, *42*, 2610.

(25) Courtney, R.; Gustafson, R.; Chaberek Jr, S.; Martell, A. *Journal of the American Chemical Society* **1958**, *80*, 2121.

(26) Xu, G.; Ma, H.; Zhong, M.; Zhou, J.; Yue, Y.; He, Z. *Journal of Magnetism and Magnetic Materials* **2006**, *301*, 383.

(27) Flynn Jr, C. M. *Chemical Reviews* **1984**, *84*, 31.

(28) Pechini, P. M.; US Patent 3,330,697: 1967.

(29) Wang, J. X.; Tao, Y. K.; Shao, J.; Wang, W. G. *Journal of Power Sources* **2009**, *186*, 344.

(30) Worayingyong, A.; Kangvansura, P.; Ausadasuk, S.; Praserthdam, P. *Colloids and Surfaces A: Physicochemical and Engineering Aspects* **2008**, *315*, 217.

(31) Stux, A. M.; Laberty-Robert, C.; Swider-Lyons, K. E. *Journal of Solid State Chemistry* **2008**, *181*, 2741.

(32) Wu, S.; Zhang, S.; Yang, J. *Materials Chemistry and Physics* **2007**, *102*, 80.

(33) Niederberger, M.; Garnweitner, G. *Chemistry-A European Journal* **2006**, *12*, 7282.

(34) Hayat, K.; Gondal, M.; Khaled, M. M.; Ahmed, S.; Shemsi, A. M. *Applied Catalysis A: General* **2011**, *393*, 122.

(35) Sun, Y.-K.; Oh, I.-H. *Ind. Eng. Chem. Res.* **1996**, *35*, 4296.

(36) Liu, T.; Xu, Y.; Zhao, J. *Journal of the American Ceramic Society* **2010**, *93*, 3637.

(37) Lukić, S.; Petrović, D.; Dramićanin, M.; Mitrić, M.; Đačanin, L. *Scripta Materialia* **2008**, *58*, 655.

(38) Kandhasamy, S.; Pandey, A.; Minakshi, M. *Electrochimica Acta* **2012**, *60*, 170.

(39) García-Márquez, A.; Portehault, D.; Giordano, C. *Journal of Materials Chemistry* **2011**, *21*, 2136.

(40) Liu, S.; Zhang, L.; Zhou, J.; Wu, R. *The Journal of Physical Chemistry C* **2008**, *112*, 4538.

(41) Alonso, B.; Belamie, E. *Angewandte Chemie International Edition* **2010**, *49*, 8201.

(42) Hall, S. R. *Biotemplating: complex structures from natural materials*; World Scientific, 2009.

(43) Gómez-Guillén, M.; Turnay, J.; Fernández-Dıaz, M.; Ulmo, N.; Lizarbe, M.; Montero, P. *Food Hydrocolloids* **2002**, *16*, 25.

(44) Yoshimura, K.; Terashima, M.; Hozan, D.; Ebato, T.; Nomura, Y.; Ishii, Y.; Shirai, K. *Journal of Agricultural and Food Chemistry* **2000**, *48*, 2023.

(45) Eastoe, J. *Biochemical Journal* **1955**, *61*, 589.

(46) Eldridge, J. E.; Ferry, J. D. *The Journal of Physical Chemistry* **1954**, *58*, 992.

(47) Djabourov, M.; Leblond, J.; Papon, P. *Journal de physique* **1988**, *49*, 319.

(48) Usov, A. I. *Food Hydrocolloids* **1998**, *12*, 301.

(49) Campo, V. L.; Kawano, D. F.; Silva Jr, D. B. d.; Carvalho, I. *Carbohydrate Polymers* **2009**, *77*, 167.

(50) Chaplin, M. http://www1.lsbu.ac.uk/water/agar.html, 2003.

(51) Walsh, D.; Arcelli, L.; Ikoma, T.; Tanaka, J.; Mann, S. *Nature materials* **2003**, *2*, 386.

(52) Gonzalez-McQuire, R.; Green, D.; Walsh, D.; Hall, S.; Chane-Ching, J.-Y.; Oreffo, R. O.; Mann, S. *Biomaterials* **2005**, *26*, 6652.

(53) Walsh, D.; Kulak, A.; Aoki, K.; Ikoma, T.; Tanaka, J.; Mann, S. *Angewandte Chemie International Edition* **2004**, *43*, 6691.

(54) Walsh, D.; Wimbush, S. C.; Hall, S. R. *Chemistry of Materials* **2007**, *19*, 647.

(55) Zhang, H.; Fu, X.; Niu, S.; Xin, Q. *Journal of Alloys and Compounds* **2008**, *457*, 61.

(56) Visinescu, D.; Paraschiv, C.; Ianculescu, A.; Jurca, B.; Vasile, B.; Carp, O. *Dyes and Pigments* **2010**, *87*, 125.

(57) Raman, V.; Bahl, O.; Dhawan, U. *Journal of Materials Science* **1995**, *30*, 2686.

CHAPTER 2

MECHANISTIC STUDY OF BIOPOLYMER SYNTHESIS FOR DESIGNER POROUS NANOCOMPOSITES

2.1 BACKGROUND

Carbon is a plentiful and cheap resource and so being able to incorporate it into any material if possible is economical and environmentally sustainable. In fact, carbon is found in many products, one of its uses is a porous structure. Porous carbons can be synthesised via many routes and biopolymer directed sol-gel chemistry offers a facile route to porous carbons. Porous carbons generally are utilised as catalysts[58,59] or their supports,[60,61] batteries/fuel cells[61] or any area where a large accessible surface area is required. Another example of where porous carbons have gained interest is environmental remediation (including nuclear waste management[62]) and obviously a green synthesis route would further increase the appeal of these materials. Here a photoactive semiconductor is spread across a large surface area and the pores means there is greater contact with the water further increasing activity.[63]

For the areas described above the embedding nanoparticles on the porous carbon has the potential to enhance its activity and reduce the size of a device by combining the support and active sites into one layer. Also for all of these areas the carbon must have a long life time (must retain most of its structure over the life time of the device) and be cost effective; this is important for reducing the overall cost of the device. In fuel cells the carbon support must remain stable whilst being heated with water or hydrogen being flown over it. A catalyst can either be in liquid or solid form but there are advantages to having a solid, for example it can be easily removed or had the reactants flown over it.

Biopolymers offer an attractive alternative to synthesising porous carbons due to their ready availability and that fact they are easy to work with. They also afford the opportunity to incorporate their chemical and structural complexity into porous carbons, both of which are important for catalysts. Potentially incorporating the hieratical nature of various porous would allow to tune their carbon support to guide the reactants in specific pathways. Commonly porous carbons are used as composites are these different components need to be within close proximity but also with high surface areas: therefore control over the active sites is as crucial as is the transport of reactants to them. In addition to generating the carbon structure biopolymers can be used to control the shape and size of the particles that decorate the surface of the carbon. Several examples of biopolymer being used to produce porous carbons exist as they offer a 'non-templated' route; this means you can remove steps where you remove the template. Alginic acid has been wet spun to produce fibres and generate pores of various shapes and sizes around nanoparticles. This allowed hierarchical structures to be made which again are useful for electrochemical capacitors, batteries, etc.[64]

The background information pertaining to the chemistry of gelatin was discussed in Chapter 1 so that information will not be repeated here, however it is important to remember that, as mentioned previously, gelatin is currently used in many industries (i.e. food, pharma, etc.). As a result a lot is known about the structure and chemistry of gelatin and through using this knowledge base it was thought that trends could be rationalised and possibly extend the theory to other biopolymers; this is necessary to the complex nature of these systems. Gelatin is a particularly interesting option for this as the structure of the polypeptide varies a lot depending on source and extraction method. There have been number of different materials synthesised using gelatin including metal oxides/nitrides/carbides and composites of these with carbon, which highlights the wide potential of this biopolymer to produce functional materials.

Synthesis of the aforementioned oxide/nitride/carbide nanocomposites has been extensively developed by Schnepp *et al* and as a result there are many examples of materials that have been produced (e.g. TiO_2/Fe_3C, TiO_2/WN or MgO/Fe_3C).[65] Interestingly, despite a homogeneous precursor, this phase separation occurs without further work and it is thought to be due to the different thermal stabilities of the metals. Further work was carried out on the

MgO/Fe_3C system and mild acid washing was found to produce carbons with trimodal (macro/meso/micro) porosity by selectivity removing some nanoparticles.[66] More recently an *in-situ* synchrotron powder diffraction study was used to ascertain the mechanism for Fe_3C formation; understanding this should provide insights on how to control particle size and possibly how to form other carbide. Initially iron oxide (FeO_x) nanoparticles, <3 nm in diameter are formed, these then react with N_2 in the carbon matrix to form Fe_3N nanoparticles which then go through a carbonitride intermediate to the final carbide.[67] As well as acting as the carbon source gelatin is also constraining the particle size by slowing sintering by binding to the metal ions.

The scope of gelatin BSG is not limited to porous carbons with embedded nanoparticles to be used as described above (i.e. as catalysts, etc), although this will be the focus of the chapter. As an example of the wide scope it is possible to prepare high purity and finely particular terbium-doped yttrium aluminium garnet(YAG:Tb). This is important for the production of scintillation counters and CRT projection and the gelatin sol-gel route has advantages over a traditional solid-state route. Gelatin has many side-chains and can bind to multiple metal centres, once bound the gelatin is able to gel and direct crystal growth. For this example, a mixture of aluminium, yttrium and terbium nitrates was mixed with hot aqueous gelatin are cooled to form a gel, the metal species were then converted to the hydroxide form by addition of ammonia. After drying *in vacuo* calcination in air produces fine powders of YAG:Tb, again the slower decomposition of the biopolymer controls multi-nucleation and small particle size (~40 - 55 nm).[68]

There are other ways of producing foams, such as combustion synthesis. Like the gelatin synthesis it has been possible to generate a wide range of oxides but also nitrides, carbides and composites.[69] In general either solid or liquid based precursor are mixed and heated to a temperature where they ignite and combust, usually at high temperatures (800 - 1500 °C).[70] It is also possible to create porous materials and over the last 10 years a great deal of control has been achieved over morphology and particle size.[71] Biopolymers have even been included to control particle growth and help to generate the porous network.[72] This work has mainly been aimed at oxides and so the gelatin foaming synthesis offers simple, low temperature route to carbides and other composites.

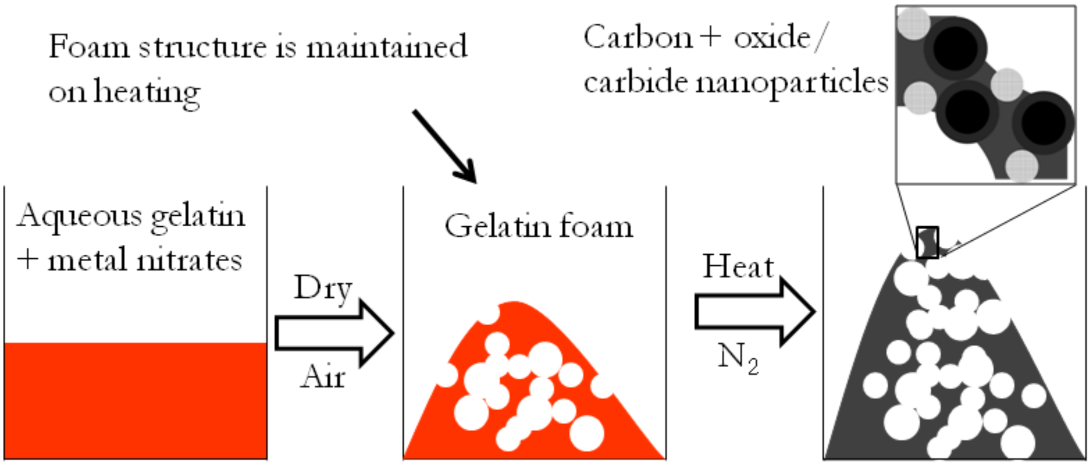

Figure 2.1 Schematic of general synthesis route showing the forming process

The gelatin BSG synthesis is described in detail in the experimental section of this chapter, but briefly the general synthesis is, gelatin is added to hot (~70 °C) water and stirred to homogeneity then a metal precursor is then added to this to form a gel. The gel is dried in an oven to remove water before being calcined under nitrogen to carbonise the gelatin and form the nanoparticles, Figure 2.1.[65] Some combinations of gelatin and metal nitrate cause spontaneous foaming upon drying and little was known about foaming mechanism.

Control over how to initiate and tailor this foaming process could lead to a designer system where the structure and composition could be controlled (e.g. x sized nanoparticles with y sized pores). This work focuses on nanocomposites of transition metal (TM) carbides/nitrides embedded on a porous carbon, as well as oxide/carbide or oxide/nitride mixtures. Another aim of this work was to use what was learnt about the gelatin system to explain why some biopolymer/metal combinations foam and others do not), this understanding would allow for even more control during the synthesis. Various techniques were employed to ascertain the mechanism, this chapter will detail these experiments and try to rationalise any trends before finally attempting to affect changes in the porous carbons by changing various parameters. Data from this chapter has been published in the Journal of Materials Chemistry A, please find the paper for this work in Appendix F from page 257.

2.2 EXPERIMENTAL

General experimental techniques, e.g. XRD, TEM, used through all chapters are described in Appendix E along with information about how the experimental techniques and how the instruments function.

2.2.1 MATERIALS

Below is a list of materials used in this chapter.

Table 2.1 list of materials used for synthesis and analysis in this chapter

Chemical	Supplier	CAS number
Gelatin, type A, porcine, G2500, 300 bloom strength	Sigma Aldrich	9000-70-8
Copper(II) nitrate hemipentahydrate	Sigma Aldrich	19004-19-4
Calcium(II) nitrate tetrahydrate	Sigma Aldrich	13477-34-4
Magnesium(II) nitrate hexahydrate	Sigma Aldrich	13446-18-9
Potassium(I) nitrate	Sigma Aldrich	7757-79-1
Sodium(I) nitrate	Sigma Aldrich	7631-99-4
Strontium(II) nitrate	Sigma Aldrich	10042-76-9
Cerium(III) nitrate hexahydrate	Sigma Aldrich	10294-41-4
Iron(III) nitrate nonahydrate	Sigma Aldrich	7782-61-8
Aluminium(III) nitrate nonahydrate	Sigma Aldrich	7784-27-2
Cobalt(II) nitrate hexahydrate	Sigma Aldrich	10026-22-9
Manganese(II) nitrate hydrate	Sigma Aldrich	15710-66-4
Nitric acid (70% w/w)	Sigma Aldrich	7697-37-2
Hydrochloric acid (37% w/w)	Sigma Aldrich	7647-01-0
Iron chloride	Sigma Aldrich	7705-08-0
Ethanol	VWR	64-17-5

2.2.3 SYNTHESIS OF GELS

Gelatin plus various metal gels were synthesised using the same method; the following paragraphs detail this method highlighting the iron system, the values required for the other metals are used in Table 2.2.

A 10% (w/v) gelatin solution was prepared by adding gelatin to hot and rapidly stirred distilled water (90 mL, 70 °C) until a homogeneous solution was obtained (solution A). A 10% (w/v) iron nitrate solution was prepared by placing iron nitrate in a 100 mL volumetric flask and filling with distilled water. Solution A (20 g) was transferred to a beaker covered with a watch glass and heated (70 °C) with rapid stirring, to this iron nitrate solution (40.40 mL) (0.01 M of metal) was added. The solution became more viscous (most metals) and brown (iron only).

From this point there were two different synthesis routes:-

1) Samples were used without further preparation for foaming experiments.

2) The solution was placed in a drying oven at 70 °C until a solid was obtained. The resulting solid was calcined under flowing nitrogen in a muffle furnace at 800 °C with a ramp rate of 10 °C min^{-1} and a 5 min hold at maximum temperature to ensure this temperature was reached.

The mixed metal systems were synthesised as below

A 10% (w/v) gelatin solution was prepared by adding gelatin to hot and rapidly stirred distilled water (90 mL, 70 °C) and stirred until a homogeneous solution was obtained (solution A). Separately, 10 % (w/v) iron and magnesium nitrate solutions were prepared by placing the respective metal nitrates in a 100 mL volumetric flask and filling with distilled water. A mixed solution was made from these stock solutions, the stock solutions were mixed at the desired ratio to give an overall concentration of metal of 0.01 M (solution B).

Solution A (20 g) was transferred to a beaker covered with a watch glass and heated (70 °C) with rapid stirring, solution B was added. The rest of the synthesis followed as above.

Samples of gelatin with nitric acid were prepared with the same concentration of NO_3^- as for the sample using $Fe(NO_3)_3.9H_2O$. To achieve this, 3.3 mL of 1 mol L^{-1} nitric acid was added to 20 g of 10% (w/v) gelatin solution.

Samples of gelatin with HCl were prepared to examine the effect of pH without NO_3^- by adding 1M HCl to 20 g of 10% (w/v) gelatin solution until the pH was the same as the HNO_3/gelatin sample.

Table 2.2 List of metal nitrates used with number of mols and volumes of stock solution used

Metal	Moles of metal	Volume of 10 % stock solution (mL)
Copper	0.01	23.30
Calcium	0.01	23.60
Magnesium	0.01	25.60
Potassium	0.01	10.10
Sodium	0.01	8.50
Strontium	0.01	21.20
Cerium	0.01	43.40
Iron	0.01	40.40
Aluminium	0.01	37.51
Cobalt	0.01	29.10
Manganese	0.01	17.90

2.2.4 CIRCULAR DICHROISM (CD)

To start with the following conditions were varied to find the optimal condition:- cell length, concentration of gelatin, type of gelatin: throughout all of these experiments and the ones to follow a constant volume was kept to minimise any unwanted concentration effects. From these results a 1% (w/v) porcine gelatin in a 0.5 mm cell was selected for the experiments.

A 2% (w/v) gelatin solution was prepared by adding gelatin (2 g) to heated and stirred distilled water (98 mL, 70 °C). The 2 % gelatin solution (5 mL) was added to a test tube and to the a total of 5 mL was added - this was made of varying amounts of 1 % w/v iron nitrate solution and topped up by additional water before it was added to the test tube. The test tube was then shaken and aliquots were immediately transferred to quartz cells and scanned from 400 - 200 nm at 200 nm min^{-1}. This method was repeated for a number of metals, Table 2.3. The instrument used for these measurements was a Jasco J-810 spectropolarmeter.

Table 2.3 Sample list for CD

Sample ID	Metal/Added chemical	Vol of metal salt (mL)	Volume of water (mL)
1gel_0_2Fe_5	Fe	1	4
1gel_0_4Fe_5	Fe	2	3
1gel_0_6Fe_5	Fe	3	2
1gel_0_8Fe_5	Fe	4	1
1gel_1Fe_5	Fe	5	0
1gel_0_1Fe_5	Fe	0.5	4.5
1gel_0_2Na	Na	1	4
1gel_0_4Na	Na	2	3
1gel_0_6Na	Na	3	2
1gel_0_8Na	Na	4	1
1gel_1Na	Na	5	0

2.2.5 RHEOLOGY

Resins were made with increasing amounts of 50% (w/v) iron nitrate solution added to distilled water to make a total of 10 mL, this was heated in a vial (70 °C). This is the maximum concentration at which it is possible to homogenise the solution. Gelatin (2 g) was added to the vials, they were sealed and quickly mixed using a vortex mixer, the solutions were then place in a oven (70 °C, <60 minutes) to homogenise before finally being vortex mixed again and left to cool to room temperature. This scheme was used for iron and various other metals, Table 2.4 shows the exact amount of metal nitrate solution added. A control was synthesised, gelatin (2 g) was added to water (10 mL) and homogenized in the same manner as before.

After trials a cone/plate geometry was adopted. The cone had a 40 mm diameter and an incline of 2 ° and the plate was a 40 mm diameter sand blasted circle. The plate was heated to 50 °C to melt the gelatin and then cooled (25 °C) once the plate and cone were brought into working distance (1000 μm). The value of G_0 was then measured at oscillation frequency of 1 Hz in a strain sweep test from 0.1 % to 50 %. This stress sweep was performed in order to determine the limit of the linear viscoelastic regime. The rest of the rheological measurements were frequency sweep tested with a % strain limit of 2 % maintained over the whole frequency range (0.01 - 100 Hz (rad/s)). Some of the rheological measurements were repeated with the concentrations shown for SANS, this was to allow for a better comparison. The instrument used was a TA instruments AR G2.

Table 2.4 Ratios of metal salt use for the gel formation to be used in rheological measurements

Metals	Moles	Volume of 50 %v/w stock (mL)	Volume of water (mL)
Iron	0.01	8.08	1.92
	0.0075	6.06	3.94
	0.005	4.04	5.96
	0.0025	2.02	7.98
Magnesium	0.01	5.12	4.88
	0.0075	3.84	6.16
	0.005	2.56	7.44
	0.0025	1.28	8.72
Iron : Magnesium	0.0075 : 0.0025	6.06 : 1.28	2.66
	0.005 : 0.005	4.04 : 2.56	3.40
	0.0025 : 0.0075	2.02 : 3.84	4.14

2.2.6 INFRARED SPECTROSCOPY

Resins were made with increasing amounts of 20% (w/v) solutions of metal nitrates to water to make a total of 10 ml, these solutions were heated in vials on a hot plate (50 °C). After gelatin (0.5 g) was added to the vials they were sealed and quickly mixed using a vortex mixer, the solutions were then placed in a oven (70 °C, <60 minutes) to homogenise before finally being vortex mixed again and left to cool to room temperature.

Scans were run from 1000 cm^{-1} to 4000 cm^{-1} for 2 minutes. Table 2.5, shows the preparation for the gels for sodium. The instrument used for IR measurements was a Perkin Elmer FT-IR spectrometer Spectrum Two.

Table 2.5 Volumes and masses needed to make resins for IR

Mol % of Metal	Moles	Vol of stock for 1.0g of gelatin (µL)	Added water (µL)	Total volume (µL)
Na				
0	0	0.00	450.00	550.00
5	0.0005	21.25	428.75	550.00
10	0.001	42.50	407.50	550.00
15	0.0015	63.75	386.25	550.00
25	0.0025	106.25	343.75	550.00
50	0.005	212.50	237.50	550.00
75	0.0075	318.75	131.25	550.00
100	0.01	425.00	25.00	550.00
Fe				
0	0	0.00	2020.00	2020.00
5	0.0005	101.00	1919.00	2020.00
10	0.001	202.00	1818.00	2020.00
15	0.0015	303.00	1717.00	2020.00
25	0.0025	505.00	1515.00	2020.00
50	0.005	1010.00	1010.00	2020.00
75	0.0075	1515.00	505.00	2020.00
100	0.01	2020.00	0.00	2020.00

2.2.7 SANS

Resins were made with increasing amounts of 20% (w/v) solutions of metal nitrates in D_2O to make a total of 10 mL, these solutions heated in vials on a hot plate (50 °C). After gelatin (0.5 g) was added to the vials they were sealed and quickly mixed using a vortex mixer, the solutions were then placed in an oven (70 °C, <60 minutes) to homogenise before finally being vortex mixed again and left to cool to room temperature. Table 2.6 shows the exact amount of metal nitrates added (20% (w/v)), other metals were also used using the corresponding amount of the relevant metal nitrate. A control was also made, gelatin (0.5 g) was added to D_2O/H_2O (10 mL) and homogenised in the same manner as before. Hydrogen has an incoherent scattering background and it is in the gelatin and bound to the hydrated metal nitrates; to account for this aliquots of H_2O were added so that all samples had a constant volume of H_2O before being topped up to 10 mL with D_2O.

The SANS measurements were carried out at the ISIS Neutron and Muon source, Rutherford Appleton Laboratory, UK on SANS2D. Samples were housed in Hellma cells with a path length of 2 mm and a thermostated sample changer provided temperature control. A beam width of 8 mm was used, providing a detectable Q range of order 0.001 – 1 $Å^{-1}$. Absolute intensities for I(Q) (in cm^{-1}) were determined by calibrating the received signal for the following variables:- sample transmission, solvent background, which was H_2O and D_2O, and a polymer standard. Other metals from the foaming experiments were used and prepared in a similar manner to the table below. The fitting procedure will be discussed with the results.

Table 2.6 Showing the ratios of metal salt use for the gel formation to be used in rheological and SANS measurements

Sample ID	Volume of Mg nitrate stock (mL)	Volume of Fe nitrate stock (mL)	Extra H_2O required (mL)	Mass of gelatin (g)
MF100	0	5.05	0.000	0.5
MF75	0.8	3.79	0.034	0.5
MF70	0.96	3.54	0.041	0.5
MF65	1.12	3.28	0.047	0.5
MF60	1.28	3.03	0.054	0.5
MF55	1.44	2.78	0.061	0.5
MF50	1.60	2.53	0.068	0.5
MF25	2.40	1.26	0.101	0.5
MF5	3.04	0.25	0.128	0.5
MF2	3.14	0.10	0.132	0.5
MF1	3.17	0.05	0.134	0.5
MF0p1	3.2	0.05 (2% (w/v))	0.135	0.5
MF0p1_20	3.2	0.005	0.135	0.5
MF0	3.2	0.00	0.135	0.5
MF75c	0.00	3.79	0.101	0.5
MF70c	0.00	3.54	0.122	0.5
MF65c	0.00	3.28	0.142	0.5
MF60c	0.00	3.03	0.162	0.5
MF55c	0.00	2.78	0.182	0.5
MF50c	0.00	2.53	0.203	0.5
MF25c	0.00	1.26	0.304	0.5
MF15c	0.00	0.76	0.344	0.5
MF5c	0.00	0.51	0.365	0.5
MF2c	0.00	0.25	0.385	0.5
MF1c	0.00	0.10	0.397	0.5
MF0p1c	0.00	0.05	0.401	0.5
MF0p1_20c	0.00	0.005	0.405	0.5
Control	0.00	0.00	0.00	0.5

2.2.8 FORMING ONSET EXPERIMENT

Liquid samples as prepared by synthesis route 1 (shown earlier) were placed in 100 mL beakers inside a vacuum oven retro fitted with a nitrogen feed, this was to prevent charring on top of the samples. Samples were dried at 70 °C over night and then the temperature was raised 10 °C and held at this temperature for 3 hours, this was repeated until 200 °C was reached.

2.2.9 THERMOGRAVAMETRIC ANALYSIS/MASS SPECTROMETRY

Samples were run separately under both argon and nitrogen (as in the standard synthesis) so that the carrier gas wouldn't overlap with peaks of interest. A drop of metal nitrate/gelatin (~6 mg, as synthesised in route 1) was placed in a dry alumina crucible and this was placed in the TGA chamber with flowing argon. Then it was heated at 10 °C min^{-1} to 800 °C. The exhaust gases passed through heated capillary tubes into a mass spectrometer. The mass spectrometer scanned through a predefined range of masses continuously. These experiments were also carried out with the dried gelatin foam, this was to minimise the effect of the water loss peak dominating the data. The TGA used was a Netzsch STA 449 F1 Jupiter and the mass spectrometer was a Netzsch QMS 403C Quardrupole Mass Spectrometer.

2.2.10 GEL STRENGTH TESTS

These tests were carried out at Healan Ingredients. A 1/2 inch plunger was pushed 20 mm into the samples and then pulled out. The instrument measures the load as a function of distance. The first 4 mm of depression from the surface of a sample gives the 'bloom strength'.

20% (w/v) solutions of iron and magnesium nitrates were prepared by dissolving them in deionised water. Gelatin solutions were prepared by dissolving gelatin (5g) in deionised water (50 mL) at 70 °C. Table 2.7 shows the volume of metal nitrate diluted to a total volume of 50 mL. Once the gelatin solution had homogenised, it was combined with the required metal nitrate solution, the mixture was stirred and cooled and then placed in a fridge overnight (~16 hours) to set. Samples were stored in a cool bag with ice blocks and removed one by one directly before the gel strength was measured. These tests were carried out at Healan Ingredients. It should be noted that to be a bloom strength test it should be in a particular shaped jar and the gelatin should be 6.66% (w/v) and other protocols should have been followed.[73] Therefore the numbers obtained cannot be quoted as actual bloom strengths but the trends are of use.

Table 2.7 Sample list for gel strength tests

Sample	Moles of iron nitrate	Vol of 20%w/v iron nitrate (mL)	Moles of magnesium nitrate	Vol of 20%w/v magnesium nitrate (mL)
MF100	0.02500	50.50	.	.
MF50	0.01250	25.25	.	.
MF25	0.00625	12.63	.	.
MF10	0.00250	5.05	.	.
MF5	0.00125	2.53	.	.
MF2	0.00050	1.01	.	.
MF1	0.00025	0.51	.	.
MG100	0.00000	0.00	0.025	32.05
Control	0.00000	0.00	0.000	0.000

2.3 INVESTIGATION OF FOAMING STEP

2.3.1 ONSET FOAMING TEMPERATURE

There are a number of questions around the foaming process, i.e. what is the cause of the foaming and what factors can affect the foaming process once is has started. To answer this seemingly easy question and to understand how the gelatin + metal nitrate system behaves, a series of gelatin + metal nitrate gels were made and dried at 70 °C. The metals had 1+ - 3+ valency and came from every block in the periodic table, their hydration also varied, such a wide range was chosen to probe the metal binding ability of gelatin and also to discover trends across the periodic table. Some of the samples formed dry 'sponge-like' foams however most of the samples did not and dried into a ‘glass-like’ disk on the bottom of the beaker. The unexpected result was that some samples foamed a small amount but did not fully dry even after days in the oven, these have been designated as sticky foams. All the results can be seen below, Figure 2.2.

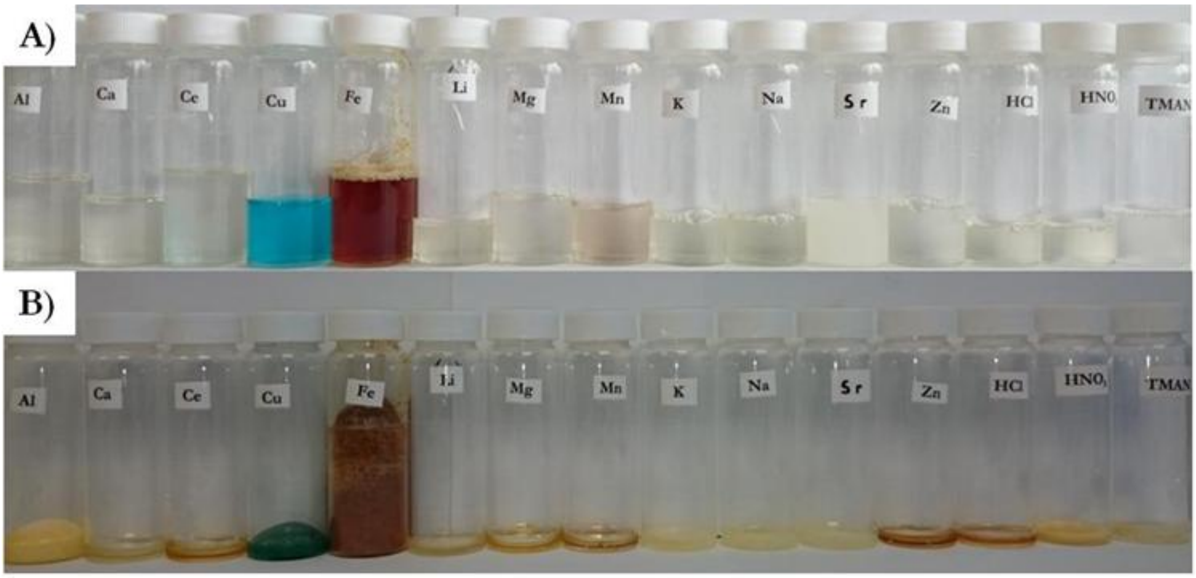

Figure 2.2 Gelatin with various metal nitrates before (A) and after (B) drying at 70 °C

Gelatin, if calcined in an inert atmosphere, will decompose at ~350 °C (this is consistent with TGA) and it forms a very open and weak foam, so it's clear the metal nitrates are having a profound effect on this process. The discovery of the sticky foams then lead to an experiment where the temperature was incrementally increased and it was conducted to find out if these sticky foams would continue to foam and dry out. These sticky foams and the 'glass-like' samples starting foaming so the study was continued to see if all the metals would cause foaming at relativity low temperatures (<200 °C). The results of the temperature controlled study are below, Figure 2.3, and included in this table are tetramethyl ammonium nitrate (TMAN) and two acids (HNO_3, HCl) with gelatin. TMAN was selected because it has no metal ions, it was thought that this would not perturb the system too much and the ammonium would have less affinity for the gelatin so the overall system would be closer to pure gelatin (i.e. a way to investigate the effect of nitrate on its own). The photos in the table show the range over which all the samples will foam whilst also showing the foam structure at the final temperature. All nitrate samples will foam below 200 °C, the exception to this is the only none nitrate sample, HCl, and two photos show that there is no foaming over this temperature range. The different valencies of the metals mean there is a different amount of nitrate in the various samples for the same molar ratio of metal ions. This combined with the varying pH's of the metal solutions means that addition of these control samples was necessary to investigate these variables. The HNO_3 sample was calculated to contain the same number of moles of NO_3^- as the iron sample and the HCl sample was adjusted to the same pH as the HNO_3 sample. The general trend with the metal nitrates is the lower valency metals foam at higher temperature than the higher valency ones. The concentration of metal ions in all the samples were the same (0.01 M) so the levels of NO_3^- will vary with valency, as mentioned earlier, so this effect could simply be an effect of the counter ion.

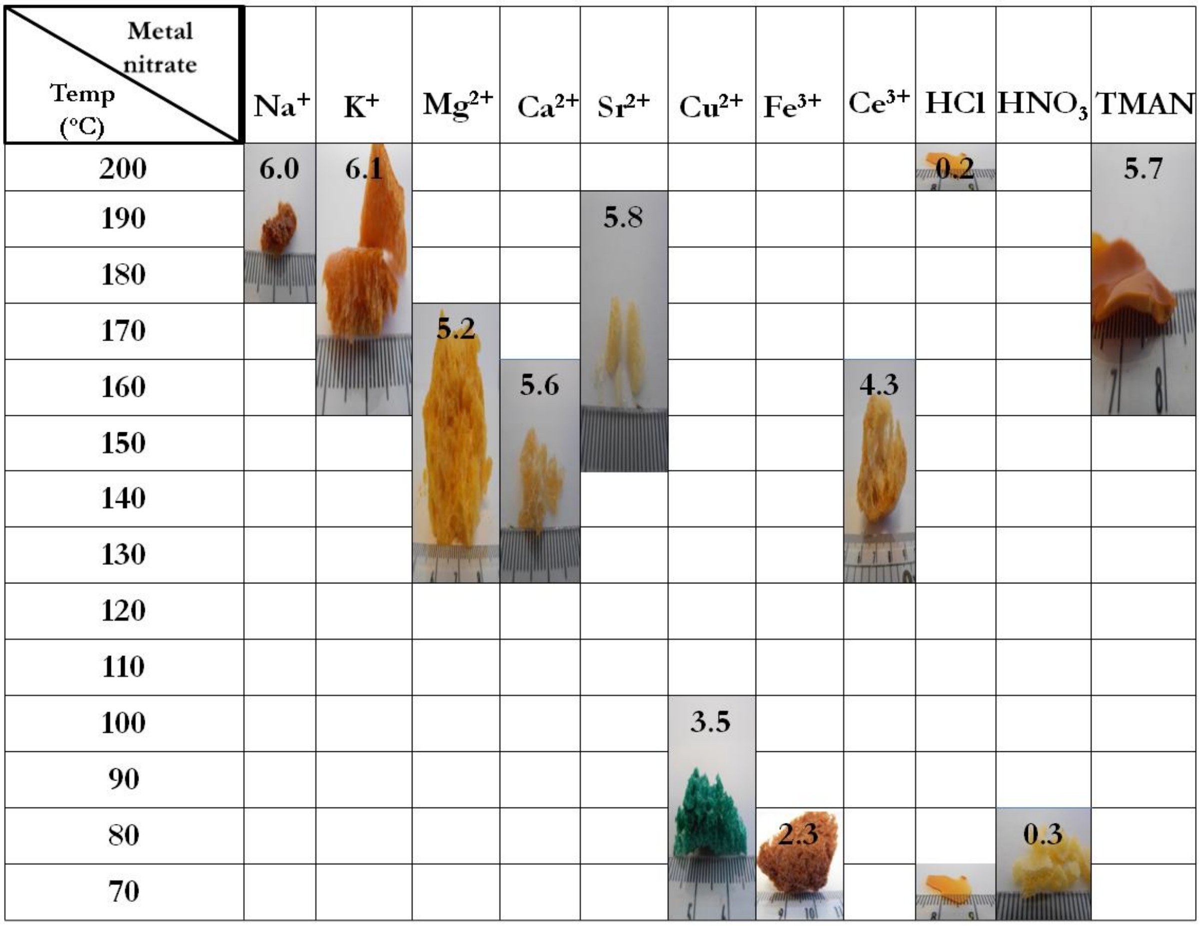

Figure 2.3 Foaming temperature for a series of metal nitrate samples, HCl, HNO_3 and TMAN. The image shows the range over which the foaming occurs. Exception - HCl has 2 pictures to symbolise no foaming over entire range. Insert over each picture is the corresponding pH of a 10% (w/v) metal nitrate solution

The pH of these systems must be considered as these nitrates are acidic, pH's are also shown in Figure 2.3. Interestingly they follow the same trend as the foaming onset study with lower pH samples foaming at lower temperatures and higher pH samples foaming at higher temperatures. There are 2 anomalies, Sr^{2+} and Ce^{3+}, these samples foam at higher temperatures than would be expected from their charge, this can be explained through their high pH's. The valency of the metal ions, $[NO_3^-]$ and the pH's show the same trend, but both are inherently linked so further tests were needed to ascertain which is more important.

From the HCl sample is it clear that low pH alone doesn't enhance the foam at low temperatures. The nitric acid sample foamed at low temperatures (as expected) and the TMAN sample foamed at a higher temperature, which was initially surprising, but easily explained using the trends in the pH. At ~200 °C TMAN forms a thin foam of densely packed small bubbles and HCl showed a few bubbles in the glass-like resin; these samples were then heated further in a nitrogen atmosphere muffle furnace to ~300 °C where they both foamed further.

2.3.2 FOAM STRUCTURE - OPTICAL, SEM AND TEM

Figure 2.5 shows that the two factors discussed so far are not only factors controlling the process as all the foam structures are very different. Their discrete structures are retained throughout the heating process as seen in Figure 2.5; after drying (A), after calcination (B) and as imaged by SEM(C). For comparison a SEM images of pure gelatin and 50 mol% Mg and Fe are shown in, Figure 2.4, calcined at 800 °C, it is clear from comparison of these images the metal nitrates are having a large effect on the final structure.

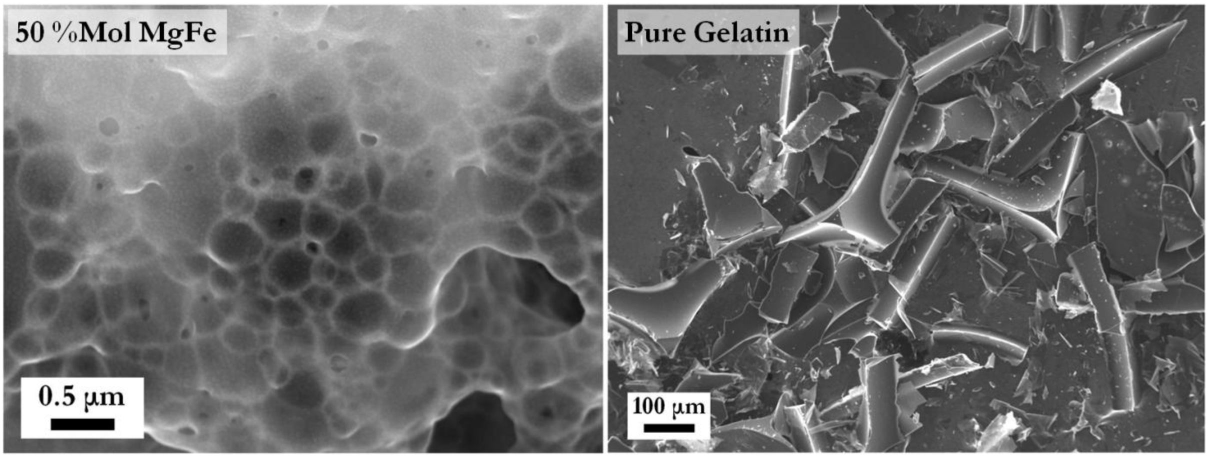

Figure 2.4 SEM images of 50 mol% MgFe and pure gelatin.

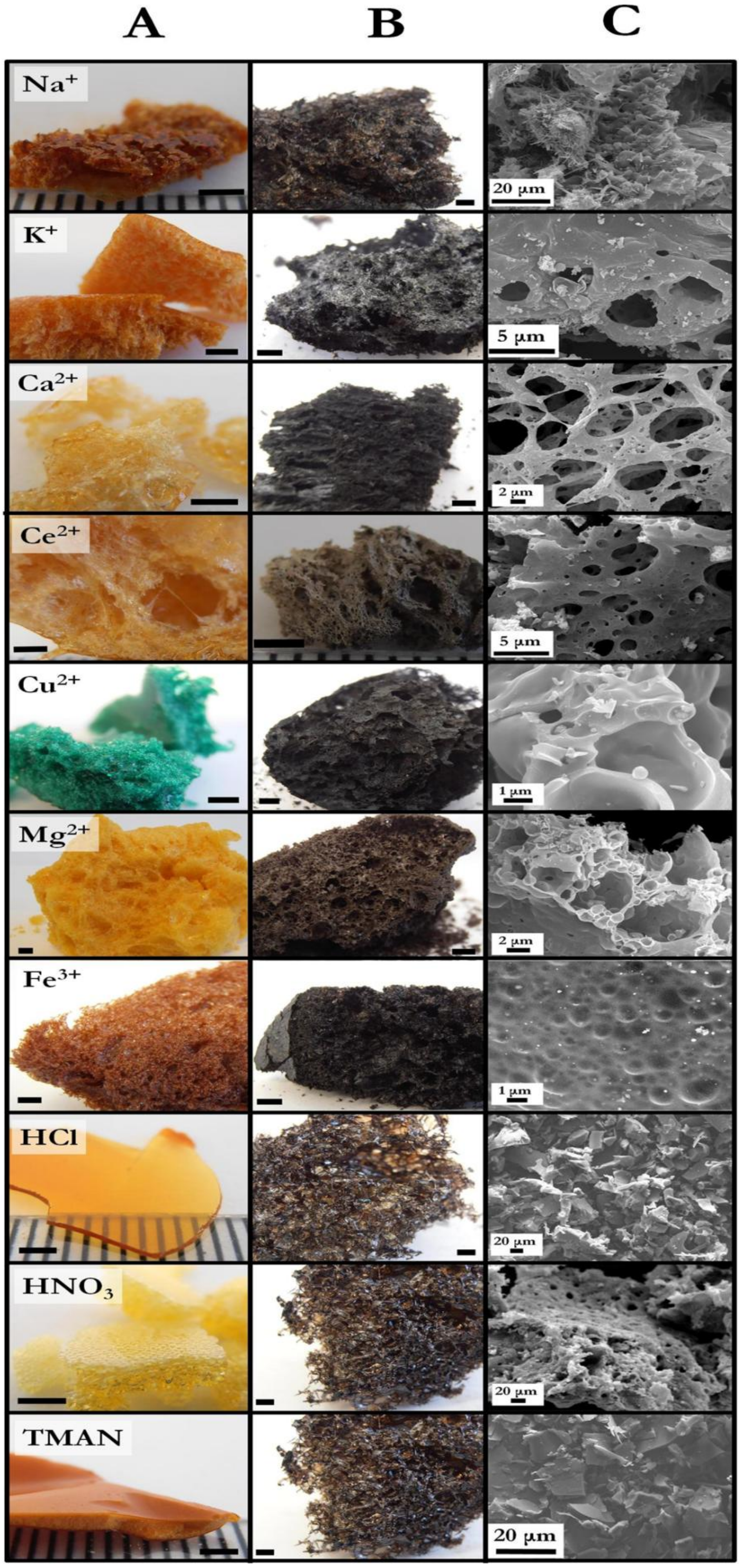

Figure 2.5 Gelatin plus various nitrates and acids - (A) photographs after drying; images (B) and SEM images (C) after calcination at 800 °C

TEM was carried out to further investigate the final material. The different metals not only cause differences in the foam structure but also in the particle size. Figure 2.6 shows TEM images of 2 different metals; the particle size for each sample is very different so for this to be a truly tuneable system if a method to control particle size can be devised. It should be noted however that size range for both samples is 2 - 20 nm, showing that the gelatin is able to slow sintering at 800 °C. Another factor that could be affecting the size is the fact that copper has fully reduced and the cerium is isolated as its oxide.

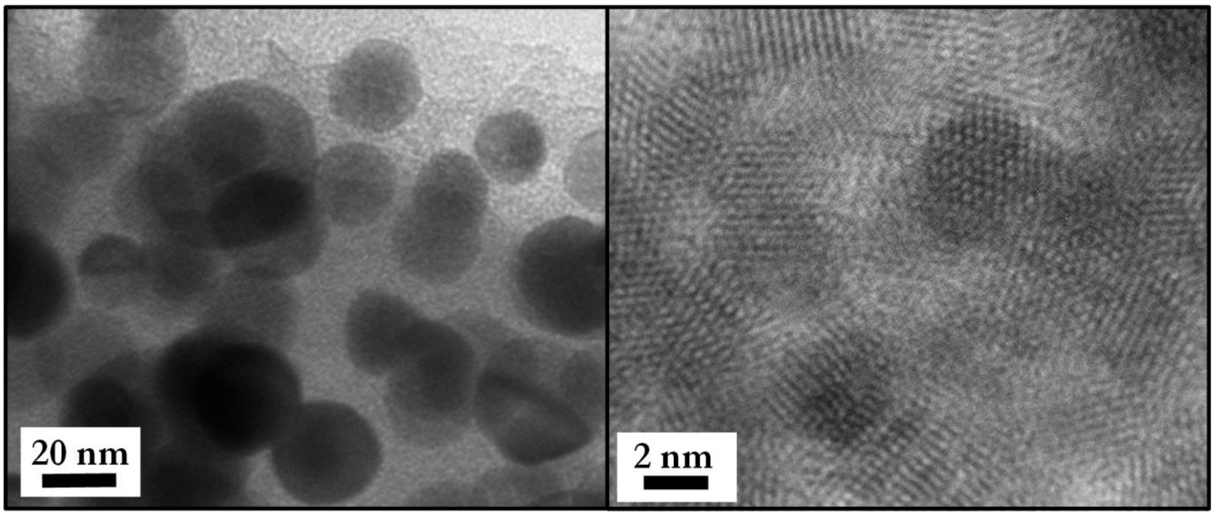

Figure 2.6 TEM images of the nano crystallites of cerium dioxide (left) and copper (right) embedded in carbon, after synthesis at 800 °C in a nitrogen atmosphere

X-ray diffraction (XRD) patterns of the gelatin + magnesium (MgGel) samples enhanced with acid (described later) show a significant change in the peak broadening from pure MgGel to MgGel plus acids, Figure 2.7. Scherrer analysis of these three patterns show the biggest change in particle size from adding nitric acid, see Scherrer analysis in Appendix A. The nitric acid sample shows particles that are outside the range of the Scherrer equation, but the trend is still useful to highlight that with further study particle size could be tuned: this is done without changing the end product, by adding acid to the precursor gel. The hydrochloric acid sample doesn't show much change in particle size so is not a good option for changing the particle size.

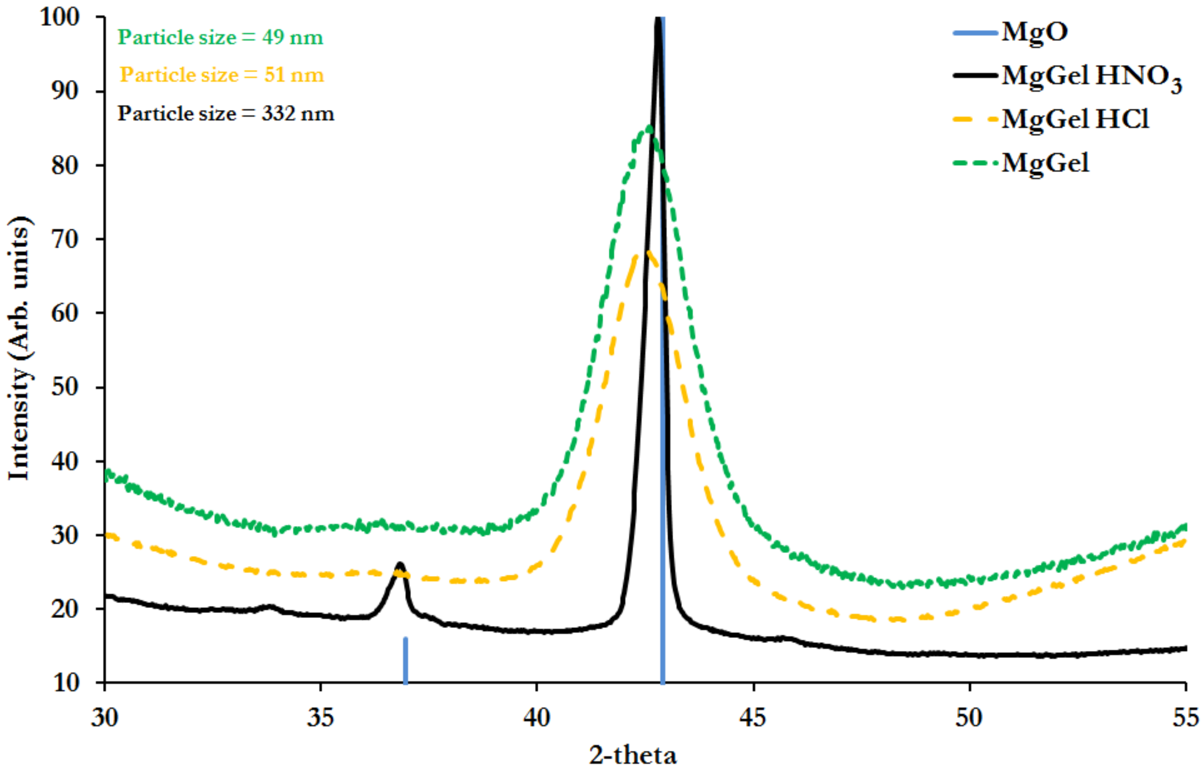

Figure 2.7 XRD patterns of MgGel with and without nitric and hydrochloride acids synthesised at 800 °C in a nitrogen atmosphere

Iron and magnesium samples were chosen to further study the effects of the nitrate on the system as we have handled these the most, so from a basic point of view, i.e. day to day handling of these, a lot is already known about them and any changes would be easier to see. The iron nitrate sample has a $^{1}/_{3}$ more nitrate than the magnesium sample (3+ vs 2+ metal salt) so nitric acid was added to the magnesium sample to increase the moles of nitrate to be the same as the iron sample. In the standard samples without additives the iron/gelatin foams, where as the magnesium sample does not. The additional nitrate added to the magnesium samples was done to see if it this is a concentration effect, the acid enhanced sample was dried as before, at 70 °C, this did foam. Foaming resulted in a dry sponge but it was not the same height as the iron sample so increased amount of nitrate ion seems to aid the process but is not the only factor at work.

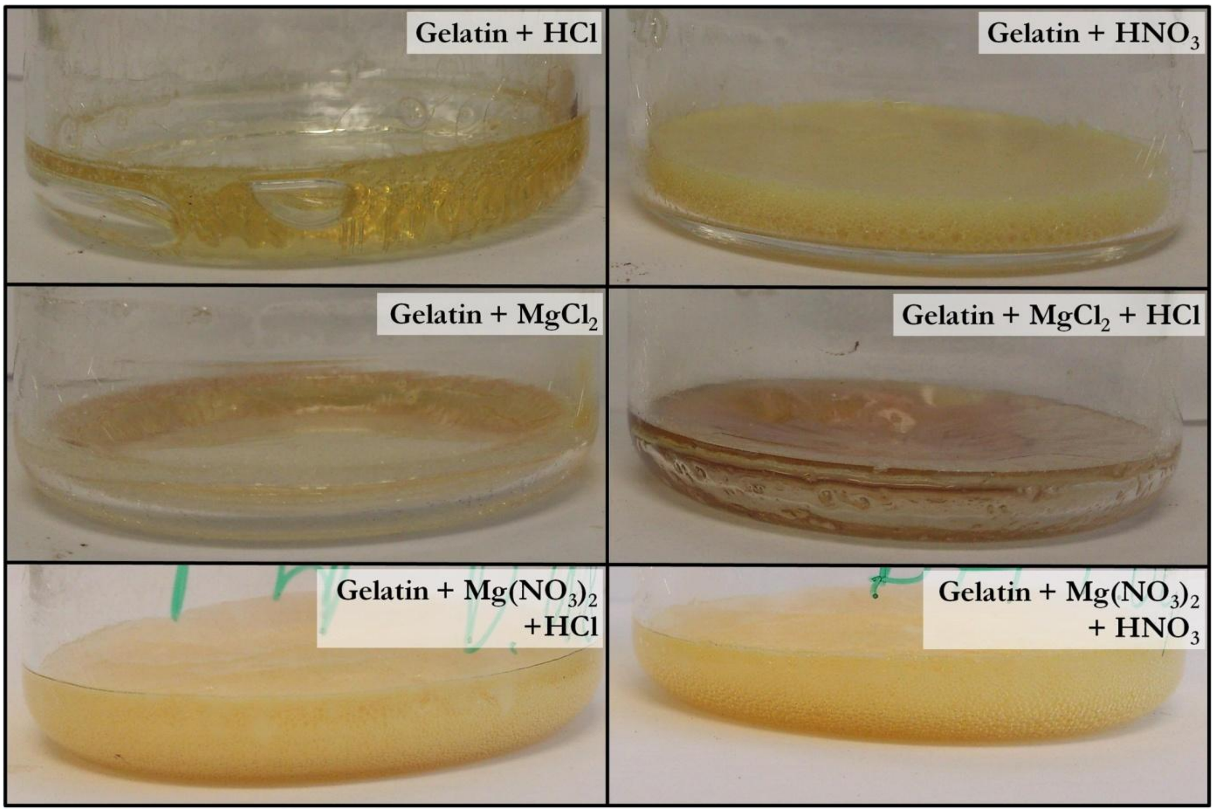

Figure 2.8 Images of gelatin samples with various additives, showing how these affect the amount of foaming

The nitric acid enhanced magnesium sample had a pH of approximately 1, so another magnesium sample was synthesised and this one was enhanced with hydrochloric acid until a pH of 1 was achieved. Figure 2.8 shows that regardless of which acid was used, the Mg/gelatin foams the same amount at pH 1, so the counter ion (NO_3^-) may not be as important as previously thought. Figure 2.8 also shows that gelatin when combined and dried with HCl and HNO_3, the former of these combinations does not foam but the latter does; interestingly not to the same height as a Mg/HNO_3/gelatin sample or Fe/gelatin sample. Finally the magnesium source was changed to $MgCl_2$, this does not foam when dried by itself or when enhanced by HCl but it does with HNO_3. These data confirms the trend indentified of needing low pH and NO_3^- present for foaming to occur at 70 °C. Following these trends TMAN with its high pH and lack of metal meant it had a high foaming temperature and did not foam to a similar height as the other metals.

TMAN forms a disc ~5 mm thick and close visual examination shows there are densely packed bubbles. TMAN has a pH of ~7.5 and foamed less than all of the lower pH metal nitrates so it could mean that the lowing the pH will make the sample foam more/at lower temperatures. To test this TMAN samples were prepared with the addition of HCl and HNO_3 (separately), these were dried and did foam into a dry sponge at 70 °C, Figure 2.9. The effect of the metal on foaming is another interesting phenomenon, it has a profound effect on the foam, but it is not needed to proceed. Also combining metals, such as iron and magnesium, leads to a synergistic effect where the bubble size is much smaller, understanding this can lead to further tuning of the foam structure, Figure 2.4, which is discussed later.

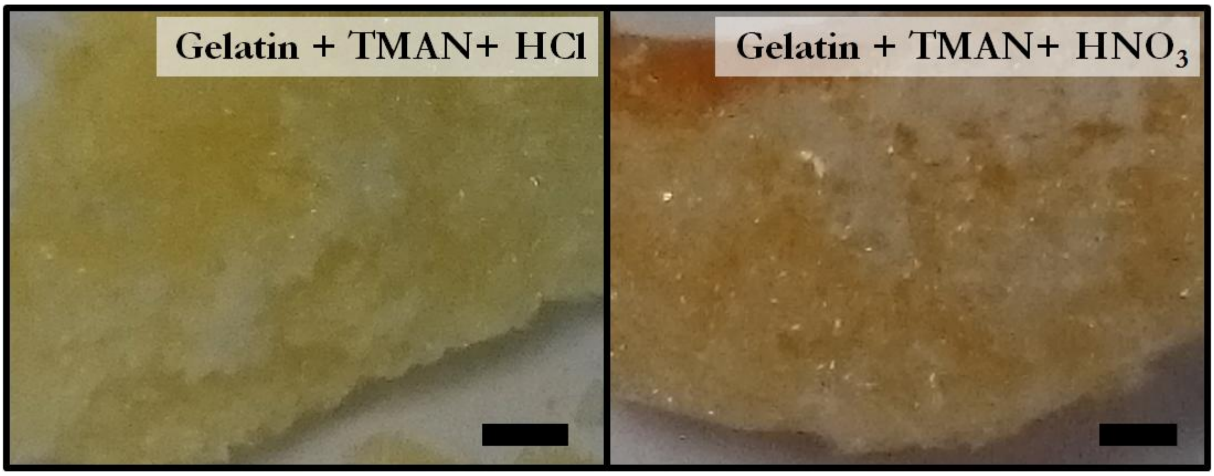

Figure 2.9 Photographs of gelatin + TMAN enhanced with acid after foaming at 70 °C, 1 cm scale bar.

2.3.3 GELATIN DECOMPOSITION AT HIGHER TEMPERATURES - TGA/MS

Knowing factors that seem to control the foaming of a sample, the next task was to find the cause of the initial foaming. As water evaporates the NO_3^- concentration will increase and highly concentrated nitrate solutions have been known to react with certain amino acids to form yellow nitrated precipitates. This process is call the xanthoproteic reaction and the precipitate is xanthoproteic acid.[74] A lot of samples turned more yellow when compared to pure gelatin, so this could be evidence of this reaction. Initially it was thought that if the NO_3^- was reacting with the biopolymer it may be giving off NO_x and this gas evolution could lead to the formation of the bubbles. Several experiments were devised to collect the gas to be analysed, in a gas chromatograph or passed through water to change the pH, Figure 2.10. These were unsuccessful as either there was no pH change detected (A) or it was not possible to dry the gel (B). This could mean that no N_yO_x is being given off or these experiments weren't able to detect it. A more sensitive experiment was needed, and this was achieved with thermogravametric analysis which passes the exhaust gases through a mass spectrometer (TGA-MS). This allowed the gases leaving the sample to be indentified and linked the processes happening; i.e. if the nitrate was reacting with the gelatin it would give off NO_x. Caution was needed for these experiments as these would normally be carried out with 30 - 60 mg of sample, however as these samples expand on calcination this would push the lid off the crucible. Very small amounts (< 8 mg) of sample were used, as a result gas detection was more difficult.

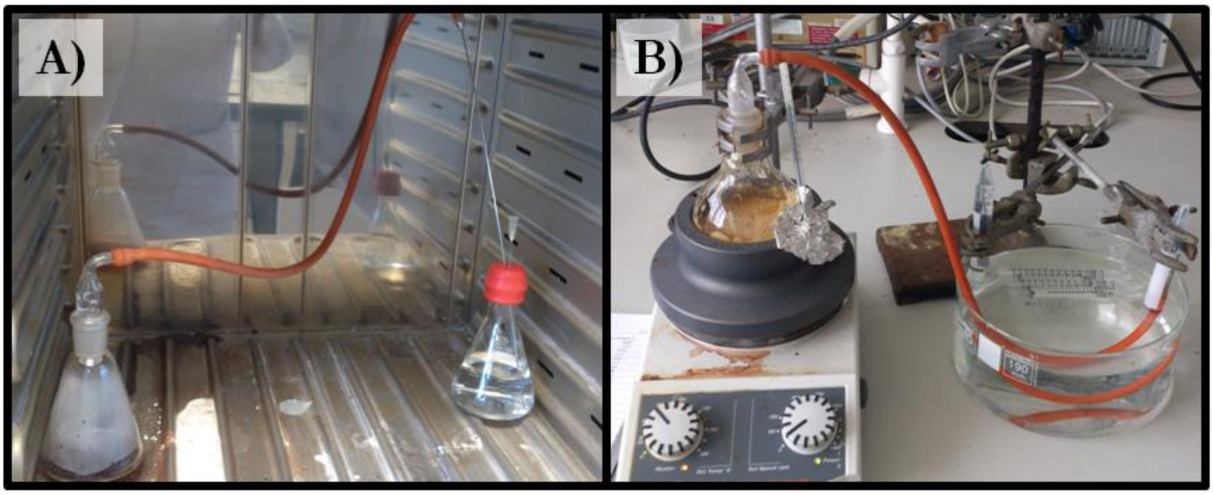

Figure 2.10 Photographs of experimental to detect a pH change; A) gelatin + iron nitrate dried in a oven; B) gelatin plus iron nitrate dried on a hot plate to collect exhaust gases.

The mass loss data with mass spectrum data for selected mass to charge ratios (m/z) are shown in Figure 2.11. For pure gelatin there are 2 peaks in the MS data for m/z = 18 (water), one at ~100 °C from water in solution around the gelatin; the second one at ~350 °C is from water between the strands in the gelatin helix, i.e. water molecules bound to gelatin. This shows that gelatin is still able to hold some of it structure even up to this higher temperature. At ~350 °C there is also mass lost due to CO_2/N_2O (m/z 44) this is from the gelatin decomposing, further supporting the hypothesis that gelatin retains some of its structure up to this temperature. It is not possible to indentify without an IR attachment which gas it is, however it is sensible to assume that it is mostly CO_2. The comparably large water loss to that of NO_x/CO_2 (~10x less) at temperatures less than 200 °C suggests that the main cause of foaming is water evaporation. Visual observations of samples in deeper beakers supports this, foaming appears to start from the top of the sample, as the gel dries forming a 'film'. This film is forced up as the remaining water is driven off; the gelatin 'traps' these bubbles, causing the 'sponge-like' structure that is seen. This also rationalises the slightly thicker shell observed in these samples.

This was repeated for gelatin with magnesium and iron both separately and as a 50 mol% mixture. All of these samples continue to lose mass above 100 °C, this is mainly from water loss but is also accompanied by peaks in the MS data for M/Z = 44. Again due to the large water loss compared to CO_2/NO_x the principal foaming mechanism is water evaporation, further supporting our previous assessment. The iron and magnesium only systems have different mass loss curves with the Mg having more steps below 350 °C. Interestingly the mixed metal system has features from both. The 50 mol% mixture also has much smaller pores compared to the other samples, because it has the greatest surface and therefore contact with the flowing nitrogen this could be linked to its low decomposition temperature. Figure 2.12 shows evidence that nitrate ions oxidise gelatin, causing it to decompose earlier, it shows the MS data for M/Z = 30 (nitric oxide (NO)). There are peaks for all of the metal nitrate containing samples below ~350 °C but this is not seen in the pure gelatin, which has a very small increase above 350 °C.

The observation of the yellow samples does not mean that nitrate oxidation is the cause of the foaming, however it can help rationalise it. As the NO_3^- concentrates (due to evaporation) it starts to attack gelatin and this affects, amongst other things (i.e. gel strength), its ability to control bubble formation. Another physical observation was the apparent change in stiffness of the gel, decreasing and increasing, with increasing amounts of the metal nitrates, especially iron nitrate. Having indentified the cause of the foaming as water evaporation, the different structures observed could be to the ability of the gelatin to stabilise the bubbles; a product of gel strength and metal interactions.

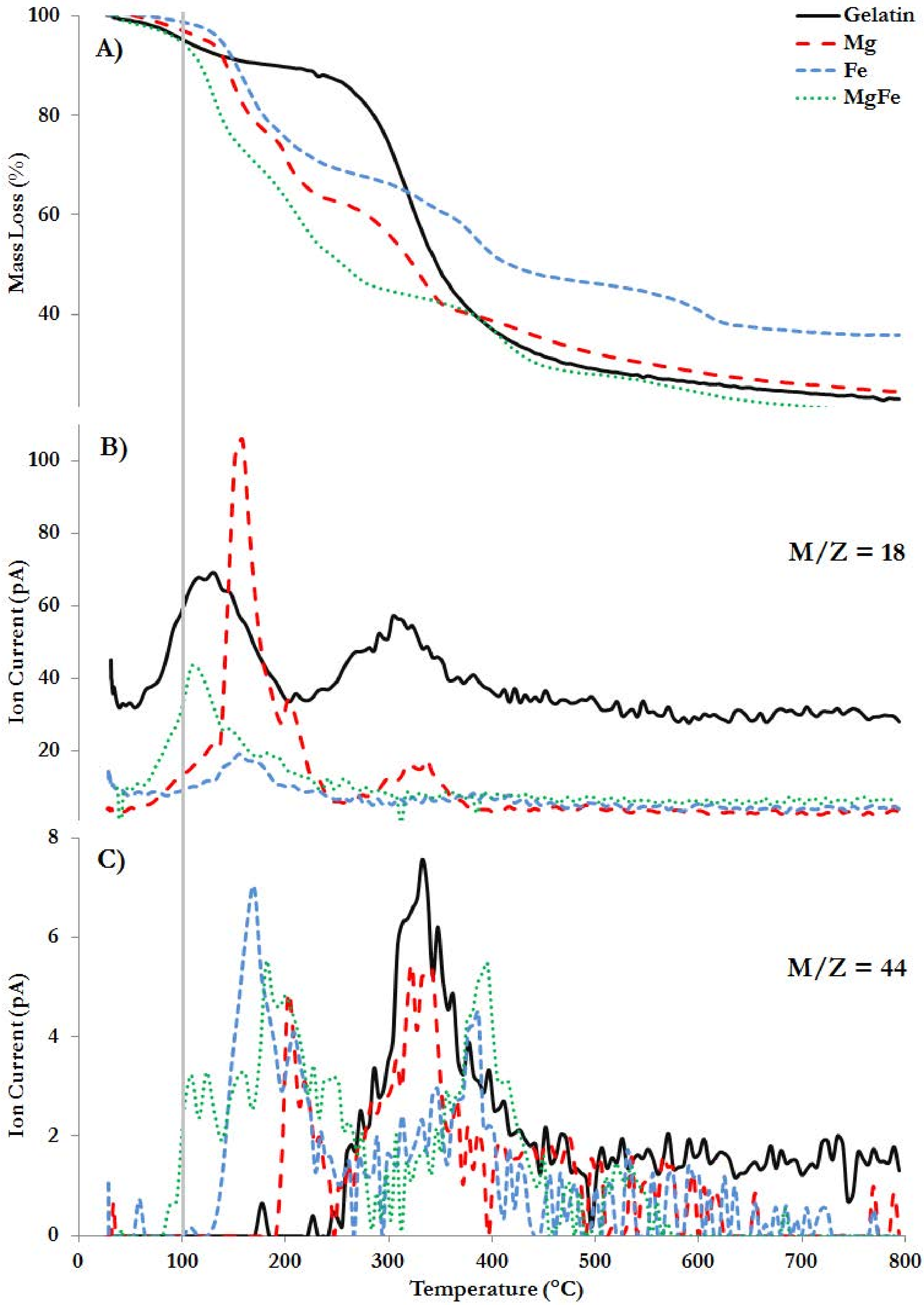

Figure 2.11 A) TGA traces showing the mass lost for a series of gelatin + metal nitrates, MS data for B) water, C) CO_2/N_2O

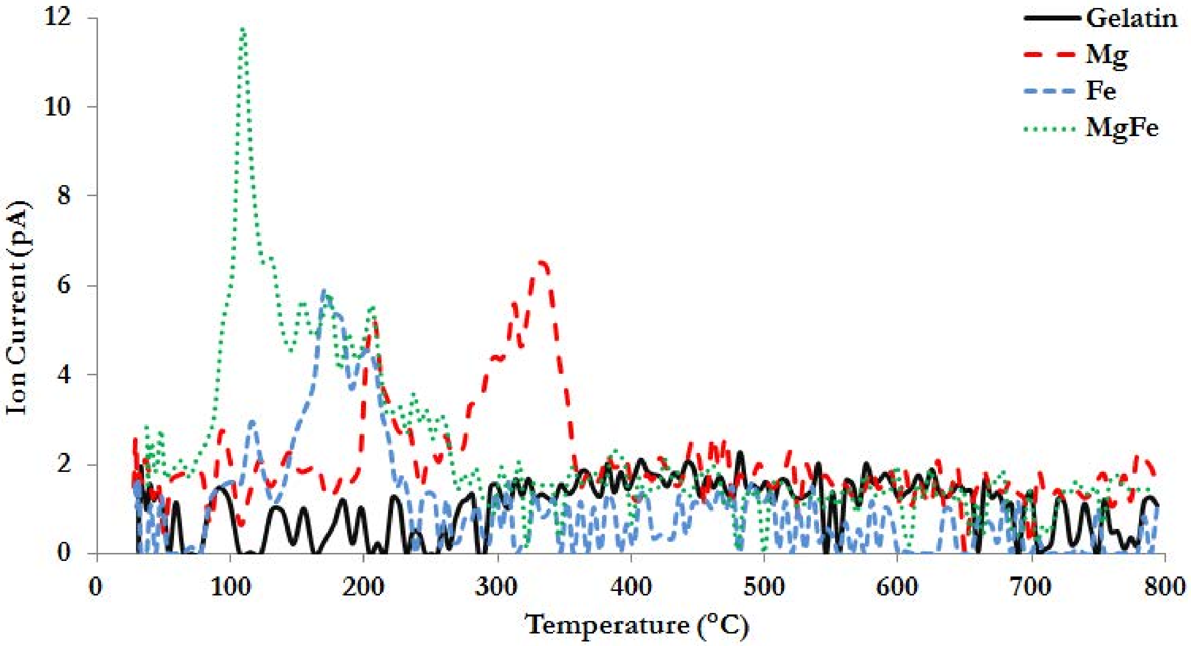

Figure 2.12 A) MS data for NO (M/Z 30)

2.3.4 INVESTIGATION OF GEL STRENGTH AND STRUCTURE - BLOOM STRENGTH AND RHEOLOGY

As previously mentioned it is well documented that gelatin forms triple helical junction zones when in water; this is what causes gelatin to form gel.[47] When metal salts are added they are visually quite different, for example for a sample with a total metal concentration of 0.01 M of iron in a 10% (w/v) (20 mL) gelatin solution once cooled the solution is very runny. The same number of moles of magnesium the gel is still able to almost re-set and a mixture of both has the consistency of golden syrup. There are a number of ways to investigate these trends, gel strength tests, rheology and SANS will now be discussed.

The bloom strength test, devised in 1925 by Oscar T. Bloom,[73] determine the number of grams needed to depress the surface of a sample by 4 mm using a 1/2 inch diameter plunger. To be a strict Bloom strength test a standard operating procedure must be followed (i.e. shape/size of jar, preparation time, concentration) so the actual numbers for this test cannot be used to calculate the actual bloom strength however the trends are still of use. The gel strength test involved pressing on the samples until the surface broke, this is indicated by a sharp decline in the load needed to depress the sample. The units for this test are gram-force (gf), this is equivalent to a 1 g mass multiplied by the acceleration due to gravity (1 gf = 9.8 mN). Figure 2.13 shows pure gelatin (Gelcont) has a breaking force of 700 gf at 11 mm, with more iron there is a slight increase in force needed indicating a firmer gel (MFB-1c). The numbers in the codes represent the molar % out of a total 0.01 M (100%) and MFB indicates these are iron and magnesium samples produced for the bloom strength tests. Increasing iron concentration, MFB-2c, requires also most the same force as the previous sample but the plunger was able to go deeper before the surface broke showing the increased elasticity of the sample. Increasing the iron concentration further to 5% weakens the gel and then the rest of the samples follow the same trend.

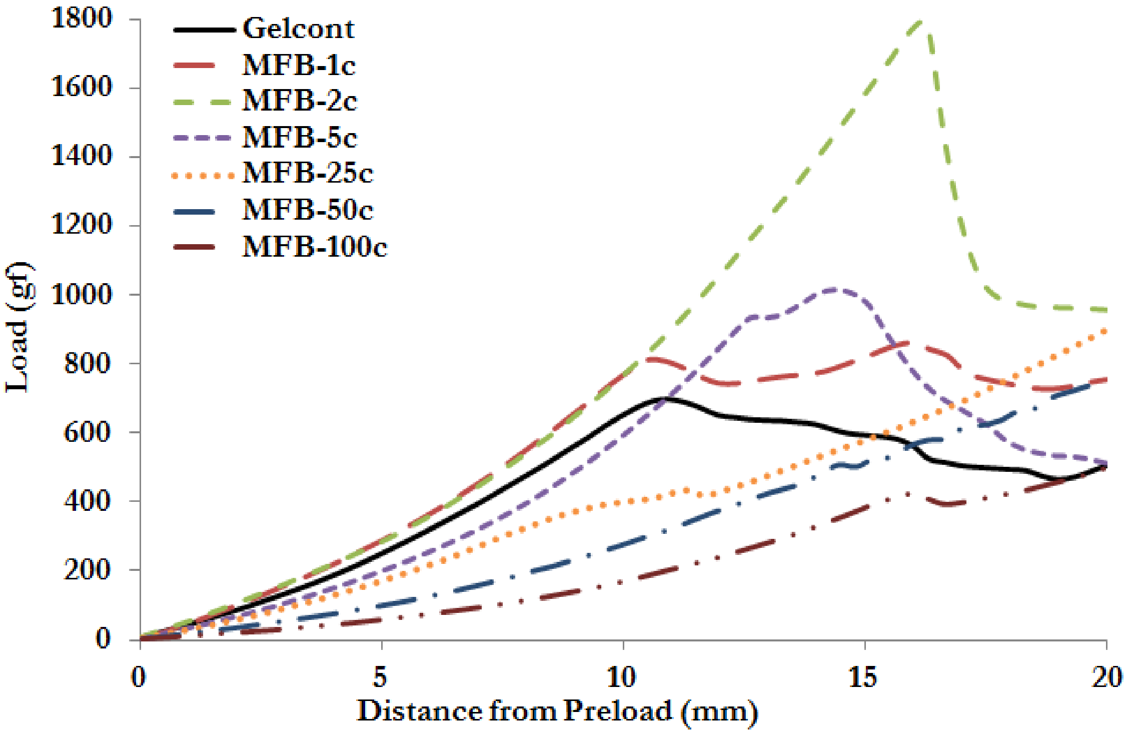

Figure 2.13 Load vs distance plot from a bloom strength test showing the breaking point for a series of gelatin + iron samples

Rheology was used to probe the visco-elastic properties to investigate to what extent the metal binding was interfering with the gelling ability of gelatin and therefore changing the visco-elastic properties. The solid black lines, Figure 2.14, refer to pure gelatin, and is the elastic modulus (G') and the dashed black line corresponds to the loss modulus (G''). This is characteristic of a visco-elastic solid, which we would expect from gelatin at 25 °C. When a small amount of iron nitrate is added (see figure legend) the sample becomes very viscous and does flow slowly, this is mirrored by the rheology. The dashed line is above the solid line in the respective pairs, which is typical for a visco-elastic liquid. The lines then converge and cross indicating the sample is responding like visco-elastic solid on the time scale of the oscillations. This means at low frequency oscillations the sample is able to flow back and forth between the cone and plate but cannot flow at higher frequency oscillations. This holds true for the even higher concentrations of iron which are less viscous and therefore are able to withstand the higher frequency oscillations before reverting to acting like a visco-elastic solid. The X's in this figure shows the crossover point from a viscous liquid to an elastic solid for each pair of lines. As this crossover point gets later in the frequency sweep, this could lead to a way of testing the resins to size select the pores in the liquid state by simply controlling the visco-elastic properties of the gel. Similar trends can be seen with magnesium samples although with a sharper transition.

The original rheology data was carried out at slightly different concentrations so a series was made at the concentrations used in the SANS data. Figure 2.15, shows the curvature of the data sets is slightly different but the cross over points are in the same place so the 'old' data is still valid.

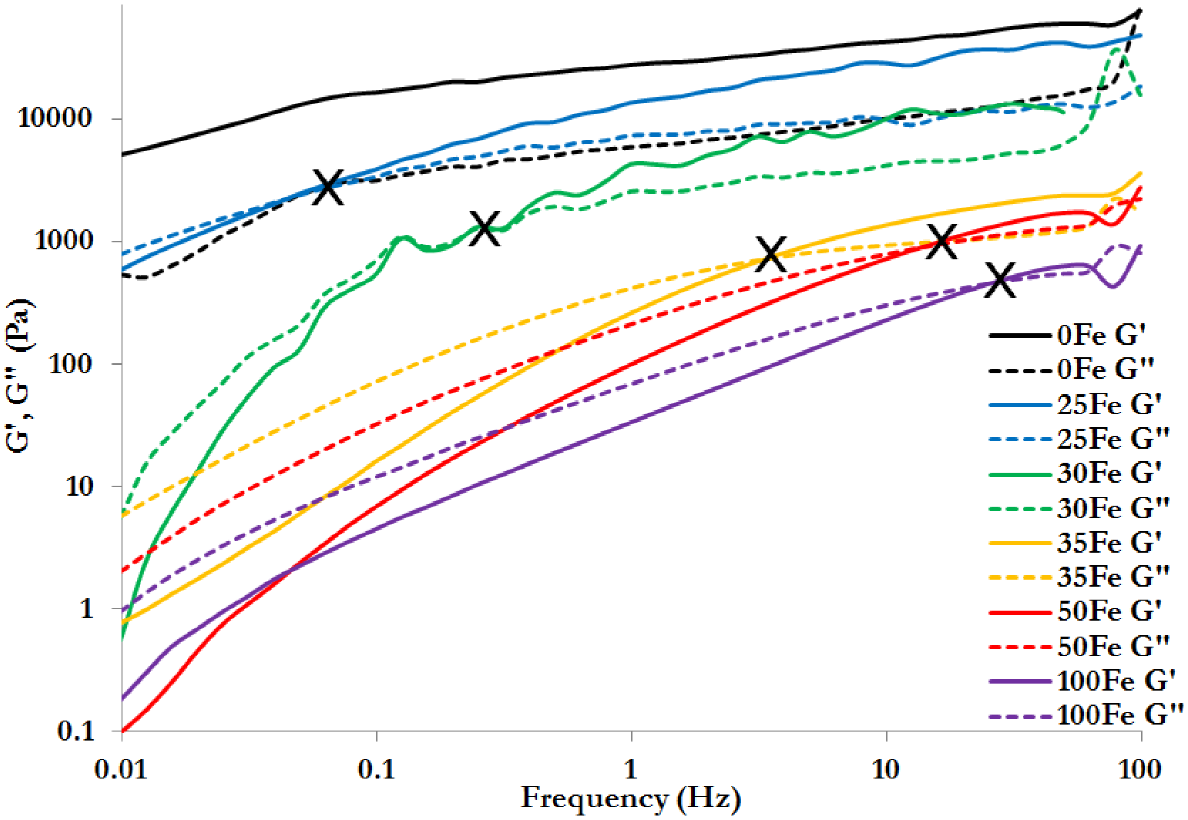

Figure 2.14 Rheological plots of gelatin + increasing mol% of iron nitrate. Dash line - G', solid line - G"

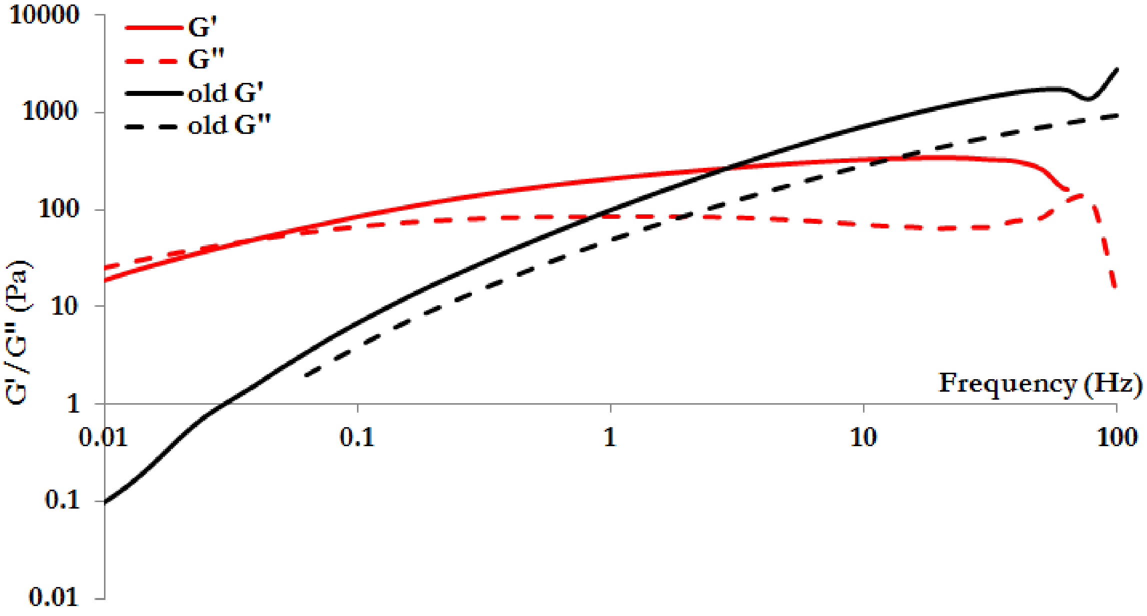

Figure 2.15 A comparison of rheology data using 2 different concentrations. Dash line - G', solid line - G"

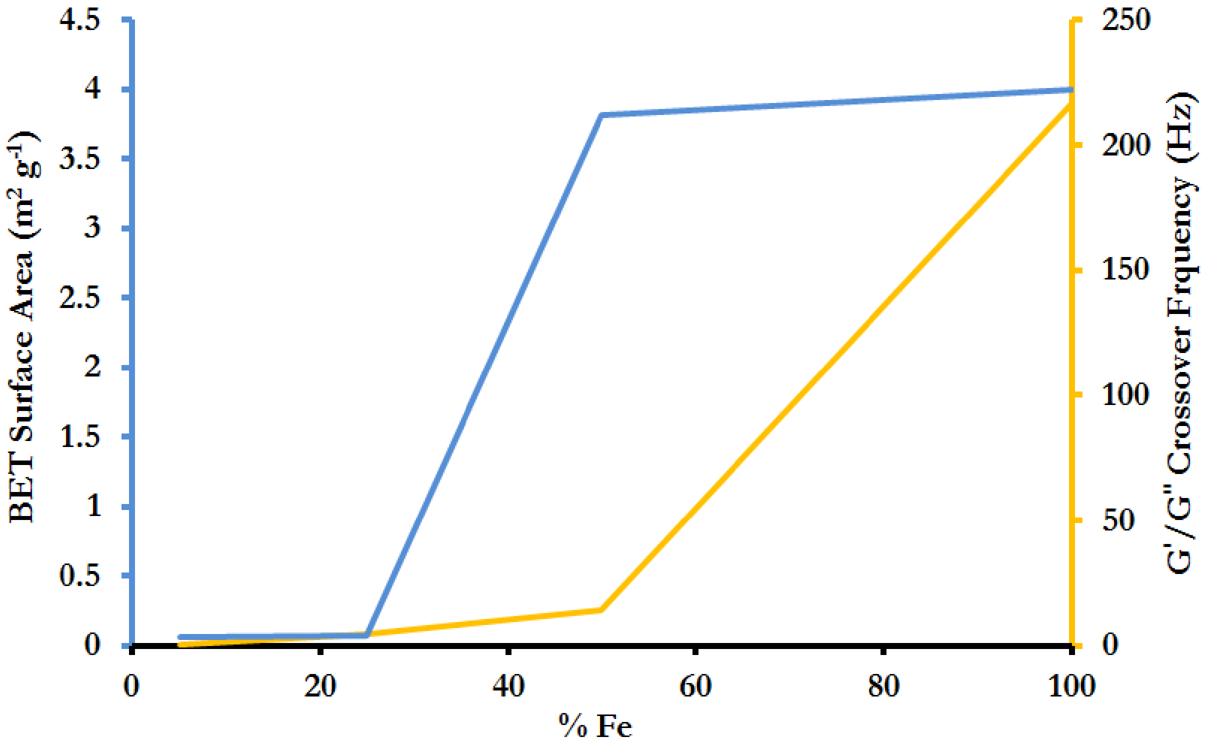

Figure 2.16 Graph showing the relationship of BET surface area, visco elastic properties and mol% iron

Nitrogen sorption experiments were carried out on the calcined MFx samples for X = 1 - 100, below 5% iron it was not possible to get a good isotherm as the surface area was too low. Figure 2.16, shows percentage iron concentration against BET surface and frequency of the G'/G" crossover. This is preliminary work and there are large differences however they both show an upward trend with increasing iron concentration; with further work this could be a step to selecting surface area, and possibly pore size, whilst still in the solution state.

2.3.5 - METAL BINDING - UV/VIS, IR AND CD

The rheological data seems to be pointing to the fact that metal ions are interacting with gelatin, two possible outcomes could be happening; 1) metal binding to gelatin or; 2) it could be metal disruption of the bonding between the gelatin strands, i.e. ionic strength of the metals screening the charges. This idea that metals are binding to gelatin has been inferred from physical properties studied so far and observations made whilst performing these studies. Using ultraviolet spectrometry (UV-Vis) for coloured metal salts (e.g. iron) would normally be one of the first techniques used and, in fact, this has been previously reported.[75] Further research has shown that gelatin plus iron solutions are at ~pH 2-4 and in this range iron has a number of equilibria, one of which that means that UV-Vis cannot be used. The equilibrium for Fe^{3+} in water is shown below and shows the dissociation of H^+ at low pH ~0 only the hexaaquo species is seen but at higher values of pH (2-3) a yellow species is seen. This is an oilgomer, a hydroxyl bridge dimer, Equations 2.1 and 2.2, and at even higher pH's eventually precipitation of red-brown Fe(III) oxide is seen.[76] This is important because also at this pH gelatin is negatively charged and therefore has the ability to act as a buffer removing H^+ and drawing the equilibrium towards the dimer. This means that UV will be detecting absorption from varying amounts of various Fe complexes. The end result is that would be difficult to draw conclusions about changing metal environments from UV-Vis data as there are a large number of possible iron species.

$$[Fe(H_2O)_6]^{3+} \rightleftharpoons [Fe(H_2O)_5(OH)]^{2+} + H^+$$ **Equation 2.1**

$$2[Fe(H_2O)_6]^{3+} \rightleftharpoons [Fe(H_2O)_4(OH)]_2^{4+} + 4H^+ + H_2O$$ **Equation 2.2**

Infrared (IR) spectroscopy was also used to investigate metal binding to gelatin. Gelatin has a complex molecular structure comprising of different amino acids with differing functional groups. The exact ratio of these is unknown so from IR spectroscopy it is difficult to pull out meaningful data, despite this several point can be highlighted. Adding to the complexity is the fact that the gelatin is a mixture of single, double and triple bonded 3 strands of gelatin that are binding to each other.[77] Finally the hydrogen bonding and steric hindrances will affect the spectrum.

The IR spectra, Figure 2.17, shows a series of gelatin + iron samples, between 2000 - 1000 cm^{-1}. There are increasing peaks around 1200 - 1400 cm^{-1} this is from the nitrate ions in solution as it is confirmed by the corresponding nitric acid titration, Figure 2.17. There are 2 peaks of interest, these are at ~1550 cm^{-1} ($_{\nu}$CO amide I) and 1625 cm^{-1} ($_{\delta}$NH amide II)[77] and with increasing concentration of iron nitrate they shift to slightly lower wavenumbers with greater intensity, Figure 2.18. Peak intensity in IR is related to the bond length,[78] in gelatin the amide group bonds will be constrained sterically in the helix and this will mean less intense peaks: so as the iron disrupts this structure these groups will have more room and therefore more intense peaks are seen. This could point to metal binding to gelatin or disruption of helix formation by the metal. The shift in wavenumber is not seen with nitric acid, Figure 2.17, so this could be evidence of metal binding to the gelatin backbone, to confirm this hypothesis a simple experiment of mixing iron nitrate with poly-glycine was carried out. Gelatin is ~30% glycine so this is a good approximation, also polyglycine is white and insoluble in water, so a colour change would be easy to detect. After soaking, the polyglycine was orange even after successive washing steps, suggesting the iron has bound to the polyglycine. The IR spectra for polyglycine before and after iron soaking shows the same shift in the peak as seen earlier further supporting this, Figure 2.18.

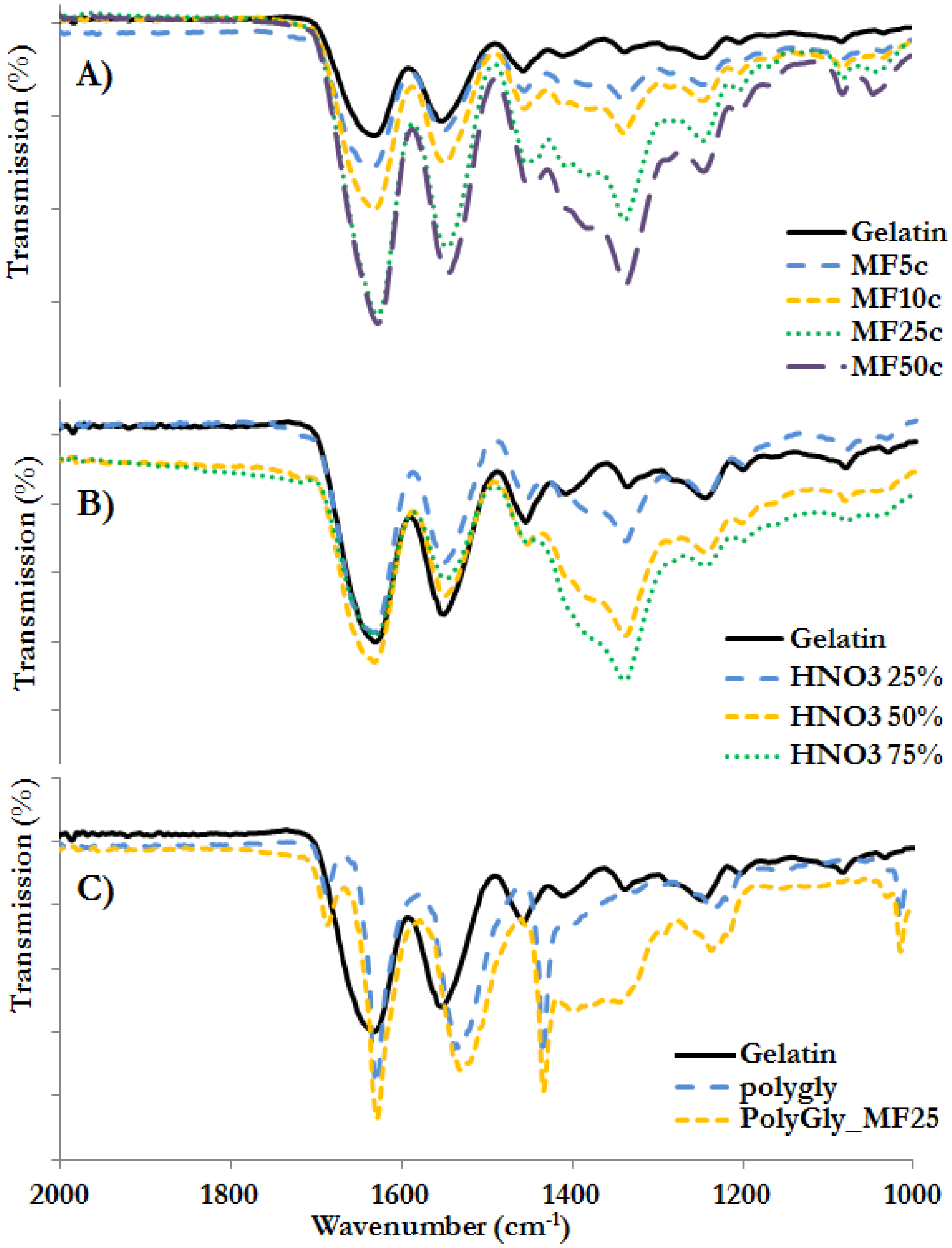

Figure 2.17 IR spectra for gelatin + A) iron nitrate; B) nitric acid; C) polyglycine and iron nitrate

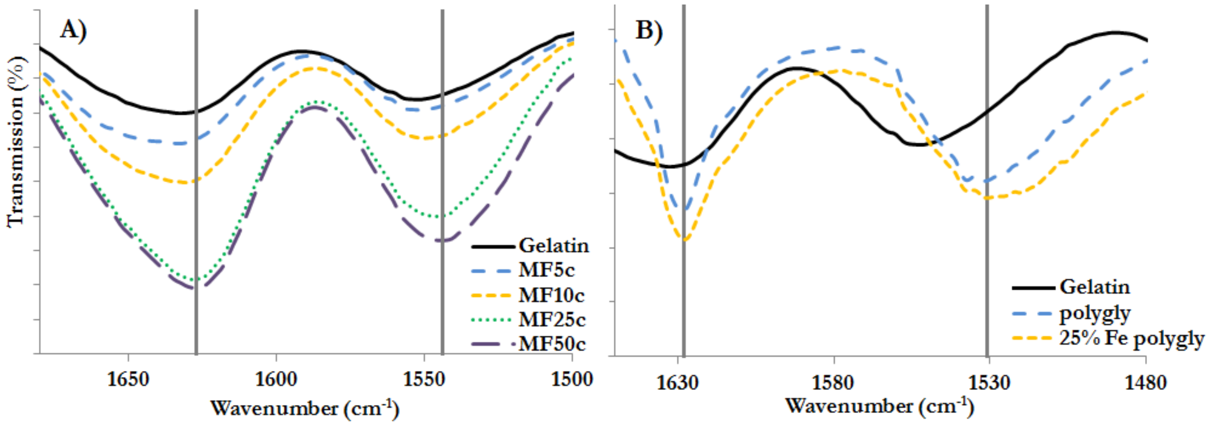

Figure 2.18 IR spectra for gelatin + A) iron nitrate; B) glycine

Further evidence for metal binding can be gathered from circular dichroism (CD). CD can be used to identify and probe chiral environments; the interaction causes a change of the polarisation of the light by a few milli-degrees, typically. CD of gelatin has been reported previously and can show the nature of the helical junction zones as they are chiral, although not much research has been done on porcine gelatin and almost all of the current research looks at anionic surfactants.[43,79,80] Rehydrated gelatin has a peak in CD at ~238 nm and another at ~220 nm;[79] the peak at ~238 nm, in our system was observed at ~245 nm (this may be due to the different composition of gelatin). This peak decreases in intensity with increasing concentration of metal ions, Figure 2.19, indicating a loss in the chirality and we have assigned this to the metal ions binding to gelatin and displacing/ disrupting the water that helps the helices form. The peak at ~275 nm is indicative of metal binding to a polymer[81] and this peak increases with increasing iron concentration so this further supports the assertion that iron is binding to the polymer rather than just disrupting the polymer network. There is conflicting information in the literature so this evidences is presented only to further support the existing hypotheses and the presented SANS data.

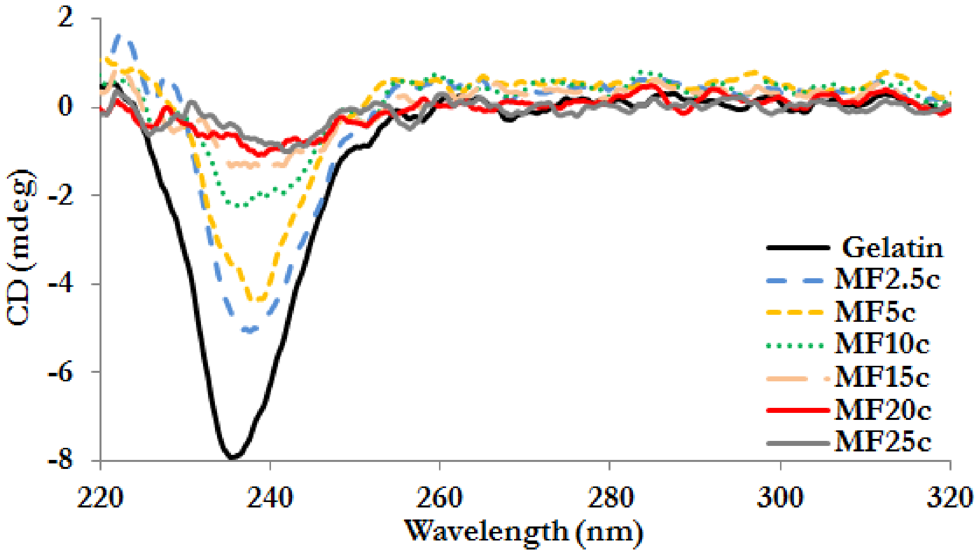

Figure 2.19 CD spectrum of iron nitrate/gelatin; iron concentration increasing with arrow.

2.3.6 INVESTIGATION OF GEL STRENGTH AND STRUCTURE - SMALL ANGLE NEUTRON SCATTERING (SANS) AND RHEOLOGY

To analyse the macroscopic observations SANS was used to investigate gelatin at the nano-scale. The gelatin solutions used for these experiments were 5% (w/v), this was the most concentrated the samples could be and still give reliable results. There are numerous SANS studies[82,83] on gelatin so it is possible to investigate gelatin, however this is the first study to look at metal interaction with the biopolymer.

Many modals and software packages exist to analyse SANS data and after trialling several including some Gaussian coil models (used by previous studies but considered too complex for this research), a modified correlation function, Equation 2.3, was chosen as this has good agreement with previous work, [84] 29±1 Å for sol and 38±3 Å for gel. Modelling was done using IGOR PRO fitting software and restricted at low Q as there aren't many data points there, Q range 0.008 - 1 $Å^{-1}$. Fitting of the low Q data is possible through use of a second power law, however this complicates the model without changing the results and having a minimal effect on correlation length. The variables are as follows:-

s = low-Q exponent/ dimensionality factor - this represents anisotropy in the structure (s=0 for isotropic globular structures to s=1 for elongated rod-like structures),

m = high-Q Porod exponents,

c = a scaling factor,

B = a Q-independent incoherent background - this is from the scattering of hydrogen in both the gelatin and hydrated metal salts,

ξ = correlation length - the distance between points of similarity between gelatin chains, Figure 2.25,

$$\left(\frac{1}{Q^{S}}\right) \times \left(\frac{c}{[1+(Q\,\xi)]^{m}}\right)^{3} \qquad \textbf{Equation 2.3}$$

Figure 2.20 shows a plot of scattering intensity (I(Q)) vs scattering vector (Q) for gelatin above (60 °C) and below (25 °C) its gel temperature (~ 30 °C[44]), this is useful to highlight many points. Early SANS studies have attributed large changes in the profile of the curves to the gel transition that occurs as a product of the rod-like triple-helix junction zones seen in gelatin; this is not the case as both traces are very similar after approximately Q <0.02 Å^{-1}, therefore the gel transformation has very little contribution to the scattering. The Porod region starting from Q = 0.008 → <0.004 Å^{-1}, studied with USANS, has been shown to be from formation of micron sized clusters which is common in these types of polymers. Finally at intermediate, Q = 0.03 Å^{-1}, there is a turnaround point (Guinier region) which can be used to extract a radius of gyration (R_g) for the system. It should be noted that at higher concentrations of iron this turnaround point disappears in the gel state so while a number can be extracted for these samples it does not have a true meaning; however it can help to explain trends in the samples. The R_g extracted here is not for the whole gelatin molecule but instead is the correlation length between region on the same chains, ξ, in our model.[85]

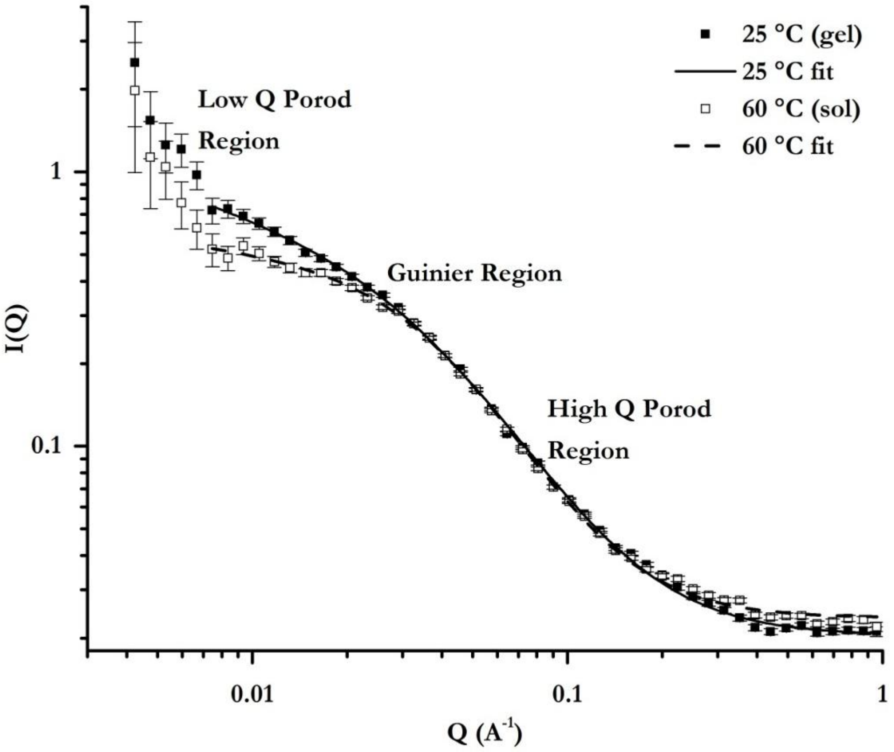

Figure 2.20 SANS data for gelatin at 25 °C and 60°C at 5% (w/v) concentration

A selection of gelatin + metals from the previous studies were to used to produce a series of samples for SANS, this was to investigate the effect of metal nitrates on the structure of gelatin. As noted in the experimental the concentration of gelatin and H_2O was carefully controlled to rule these out as possible causes of changes. The numbers shown in the sample ID's denote the total metal concentration as a percentage of the total 0.01 M of metal (e.g. MF75 is 75% Fe (0.0075 M) and 25% Mg (0.0025 M); a small 'c' after the ID indicates a control sample containing only iron. The SANS profile for this series is shown at 25 °C and 60 °C, Figure 2.21, all samples in the sol state start to show very similar scattering, although all metal nitrates do have an effect on the scattering. The 25 °C (gel) state data is where the biggest effect is seen to be due to iron nitrate, although again all metal nitrates are impacting the scattering. The correlation length from the model above are summarised in Table 2.8. An interesting point here is a Hofmeister trend[86] is observed in scattering of gelatin with the alkali and alkali earth metal nitrates. The Hofmeister series is an ordering of cations and anions by their ability to affect the solubility of a protein, Figure 2.21 shows this trend for several metal ions above and below the gel temperature. In the Q range below 0.02 Å^{-1} there is an increase in the scattering intensity that is greater in the gel state than in the liquid state. In the gel state there is an increase in scattering intensity that mirrors the increase in effective nuclear charge on the metals, this could indicate that the relative size and charge ions is effecting the gelatin gelling mechanism by different amounts. Using this information and trends in the iron data (investigated in more detail later) it may be possible to rationalise and extend any links between gel formation and the final nanocomposites to other metals. This would mean SANS of all samples would not be need, by simply considering the metals ions position in the Hofmeister series predictions on properties of the nanocomposite could be made. As a final point above the gel temperature the order changes and seems to change and now the trend followings the relative sizes of the metal ions.

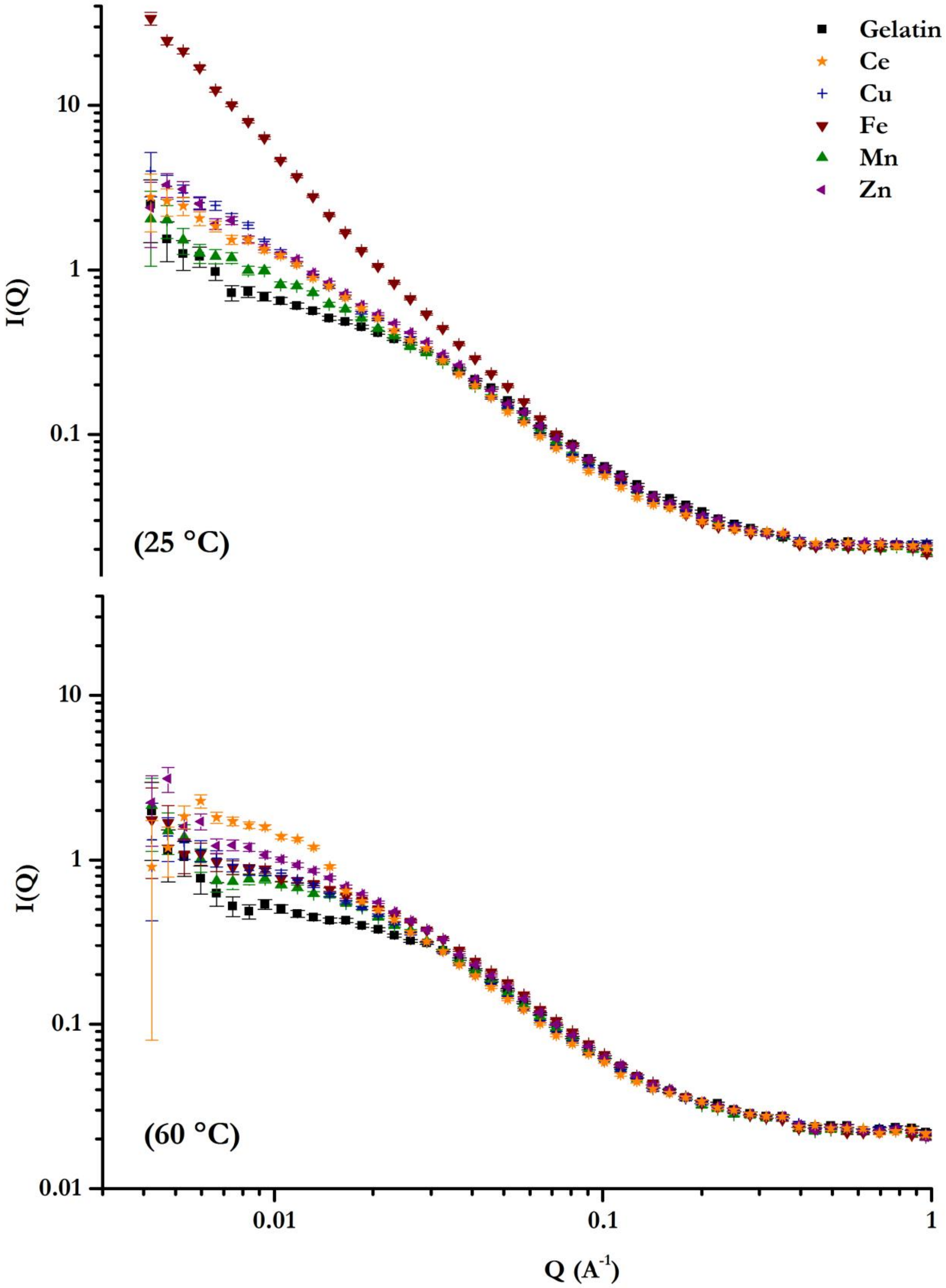

Figure 2.21 SANS data for gelatin with various metal nitrate salts at 25 °C and 60 °C

Table 2.8 Values for the correlation length (ξ) and Porod exponents for gelatin with different iron concentrations at 25 °C (RED = 60 °C data)

Iron conc. (mol%)	**Correlation length, ξ (Å)**	**High Q Porod, m**	**χ^2**
0	**38±3**	**1.9±0.1**	**1.7**
0	29±1	2.1±0.1	2.7
1	**28±1**	**2.1±0.1**	**2.2**
2	**20±1**	**2.3±0.1**	**2.4**
5	**14±1**	**2.5±0.1**	**1.1**
5	14±1	2.4±0.4	1.8
10	**19±1**	**2.3±0.1**	**1.6**
15	**27±2**	**1.9±0.1**	**2.5**
25	32±2	2.0±0.1	1.3
50	32±2	1.9±0.1	1.3
75	33±2	1.9±0.1	1.2

The large effect on scattering of gelatin + iron could be due to the highly charge dense Fe^{3+} ion (smallest studied here) having the most interaction with gelatin. This was investigated using a series of gelatin + iron gels, with increasing iron concentrations, Figure 2.23. Figure 2.22 also shows this data without fitting lines and in a 3D plot which helps highlight the trends discussed below. Initially small amounts of iron, up to 5 mol% results in a small decrease in scattering intensity in the range of Q = 0.007 - 0.04 $Å^{-1}$. To accompany this the Guinier region shifts to higher Q meaning there is a reduction in the correlation length.

Between 5 and 25 mol% iron there is a shift in the Guinier region to lower Q, i.e. an increase in correlation length. The contraction and expansion highlighted here mirrors the trend seen in the gel strength tests, Figure 2.13. This gelatin, Type A, at 5% (w/v) in water has a pH of 4.7, meaning it has overall negative charge. Aqueous iron nitrate is very acidic so the drop and then rise in correlation length could be linked to the idea of gelatin buffering the solution, as mentioned earlier. This would involve the protonation of the negatively-charged gelatin to minimise the intramolecular electrostatic repulsions and form a net neutral charge and allowing the biopolymer to contract. Adding further amounts of iron nitrate then causes excess protonation, causing an expansion in the polymer due to an overall positive charge on the polymer and increased electrostatic repulsions. A large Porod region is seen from above 25 mol% in the gel state (25 °C) and the Guinier region becomes less obvious. This transition to a long slope is consistent with an extended fractal network.

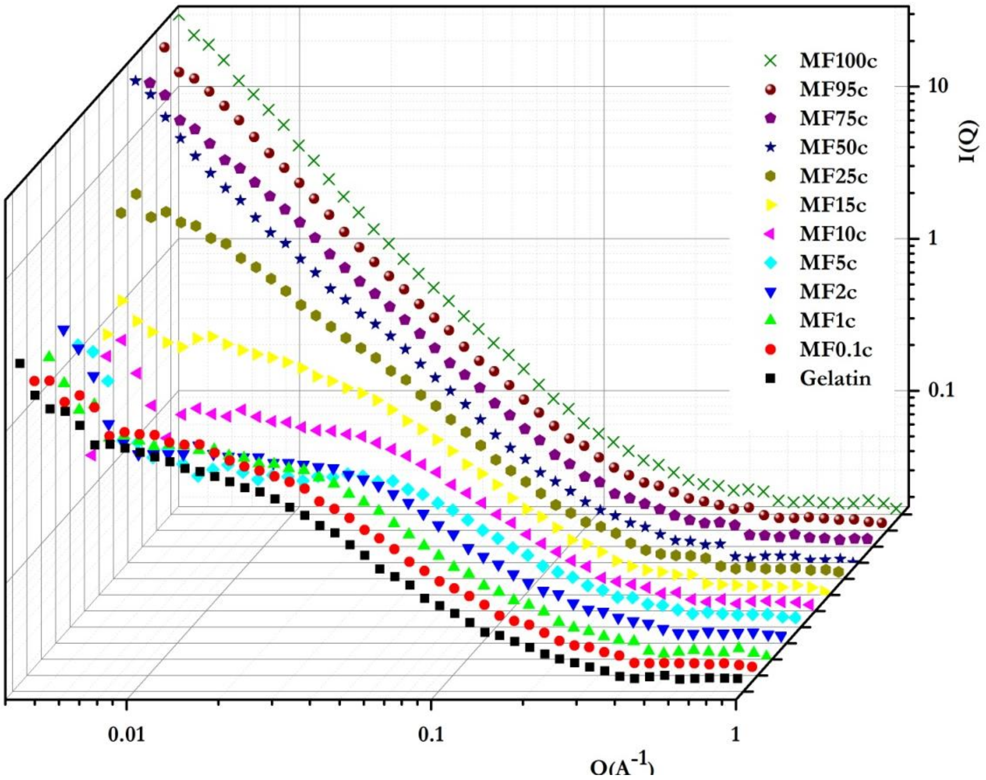

Figure 2.22 SANS data for gelatin with various iron concentrations at 25 °C

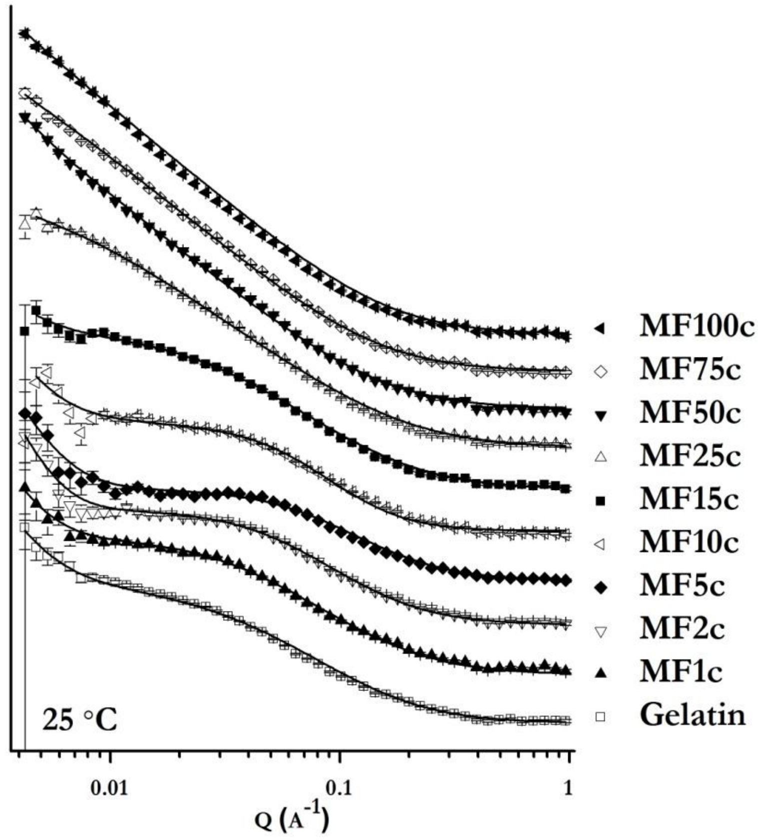

Figure 2.23 SANS data for gelatin with various iron concentrations at 25 °C

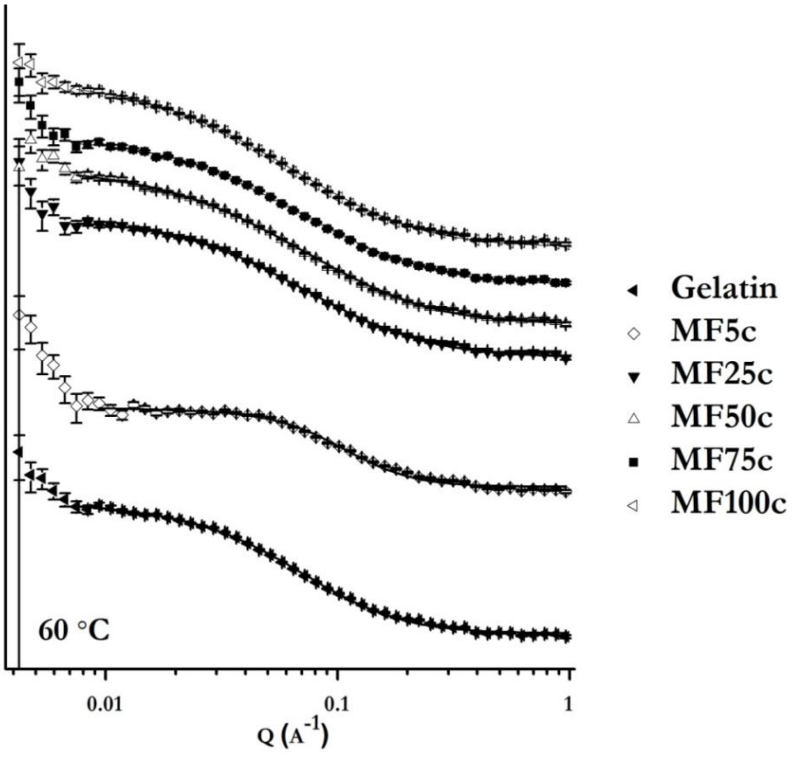

Figure 2.24 SANS data for gelatin with various iron concentrations at 60 °C

This fractal network is not seen in 60 °C data (i.e. in the sol state), Figure 2.24, and this suggests that there is a different mechanism directing gelation at high [Fe^{3+}]. It has already been shown that the polymer swells and contracts with varying molar amounts of iron and also that iron can bind to a simple peptide backbone (i.e. polyglycine), based on this the following is proposed. As the gelatin chains swell with moderate amounts of iron nitrate the binding sites for iron ions become more accessible. Additional iron ions result in more metal ions binding to the peptide backbone and then this, iron cross-linking, becomes the dominant gelling mechanism instead of the traditional triple helix formation, Figure 2.25. This could explain the very large difference in scattering between 25 °C and 60 °C from high iron concentration samples. This hypothesis is supported by data from circular dichroism, which suggests that addition of iron nitrate to gelatin disrupts triple helix formation.

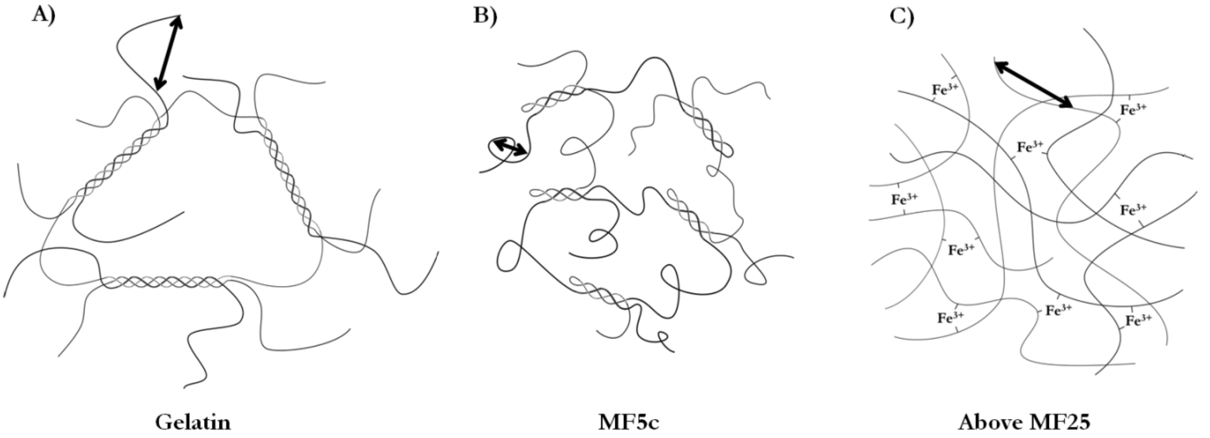

Figure 2.25 Proposed schematic structures of gelatin + iron nitrate at A) 0 mol% Fe; B) approximately 5 mol% Fe; above 25 mol% Fe. Arrows showing the decrease and then increase in correlation length as the polymer contracts and then swells. Figure copied from REF [87] with authors permission.

Figure 2.4 shows an SEM image of an apparent synergy between iron and magnesium, to understand this mixed Fe and Mg nitrates were used to produce a series for SANS. Firstly the following samples could not be analysed as they formed tight-knit rubbery balls that expelled H_2O/D_2O, these were 5, 10 and 25 mol% iron. When discussing these samples all percentages will relate to the mol% of iron unless otherwise stated (i.e. a 5 % iron sample would also have 95 % Mg of the total metal ion content. SANS data of the magnesium and iron helps to shed light on the effect seen in the SEM images. The data at low iron (high magnesium) and at 25 °C is most helpful for this, Figure 2.26, and the biggest effect is shown at low $Q < 0.1$ Å^{-1}. In line with visual observations and rheology, with little/no change in viscosity, 100 mol% Mg sample has very slight increase in scattering and therefore a small effect on the gel structure. 1 and 2 mol% iron have greatly increased scattering intensity when accompanied by magnesium than without. The long Porod region in these samples provides more evidence of the extended fractal network; this combined with the fact that there is minimal effect on the scattering for 100 mol% Mg confirms that synergy of iron and magnesium must be the cause of the high intensity seen in the SANS data. The 60 °C data also helps to support the hypothesis that magnesium alone does very little to change the biopolymers structure but changes how the iron binds, enhancing it. There is an increase in scattering intensity at low Q in the 60 °C data when compared to 25 °C, Figure 2.27, this is presumed to be due to structural changes that occur when transitioning from sol to gel. The evidence for this comes from the magnesium only sample which only has a minor difference in scattering intensity from sol to gel; also the mixed metal sample shows a large increase in scattering intensity. Further confirmation of this effect comes from visual inspection of the samples where some samples form cloudy gels. Most samples formed a clear brown/orange gel with the exceptions of 1 and 2 mol% when these gelled they formed a cloudy gel, this is indicative of light scattering from some large structure/ clusters within the gel.[88,89] This effect is seen both when the metal nitrates were mixed prior to being added to the gelatin or adding magnesium to gelatin then the iron. It is possible that the effects described so far could be linked to the ionic strength of the metal nitrates, however if this were the case samples with the highest amounts of the metal nitrate would have the highest scattering intensity.

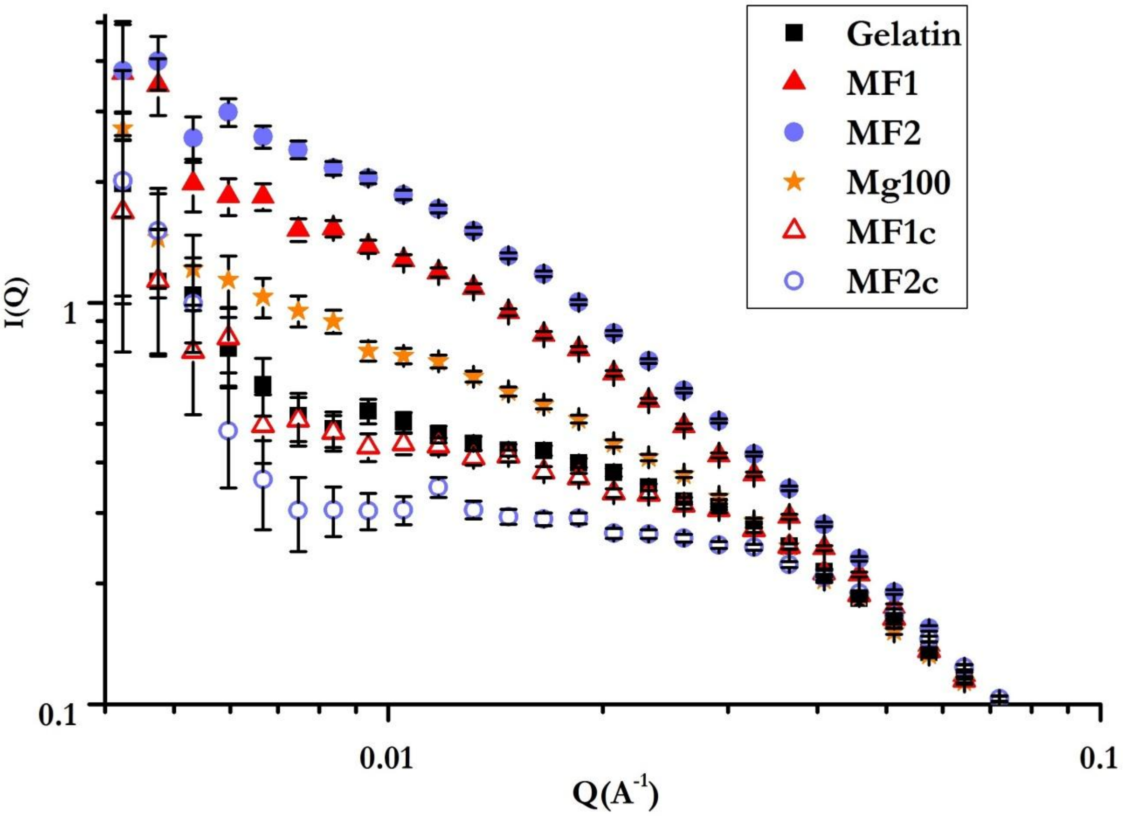

Figure 2.26 SANS profile of gelatin with iron nitrate, with and without magnesium nitrate

At higher iron to magnesium ratios there are a number of interesting features, Figure 2.28, shows SANS data for 50 mol% Fe or Mg and as well the two combined, this is shown at 25 and 60 °C. The mixed iron and magnesium samples show a Guinier region at Q ≈ 0.04 Å^{-1} and both the single metal systems also have features in this range. The Guinier region shifts to lower Q from 50 mol% Mg to 50:50 iron/magnesium, as before this indicates a larger correlation length or a more open network. At low Q there is the start of a Porod region, which like pure gelatin is expected to extend well into the range of USANS.[90] At 25 °C the steep gradient in the Q range of Q ≈ 0.004-0.01 Å^{-1} is again indicative of an extended fractal structure. The fact that this is missing at 60 °C indicates that this mass fractal is the formation of the gel network formed on cooling.

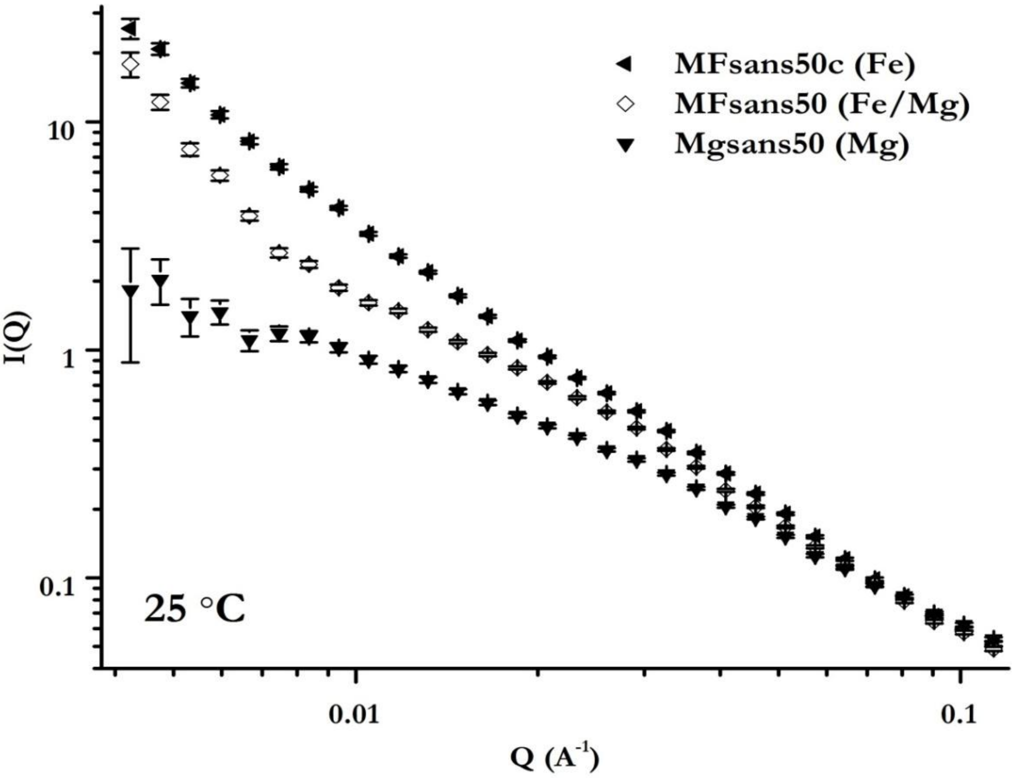

Figure 2.27 SANS data of iron and magnesium at 50 mol% and a mixture of both at 50 %mol

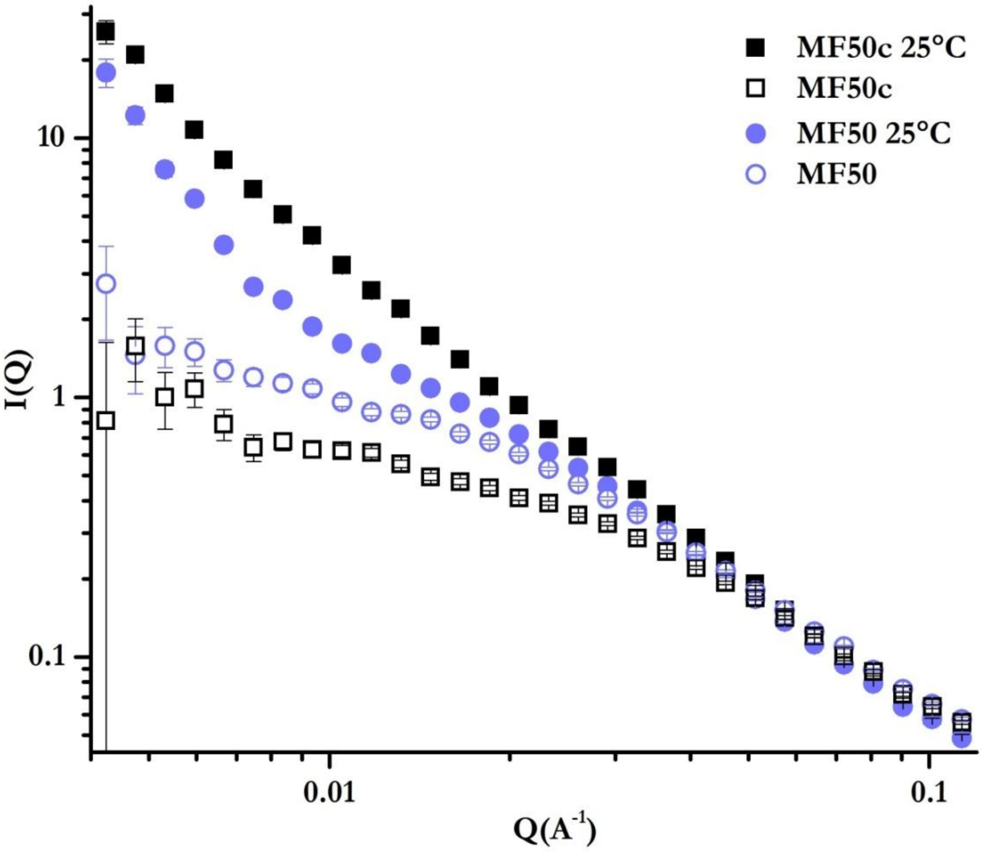

Figure 2.28 SANS data of MF50 and MF50c at 25 °C and 60 °C

Very little has been said about the high Q region Q = 0.1 - 1 Å^{-1}, these are similar in the vast majority of all the small angle neutron scattering curves. This area of Q describes the polymers' ‘solvation’, i.e. its interaction with the surrounding solvent. A 'polyelectrolyte peak' is often seen for charged polymers, whilst neutral polymers show high-Q a peak. Gelatin is a polyampholyte (as are all proteins) containing carboxyl and amino groups along its length: this combined with it being charged at this pH it is possible that these features would be visible. However, this is not the case as it is obscured by the low-Q clustering features. A Porod exponent of 1.7 can be extracted through linear analysis, using a Porod plot, of the high-Q solvation region, for gelatin at both 25 and 60 °C. This value is characteristic of a fully swollen polymer coil (i.e. a coil in a good solvent).

2.4 CONCLUDING REMARKS

The gelatin plus metal nitrate foaming reaction has been investigated. The foaming is caused by gelatin stabilising bubbles in the resin as the final evaporation of water occurs. Nitrate ion attack the gelatin as the solution concentrates affecting the ability of the biopolymers to stabilise these bubbles. This also works in conjunction with low pH and low temperatures to radically change the pore structure. As a result the system is more flexible and more able to stabilise the bubbles.

From various experiments, especially SANS, it is clear that iron interacts with gelatin changing the structure of the gelatin gel. It is proposed this change is from the conventional triple-helical junction zones of gelatin to a network crosslinked by Fe^{3+}. These data combined with visual observations confirm that magnesium enhances iron binding to gelatin. The cloudy precipitates/ rubbery solids are an example of the Hofmeister effect,[91] where both the iron and magnesium ions combine in such a way to ‘salt out’ gelatin. One such sample also has interesting properties. MF25 (i.e. 25 mol% Fe, 75 mol% Mg) gives the smallest cells in the dried foam and calcined carbon; also it forms a rubbery solid which is thought to be able to stabilise the bubbles to the greatest extent. The iron and magnesium samples were focussed on here but it is responsible to assume similar processes occur with the other metals.

Using the working knowledge of how the samples foam, several simple experiments have been carried out to show how particle size can be controlled without changing the end phase. The addition of nitric acid has been shown to increase the particle size; further work should involve testing other acids and additives to refine control over the particles. Rheology has been used to measure visco-elastic properties to link this to BET surface area. Further work should investigate this to size select the pores of the final material whilst in the liquid state. These studies have shown a link between the G'/G" crossover frequency and BET surface and further work should allow this to be used to tune these in advance of making the samples. Further studies using these techniques and other (i.e. freeze drying samples) will allow a system to create truly designer carbon with nano particles of choice for a wide range of applications.

2.6 REFERENCES

(58) Rodriguez, N. M.; Chambers, A.; Baker, R. T. K. *Langmuir* **1995**, *11*, 3862.

(59) Figueiredo, J. L. *Journal of Materials Chemistry A* **2013**, *1*, 9351.

(60) Job, N.; Pirard, R.; Marien, J.; Pirard, J.-P. *Carbon* **2004**, *42*, 619.

(61) Yu, J.-S.; Kang, S.; Yoon, S. B.; Chai, G. *Journal of the American Chemical Society* **2002**, *124*, 9382.

(62) Belloni, F.; Kutahyali, C.; Rondinella, V. V.; Carbol, P.; Wiss, T.; Mangione, A. *Environmental Science & Technology* **2009**, *43*, 1250.

(63) Lim, T.-T.; Yap, P.-S.; Srinivasan, M.; Fane, A. G. *Critical Reviews in Environmental Science and Technology* **2011**, *41*, 1173.

(64) Dutta, S.; Bhaumik, A.; Wu, K. C. W. *Energy & Environmental Science* **2014**, *7*, 3574.

(65) Schnepp, Z.; Hollamby, M.; Tanaka, M.; Matsushita, Y.; Xu, Y.; Sakka, Y. *Chemical Communications* **2013**, 5364.

(66) Schnepp, Z.; Zhang, Y.; Hollamby, M. J.; Pauw, B. R.; Tanaka, M.; Matsushita, Y.; Sakka, Y. *Journal of Materials Chemistry A* **2013**, *1*, 13576.

(67) Schnepp, Z.; Danks, A. E.; Hollamby, M. J.; Pauw, B. R.; Murray, C. A.; Tang, C. C. *Chemistry of Materials* **2015**, *27*, 5094.

(68) Zhou, J.; Zhao, F.; Wang, X.; Li, Z.; Zhang, Y.; Yang, L. *Journal of luminescence* **2006**, *119*, 237.

(69) Patil, K. C.; Aruna, S. T.; Mimani, T. *Current Opinion in Solid State and Materials Science* **2002**, *6*, 507.

(70) Chick, L. A.; Pederson, L. R.; Maupin, G. D.; Bates, J. L.; Thomas, L. E.; Exarhos, G. J. *Materials Letters* **1990**, *10*, 6.

(71) Wen, W.; Wu, J.-M. *RSC Advances* **2014**, *4*, 58090.

(72) Ashok, A.; Kumar, A.; Bhosale, R. R.; Saleh, M. A. H.; van den Broeke, L. J. P. *RSC Advances* **2015**, *5*, 28703.

(73) Bloom, O. T.; US1540979 A: 1925.

(74) Chatterjea, M. *Jaypee, New Delhi* **2004**.

(75) Schnepp, Z.; Thomas, M.; Glatzel, S.; Schlichte, K.; Palkovits, R.; Giordano, C. *Journal of Materials Chemistry* **2011**, *21*, 17760.

(76) In *Chemistry of the Elements (Second Edition)*; Butterworth-Heinemann: Oxford, 1997, p 1070.

(77) Benbettaïeb, N.; Kurek, M.; Bornaz, S.; Debeaufort, F. *Journal of the Science of Food and Agriculture* **2014**, *94*, 2409.

(78) Lazarev, Y. A.; Grishkovsky, B.; Khromova, T. *Biopolymers* **1985**, *24*, 1449.

(79) Wetzel, R.; Buder, E.; Hermel, H.; Hüttner, A. *Colloid & Polymer Sci* **1987**, *265*, 1036.

(80) Kelly, S. M.; Price, N. C. *Current protein and peptide science* **2000**, *1*, 349.

(81) Barton, J. K.; Danishefsky, A.; Goldberg, J. *Journal of the American Chemical Society* **1984**, *106*, 2172.

(82) Cosgrove, T.; White, S. J.; Zarbakhsh, A.; Heenan, R. K.; Howe, A. M. *Journal of the Chemical Society, Faraday Transactions* **1996**, *92*, 595.

(83) Pezron, I.; Djabourov, M.; Leblond, J. *Polymer* **1991**, *32*, 3201.

(84) Carn, F.; Boué, F.; Djabourov, M.; Steunou, N.; Coradin, T.; Livage, J.; Floquet, S.; Cadot, E.; Buhler, E. *Soft Matter* **2012**, *8*, 2930.

(85) Akyol, E.; Kirboga, S.; Öner, M. In *Polyelectrolytes*; Springer: 2014, p 87.

(86) Hofmeister, F. *Archiv for Experimentelle Pathologie und Pharmakologie* **1888**, *24*, 247.

(87) Danks, A. E.; Hollamby, M. J.; Hammouda, B.; Fletcher, D. C.; Johnston-Banks, F.; Rogers, S. E.; Schnepp, Z. *Journal of Materials Chemistry A* **2017**.

(88) Schulz, D. N.; Peiffer, D. G.; Agarwal, P. K.; Larabee, J.; Kaladas, J. J.; Soni, L.; Handwerker, B.; Garner, R. T. *Polymer* **1986**, *27*, 1734.

(89) Güner, A.; Ataman, M. *Colloid & Polymer Sci* **1994**, *272*, 175.

(90) Yang, Z.; Chaieb, S.; Hemar, Y.; de Campo, L.; Rehm, C.; McGillivray, D. J. *RSC Advances* **2015**, *5*, 107916.

(91) Hofmeister, F. *Archiv für Experimentelle Pathologie und Pharmakologie* **1888**, *24*, 247.

CHAPTER 3

MICROWAVE SYNTHESIS OF METAL CARBIDE/OXIDE/CARBON NANOCOMPOSITES

3.1 BACKGROUND

This thesis aims to highlight general routes to a host of functional materials and this chapter further explores the flexibility of the systems described thus far. This chapter also demonstrates the lengths taken to achieve a synthesis that is as 'green' as possible by using microwaves as a heating source.

Microwave (MW) reactors have been used for the synthesis of materials including organic[92,93] and solid-state[94] reactions and as such they are fairly common in laboratories. The main benefits of these reactors are that they offer faster and more energy efficient processing compared to traditional heating techniques and in some cases MW reactors even produce higher yield and higher purity products.[95] Commercial MW reactors are readily available to purchase however they can be costly (for reasons explained later) and are usually calibrated for specific purposes. Modification of domestic microwave ovens (DMOs) then is a cost effective way to design and test new set-ups although care should be taken both for safety and that the new design leads to reproducible results. The basic operation of microwaves and their generation will be discussed before their use in materials synthesis.

The term microwave refers to the wavelengths from 0.01 to 1 m (i.e. between radio waves and infrared) with the corresponding frequencies of 0.03 - 300 GHz, Figure 5.1. Most of this frequency range is used for telecommunication so cooperation at national and international levels is required to help with regulations to avoid interference for important services such as radar (1 - 30 GHz). There are a number of assigned frequencies for industrial and medical uses but the most commonly used ones are 915 MHz in the UK (896 MHz, USA) and 2.45 GHz which is used in all DMOs.

There are a number of ways to generate microwaves the most widely used is the magnetron, Figure 3.1, which was invented by Hans Gerdien in 1910.[96] Several different types of magnetron were developed in the following years but the first patent for a multicavity magnetron (which is the design used in DMOs currently) was in 1935[97] and it this type of microwave generation that will be discussed. The other microwave generation techniques that should be mentioned are klystron tubes, triodes and gyrotrons.[98]

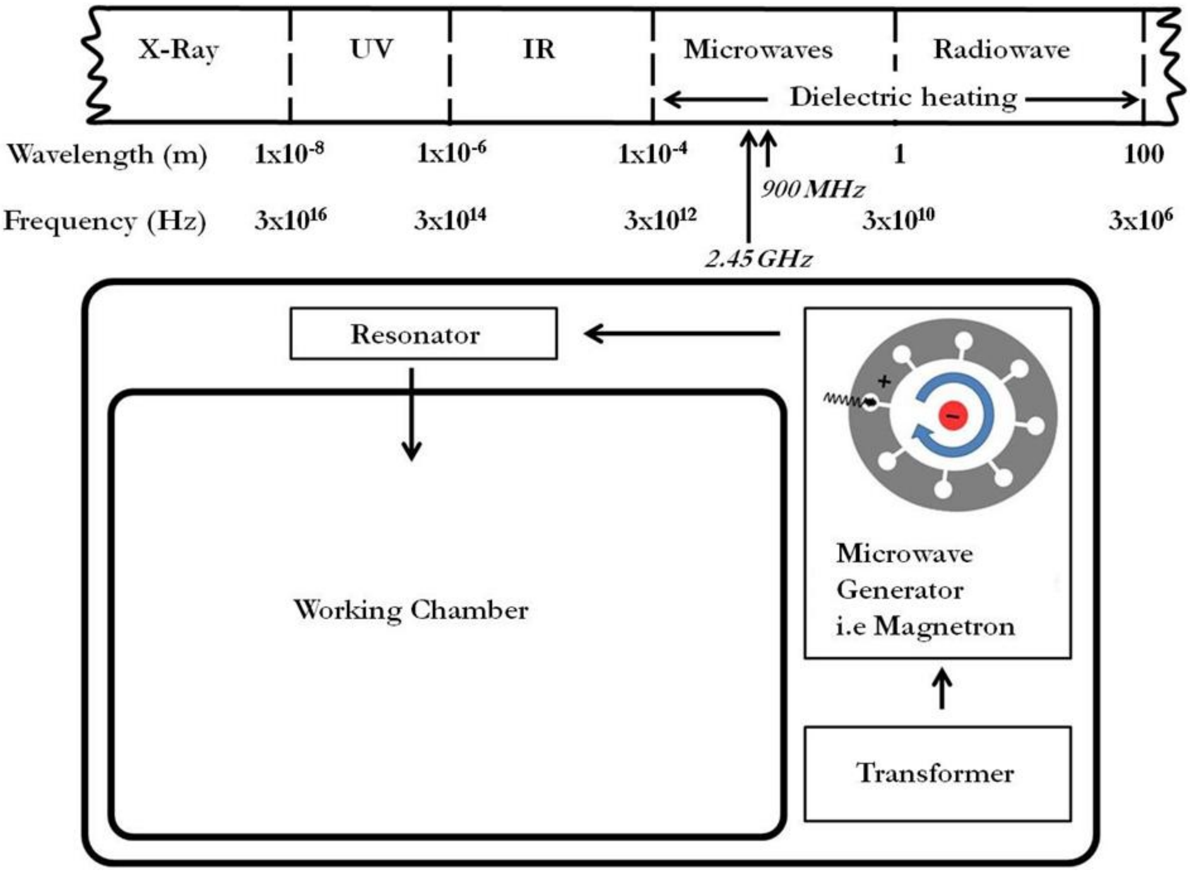

Figure 3.1 Schematic of microwave operation and the wavelengths involved

Most microwave reactors have the same basic layout, Figure 3.1. A transformer provides the heated cathode of the magnetron with a high DC current; the electrons are then drawn to the anode. At one end of the cathode there is a strong magnet and the magnetic field causes the electron to curve (blue arrow) and as they past the holes in the cavities they cause the cavities to resonate generating MWs. These MW are then directed through a resonator into the working chamber and this is all linked by a control system. Some laboratory and commercial MW reactors also include a feedback system used to vary power levels as the temperature rises in the sample, but this is not the case in DMOs.

The main drawback from using a DMO for synthesis is the inhomogeneity of the field in the working chamber. MWs are directed into the chamber and are reflected off the metal walls, which tend to concentrate at random intervals called 'hot spots'. This is not a problem for normal operation because there is a rotating plate to ensure food is uniformly heated by rotating through the hot spots and thermal conduction to heat the rest of the food. This is unacceptable for research samples as it would result in cooling down periods in the synthesis and uneven heating leading to possible impure samples. Modifying the DMO first involves finding a constant and reliable hot spot. This was achieved by using graphite powder in a quartz tube. After finding a potential hot spot, samples of graphite were heated repeatedly to check the hot spot did not move. Several hotspots were found and the one that was used for these experiments was as far away from the control system as possible so the high temperatures did not damage the microwave. Purpose built MW reactors (e.g. Mars 6) do not suffer this problem as they have a much more uniform field, but as mentioned earlier this comes with a high price due the resonator field having been extensively studied.

Both liquid and solid precursors can be used in the microwave synthesis of solid-state materials. Heating induced by microwaves occurs mainly through interaction of charge carriers with the electrical component of the electromagnetic wave. The 2 classes of charges are 'free' and 'bound' and these have related equations[99] but regardless of their state their movement will set up a current causing heating to occur in solids. In solution based syntheses the heating occurs mainly through dipolar polarization, this is where the bound charges are displaced from their equilibrium position until this is balanced by electrostatic interactions. This also happens to occur generally at lower temperatures and use a polar solvent to help drive the reaction. A number of nanomaterials have been synthesised this way including metals, via ionic liquids,[100] metal oxide nanosheets[101] and nanocomposites.[102] In the case of the SnO_2 nanosheets, when compared to conventionally made nanorods, they have shown significantly improved electrochemical properties. For solid state reactions, heating occurs through both polarization of dielectrics or resistive heating in materials with free charge carriers, i.e. as the charge moves back and forth the resistance it encounters heats the material. As a result, solid state syntheses require one or more of the components to be susceptible to MWs and if one of a multicomponent system is MW active then intimate mixing of precursors is essential. Excellent examples of this show that refractory carbides can be synthesised in subminute time scales[103,104] to just over an hour for much larger samples;[105] this is compared to 10+ hours if heated conventionally in a furnace.

The fact that MWs interact directly with the materials being heated means the heating is much more efficient than conventional ovens/ furnaces. As the heating takes place directly in the samples this means it is also being heated volumetrically (i.e. uniform heating), meaning there is no damage in the samples due to temperature gradients. A comparison of MW heating and traditional heating is shown in Figure 3.2. In susceptible materials the conversion of MWs to heat can be almost instantaneous meaning very fast temperature rises: this combined with the direct heating means the surroundings are cool and so very fast cooling is also possible allowing meta-stable phases to be 'trapped'. There are a number of other factors that must be taken into account when selecting materials for MW synthesis, such as the penetration depth of MW which can range from a few microns to several meters. This potential limitation can be overcome through practical solutions (i.e. flow/ continuous feed reactors) and by changing the frequency of the MW although this option also changes heating uniformity in the sample.

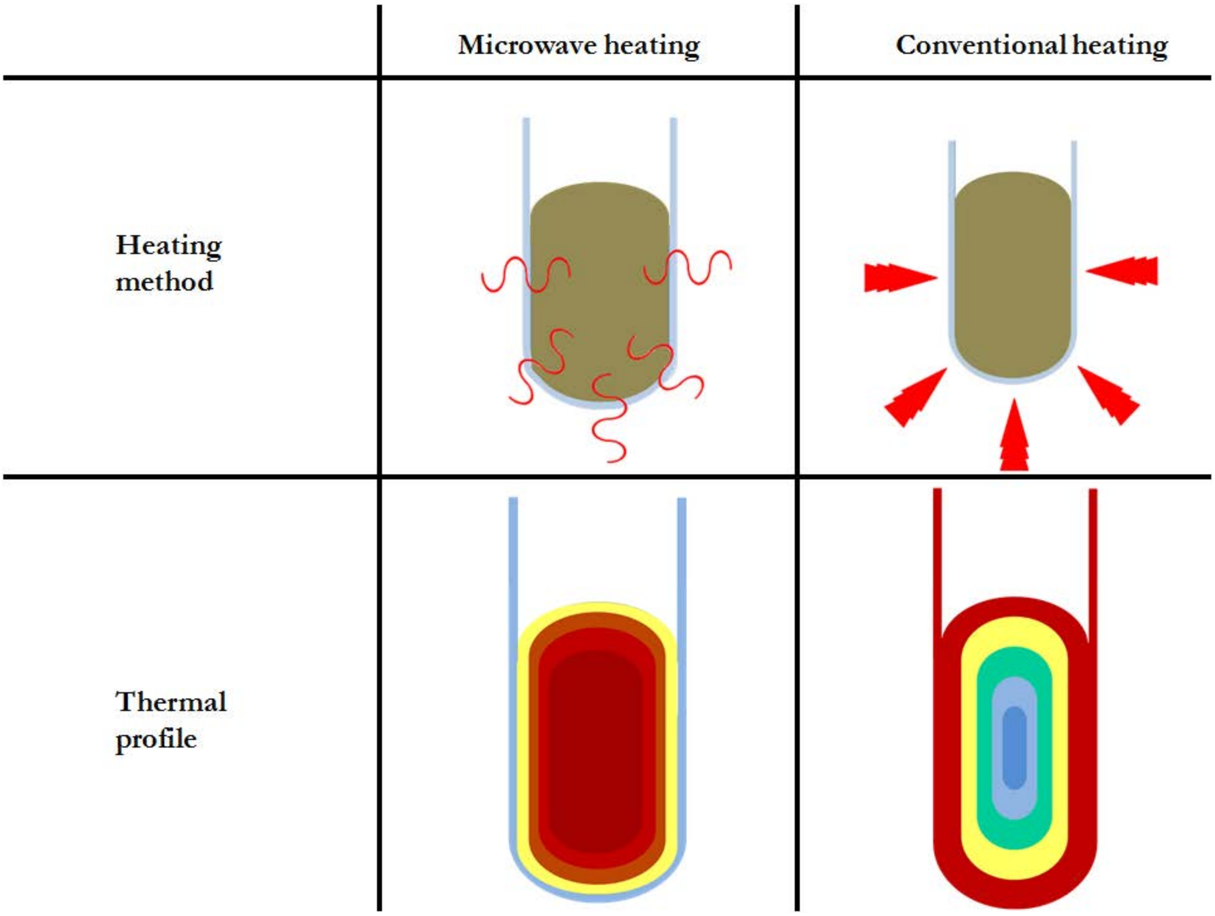

Figure 3.2 Schematic showing how heat is introduced into a sample and the resulting thermal profile for microwave and conventional (furnace) heat treatments

A number of examples that have already been used highlight the range of materials that can be synthesised using microwaves but the group of materials that were investigated in this work were metal carbides. These will be discussed in detail in Chapter 5 but briefly they are of great interest due to their wide range of useful physical properties and chemical properties. The former includes corrosion and temperature resistance, hardness, metallic conductivity and ferromagnetism, such as in iron carbide.[106-108] The interest in the chemical properties is more recent but still these materials have shown significant catalytic activity, e.g. oxygen reduction reaction in hydrogen fuel cells.[109] The main obstacle in the way of them potentially replacing costly noble metals is achieving high accessible surface areas; this has been tackled by conventional means, i.e. furnaces and sol-gel chemistry, but these are time and energy intensive.[66] The aim of this chapter is to combine the lower temperature sol-gel synthesis routes with the ultra-fast reaction times of MW heating and this chapter demonstrates that a modified domestic microwave oven was used to prepare a range of metal carbide/nitride/oxide nanocomposites in under 4 minutes.

3.2 EXPERIMENTAL

General experimental techniques, e.g. XRD, TEM, used through all chapters are described in Appendix E along with information about how the experimental techniques and how the instruments function.

3.2.1 MATERIALS

Below is a list of materials used in this chapter.

Table 3.1 List of materials used for synthesis and analysis in this chapter

Chemical	Supplier	CAS number
Gelatin, type A, porcine, G2500, 300 bloom strength	Sigma Aldrich	9000-70-8
Gelatin, type B, bovine, G9382, 225 bloom strength	Sigma Aldrich	9000-70-8
Magnesium(II) nitrate hexahydrate	Sigma Aldrich	13446-18-9
Cerium(III) nitrate hexahydrate	Sigma Aldrich	10294-41-4
Iron(III) nitrate nonahydrate	Sigma Aldrich	7782-61-8
Nitric acid 70% (w/w)	Sigma Aldrich	7697-37-2
Ammonium metatungstate hydrate	Sigma Aldrich	12333-11-8
Tungsten chloride	Sigma Aldrich	13283-01-7
Urea	Sigma Aldrich	57-13-6
Ethanol	VWR	64-17-5
Sawdust, from soft wood	Pets at Home	-
Graphite powder	Sigma Aldrich	7782-42-5
Silicon dioxide, quartz powder	Sigma Aldrich	14808-60-7

3.2.2 SYNTHESIS OF IRON CONTAINING GELS

These samples were prepared in the same manner as samples from Chapter 2. The following paragraphs detail the synthesis of the precursor gels. Following their production, samples (~0.5 g) were placed in a quartz tube and calcined using 700 W of applied microwave power under flowing nitrogen or argon.

A 10% (w/v) gelatin solution was prepared by adding porcine gelatin to hot and rapidly stirred distilled water (90 mL, 70 °C) until a homogeneous solution was obtained (solution A). A 10% (w/v) iron nitrate solution was prepared by placing iron nitrate, 10g, in a 100 mL volumetric flask and filling with distilled water. Solution A (20 g) was transferred to a beaker, covered with a watch glass and heated (70 °C) with rapid stirring. To this, iron nitrate solution (40.40 mL) (0.01 M of metal) was added. The solution became more viscous and brown.

From this point there were two different synthesis routes:-

1) The solution was placed in a drying oven at 70 °C until a solid was obtained.

2) The solution was place in an unmodified microwave oven and heated at 240 - 800 W of applied microwave power.

The mixed metal systems for the complex nanocomposites were synthesised as below

A 10% (w/v) gelatin solution was prepared by adding gelatin to hot and rapidly stirred distilled water (90 mL, 70 °C) and stirred until a homogeneous solution was obtained (solution A). Separately 10% (w/v) iron and magnesium nitrate solutions were prepared by placing the respective metal nitrate (10 g) in a 100 mL volumetric flask and filling with distilled water. A mixed solution was made from these stock solutions, the stock solutions were mixed at the desired ratio to give an overall concentration of metal of 0.01 M (solution B).

Solution A (20 g) was transferred to a beaker, covered with a watch glass and heated (70 °C) with rapid stirring, solution B was added. The rest of the synthesis followed as above.

3.2.3 SYNTHESIS OF IRON SOAKED SAWDUST SAMPLES

These samples were synthesised as described in our previous paper.[7] A 10% (w/v) iron nitrate solution was prepared as before. Sawdust (5 g) was placed in a beaker and the iron nitrate solution (20 mL) was added and stirred by hand until the sawdust was saturated. This iron soaked sawdust was then placed in an oven at 70 °C until dry. The final product (0.25 g) was placed in a quartz tube and heated as described above.

3.2.4 SYNTHESIS OF TUNGSTEN CONTAINING GELS

A 10% (w/v) gelatin solution was prepared by adding bovine gelatin to hot and rapidly stirred distilled water (90 mL, 70 °C) until a homogeneous solution was obtained (solution A). A 10% (w/v) ammonium metatungstate solution was prepared by placing ammonium metatungstate, 10 g, in a 100 mL volumetric flask and filling with distilled water. Solution A (20 g) was transferred to a beaker, covered with a watch glass and heated (70 °C) with rapid stirring. To this, ammonium metatungstate solution (24.64 mL) (0.01 M of metal) was added. The solution was stirred for a further 10 minutes to ensure it was homogenous. This was then place in an oven at 70 °C until a solid was obtained.

3.2.5 SYNTHESIS OF TUNGSTEN-UREA COMPLEXES

Several tungsten : urea ratios were trialled. A 20% (w/v) tungsten ethoxide solution was made by dissolving tungsten(VI) chloride (20 g) in ethanol (80 mL) and stirred at 50 °C (Solution A), this should be done slowly to limit the release of HCl gas. Solution A (19.83 mL) was stirred at 50 °C, to this the correct amount of solid urea was added to achieve the desired tungsten : urea ratio. This mixture was stirred for 20 minutes to dissolve and homogenise the sample, it was then dried at 70 °C until a solid was obtained.

3.2.6 ACID WASHING PROCEDURE

To acid wash Fe_3C/MgO samples, 0.5 g was added to 10 mL of HCl (0.1 M) in a Duran bottle and sonicated for 1 h followed by 23 h of moderate stirring. This will remove all nanoparticles. HCl (0.001 M) can be used to wash out the MgO and leave most of the Fe_3C.

3.3 RESULTS AND DISCUSSION

Using the consideration of microwaves described in the introduction to this chapter, a multimode cavity microwave (MMC) furnace was designed from the modified (DMO) as described by Vallance *et al*, Figure 3.3A.[104] Several experiments were carried out but as the starting materials do not couple with microwaves very well the results were not reliable or reproducible. As a result, the reactor was adapted to include a graphite 'jacket'. Graphite is an excellent microwave susceptor with high penetration depth and by having it in close proximity to the reaction mixture it caused rapid and localized heating, Figure 3.3B. To test the suitability of this as a synthetic route for our materials several final products were targeted.

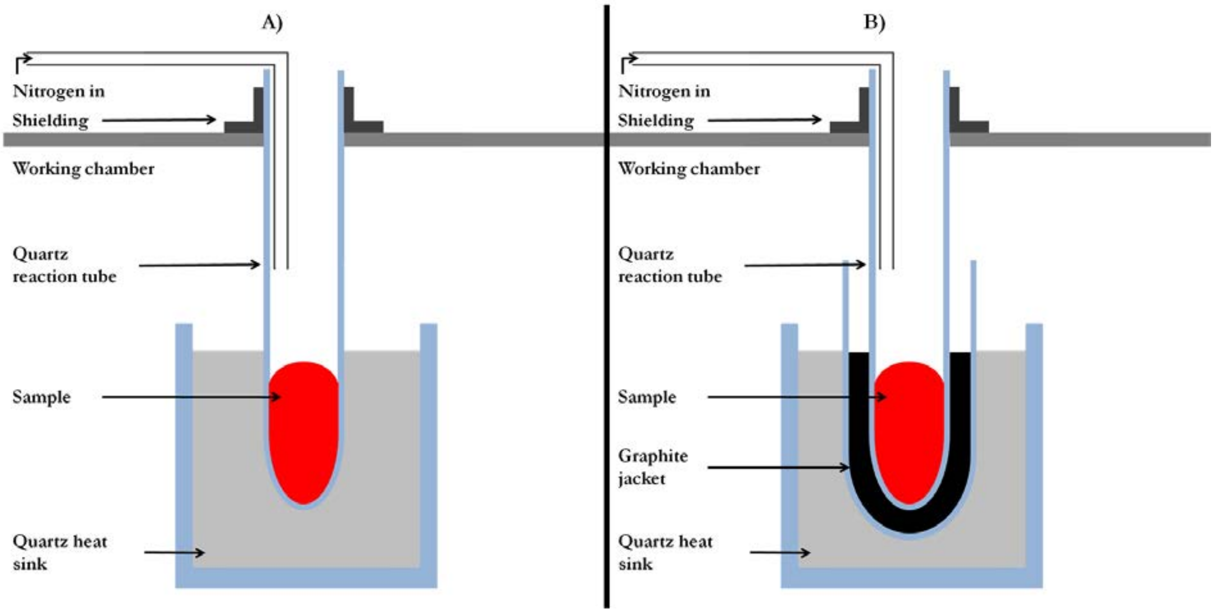

Figure 3.3 Schematic of the modified DMO A) without and B) with graphite jacket

3.3.1 SYNTHESIS OF IRON NANOCOMPOSITES FROM GELATIN

Figure 3.3 A shows the initial set up, which was abandoned after several issues were identified. Firstly as the starting materials did not couple very well with the MWs so long synthesis times were required (> 30 minutes); due to the low volume of sample this meant MWs bounced back into the magnetron causing it to overheat and greatly shortening it life span (< 6 months). Attempts were taken to absorb the excess MWs in both this design and the modified version by using a beaker of water, but it was found that as the water evaporated it cooled the sample/ graphite jacket preventing higher temperatures being reached. Using the graphite jacket solved these problems by significantly reducing the reaction times (< 4 minutes) and increasing the volume of MW absorbing material. The graphite powder that formed the jacket typically would show signs of arcing within the powder from approximately 10 - 30 seconds, after which it would then glow for the remainder of the synthesis. After a number of syntheses the XRD patterns of the products seemed to show that lower temperatures were being reached for the same synthesis times. XRD of the graphite powder showed a loss in crystallinity with less sharp peaks, this was confirmed by Raman spectroscopy which showed a decrease in the 'G' peak and an increase in the 'D' peak, Figure 3.4: as a result the graphite powder was then replaced after every use.

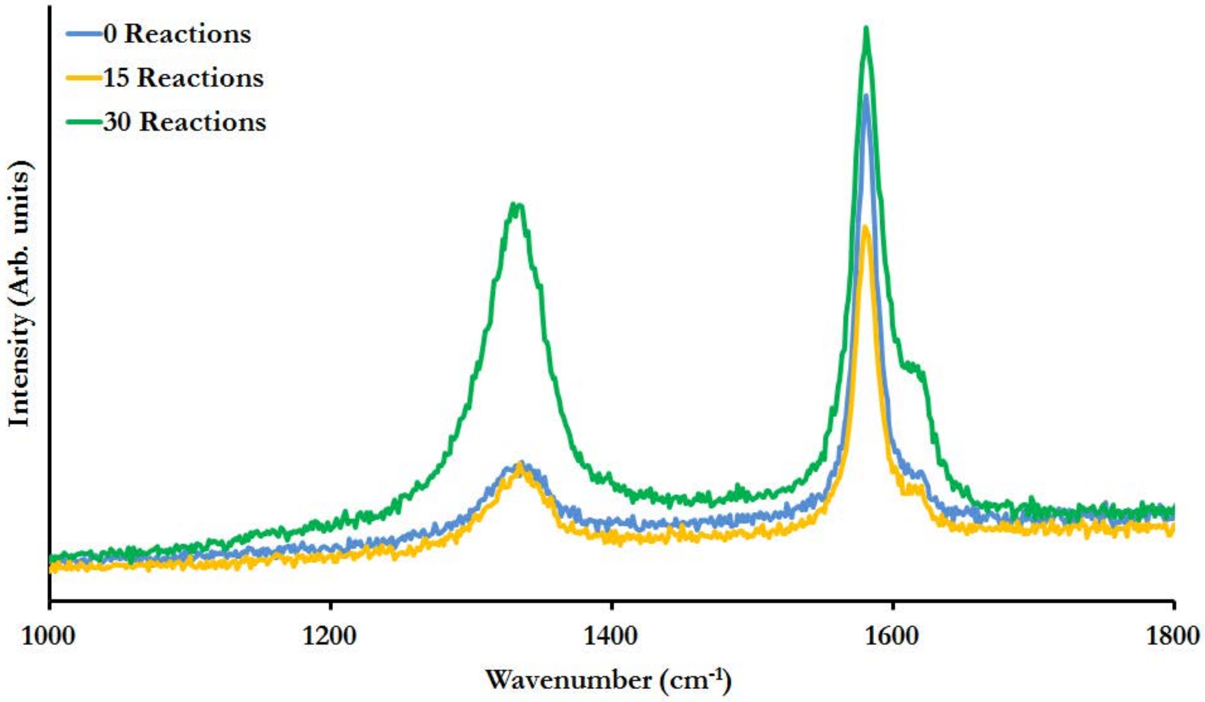

Figure 3.4 Raman spectra showing the amorphisation of graphite with an increasing number of reactions

The first synthesis to be trialled was the gelatin plus iron nitrate from the second chapter to produce Fe_3C or Fe_3N,[75] this seemed to be a good starting point as this had been done in both a conventional furnace and via in-situ X-ray diffraction and scattering experiments.[67] Samples were prepared by either drying them in an oven or in a standard DMO then calcining them in the modified DMO as described above, Figure 5.5 shows there are some differences in the resulting product.

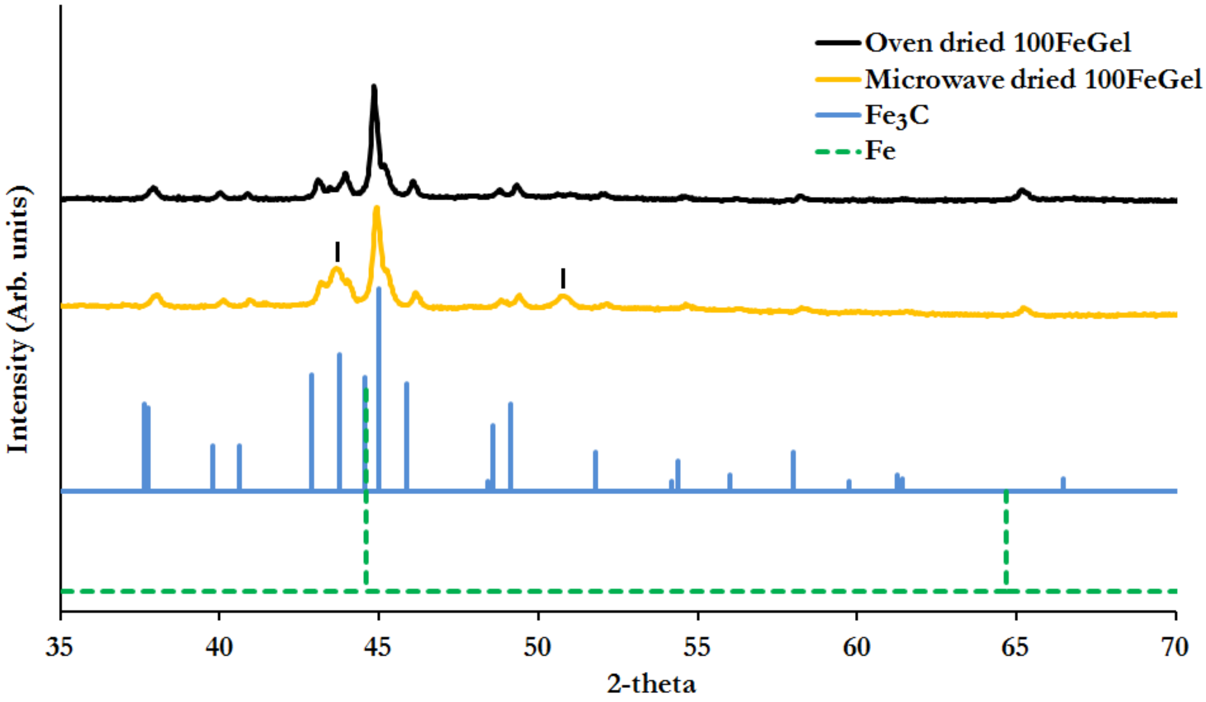

Figure 3.5 XRD patterns comparing oven versus microwave drying. Ticks mark the peaks for $FeN_{0.0324}$

A step-wise time, and therefore temperature, study was conducted to see if Fe_3C could be synthesised. Due to the rapid temperature increase a number of different iron phases can be isolated very quickly, Figure 3.6. For heating times less than 45 seconds no crystalline phase can be observed, but from 45 seconds the nucleation of Fe_3O_4 is shown by the appearance of iron oxide peaks in the powder X-ray diffraction patterns. 15 seconds later, at 1 minute, this extreme temperature gradient is highlighted by the iron oxide becoming iron nitride (ε-Fe_3N, PDF #01-

083-0877). The temperature can be estimated here since it was not possible to measure it. Iron nitride forms via this method in a conventional furnace at approximately 580 °C. Further heating up to 2 minutes produces a cubic (Fm-3m) nitrogen doped iron phase, a variety of compositions have been reported (i.e. $FeN_{0.032}$ PDF #01-075-2127) for between 3.2 and 9.5 mol% nitrogen.[110] Identifications of the exact composition is not possible due to the sample being a mixture of iron phases and nitrogen doped carbon, however the estimated temperature is approximately 625 - 650 °C. The appearance of low levels of nitrogen doping is interesting because previous studies have shown that formation of iron carbide from gelatin and iron nitrate at 10 °C min^{-1} to 800 °C under N_2 occurs from ε-Fe_3N to θ-Fe_3C through a mixed $Fe_3N_xC_y$ intermediate.[67] It was proposed that the interstitial nitrogen atoms were gradually replaced by carbons, this assumption was supported by ε-Fe_3N being able to contain high levels of carbon before changing its structure to θ-Fe_3C. Furthermore, the fact the *in-situ* studies showed no evidence of this low-nitrogen FeN_x phase and its obvious presence in the XRD patterns for the microwave synthesis may suggest a different mechanism. It is possible this is a kinetic product and it is proposed that the nitrogen diffuses out of the interstices in the ε-Fe_3N structure quickly and before the introduction of carbon, producing the low-nitrogen Fe_3N_x phase. Iron carbide (θ-Fe_3C, PDF #01-074-3843) is seen from 3 minutes (estimated temperature equals approximately 750 °C) and it appears alongside the low nitrogen Fm-3m phase. Samples heated for longer than 4 minutes are composed of iron carbide (cementite) with increasing amounts of metallic iron, which makes sense as this is the most stable product, thermodynamically.

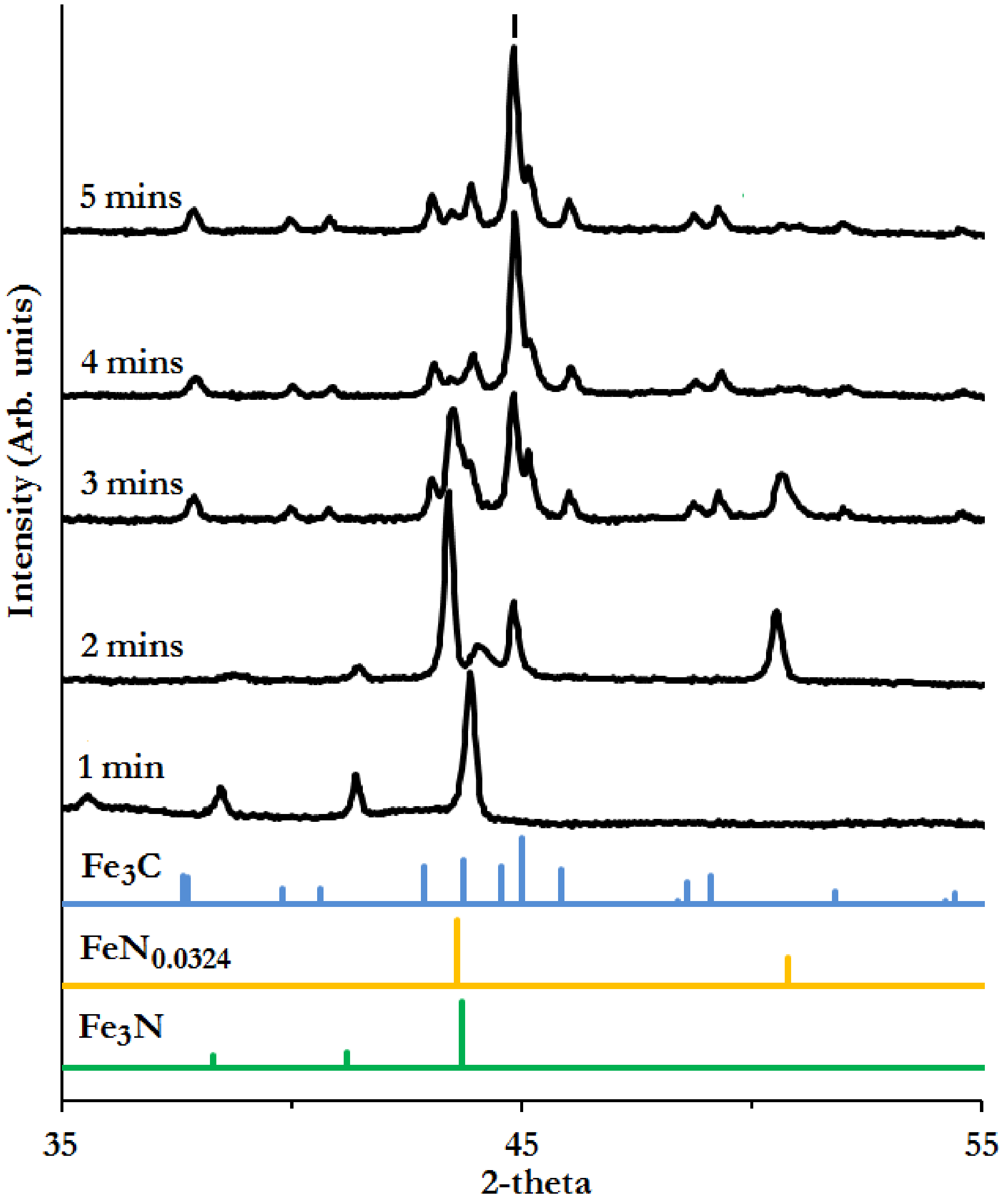

Figure 3.6 XRD patterns of gelatin plus iron nitrate calcined in a MMC at 700 W. Tick marks peak for metallic iron

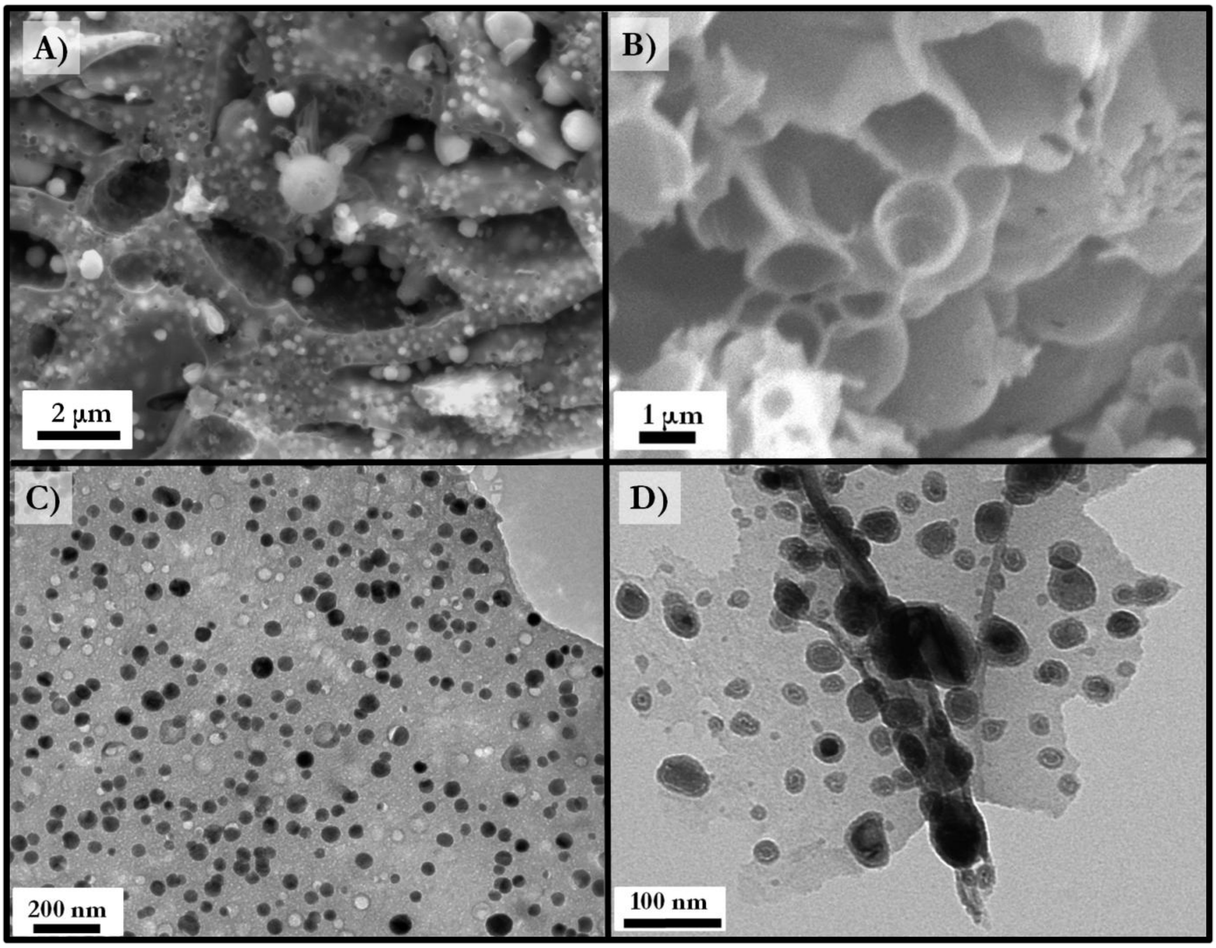

Figure 3.7 A) and B) SEM and C) and D) TEM images for carbon nanocomposites which were synthesised from gelatin plus iron nitrate. A) and C) were synthesised in 4 minutes in a MMC at 700 W and B) and D) were synthesised in a conventional furnace. Images reproduced with permission from reference [75]

Having successfully made iron carbide, SEM, TEM and Raman microscopy were carried out to compare the quality of the samples to the conventionally heated samples, Figure 3.7. The electron microscopy was used to investigate the microstructure. SEM shows a 'sponge-like' foam with embedded nanoparticles similar to that seen in the furnace treated samples. It does show small signs of sintering due to the lack of temperature control but TEM shows particles of a comparable size range of 20 - 100 nm.[75]

There is an absence of the graphite peak in the XRD and no graphite lattice fringes in the TEM so Raman microscopy was used to provide some information about carbon around the iron carbide particles seen in SEM, Figure 3.8. Above 1 minute of heating time the characteristic D (1330 cm^{-1}) and G (1600 cm^{-1}) peaks were seen for amorphous carbon. The increased intensity of the D peak is indicative of smaller aromatic clusters. The G peak has shifted to a higher frequency and D/G ratio has increased showing that the graphite has become nano-graphitic.[111] These broad peaks also suggest that the carbon is very disordered,[111] supporting the XRD and TEM data. The peaks below 500 cm^{-1} correspond to Fe_3O_4, probably due to surface oxidation [112] as iron carbide is air sensitive. The 'bump' at mid wavenumber, approximately 700 cm^{-1}, could be the start of a nitrate peak.

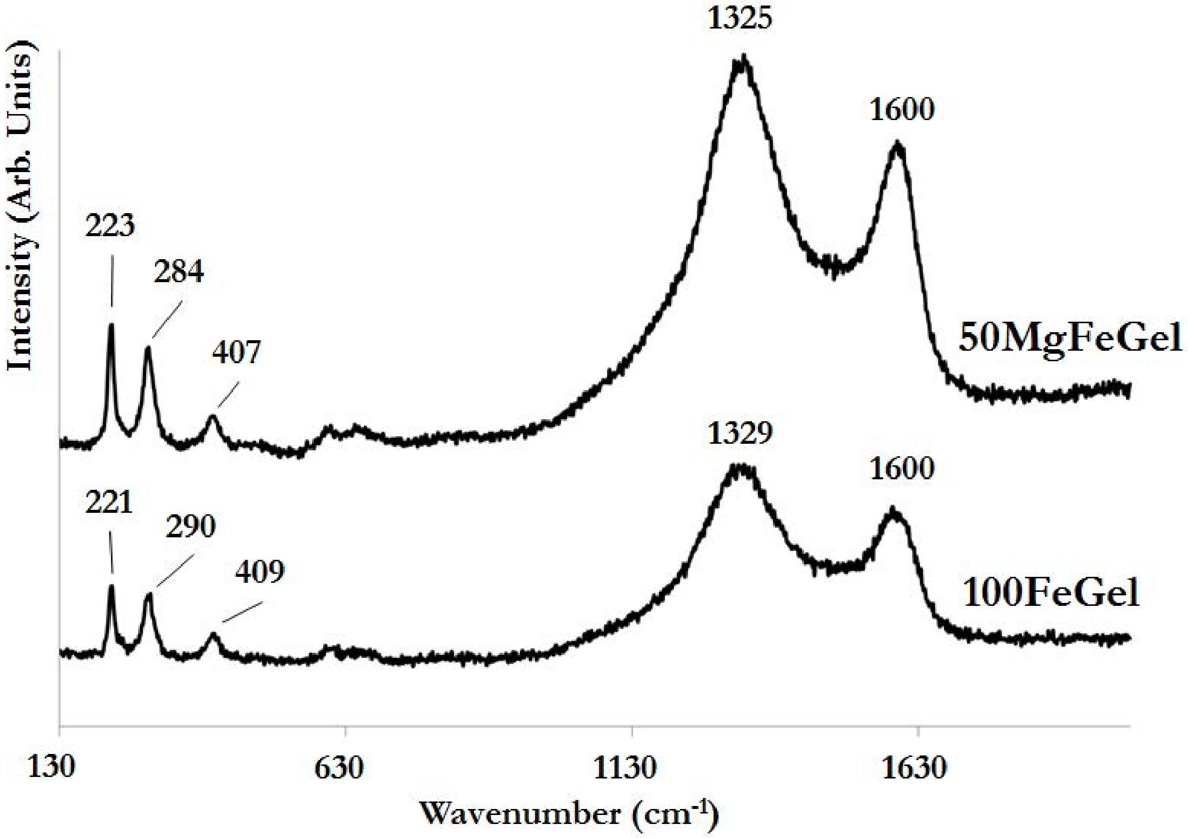

Figure 3.8 Raman of carbon nanocomposites with iron carbide, with and without magnesium oxide

The final variable tested was that effect of the atmosphere on the reaction, the same MW synthesis was carried out in an argon atmosphere. Heated for the same time under argon the sample showed the same phases in the XRD, Figure 3.9. The main difference is the reaction speed which appears to be slower under argon; this could indicate that atmospheric nitrogen plays a role in the reaction. The reaction appears to proceed slightly more slowly but follows the same mechanism. Finally a sample was prepared by first flushing the quartz tube for a few minutes and then stopping the nitrogen flow prior to synthesis and again this produced Fe_3C and the low nitrogen doped iron phase.

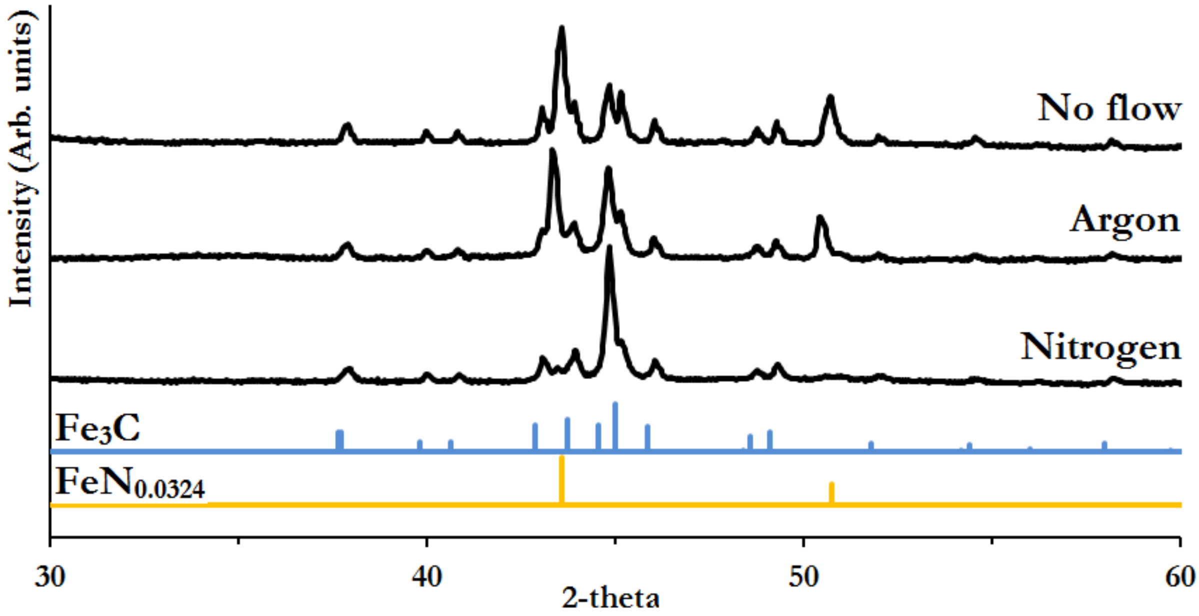

Figure 3.9 XRD patterns comparing phase formed under different atmospheres

One of the main interests of these materials is their use as catalysts, where porosity is an important factor and so previous studies that used conventional heating have synthesised iron carbide nanocomposites with other species such as magnesium oxide.[65] The magnesium oxide can then be removed by acid washing to increase porosity. The microwave synthesis method was also tested on this MgO/Fe_3C system. A gelatin plus magnesium and iron nitrate mixture, similar to the samples prepared earlier, was also made. 1 minute of applied MW power produces ε-Fe_3N, MgO (PDF #00-004-0829) and a small amount of Fe_3O_4, Figure 3.10. Additional heating causes the magnesium oxide peak intensity to increase indicating an increase in crystallinity/particle size, alongside this the low nitrogen iron phase forms from iron nitride before this too disappears and iron carbide is formed. The presence of magnesium oxide does not seem to change the reaction mechanism of the iron system and in a similar manner to the iron only system, heating the sample for more than 4 minutes results in increasing amounts of metallic iron.

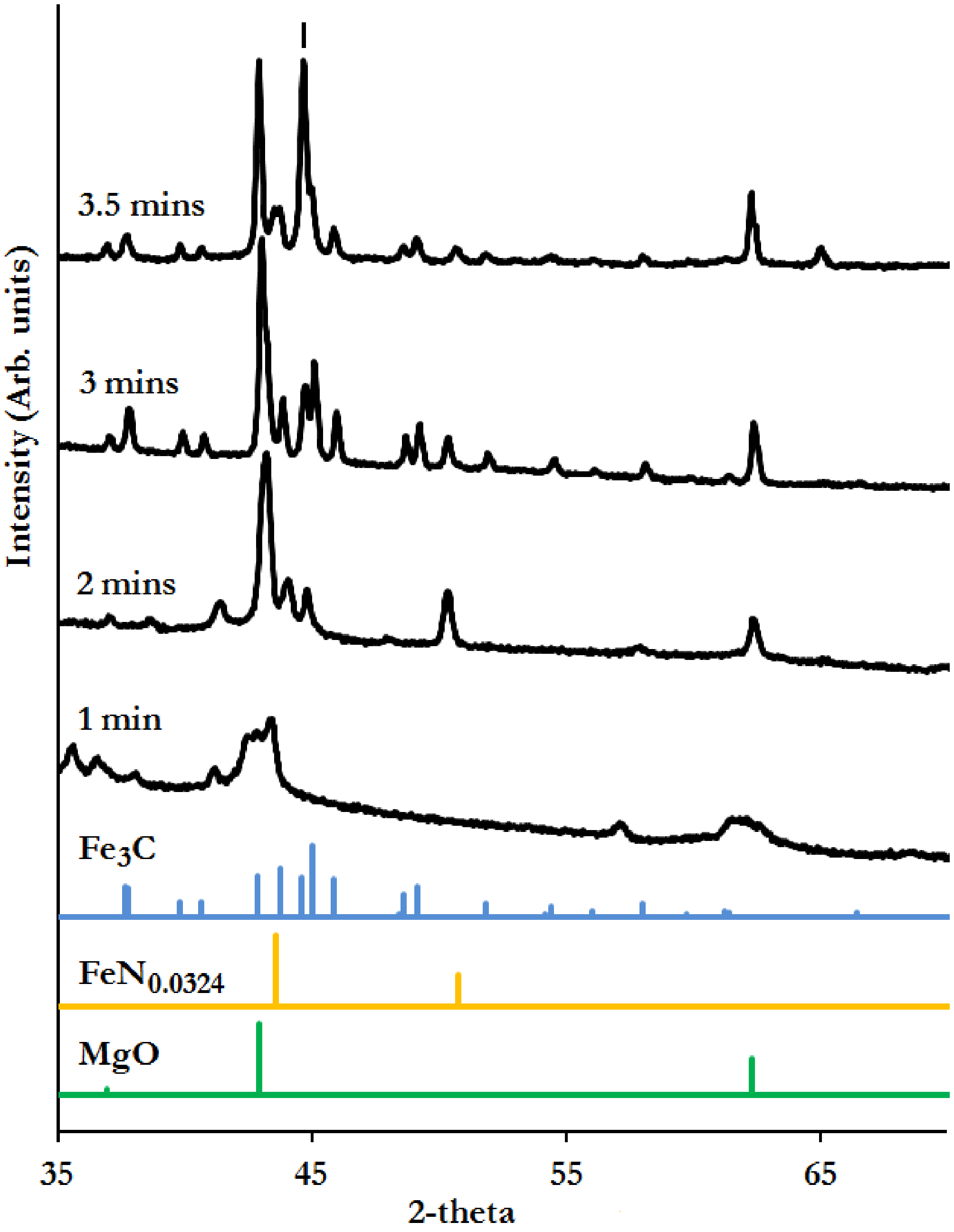

Figure 3.10 XRD patterns for gelatin plus magnesium and iron nitrates calcined in a MMC at 700 W. Tick marks the main peak for metallic iron

An interesting feature of these XRDs is the sharpness of the peaks, these are narrower than the samples from conventional heating[65] and this indicates the iron carbide and magnesium oxide particles are larger. This is remarkable as the synthesis times are much shorter in a MMC compared to a furnace and longer heating times generally are attributed to sintering effects. As mentioned before there is a lack of temperature control so the temperature may be significantly higher than in a furnace. Another reason for larger particles could be due to magnetic effects, materials with strong magnetic properties (i.e. Fe_3C) experience an additional term for heat evolution:[99] therefore as the iron carbide forms it then gains additional heating which could be contributing to the larger particle size. The difference in particles size between the two techniques by TEM is shown, Figure 3.11, this should be investigated further with a bulk technique like SAXS. The Raman spectra, Figure 3.8, of these samples again shows characteristic broad D and G peaks for disordered carbon: these spectra have much sharper between 200 - 400 cm^{-1} which can be assigned to iron oxide (haematite) and is probably from surface oxidation of the sample.[113]

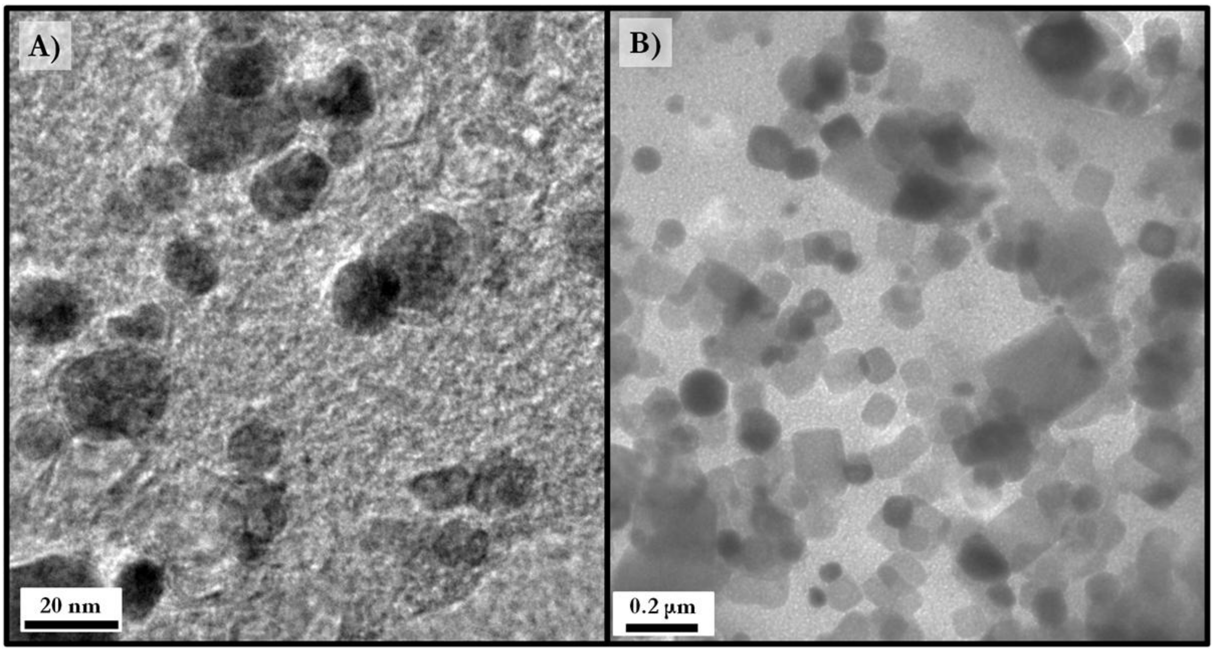

Figure 3.11 TEM images of gelatin plus magnesium and iron nitrates after being calcined in A) a conventional furnace at 800 °C[66] and B) a MMC for 3 minutes at 700 W

3.3.2 SYNTHESIS OF IRON NANOCOMPOSITES FROM BIOMASS

The next step in green synthesis for these iron carbide nanocomposites is to prepare them from raw biomass and this has been done before by soaking biomass (i.e. sawdust) in a iron nitrate solution followed by calcination under nitrogen in a furnace.[7] Irregularly-shaped multiwalled carbon nanotubes were seen in the TEM and these were shown to be formed by iron carbide nanoparticles 'melting' and 'burrowing' through the biomass. This mechanism has similarities with chemical vapour deposition synthesis of carbon nanotubes[114] and graphitisation of amorphous carbon.[115] XRD patterns, Figure 3.12, show traces for sawdust samples soaked in iron nitrate solutions of different concentrations. These samples were heated at 700 W in a MMC under flowing nitrogen for 3.5 minutes (a time found to produce iron carbide), this was done to investigate if it followed the same trends as samples heated conventionally. The XRD patterns show the iron carbide peaks as expected and also a broad peak at 26 ° for graphite.

TEM shows that both syntheses produce very similar samples, Figure 3.13, despite the much shorter synthesis times; this suggests the catalytic graphitization step still occurs however this would need to be confirmed by in-situ measurements (i.e. TEM, XRD). A consequence of the carbon nanotubes is that the resulting carbon is highly mesoporous and is of interest for catalysis and filters and can be characterized by nitrogen porosimetry. The conventionally heated samples had a reported Brunauer-Emmett-Teller (BET) surface area of 210 m^2g^{-1} which is very similar to the current samples synthesised in the MMC, which have a BET surface area of 220 m^2g^{-1}; the sorption isotherms for these samples are shown in Figure 3.14.[7]

These samples, like the gelatin ones, underwent acid washing to further increase porosity by removing the iron carbide nanoparticles. The result was an increase in the BET surface area to 330 m^2g^{-1}. Raman microscopy was again carried out to investigate the nature of the carbon, Figure 3.15, and it shows a smaller D/G peak ratio and sharper peaks indicating more ordered graphitic carbon.

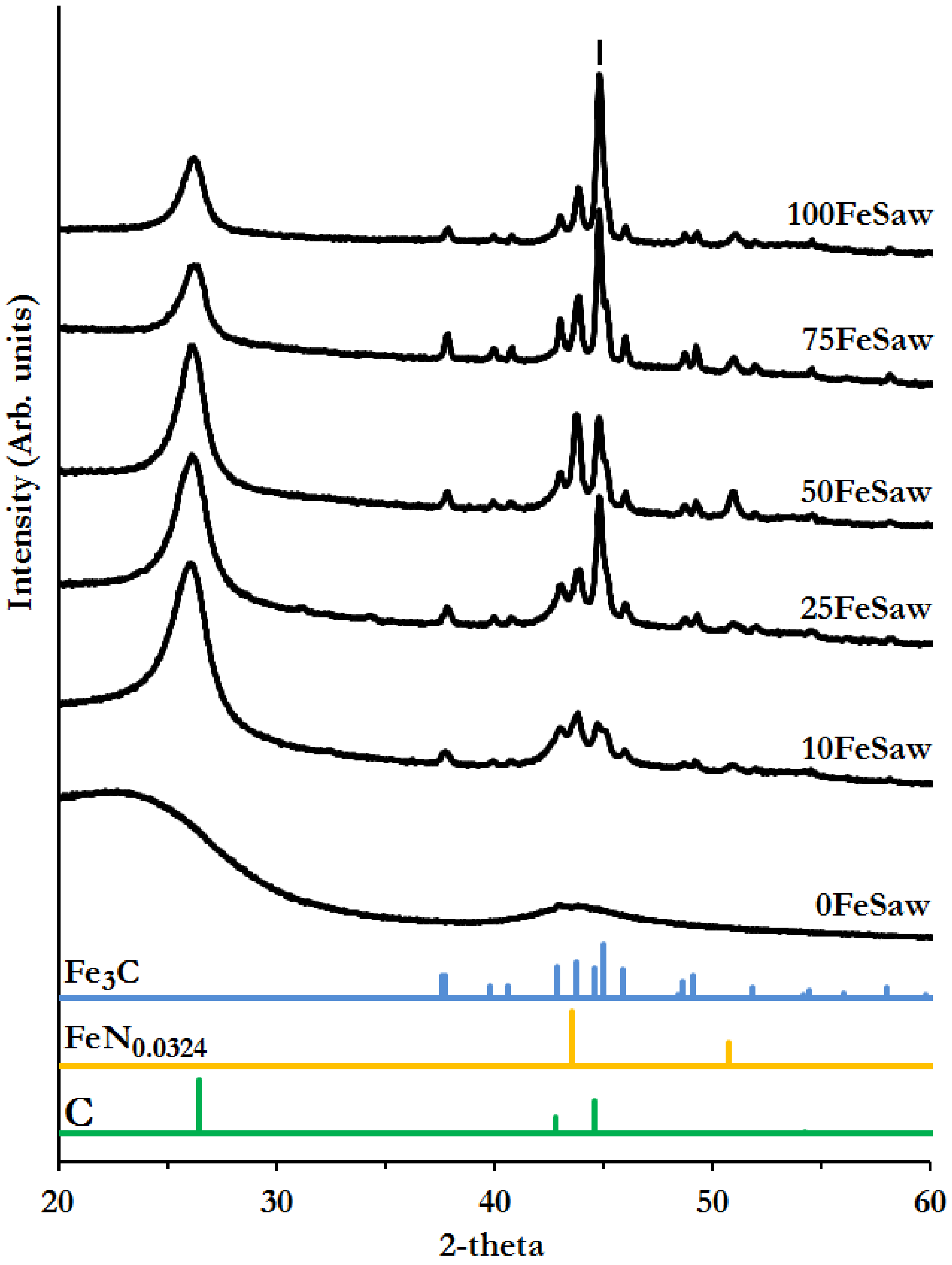

Figure 3.12 XRD patterns for samples prepared from sawdust with increasing amounts of iron nitrate. Tick marks the main peak for metallic iron

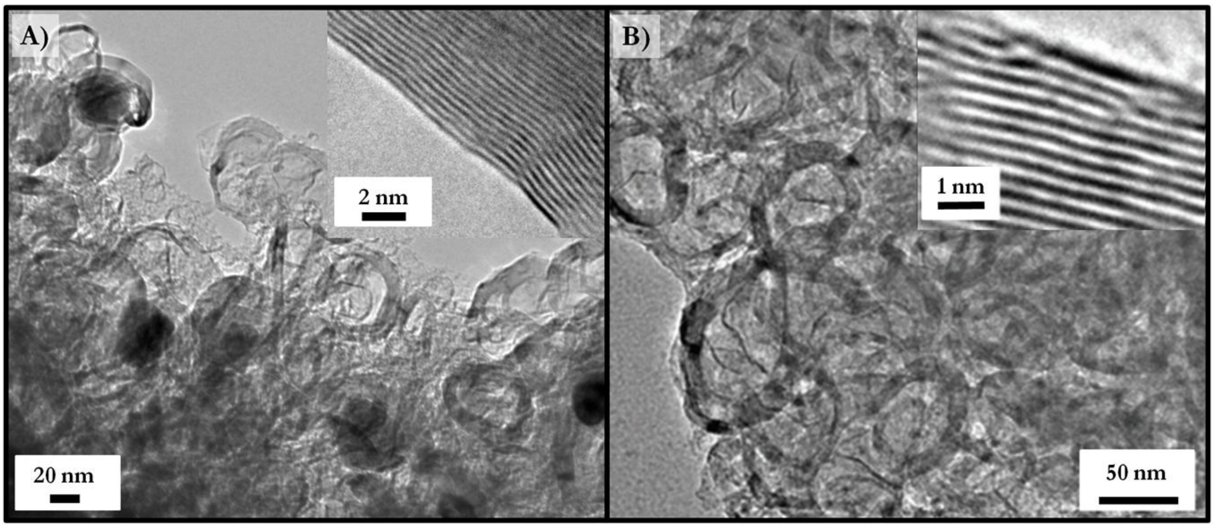

Figure 3.13 TEM images 100FeSaw synthesised in A) a MMC at 700 W for 3.5 minutes and B) in a conventional furnace; inset in both images a magnified section showing the d-spacing for the interplanar distances in graphite.

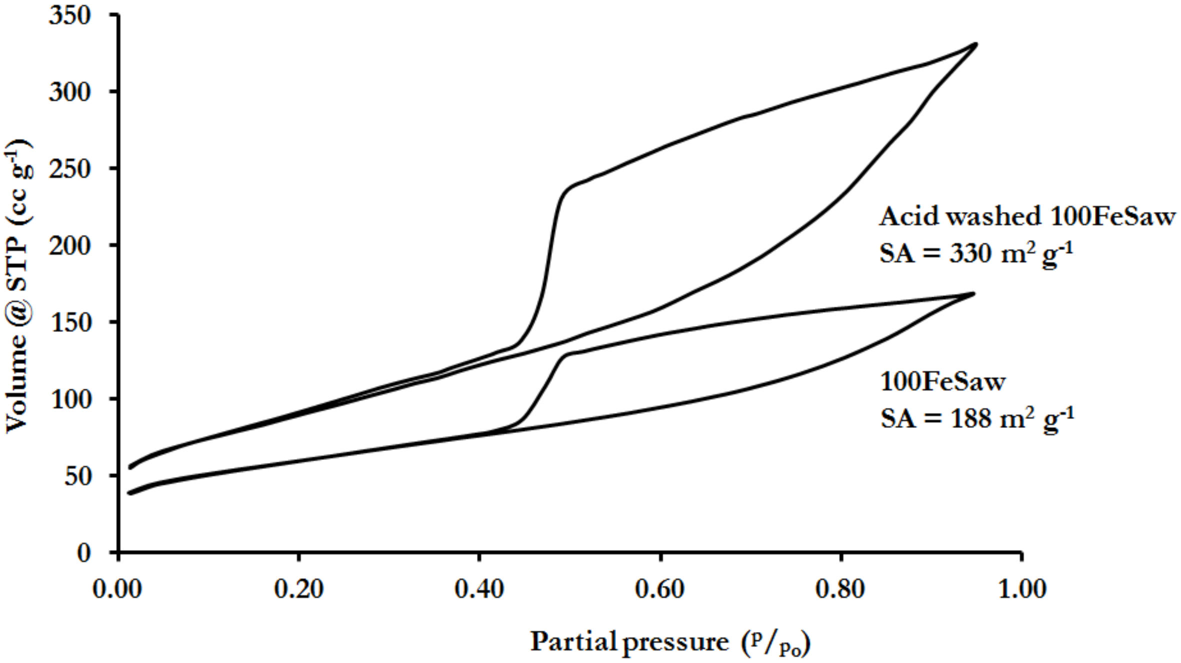

Figure 3.14 Nitrogen sorption isotherms 100FeSaw as synthesised and after acid washing

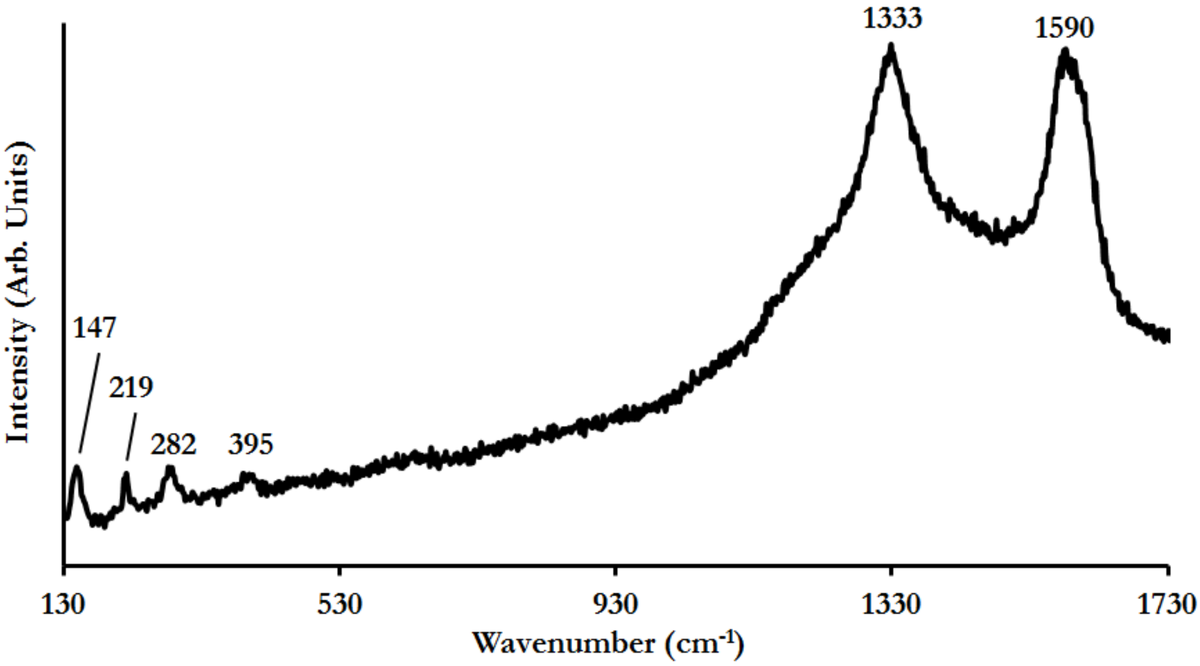

Figure 3.15 Raman spectra of 100FeSaw synthesised by a MMC at 700 W in 3.5 minutes

3.3.3 SYNTHESIS OF TUNGSTEN NANOCOMPOSITES

Transition metal carbides such as iron and tungsten are of interest at the moment due to their catalytic properties and the fact that they are similar to those of platinum. Tungsten carbide will be the focus of Chapter 5 and it was synthesised via the biopolymer sol-gel route, however it was difficult so it was attempted in the MMC. Tungsten carbide has been synthesised by the Gregory group, in Glasgow, via the original modified DMO, Figure 3.3 A, using powders of the precursors (W and C). In Chapter 5 tungsten carbide was also synthesised by 'traditional' metal : urea chelating method, so this method we used to see if it could work in a MMC.

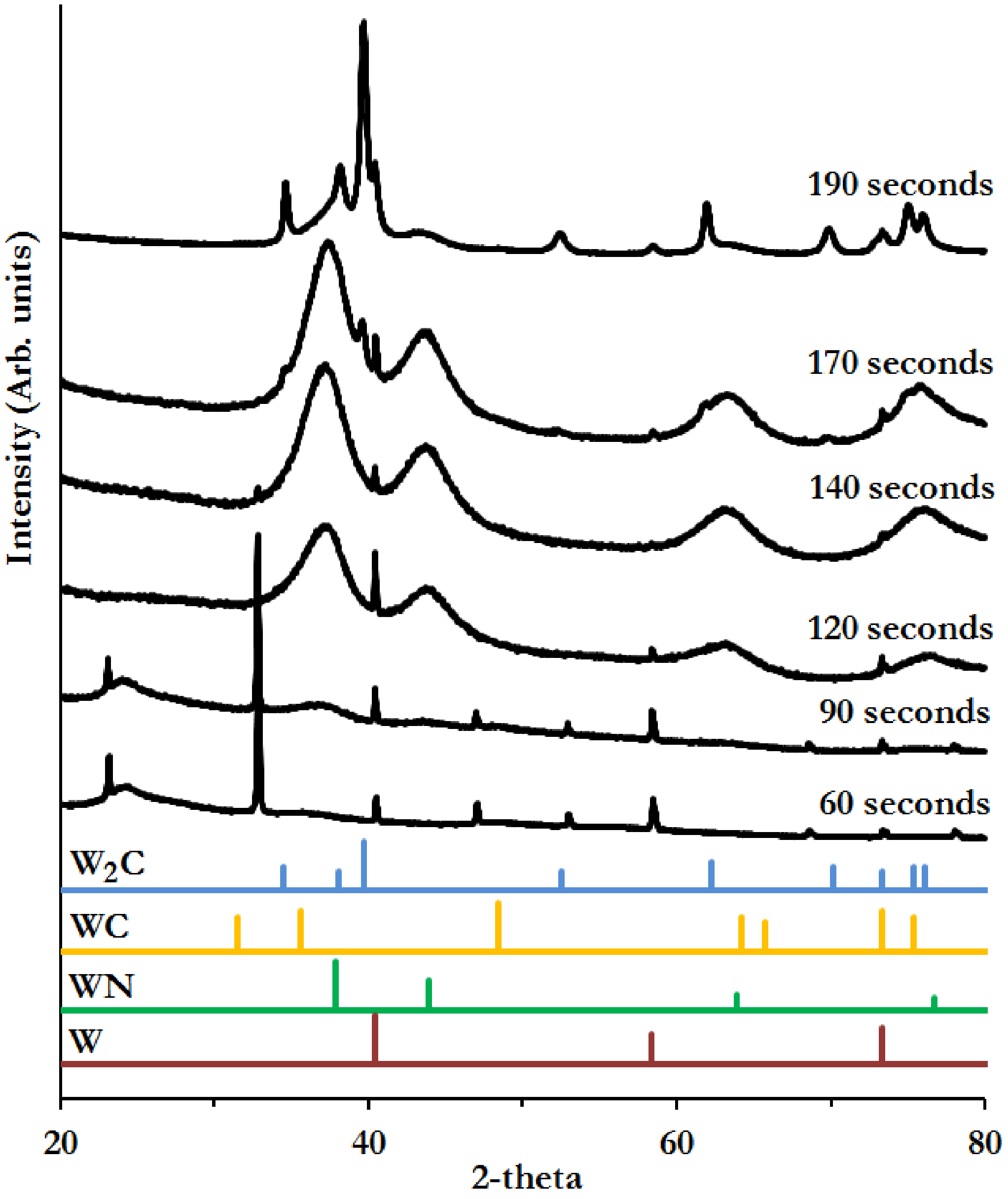

Figure 3.16 XRD patterns of various tungsten compounds synthesised by a 1:14 ratio of tungsten to urea in a MMC at 700 W

A tungsten to urea ratio (W:U) of 1:14 was chosen as it has the most urea and as the urea decomposes it helps produce the carbide and the higher ratio of W:U to maximum the chance of it being synthesised. In a similar manner to the iron carbide synthesis a range of times were trialled to probe the phases isolated at different time/temperatures, Figure 3.16. It is possible to synthesise crystalline phases in very short times (~ 1 minute). Tungsten nitride (WN, PDF #04-

015-0316) is seen from approximately 2 minutes and tungsten hemi-carbide (W_2C, PDF #00-002-1143) is seen from 2 minutes 40 seconds. It should be noted that the times quoted above do not refer to the synthesis times for which the XRD patterns show phase pure patterns (i.e. only WC), but are the times for when that phase was seen. The fact that these different phases are isolated with such short time gaps between them again highlights the steep temperature gradient. Another interesting point is the particle size which can be estimated from the peak broadening and it clearly shows that particle size dramatically increases with heating times. Some sintering is expected but even the longest heating times in the microwave are orders of magnitude shorter and the microwave synthesised particles are bigger than the furnace samples: this is further evidence that the temperatures being reached are much higher than in the furnace causing significant sintering.

Figure 3.17, shows a series of metal : urea ratios that were used here as they were in the furnace, the samples were calcined for 2 minutes and 30 seconds at 700 W in a MMC. These samples were synthesised to investigate how changing the W:U ratio would affect the phases being formed. The highest 2 W:U ratios (1:14 and 1:6) produced WN (PDF #04-015-0316) and W (PDF #00-001-1203) -whilst a W:U of 1:2 produced a mixture of tungsten oxides - WO_2 (PDF #00-003-0664) and (WO_3 #04-007-2322). This could mean that with lower ratios, the urea is burnt off early and that tungsten carbide can be isolated at shorter times, further experiments would be needed to test this. Interestingly a W:U of 1:6 produced less metallic W, further work should also include work with ratios in this region to try to isolate pure WN.

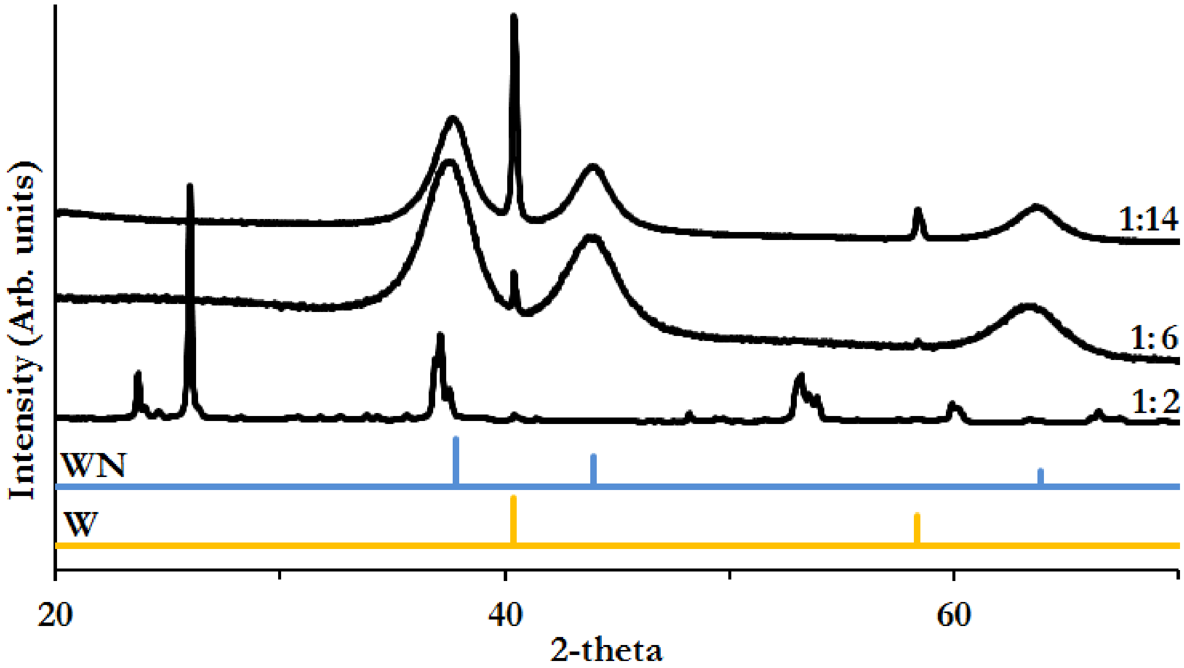

Figure 3.17 XRD patterns for various tungsten compounds synthesised in a MMC at 700 W for 2.5 minutes with varying tungsten to urea ratios

Having successfully synthesised tungsten carbide in a microwave via the urea chelating method, it was then attempted using a biopolymer sol-gel method. A number of different biopolymers were trialled, Figure 3.18, a few different times were tried and the data for 3 minutes 15 seconds is shown. Both agar and dextran produced a mixture of phases consisting mainly of WO_3 WO_2, but also smaller amounts of W and WN. Synthesis of the oxide is undesirable so research was focussed on gelatin where the main phases were W_2C and WC; the bovine gelatin was selected as it produced less metallic W and WN. Whilst this is not a pure product it does represent a breakthrough, by being a refractory carbide that has been produced in minutes instead of hours with reasonable particle size and through the use of a biopolymer. The particle size was estimated by using the Scherrer equation but it was outside the operational range of the equation at 400 nm.

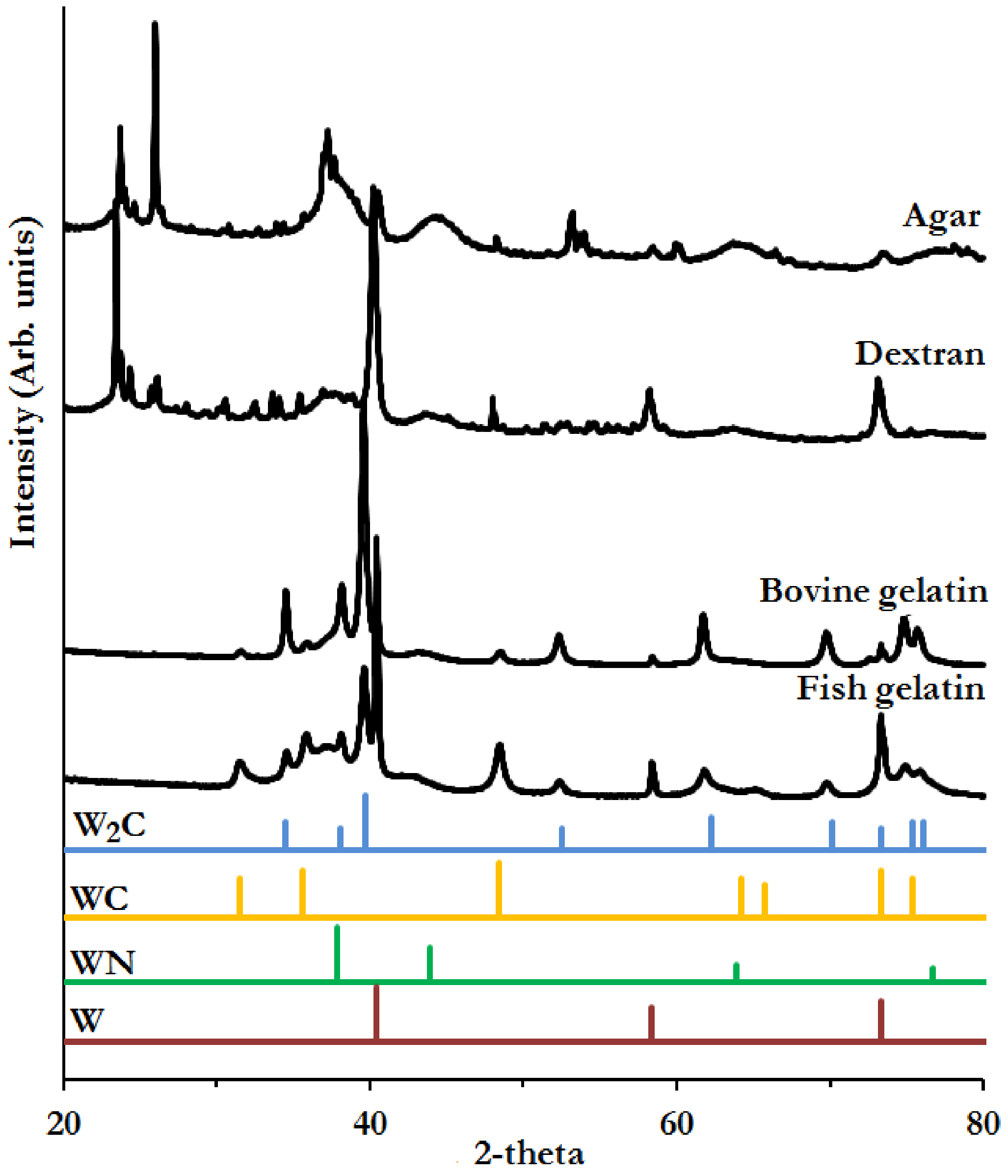

Figure 3.18 XRD patterns for various tungsten compounds synthesised in a MMC at 700 W for 3.25 minutes using ammonium metatungstate with different biopolymers

Using bovine gelatin a temperature/time study was carried out to investigate the mechanism of tungsten carbide formation in a microwave to ascertain if it is possible to isolate the pure product. Figure 3.19, shows these data and once more shows that it is possible to generate a crystalline phase on a subminute time scale, but it is not until 2 minutes 30 seconds that a mixture of WN and W are seen in the XRD. Further work should be focused here to obtain pure WN. A zoomed in version of this figure is shown in Figure 3.20, it focuses on the longer synthesis times and has a constrained 2-theta range for clarity. A synthesis time of 4 minutes shows increased amounts of WC and W_2C whilst for 3 minutes 15 seconds shows more W_2C and a small amount W. To get from one time to the other the system appears to go through metallic tungsten, this is unexpected as the tungsten would be reducing and then oxidising again which is unusual behaviour and currently not explainable with current data. That said it could be a similar process to the eutectoid decomposition shown here,[116] but this occurs at very high temperatures. Future work should verify this and if real it should be studied further as it would give insights into the formation of the carbide.

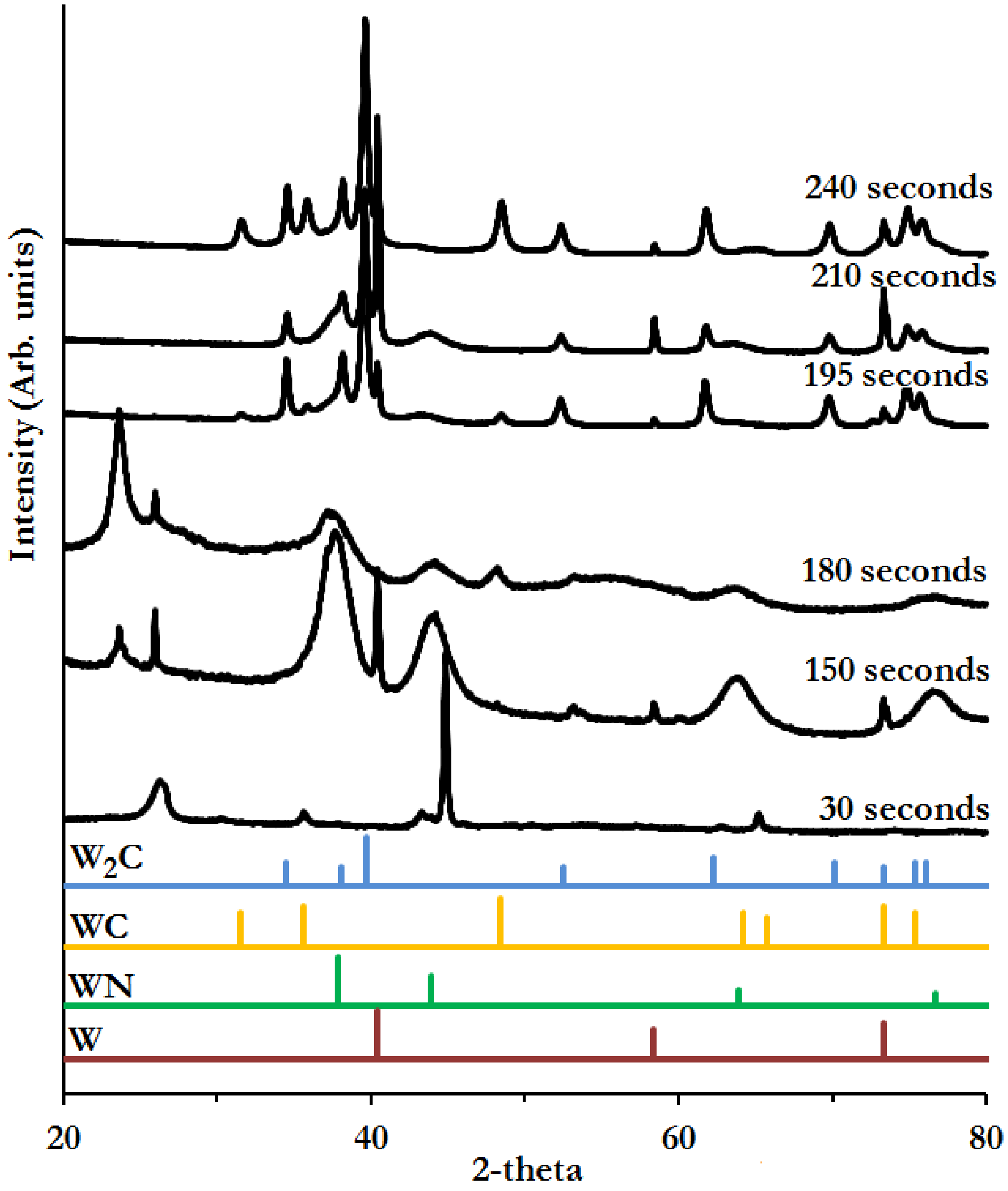

Figure 3.19 XRD patterns for various tungsten compounds synthesised in a MMC at 700 W using ammonium metatungstate for increasing reaction times

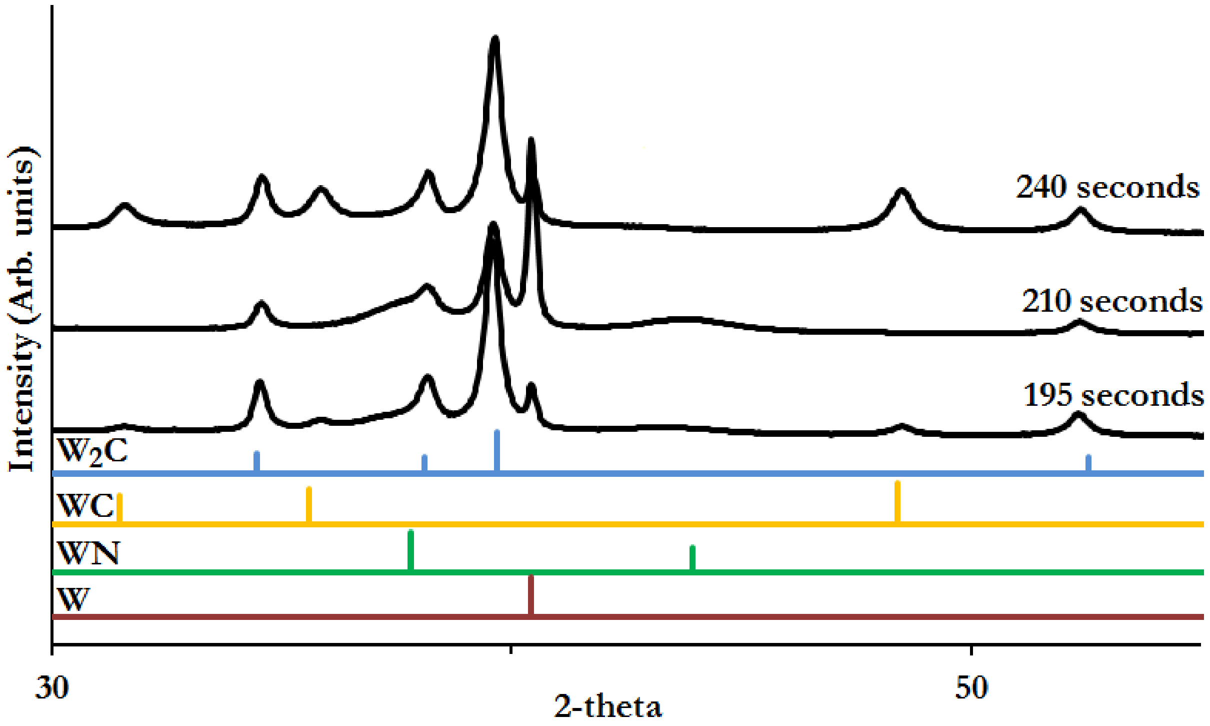

Figure 3.20 XRD patterns for various tungsten compounds synthesised in a MMC at 700 W using ammonium metatungstate for increasing reaction times

Mixed nanocomposites, similar to the iron carbide and magnesium oxide system, have been synthesised previously by sol-gel routes and Figure 3.21, shows the first attempts to recreate this in the microwave reactor. The XRD pattern shows magnesium oxide and tungsten hemi-carbide with a small amount of tungsten carbide. This is interesting because the conventional furnace-synthesised sample shows magnesium oxide and tungsten nitride.[65] This difference could again be due to overheating in the microwave, however this now presents the option to produce both W_2C and WN with MgO this should allow for porosity to be increased.

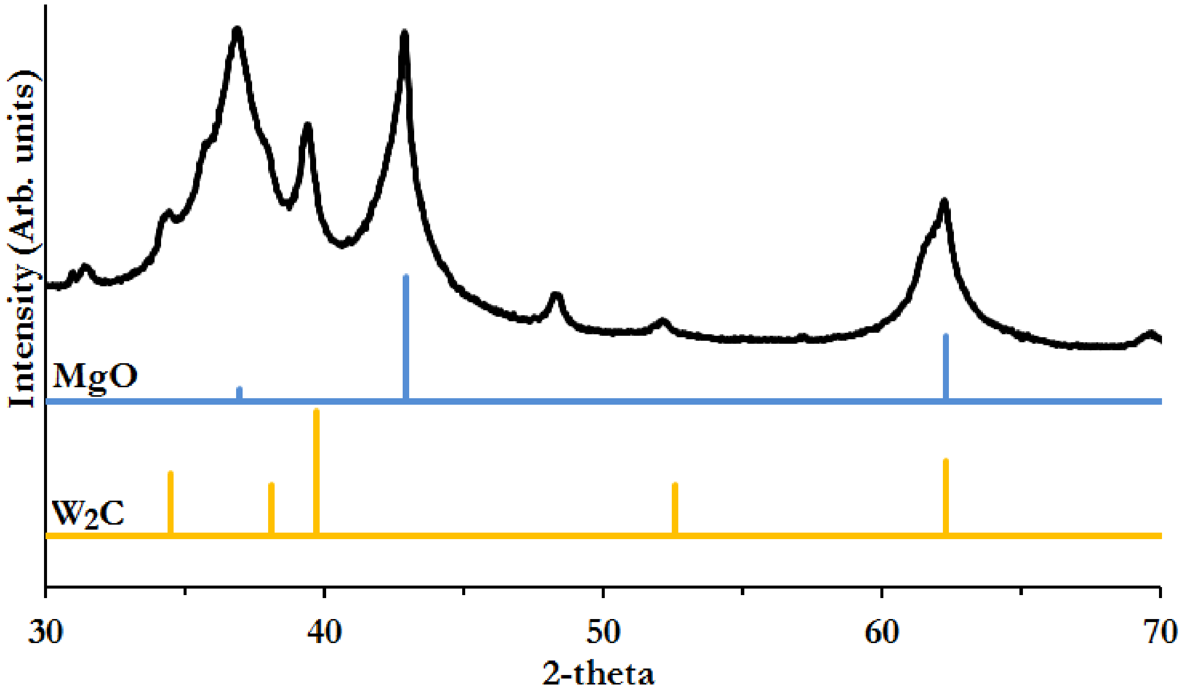

Figure 3.21 XRD pattern of MW25 synthesised in a MMC at 700 W for 3.5 minutes

3.3.4 SYNTHESIS OF OXIDE NANOCOMPOSITES

The final category of material synthesised was metal oxides; this was done to show the range of this synthesis method. Initially experiments were carried out without flowing gas, to investigate if the air in the tube would be sufficient to oxidise the samples. This first test resulted in a solid that was half black and half white (cerium dioxide). The gas inlet tube was fitted with air so this could be flown over the sample, but the result was the same so the end of the inlet tube was moved closer to the sample. Figure 3.22, shows the XRD pattern for cerium dioxide (CeO_2, PDF #01-071-4199) synthesised using the modified gas inlet and an increased synthesis time. This indicates the need for flowing air to provide enough oxygen for the reaction and to drive off the CO_x compounds generated.

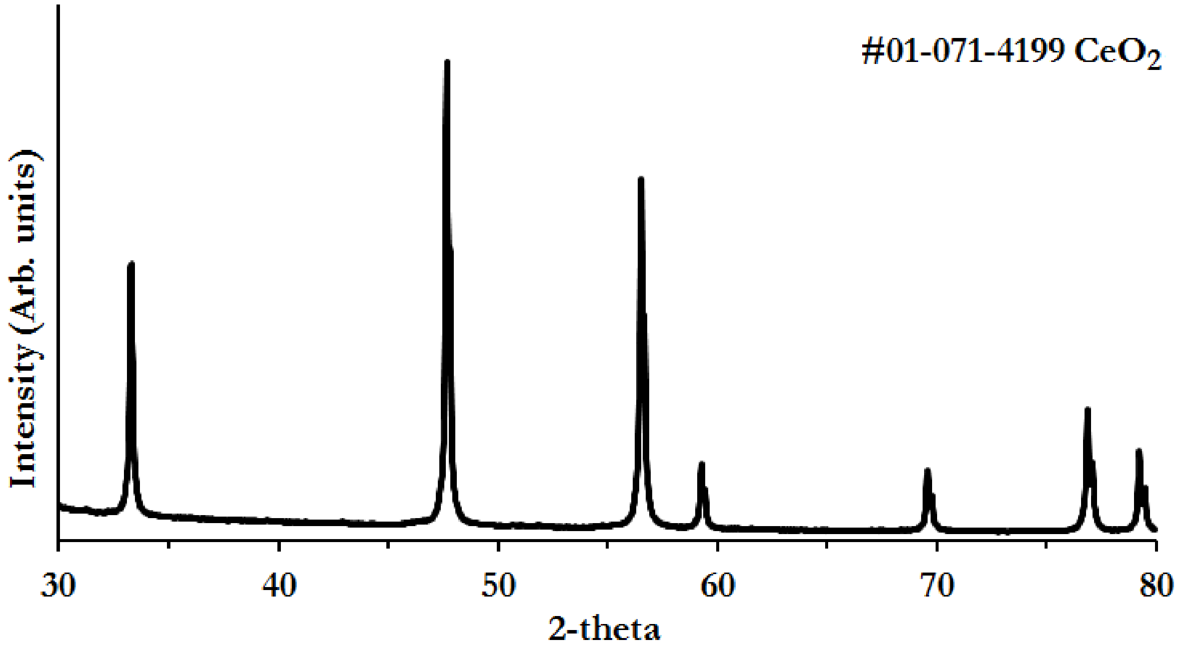

Figure 3.22 XRD of CeO$_2$ produced in a microwave, peak splitting due to Kα2

3.4.5 ESTIMATION OF TIME AND POWER SAVING

Microwaves are known as a rapid and energy efficient way to heat things, to quantify this claim a calculation has been carried out to substantiate the time and power savings, Table 3.2. The calculation below is the comparison of the synthesis of iron carbide in a microwave and furnace. Data on the power usage of the furnace and oven was gathered from Carbolite and Memmert and is shown in Appendix B and data for the microwave was collected from the instruction and safety information on the back of the microwave. The total energy usage for each step was calculated using Equation 3.1, this is the maximum possible amount of power used. Not all this energy will be converted to heat and it does not account for losses due to heat escaping the system. As a result no conclusion can be made about the efficiency of each process only the amount of power saving as a result of using microwaves. After calculating the energy consumption for each step the energy and time savings can be worked out using Equations 3.2

and 3.3. The results show an energy saving of 97% and time saving of 99% this highlights the benefits of microwave synthesis both from an economic and green chemistry point of view.

Table 3.2 Summary of the energy saving from using a microwave vs. a furnace. * Full power pulsed for half the time. #output 700W, actual power consumption 1150W

Furnace synthesis	Microwave Synthesis	Time (h)	Power (W)	Energy (kWh)
Oven drying	**-**	24	108	2.592
Furnace ramping	**-**	1.3	1550 (3100)*	2.015
Furnace holding	**-**	0.083	911	0.076
Furnace cooling	**-**	22.62	-	-
Total		**48**	**-**	**4.683**
-	**Drying**	0.065	700 (1150)#	0.075
-	**Heating**	0.065	700 (1150)#	0.075
-	**Cooling**	30	-	-
	Total	**0.57**	**-**	**0.15**

$$\boldsymbol{Time(H)} \times \frac{\boldsymbol{Power\ output\ (W)}}{\mathbf{1000}} = \boldsymbol{total\ energy\ usage\ (kWh)}$$ **Equation 3.1**

$$\mathbf{100} - \left(\frac{\boldsymbol{Microwave\ output}}{\boldsymbol{Furnace\ output}} \times \mathbf{100}\right) = \boldsymbol{energy\ saving}\ (\%)$$ **Equation 3.2**

$$\mathbf{100} - \left(\frac{\boldsymbol{Microwave\ time}}{\boldsymbol{furnace\ time}} \times \mathbf{100}\right) = \boldsymbol{time\ saving}\ (\%)$$ **Equation 3.3**

3.5 CONCLUDING REMARKS

This chapter details the preliminary work for a highly efficient and green synthesis route to generate a wide array of composites including metal oxide/carbide/carbon, metal carbide and metal oxides from biopolymers or biomass. Due to the low volumes of sample used and that the precursors do not couple with microwaves, a graphite powder jacket was included. This improved heating and reliability by coupling well to the microwaves and by increasing the volume of samples absorbing microwaves therefore reducing and amount reflecting back into the magnetron and preventing it from overheating.

It was possible to estimate the energy and time savings to be 97% and 99% respectively, compared to heating in a conventional muffle furnace. Future work should include calculations on the efficiency of microwave absorption for graphite in this set up and investigate alternatives. At present the sample size is approximately ~0.5 g which is significantly less than the mass of sample that can be calcined at once in the furnace, taking this into account with the current set would massively decrease estimated calculation. However this can be overcome and to do this further work should include design of a custom built flow reactor with plates of a microwave susceptor surrounding the sample as it is flowed/ carried through for example, Figure 3.23. This would allow the output from the magnetron to be used efficiently through clever design of resonators and control systems. It would also help to eliminate several other problems, the larger particle sizes seen in this study is probably a result of 'overheating' in the MW. A flow system would allow for temperature control by having ports for IR thermometers and either variable outputs on the magnetrons or having magnetron of differing constant outputs to ensure a constant temperature through constant feedback. Such a system would also allow control over the speed at which the sample reached synthesis time and total reaction time, which should allow for control over particle size. A possible first step towards this could be further modification of the DMO to including a fibre optic thermometer and possibly feed this into the power supply to pulse the magnetron to control temperature.

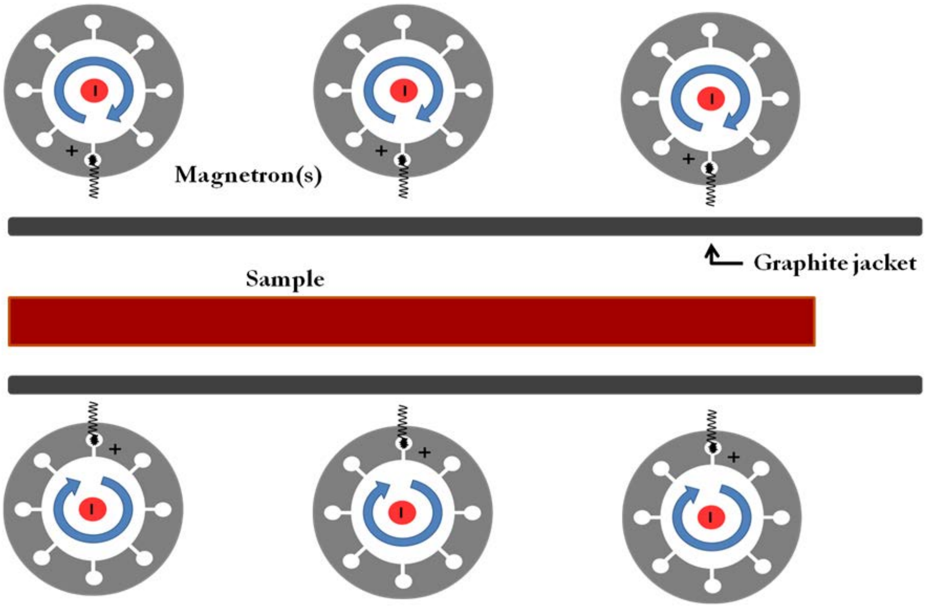

Figure 3.23 Example of possible flow reactor

Another area of research that should be investigated is the meta-stable phases, for example, this work highlights the formation of the iron carbide proceeding through a different route than that observed in a furnace and a $FeN_{0.0324}$ intermediate phase is seen. It is possible that other meta-stable phases can be found with interesting properties. The samples produced during this study are not all pure products so future work should try to isolate these; this would be a simple task of varying parameters such as the metal to biopolymer precursor.

Finally this simple method, with large energy and time savings, has shown promise in the synthesis of metal carbide composites and should expand microwave processing by exploiting the morphological diversity offered by a wide range of natural and synthetic precursors.

3.6 REFERNCES

(92) Lidström, P.; Tierney, J.; Wathey, B.; Westman, J. *Tetrahedron* **2001**, *57*, 9225.

(93) Kappe, C. O. *Angewandte Chemie International Edition* **2004**, *43*, 6250.

(94) Kitchen, H. J.; Vallance, S. R.; Kennedy, J. L.; Tapia-Ruiz, N.; Carassiti, L.; Harrison, A.; Whittaker, A. G.; Drysdale, T. D.; Kingman, S. W.; Gregory, D. H. *Chemical Reviews* **2014**, *114*, 1170.

(95) Adam, D. *Nature* **2003**, *421*, 571.

(96) Gerdien, H.; Google Patents: 1004012 A: 1911.

(97) Hans, E. H.; Google Patents: 2123728A: 1938.

(98) Kosmahl, H. G.; Branch, G. M. *IEEE Transactions on Electron Devices* **1973**, *20*, 621.

(99) Vanetsev, A. S.; Tretyakov, Y. D. *Russian Chemical Reviews* **2007**, *76*, 397.

(100) Vollmer, C.; Janiak, C. *Coordination Chemistry Reviews* **2011**, *255*, 2039.

(101) Zhu, Y.; Guo, H.; Zhai, H.; Cao, C. *ACS applied materials & interfaces* **2015**, *7*, 2745.

(102) Glaspell, G.; Fuoco, L.; El-Shall, M. S. *The Journal of Physical Chemistry B* **2005**, *109*, 17350.

(103) Vallance, S. R.; Kingman, S.; Gregory, D. H. *Advanced Materials* **2007**, *19*, 138.

(104) Vallance, S. R.; Kingman, S.; Gregory, D. H. *Chemical Communications* **2007**, 742.

(105) Hassine, N.; Binner, J.; Cross, T. *International Journal of Refractory Metals and Hard Materials* **1995**, *13*, 353.

(106) Oyama, S. T. In *The chemistry of transition metal carbides and nitrides*; Springer: 1996, p 1.

(107) Lengauer, W. *Nitrides: Transition Metal Solid‐State Chemistry*; Wiley Online Library, 2005.

(108) Ettmayer, P.; Lengauer, W. *J. Wiley, Chichester* **1994**, 519.

(109) Wen, Z.; Ci, S.; Zhang, F.; Feng, X.; Cui, S.; Mao, S.; Luo, S.; He, Z.; Chen, J. *Advanced Materials* **2012**, *24*, 1399.

(110) Jack, K. H. *Proceedings of the Royal Society of London. Series A. Mathematical and Physical Sciences* **1951**, *208*, 200.

(111) Ferrari, A. C.; Robertson, J. *Physical review B* **2000**, *61*, 14095.

(112) Lu, J.-f.; Tsai, C.-J. *Nanoscale Research Letters* **2014**, *9*, 230.

(113) Colomban, P. *Potential and drawbacks of Raman (micro) spectrometry for the understanding of iron and steel corrosion*; INTECH Open Access Publisher, 2011.

(114) Yoshida, H.; Takeda, S.; Uchiyama, T.; Kohno, H.; Homma, Y. *Nano letters* **2008**, *8*, 2082.

(115) Higashi, K.; Ishida, M.; Matsui, S.; Fujita, J.-i. *Japanese Journal of Applied Physics* **2007**, *46*, 6282.

(116) Kurlov, A.; Gusev, A. *Inorganic Materials* **2006**, *42*, 121.

CHAPTER 4

REFORMING REACTIONS OF METHANOL

4.1 'THE HYDROGEN ECONOMY'

One of the biggest challenges for humanity is the production and storage of energy. Global energy consumption reached 13,147 toe (tonne oil equivalent) in 2016 which is a 1% increase on the previous year,[117] and is nearly half the previous 10 year average. This is a sign that the global attitudes to energy consumption are changing and more thought is being given to conservation of existing reserves. However even with this renewed interest in responsible energy usage, coal is the only fossil fuel expected to be available into the next century. Therefore a replacement is needed that is renewable in the long term and that is as convenient as current technology. For medium/large stationary energy generation, renewable sources such as wind and solar energy can be harnessed. For smaller or portable applications, i.e. cars, this is not suitable. One possibility is electric cars with the energy being supplied by either batteries or a fuel cell (i.e. using hydrogen). It is worth noting that hydrogen is not an energy source but an energy store, because it only exists naturally in trace amounts so for human use it must be made. This means that hydrogen could be used in conjunction with renewable energy to store excess energy like a battery and release the energy when there is a deficit.

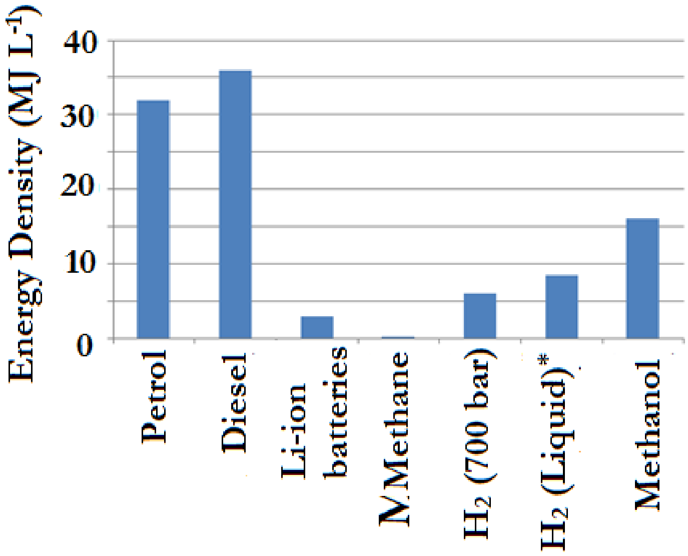

Figure 4.1 Energy densities of common fuels. *assumes is freely available[118]

Many believe the solution to be hydrogen, due to its higher energy density compared to other fossil fuel replacements, Figure 4.1. However, there are many problems with storage, production and use that need to be overcome before hydrogen fuel cell cars become a viable technology. Battery powered cars already exist and have reasonable performances in terms of range and speed but suffer in other areas. For example these cars tend to have large arrays of batteries which adds weight and cost (e.g. the Tesla model S has approximately 500 kg of batteries)[119] this makes the vehicles too expensive for most people. Another issue with batteries is the recharging time and number of cycles that is possible before the batteries need replacing. In the short term, battery powered cars have their role to play as society moves from oil to renewable energy and hydrogen.

Table 4.1 List of hydrogen storage techniques with their advantages and disadvantages

Storage technique	**Advantage**	**Disadvantage**
Compressed gas	Well established technology Low cost	Low gravimetric and volumetric energy density (E_d) Safety and weigh concerns
Liquid	High volumetric E_d Gas released at atmospheric pressure	Expensive losses due to boil off leading to long term storage problems ~35 % of energy used to liquefy
Cyro-compressed	Good for long term storage as better able to withstand external heat	Heavy and take up a lot of room. Expensive Inefficient
Absorbents E.g. MOF	Very high gravimetric / volumetric E_d	Requires low temperatures for high capacity.
Metal hydrides E.g. Mg_2NiH_4	Very high gravimetric / volumetric E_d	Slow hydrogen release at desired operation temperature/pressure Release of pollutants
Chemical hydrogen E.g. NH_3	Very high gravimetric / volumetric E_d	Slow release of hydrogen, high temperatures needed
Organic hydrides E.g. CH_3OH	Very high gravimetric / volumetric E_d Could make use of existing infrastructure	Hydrogen release at high temperature by reforming reaction Release of pollutants

There are many ways to store hydrogen with various advantages and disadvantages some of which are summarised in Table 4.1 and these are separated into physical and chemical solutions.

From this table is it clear to see that some solutions have good gravimetric and/ or volumetric storage capacity but are expensive; or they are relativity cost efficient but there are safety concerns/ do not release the hydrogen easily. The United States of America Department of Energy has set out a series of targets for hydrogen storage for the cost, storage capacity, operational conditions and safety. The targets for 2020 are summarised in Table 4.2 and comparison of the systems above show that these currently fail on one or more of the targets and as such much research still occurs in this field.[120]

Table 4.2 List of storage capacity of various hydrogen storage systems, compared to the US:DoE targets[121]

Storage technique	Gravimetric capacity (wt% H_2)	Volumetric capacity (g H_2 L^{-1})	System cost	
			System \$/kWh	Fuel (\$/kg)
US:DoE Target 2020	**5.5**	**28**	**10**	**2-4**
US:DoE ultimate Target	**7.5**	**70**	**8**	**2-4**
Compressed gas (690 atm)[122]	5.2	26.3	18.7	4.33
Liquid[121]	5	35	-	6-8
Cyro- compressed[122]	9.5	47.8	8	4.57
Absorbents[123]	1.65	7-110	-	-
Metal hydrides[124]	18.5	121	-	-
Chemical hydrogen[125]	17.8	1.08	17.2	0.38
Organic hydrides[126]	12.6	98.8	9.7	8

Out of these options one promising possibility is to 'store' hydrogen as a molecule that contains a lot of hydrogen (XH_y) and can easily be broken into hydrogen and X (e.g. methanol: $CH_3OH \rightarrow CO_2 + H_2$).[127] This could in theory be done in an on-board reactor, allowing the liquid to be carried and refilled in a similar fashion to petrol, meaning that existing infrastructure could be used. The added benefit of this would be that the fuelling process for the customer would be the same as it is now. There are a number of compounds that could be used for this (e.g. ethanol) but methanol has a number of advantages over other compounds. For example methanol has no C-C bonds that need to be broken which saves energy and it also ensures the only products are CO_x and hydrogen. It is also possible to remove all of the hydrogen from methanol which means 2 moles of hydrogen can be released from a single mole of methanol and as such it has a higher energy density than the other forms of hydrogen storage. Methanol can be used directly in a fuel cell with the efficiency of 62%,[128] this is compared to 50% of current methanol reforming systems ;[129] this indicates that both have potential in the future.

There are currently a number of issues with methanol reforming that must be addressed before it can be used. The first of which is the high temperatures needed for the reforming to occur, this would mean that a person would have to wait for the reformer to warm up before driving or have some other way of starting the car and warming the reformer during the start of the drive; also the temperatures required are too high to be in a car. This reduces efficiency and increases weight and system complexity. Another issue is the by-products but this will be discussed in the next section.

Methanol is currently produced from syngas, a product from heating coal which is obviously not removing the dependents on fossil fuels but it can be renewably sourced: it can also be formed through steam reforming. This can be done by using renewable energy sources (e.g. excess solar energy, during the day demand for electricity is lower) and collecting carbon dioxide (reducing a green house gas) from the atmosphere or exhaust gases of other industries.[130]

A plethora of elements have been used as catalysts for methanol steam reforming (MSR), these studies have focussed on the Group 8 - 10 metals[131,132] and copper[133-135] with supports such as aluminium oxide and silicon dioxide. The range of catalysts that have been developed is vast, from a single metal supported on a substrate to mixed metal hydroxides and alloys. There have been periodic reviews of the current catalysts for this reaction and several things stand out.[136-138] In both Group 8 - 10 metals and copper, zinc oxide seems to have the synergistic effect of increasing activity and selectivity for carbon dioxide over carbon monoxide (the importance of this will be discussed in the next section).[139] Also important for stability and activity is the accessible surface of the catalysis and surface area of the support. A compromise must be struck between small particle size, for more activity, and long term stability which can be tuned by larger particles and the morphology and composition of the support.[140] The main difference of these two groups of catalysts is that the copper based samples have greater activity (i.e. can produce more hydrogen) than the Group 8 - 10 metals but the latter group of metals have greater thermal stability.[141] Also some of the heavier transition metals are expensive.

For this research which was carried out over two trips to the National Institute for Materials Science (NIMS), Japan through collaboration with Prof Ya Xu, copper and zinc were supported on porous carbon. The reason for this is that this work was as a preliminary experiment to test the suitability of our catalysts for this purpose. It was thought that if there was good activity it could be tuned by using the biopolymer sol-gel synthesis from Chapter 2 to control the carbon support and the particle size. Copper and zinc were chosen as they have high activity for methanol steam reforming, they are relativity inexpensive and the combination of the two should be more stable.

4.1.1 IMPORTANT REACTIONS

For these catalysts and under the reaction conditions studied, there are a number of possible reactions that can occur and that are relevant to hydrogen production, these are listed below. Methanol steam reforming (MSR) (Equation 4.1) is the preferred reaction. It is also possible to get methanol decomposition, (Equation 4.2) however these conditions should not favour this reaction because of the presence of water and because it is more endothermic. Side reactions include the reverse water-gas shift reaction (Equation 4.3) and methanation (Equation 4.4), the former has recently been shown to be a slow reaction and so it may be possible that this could be eliminated through engineering solutions (i.e. increased flow rates - meaning less time to react). MSR is preferred because currently fuel cells use platinum and this is deactivated by carbon monoxide so it is to minimise the amount of this in the exhaust gases; also it is exothermic so once started it require less external heating to maintain the reaction temperature.

$$CH_3OH + H_2O \leftrightarrow 3H_2 + CO_2$$ **Equation 4.1**

$$CH_3OH \leftrightarrow 2H_2 + CO$$ **Equation 4.2**

$$H_2 + CO_2 \leftrightarrow CO + H_2O$$ **Equation 4.3**

$$CO + 3H_2 \leftrightarrow CH_4 + H_2O$$ **Equation 4.4**

Equation 1 is a specific condition of the general equation shown below, Equation 4.5, where x=0. If x=0.5 then the reaction taking place is the partial oxidation of methanol, this has been mentioned as a side note for one of the samples shown later.

$$CH_3OH + xO_2 + (1\text{-}2x)H_2O \leftrightarrow (3\text{-}2x)H_2 + CO_2$$ **Equation 4.5**

4.2 EXPERIMENTAL

4.2.1 MATERIALS

Below is a list of materials used in this chapter.

Table 4.3 List of materials used for synthesis and analysis in this chapter

Chemical	Supplier	CAS number
Gelatin, type A, porcine, G2500, 300 bloom strength	Sigma Aldrich	9000-70-8
Agar, microbiology tested	Sigma Aldrich	9002-18-0
Starch, puriss. p.a., from potatoes.	Sigma Aldrich	9005-84-9
Chitin, from crab shells	Sigma Aldrich	1398-61-4
Chitin, from shrimp shells	Sigma Aldrich	9012-76-4
Copper nitrate(II) hemi(pentahydrate)	Sigma Aldrich	19004-19-4
Zinc nitrate hydrate	Sigma Aldrich	13778-30-8
Zirconium(IV) oxynitrate hydrate	Sigma Aldrich	14985-18-3
Hydrochloric acid	Sigma Aldrich	7647-01-0
Ethanol, absolute	VWR	64-17-5
Methanol, anhydrous	Sigma Aldrich	67-56-1

4.2.2 SYNTHESIS OF SAMPLES

Various ratios of zinc/copper : carbon composites were made using the same method, the details are as below; the required masses, volumes, etc. for the different ratios are in Table 4.4. The following biopolymers were made using following the synthesis below: - Agar, Chitin and Starch.

A 10% (w/v) gelatin solution was prepared by adding gelatin, from porcine skin (10 g) to hot rapidly stirred distilled water (90 mL, 70 °C), this was stirred until a homogeneous solution was obtained (solution A). A 10% (w/v) solution of zinc and cooper nitrates were prepared separately by placing the respective nitrate (10 g) in a 100 mL volumetric flask and filling with distilled water. Solution A (20 g) was transferred to a beaker covered with a watch glass and heated (60 - 70 °C) with rapid stirring, to this a pre-mixed metal solution was added, the solution became more viscous. Once the solution had homogenised it was placed in a drying oven at 80 °C and dried until a solid was obtained. The resulting solid was placed into a crucible and heated to 800 °C (10 °C min^{-1}) under flowing nitrogen, using a muffle furnace with a metal retort to contain the gas, held for 5 minutes and then allowed to cool to room temperature. A black powder was recovered.

Table 4.4 Ratios and mass/volumes used for synthesis of catalysts

Zn:Cu			
Metal ratio (0.01 M total)	**Moles of metal**	**Mass of Metal (g)**	**Volume of 10% (w/v) stock (mL)**
100 : 0	0.0100 : 0.0000	2.97 : 0.00	29.70 : 0.00
98 : 2	0.0098 : 0.0002	2.91 : 0.05	29.10 : 10.47
95 : 5	0.0095 : 0.0005	2.82 : 0.12	28.22 : 1.17
90 : 10	0.0090 : 0.0010	2.67 : 0.23	26.73 : 2.33
75 : 25	0.0075 : 0.0025	2.23 : 0.58	22.30 : 5.80
50 : 50	0.0050 : 0.0050	1.49 : 1.17	14.90 : 11.70
25 : 75	0.0025 : 0.0075	0.74 : 1.75	7.40 : 17.50
10 : 90	0.0010 : 0.0090	0.30 : 2.10	2.97 : 20.97
5 : 95	0.0005 : 0.0095	0.15 : 2.14	1.50 : 22.14
0 : 100	0.0000 : 0.0100	0.00 : 2.33	0.00 : 23.30

Using the synthesis above samples for zinc : copper ratios of 98:2 and 75:25 were prepared with zirconium. The total molar concentration of 0.01 M per 20 g 10% (w/v) was maintained. The molar ratio of zinc to copper was calculated and then reduced to account for the molar percentage of the zirconium.

Table 4.5 Ratios and mass/volumes used for synthesis of catalysts. Stock solutions were 10% (w/v)

Moles Zn (as % of total 0.01 M)	**Moles Cu (as % of total 0.01 M)**	**Volume Zn nitrate Stock (ml)**	**Volume Cu nitrate Stock (ml)**	**Moles Zr (as % of total 0.01 M)**	**Volume Zr nitrate Stock (ml)**
Zn/Cu (98/2) : Zr ratio 98:2					
96.04	1.96	28.52	0.46	2	0.46
88.2	1.8	26.20	0.42	10	2.31
73.5	1.5	21.83	0.35	25	5.78
Zn/Cu (75/25) : Zr ratio 98:2					
73.5	24.5	21.83	5.71	2	0.46
67.5	22.5	20.05	5.24	10	2.31
56.25	18.75	16.71	4.37	25	5.78

4.2.3 METHANOL REFORMING - STEPWISE REACTION

Figure 4.2 Sample packed ready to be placed into reactor

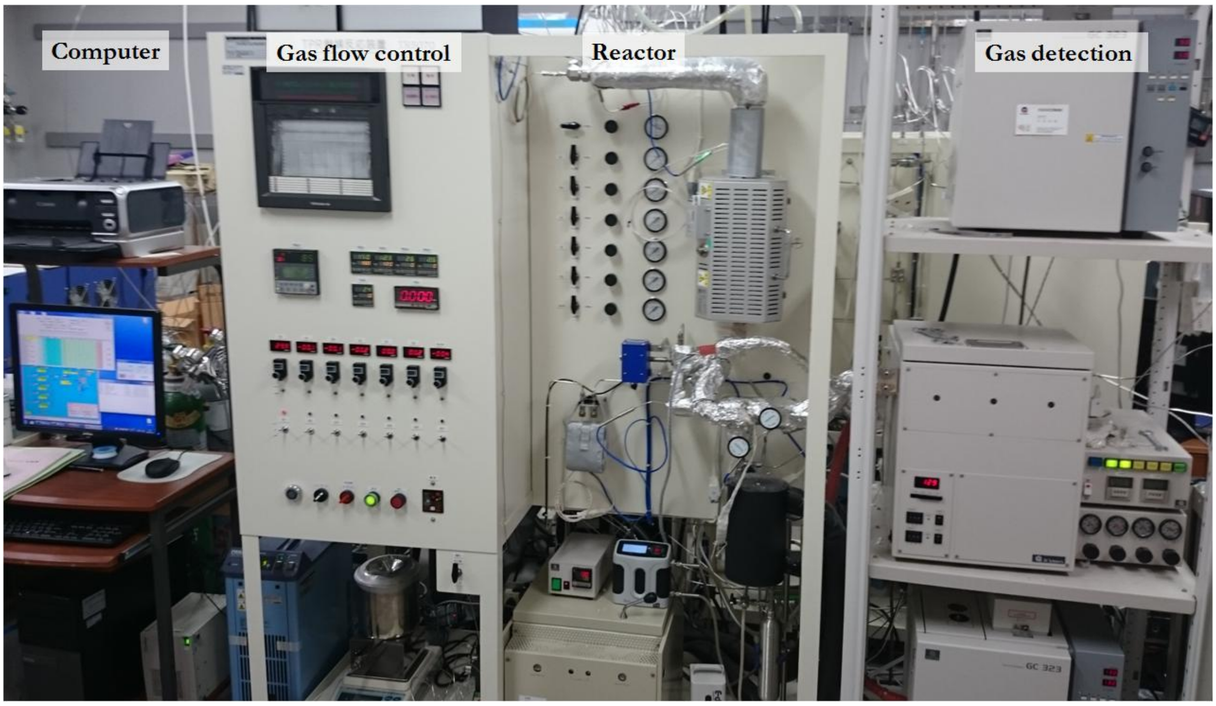

Figure 4.3 Photograph of methanol reactor

A photograph of reactor can be seen in Figure 4.3, it shows the furnace, gas flow and detection as well as the computer that controls the timing for everything. The catalyst material was weighed (~0.015 g) and packed with glass wool into a quartz tube (Ø 8 mm) which forms the reactor, Figure 4.2. There was a thermocouple inside a quartz tube (Ø 4 mm) inside the quartz wool. After checking for leaks, the sample was heated to 350 °C under flowing nitrogen, once at temperature, the atmosphere was changed to a hydrogen/nitrogen (90%/10%) gas flow for 1 hour to reduce any surface oxidation on the sample. The reactor was cooled to 280 °C whilst the atmosphere was changed back to nitrogen and after 30 minutes the presence of hydrogen was checked. When this was zero a methanol/water (30 μL min^{-1}) stream (150 °C) was introduced and held for 20 minutes at this temperature. The exhaust which normally passed through a cold trap (to remove water and methanol), the flow meter and then out of the building, is instead then sampled (10 second burst) by passing through 2 gas chromatograph-mass spectrographs (GC-MS-MS): one for detecting H_2O, CO_2 and CH_3OH; one for detecting H_2, N_2, O_2, CO and CH_4. The total flow rate, excluding water and methanol, was taken just after the GC-MS had taken its 10 burst of gas. The temperature was raised 20 °C and held for 20 minutes. The procedure of 20 mins at temperature, 5 mins for GC-MS, 15 mins heating, etc was repeated until maximum temperature (540 °C) was achieved.

The methanol : water ratio was varied for some experiments, these followed the rest of the experiment as described above.

4.2.4 METHANOL REFORMING - ISOTHERMAL/ LONG DURATION REACTION

The catalyst material was weighed (~0.015 g) and packed with cotton into a quartz tube (Ø 8 mm) which forms the reactor. There was a thermocouple inside a quartz tube (Ø 4 mm) inside the cotton wool. After checking for leaks, the sample was heated to 350 °C under flowing nitrogen, once at temperature, the atmosphere was changed to a hydrogen/nitrogen (90%/10%) gas flow for 1 hour to reduce any surface oxidation on the sample. The reactor was heated to 440 °C whilst the atmosphere was changed back to nitrogen and after 30 minutes the presence of hydrogen was checked. When this was zero a methanol/water (30 μL min^{-1}) stream was introduced and held for 60 minutes at this temperature. The exhaust which normally passed through a cold trap (to remove water and methanol), the flow meter and then out of the building, is instead then sampled (10 second burst) by passing through 2 gas chromatograph-mass spectrographs: one for detecting H_2O, CO_2 and CH_3OH; one for detecting H_2, N_2, O_2, CO and CH_4. The total flow rate, minus water and methanol, was taken just after the GC-MS started. Measurements were taken periodically for 40 hours.

4.3 RESULTS AND DISCUSSION

As mentioned previously this was carried out over 2 trips to NIMS, Japan. A few experiments were carried out during the first trip but there were a number of problems to overcome (detailed later) and as a result these experiments were repeated during the second trip. Despite this though, these experiments did help to direct the research during the second trip; for example the samples with a higher ratio of zinc in them seemed to have more selectivity toward carbon dioxide production but lower activity. This is in line with current research and so more samples that had higher zinc ratios were used. The following short hand will be used for sample identification; for example CZ98 - this indicated the sample is a mixed ratio of zinc and copper and the number indicates the molar percentage of zinc in the samples out of the total (0.01 M) of metal content per sample (i.e. CZ98 means 98 mol% zinc and 2 mol% copper).

4.3.1 STRUCTURE AND STABILITY OF ZINC OXIDE/COPPER/CARBON CATALYSTS

X-ray diffraction (XRD) was used to identify the crystallite phases in the catalysts. Figure 4.4 shows a comparison of the samples with varying ratios of zinc (PDF #00-003-0891) and copper (PDF #00-001-1241). It shows that zinc oxide and copper are the main phases present, with a small amount of copper (I) oxide (Cu_2O, PDF #01-078-5772) possibly also being present in some samples. Interestingly for samples with less zinc, the XRD patterns do not show any zinc oxide peak; however the presence of zinc in these samples was confirmed by X-ray fluorescence.

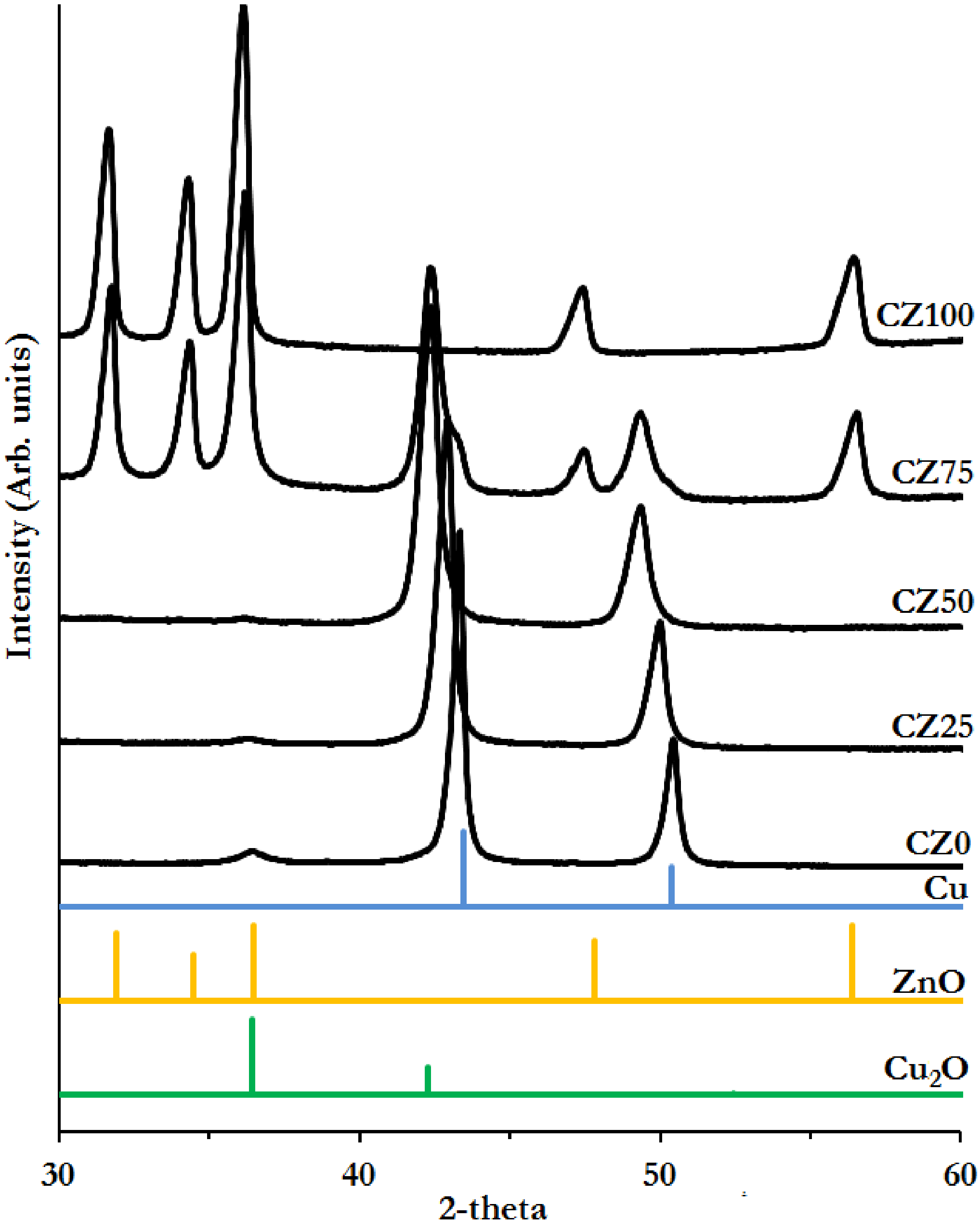

Figure 4.4 XRD of CZ25 before MSR and after MSR, ZnO reference pattern, unmark peaks are copper

The reason for zinc in these samples not forming a crystalline phase is unknown but these samples were scanned again after MSR and these patterns clearly show zinc oxide, Figure 4.5. This suggests that the zinc oxide particles anneal/sinter during the MSR reaction experiment, this should be investigated further to ascertain if this is simply the zinc annealing and becoming stable or the start of a process where the zinc starts to decompose. The copper, on the other hand, is relativity stable only showing a slight peak shift and narrowing of the peaks from before and after MSR. The shift in peak position indicates a slightly smaller unit cell this could be from relief of the stress and strain in the crystals structure from forming larger particles. This narrowing of the peaks is could be due to sintering of the crystallites and this was investigated with Scherrer analysis, small angle x-ray scattering (SAXS) and scanning electron microscopy (SEM) was used to look at particle size. However from Figure 4.5 it could also be the formation of brass, a copper and zinc alloy (Cu_3Zn, PDF #03-065-6567), EDX alongside TEM could be used to ascertain if this is the case and further MSR experiments should be carried out to see how this affects it performance over time.

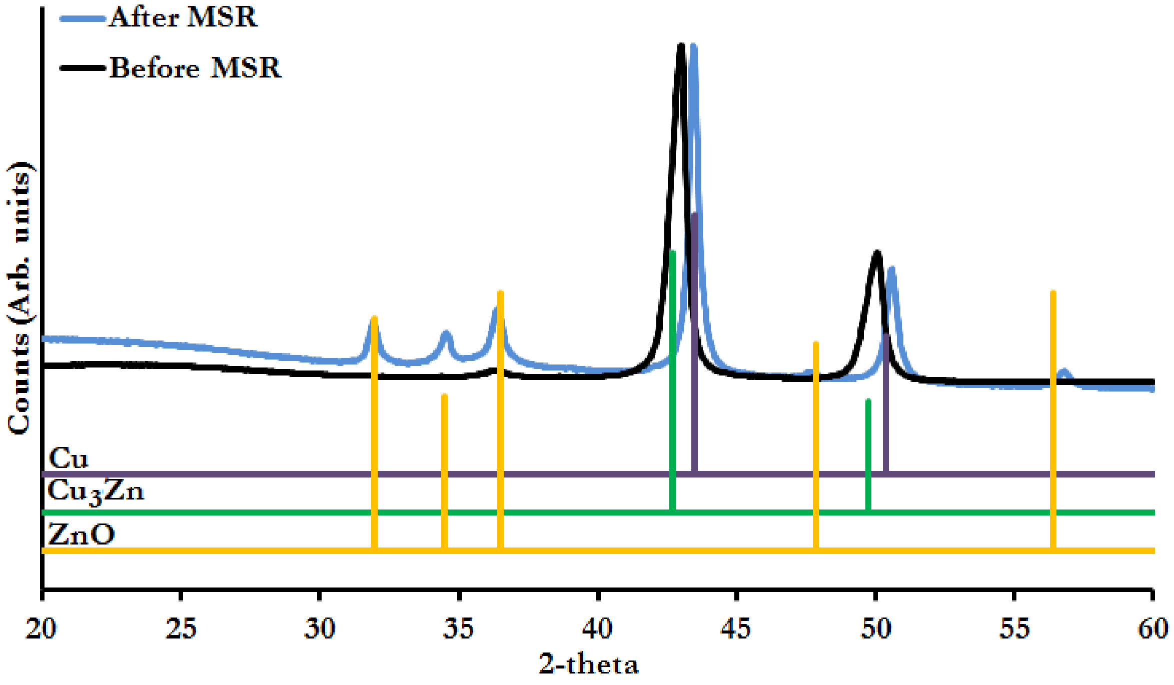

Figure 4.5 XRD of CZ25 before MSR and after MSR, showing the possible formation of a copper/zinc alloy

Initially the particle size was estimated with the Scherrer equation and the investigation of particle size have mostly been carried out on the CZ100; this was so only one phase had to be considered in the XRD and one species for SAXS. From the Scherrer analysis of these as-prepared CZ100 samples the particle diameter was calculated at 25 nm. The particle size of the sample after MSR is approximately 91 nm. This shows that initially there is some sintering, this can be confirmed by SEM. Figure 4.6 shows SEM images of CZ100 before and after the MSR experiment, image C shows that there is a large distribution of particles size before MSR, afterward (image D) shows a narrower distribution of particles however there are still some aggregates. Image processing of the before MSR image reveals an average particle diameter of 45 nm, this analysis is difficult due to the wide range of particle sizes and shapes. This is significantly different from the Scherrer analysis and caution should be taken when regarding both numbers as assumptions were made for both. For the Scherrer analysis carried out here it is assumed that the particles are unstrained and spherical and for the image processing there are 2 main assumptions; 1) the area for each particle is calculated and from that the diameter and; 2) only the area in the SEM image is statistically significant as only a very small area is imaged. These assumptions lead to errors when the particles are not spherical. Figure 4.6 also has an SEM image showing the morphology of the sample. From images A and B it is clear the sample is very porous from tens to a few microns and the reaction does not seem to affect this very much, this suggests that the carbon is fairly stable under the reaction conditions. Finally image A is a hybrid image, it overlays the morphological information from the secondary electrons and the atomic information from the back scattered electrons. It is possible to see that the zinc oxide particles are fairly evenly distributed, with slightly higher concentrations at the edges of the pores, so controlling the pore structure/ size will increase surface area and potentially promote further nucleation at these sites.

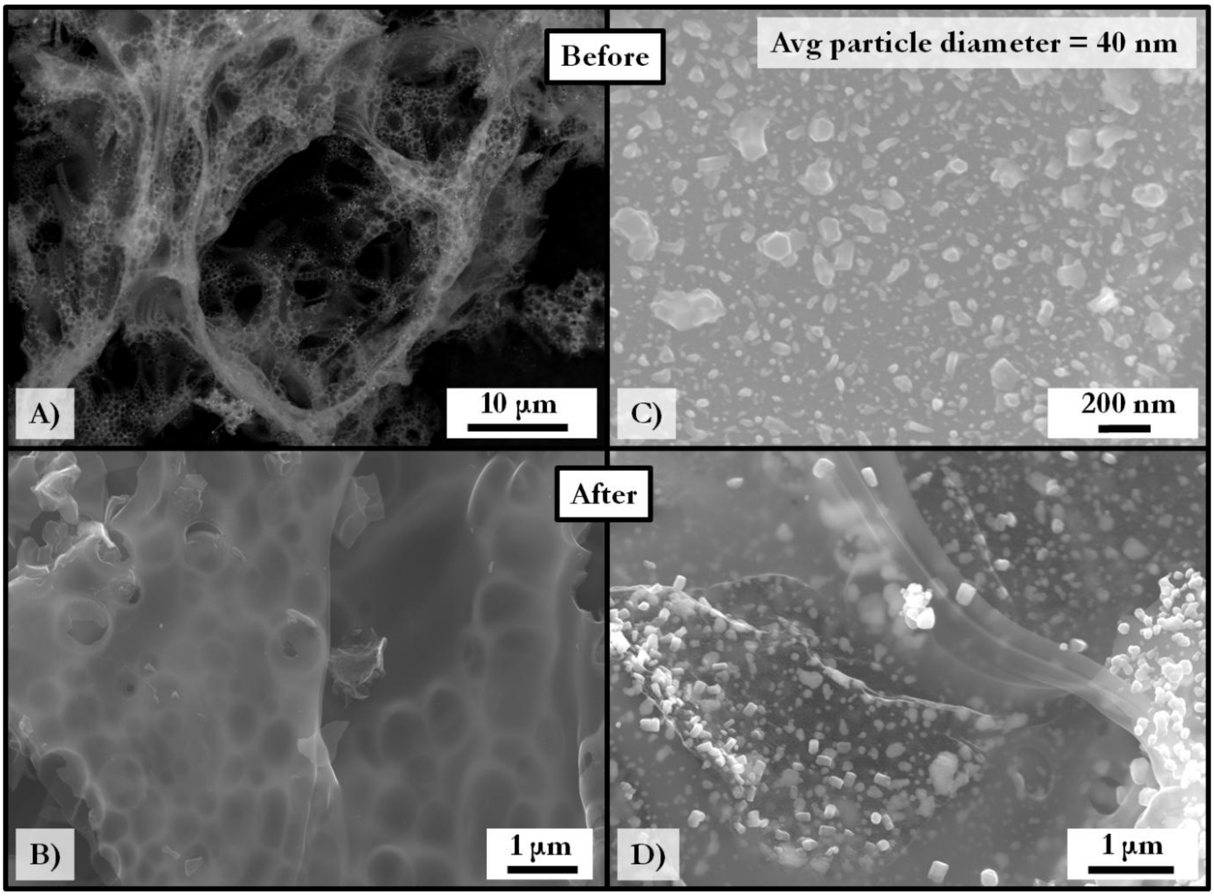

Figure 4.6 SEM images of CZ100; A) and C) before MSR and; B) and D) after MSR experiments

Whilst at NIMS it was possible to use a laboratory based SAXS instrument, experiments were carried out to compare with the other size measurement. These experiments and data analysis were carried out in collaboration with Dr Brian Pauw;[142] the raw data (fitted) and distribution of particle radii are shown in Figure 4.7. From this analysis there is a distribution of particle diameters from 2 to 30 nm with most of the particles being the 20 to 30 nm size range, this agrees well with the Scherrer analysis and means that the assumptions have not skewed the data too much. SAXS was also carried out on other zinc to copper ratios and this is summarised in Table 4.6. CZ50 has the smallest distribution of particle size and could indicate that the formation of copper and zinc oxide happens at a similar rate resulting in a synergy of these metals, like in the MF50 from Chapter 2. In the mixed metal samples it is not possible to assign sizes to individual species in SAXS without doing anomalous small angle x-ray scattering (ASAXS), this could be calculated from Scherrer analysis though. As all the samples have a similar size, small differences in the relative sizes is thought to have a minimal effect on the activity.

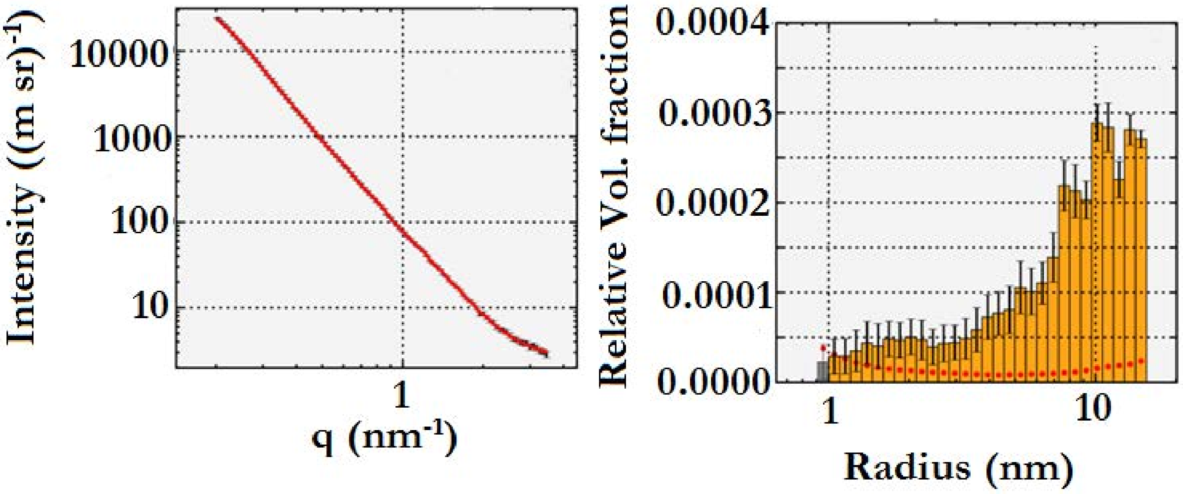

Figure 4.7 SAXS data of 100%Zn catalyst

Table 4.6 Summary of crystallite diameters from SAXS

Catalyst	Mean Size (nm)	Distribution
100%Cu	16.72	6-30 nm)
75%Cu25%Zn	15.00	(6-30 nm)
50%Cu50%Zn	14.02	(8-22 nm)
25%Cu75%Zn	19.66	(8-30 nm)
100%Zn	16.52	(2-30 nm)

The stability of the samples was further tested through two isothermal tests for 24 hours and XRD was carried out on the samples after the reaction. Figure 4.8 shows the XRD pattern of one of these samples as synthesised, after the stepwise reaction and after the long isothermal experiment. Again a shift is seen in the peaks and the peaks are narrower, the interesting fact is that the samples after the reaction both have very similar XRD patterns. This indicates that after the initial rearrangement, the particles are stable; this should be tested by cycling the catalysis through multiple experiments and tracking the XRD patterns and catalytic activity. The shift is the peaks indicates a smaller unit cell, this could be as a result of releasing stress/strain in the nanoparticles as they sinter/anneal.

Particle size was estimated by Scherrer analysis for the samples after both MSR and isothermal as 90 nm and 83 nm respectively. As a final check of stability the samples were weighed before and after the MSR and isothermal experiments, both weights were the same (within error), this further indicates that the particles are stable but also the carbon support is not being lost.

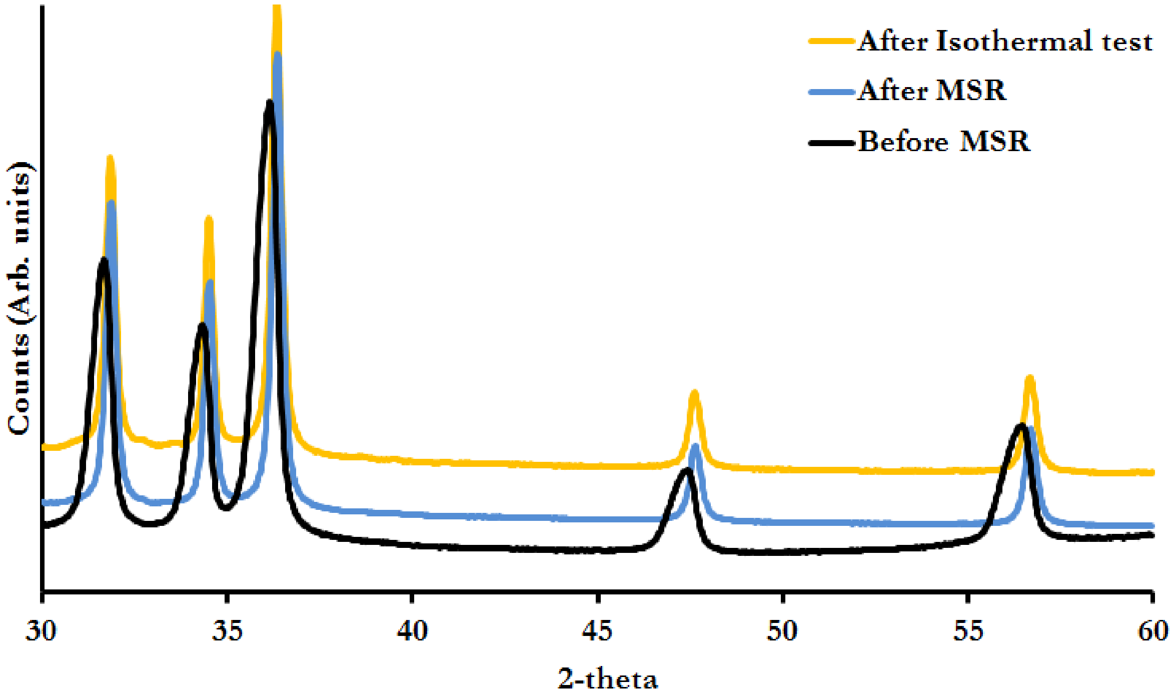

Figure 4.8 XRD of CZ100 before MSR, after MSR and after 24 hour isothermal experiments

4.3.2 EFFECT OF LONG TERM ISOTHERMAL OPERATION ON ACTIVITY

An isothermal test was carried out on a sample using the new experimental conditions but the samples moved during the 40 hour experiment and gave inaccurate results, due the length of the experiment it was not possible to repeat it. As a result the isothermal test from the first trip will be discussed, it should be noted that the exact number should be treated with caution as this experiment was carried out prior to removing the water related errors (see 4.3.3).

CZ100 was tested for 24 hours to check stability and this was done at 440 °C. This temperature was chosen because the stepwise temperature experiment showed a ~90% conversion rate; this allows for the catalyst to increase or decrease in activity and this to be detected. Figure 4.9 shows that there is an initial increase in the production of all gases before they settle down and stabilise. There is a slow decrease in the production rates of the gases from approximately 8 hours onwards, this could indicate a relatively stable system or this could be the start of a slow but steady decline in activity due to sintering, so future work should include longer experiments (e.g. 72 hours). However from the XRD patterns from the samples both after the stepwise and isothermal MSR experiments are very similar, this suggests that there is an initial rearrangement and then the sample stabilises.

Figure 4.9 also shows the production rate of H_2, CO_2, CO and CH_4, and the levels of CO and CH_4 are 2 orders of magnitude lower than H_2 and CO_2, this is consistent with other samples and indicates that MSR is the main reaction. The rates of production for H_2 and CO_2 mirror each other and the percentage methanol conversion ($\%_{MC}$), Figure 4.10: minor variations are seen and this is thought to be due to the carbon dioxide production rate (i.e. reverse water-gas shift reaction). The H_2 : CO_2 ratio is also shown in Figure 4.10 and shows that the ratio is approximately 3, this indicates that MSR is the main reaction occurring.

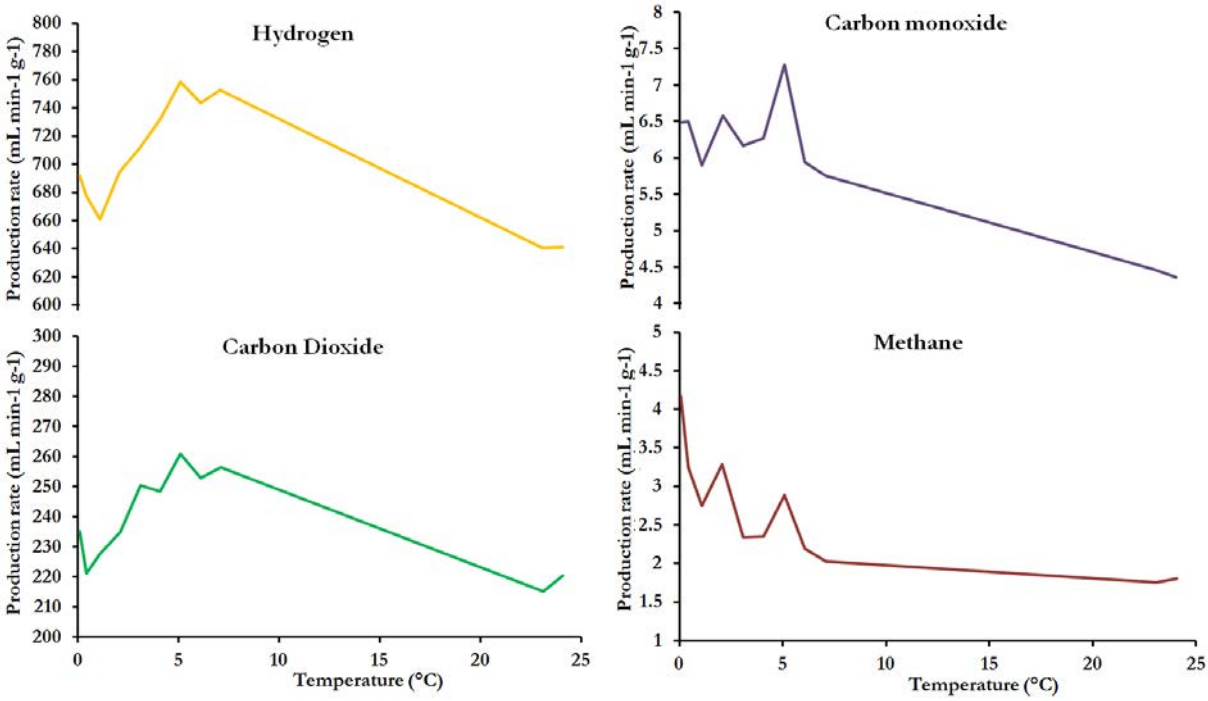

Figure 4.9 Production rates for hydrogen, carbon dioxide, carbon monoxide and methane over 24 hours during an isothermal experiment

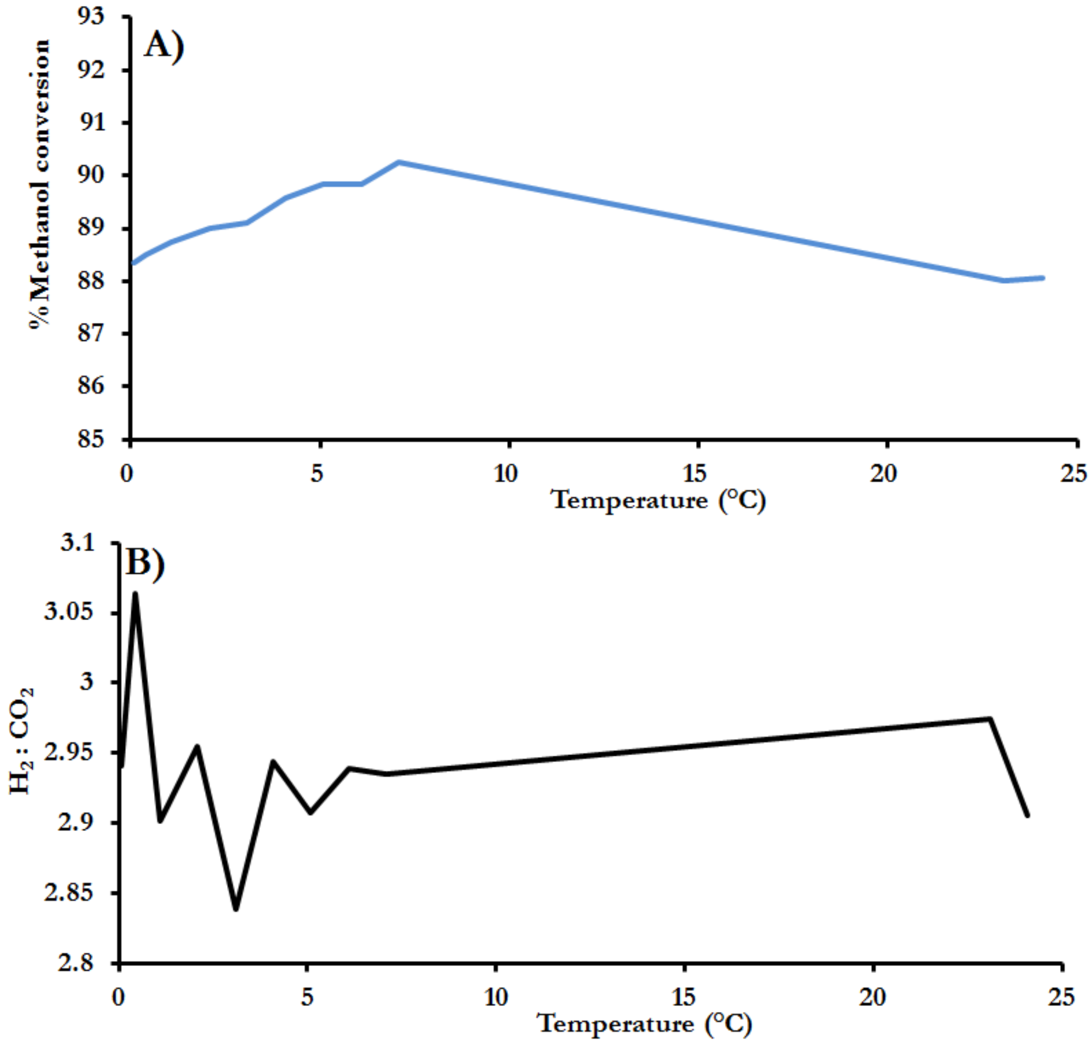

Figure 4.10 H_2 : CO_2 ratio over 24 hours during an isothermal experiment

4.3.3 METHANOL STEAM REFORMING (MSR)

There were a number of problems that prevented the data from the first trip being used, once these had been indentified, attempts were made to minimise their impact on the data and this will be discussed first. The main issue was the accurate detection of water in the exhaust gases by gas chromatography, previously the water levels were so high the water concentration had to be determined by the equation as shown below, Equation 4.6, this allowed for a more accurate determination of the water levels but this still contained large errors.

$$Water\ [\quad] = 100 - (total\ concentration\ of\ other\ products)\% \qquad \textbf{Equation 4.6}$$

The previous flow rate was reduced from 150 μL min^{-1} to 30 μL min^{-1} and then again to 10 μL min^{-1} as 30 μL min^{-1} was still too high; 10 μL min^{-1} was chosen as this was at the lower end of the flow rates discussed in the existing relevant literature. In order to use this lower flow rate new calibration files had to be made for water, methanol and carbon monoxide. Another water related error was a time/temperature dependence where the water level increased during a test with no catalysis. The exhaust gases are measured as a percentage of the overall composition and from this, and the gas flow rate, the exact quantity of each gas can be determined. Figure 4.11 (below) shows the raw data for an experiment in which the standard reaction conditions were followed with the exception no sample in the reactor. Water shows an increase with temperature up to ~400 °C followed by a slight decrease (black line), in contrast, the methanol is a stable output throughout the whole experiment (blue line). The water : methanol ratio is fixed so both outputs should be stable relative to each other; Also the whole reaction and gas detection systems are kept above 120 °C so there cannot be condensation anywhere is the system, so the source of this error could not be explained. The exhaust system was also shortened to minimise the distance between the furnace and gas detection. This increase also occurs during all of the experiments with catalysis in, so it was decided to subtract the percentage excess at each point relative to the starting point (black dashed line). Percentage increase was decided because the starting value changes for each sample and it is also possible that water is being produced in the reaction and this method allows for the slow increase to be accounted for without impacting the catalysis effect too much. The end result was a calculated ratio in the GC-MS results of water to methanol that is approximately 1.15, this is not the actual ratio but it is constant through all the experiments which mean the results can be more accurately compared.

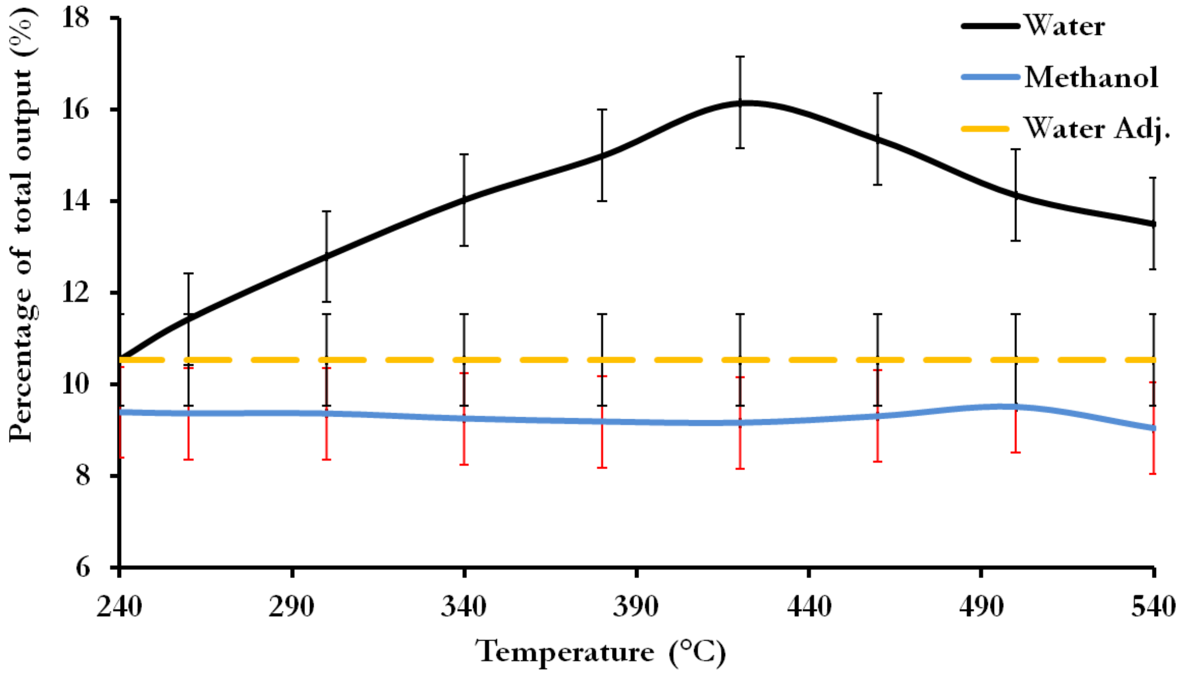

Figure 4.11 A graph showing the percentage of methanol and water compared to the temperature

4.3.4 INTITAL TESTING

The activity for MSR mixed ratios of zinc to copper and 100 mol% zinc was carried out using the step wise temperature increases as described above. A number of other variables were also trialled and the following sections will primarily focus on the effect of these on the percentage methanol conversion ($\%_{MC}$), carbon monoxide and carbon dioxide selectivities (S_{co} and S_{co2} respectively). Firstly though, this section will discuss one sample in detail and the output from the experiment and data analysis; an example spreadsheet can be found in the Appendix C, Figures C1 to C6 along with the calculation use for $\%_{MC}$, etc.

Most of the literature using copper based catalysts has reaction temperatures between 160 - 320 °C[143] however during the first trip it was shown that most the samples synthesised here are active from approximately 240 - 600 °C. As a result the experiments were carried out in the range 240 - 540 °C. The first sample tested was CZ75.

To be able to calculate the $\%_{MC}$ the actual rates of production of all gases must be extracted from what is measured. To get from measured to actual results requires the percentages from all gases collected by the GC-MS being totalled. This is then used to calculate new percentages for the gases and multiplied by the combined flow rate of the gases (measured independently by a flow meter) and then this is adjusted by the catalyst mass. Finally the percentage concentration of nitrogen is removed to find out the 'true' concentration of the products. These percentages are slightly out from the correct value because the GC-MS measures all of output gases, but the flow meter does not measure the methanol and water which are removed prior to the flow meter. To attempt to correct this, the percentage concentrations of methanol and water are removed and the gases percentages are re-calculated. The percentage methanol conversion was calculated by using the 'true' concentration of methanol (as a percentage of the output gases) detected at 240 °C as 100% and taking the other values of methanol at the higher temperatures as a percentage of that. This gives an indication of the conversion rate but assumed zero activity at 240 °C, this is a reasonable assumption as most of the experiments from the first trip indicated none or very low activity at this temperature. The $\%_{MC}$ for CZ75 shows a gradual increase from 0% conversion up to 100% at 540 °C, Figure 4.12, this is in line with the data from the first trip and verifies that the calculations and corrections carried out are appropriate. It should be noted that some literature reports methanol conversion at 260 °C of between 0 - 97% so the conversion rate of this sample is similar to the literature.[144-146]

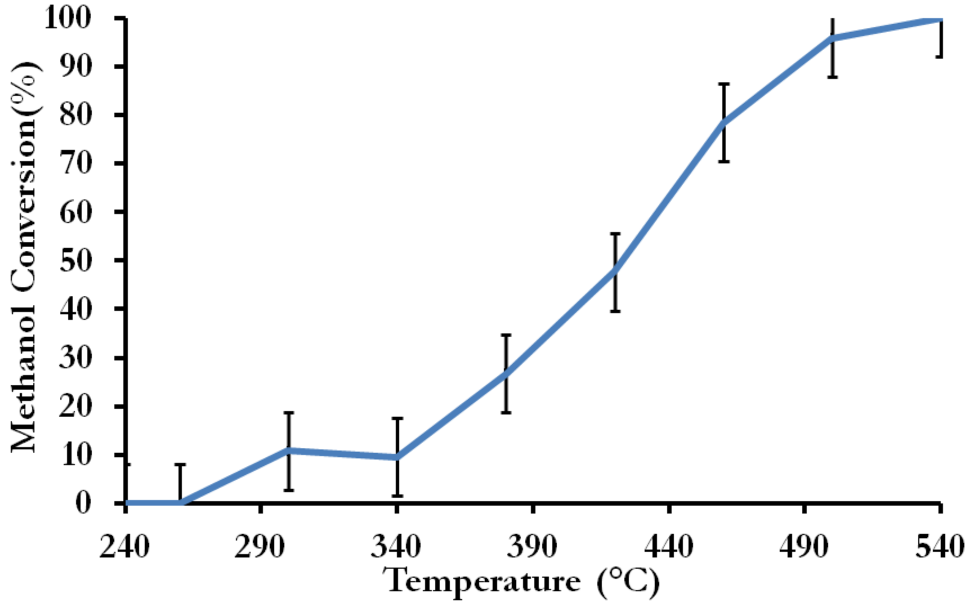

Figure 4.12 Percentage of methanol conversion for CZ75

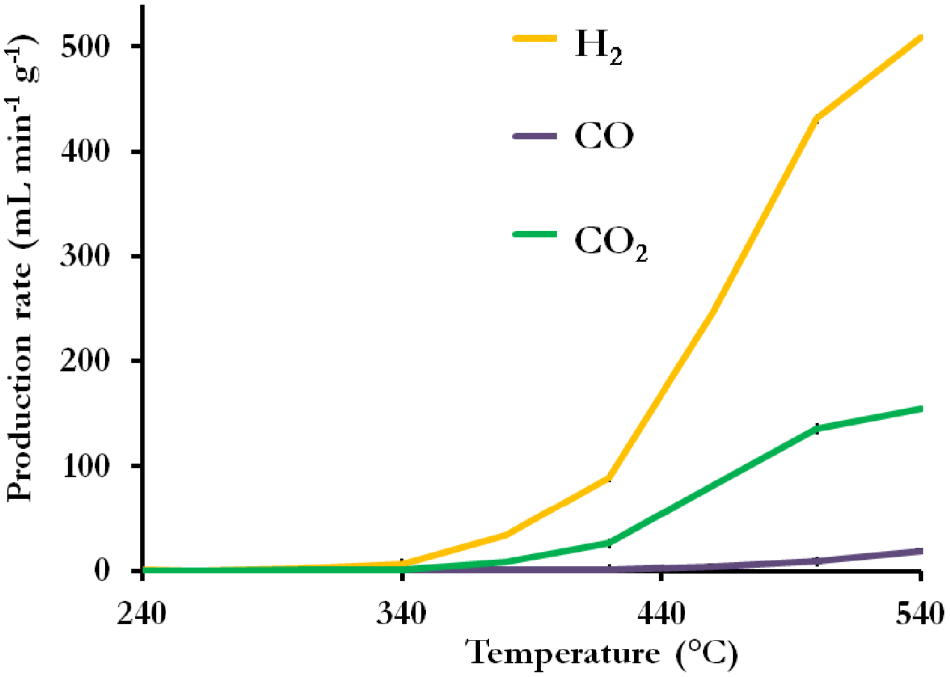

Figure 4.13 H_2, CO_2 and CO production rates for CZ75

Examination of the other exhaust gases can be used to determine which reactions are favoured by the catalyst. Figure 4.13 shows the gas production rates of H_2, CO and CO_2 per minute per gram of sample. Above 300 °C there is a steady increase in the production rate of H_2 and CO_2, indicating that the main reaction that is occurring is MSR. At these temperatures there is also a small amount of CO. As mentioned earlier, there are a number of possibilities for this; 1) methanol decomposition is occurring or; 2) CO production is the result of the reverse water-gas shift reaction. The ratio of H_2 to CO_2 should be 3 if the only reaction occurring is MSR, if methanol decomposition was occurring then this ratio would be closer to 2 and if the water shift reaction was occurring then there would be no change in the ratio as they would both be decreasing. Figure 4.14 shows a graph of H_2 to CO_2 ratio against temperature, the reason for the initial spike is unknown but it eventually settles to approximately 3 as expected. To investigate this further more research would be needed but one possible explanation for this is that MSR is the main reaction throughout and at the lower temperatures the side reactions are happening (i.e. water splitting) to change the H_2 to CO_2 ratio.

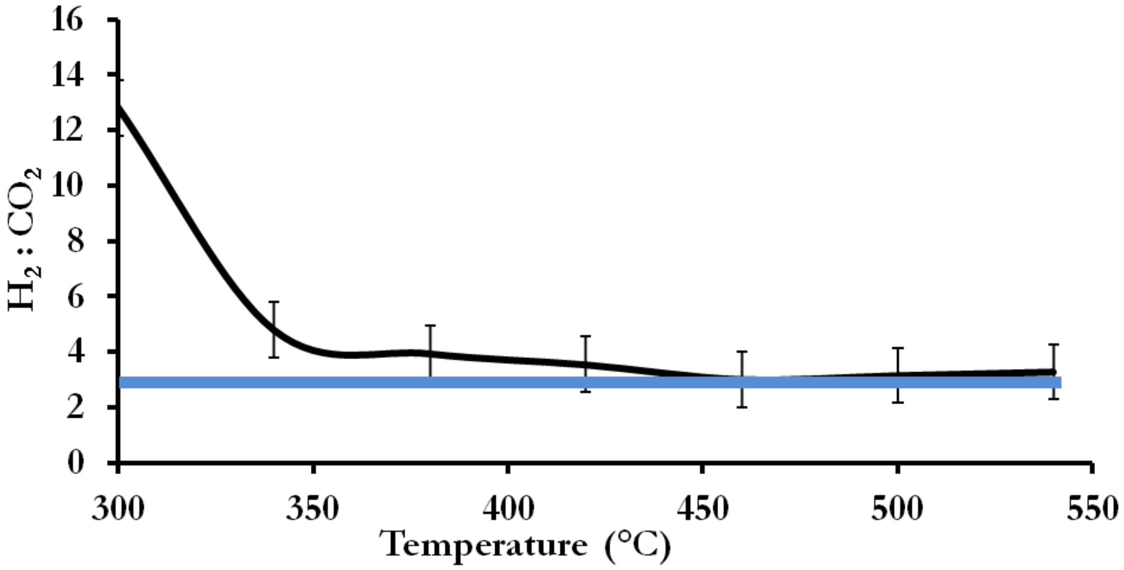

Figure 4.14 Hydrogen : carbon dioxide ratio for CZ75

The production of CO is extremely important for this family of catalysts for the reasons mentioned earlier and for these samples, CZ75, the production rate is low but still significant.

CO_2 over CO selectivity is important, Figure 4.15 shows that CO selectivity is 10 times less than CO_2 which is good but this is still too high and would deactivate a platinum fuel cell. If the reverse water-gas shift reaction is the cause of the CO then the production rate could potentially be reduced by an engineering solution (e.g. faster flow rates) because this reaction is relativity slow so faster gas flows would reduce the contact time with the catalysts and may stop this reaction from happening.

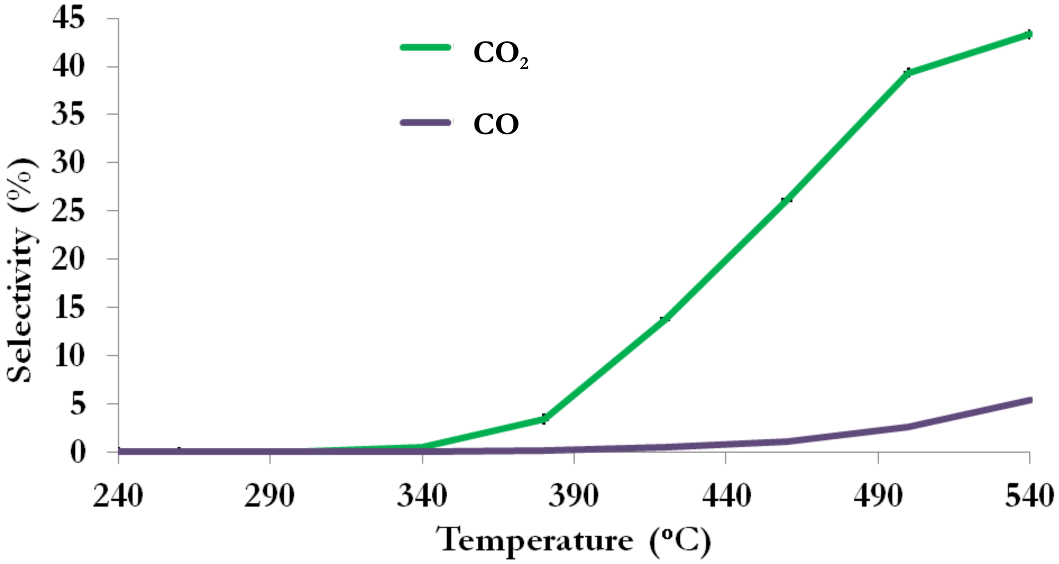

Figure 4.15 CO and CO_2 selectivity for CZ75

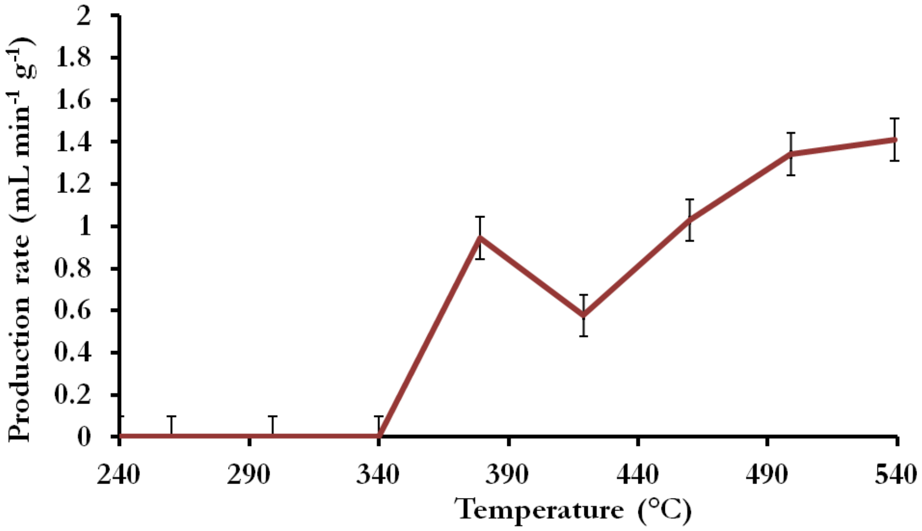

Figure 4.16 Methane production rate

Due to the production of CO the gas stream has a make-up similar to syngas (CO and H_2) this mean that methane (CH_4) can be formed and a small amount is seen, Figure 4.16. The amount created is an order of magnitude lower than CO, given that such a small amount is produced and this will have minimal effect on the finding of this research this will be ignored at this stage. It is important to note that if CO production can be stopped then CH_4 production would also be stopped.

Finally samples were initially reduced (as described in the experimental, under flowing hydrogen) as some of them had copper(I) oxide in the XRD pattern, in addition to copper and zinc oxide. Figure 4.17 shows the difference in the $\%_{MC}$ for a sample of CZ75 both reduced and not reduced prior to the MSR experiment, from this figure it is clear to see that there is little difference between these samples and the production rates of the various gases showed the same trend. This indicates that the reduction step is not needed for these samples, this is beneficial as it saves time, and therefore energy and money, and the catalyst can be used without having to activate it.

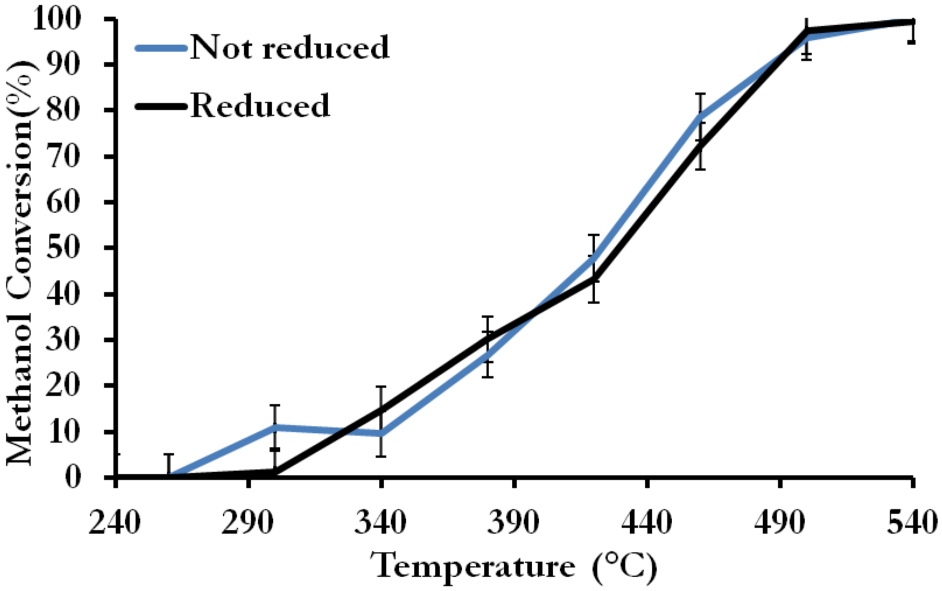

Figure 4.17 Comparison of reduction effect of samples methanol conversion rate.

4.3.5 COMPOSITION COMPARISON

The Zn : Cu ratio should have a small influence on the hydrogen production as both metals are active for MSR. In these experiments high zinc ratios were favoured as zinc oxide has been shown to have greater selectivity for CO_2 production over CO. Figure 4.18 shows the $\%_{MC}$ it shows that CZ0 has much lower activity than CZ100 - CZ50 which all reach 100 $\%_{MC}$ by 540 °C. This is interesting because these high temperature are different to reported literature[129,147] for methanol conversion and the reason for this are currently unknown, but it could be linked to the nanoparticulate structure.

Figure 4.18 shows the CO production rate for these samples, varying the ratio of zinc and copper does have a small effect on the CO production rate but all of these samples are very similar so this is not a good method for reducing the amount of CO produced.

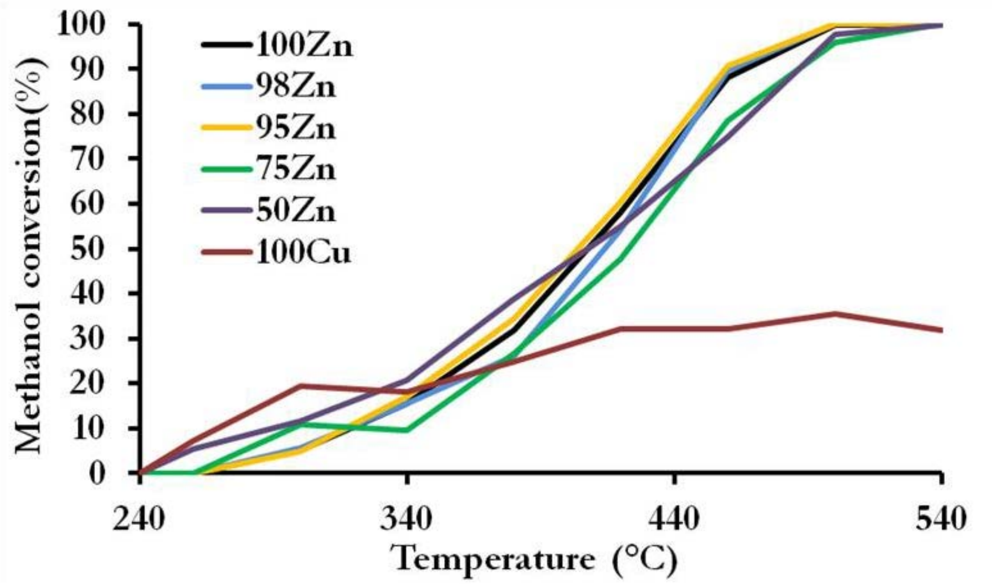

Figure 4.18 Percentage of methanol conversion for various ratios of CZ samples

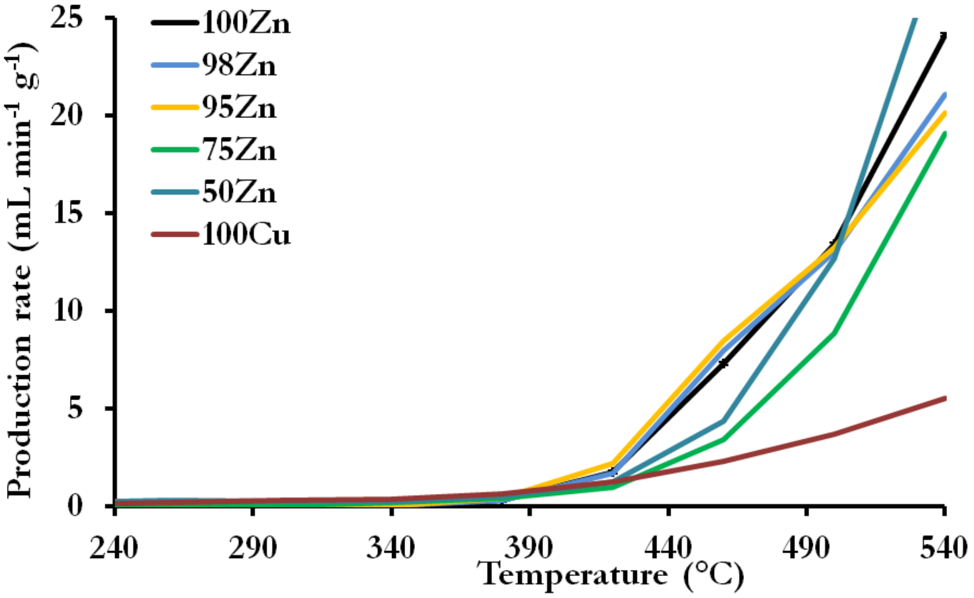

Figure 4.19 CO production rate for various ratios of CZ samples

4.3.6 EFFECT OF SYNTHESIS TEMPERATURE ON ACTIVITY

A series of samples with the same composition of CZ75 were synthesised at different temperatures to investigate if this would have an effect on the catalytic activity. From Figure 4.20 it is clear that there are some small differences at low temperatures, but at high temperatures there is almost no change. This indicates that the synthesis temperature makes no difference to the rate of methanol conversion; it should be noted that the production rates of the gases have not been shown here as they too are similar. The XRD patterns of these samples, Figure 4.21, are very different before the MSR, showing only copper and copper oxide phases. After the MSR experiment the XRD patterns are similar, this again shows that during the MSR some annealing/sintering is occurring. Overall changing the synthesis temperature is not a good way to change the activity of these samples.

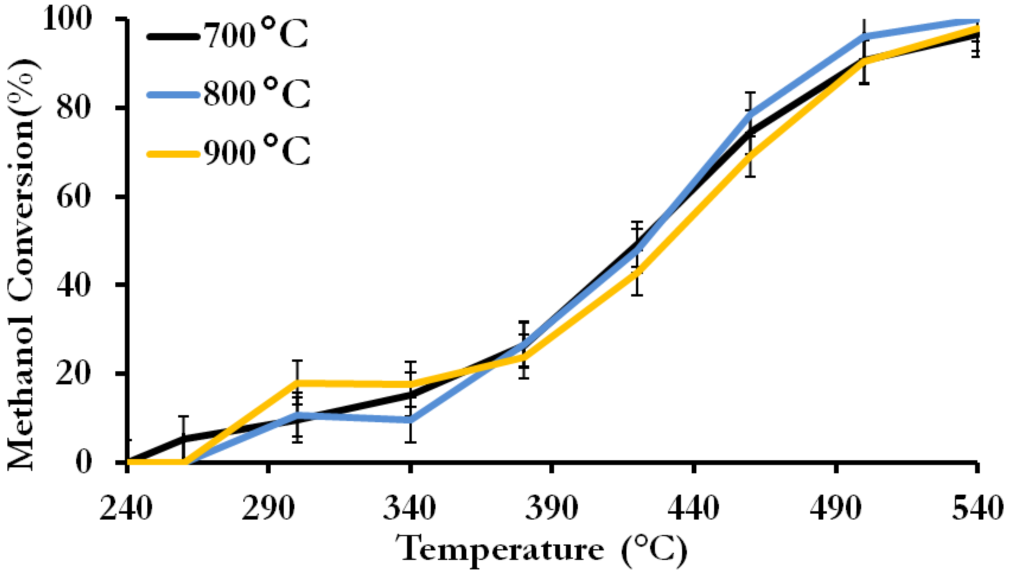

Figure 4.20 Comparison of synthesis temperature on methanol conversion

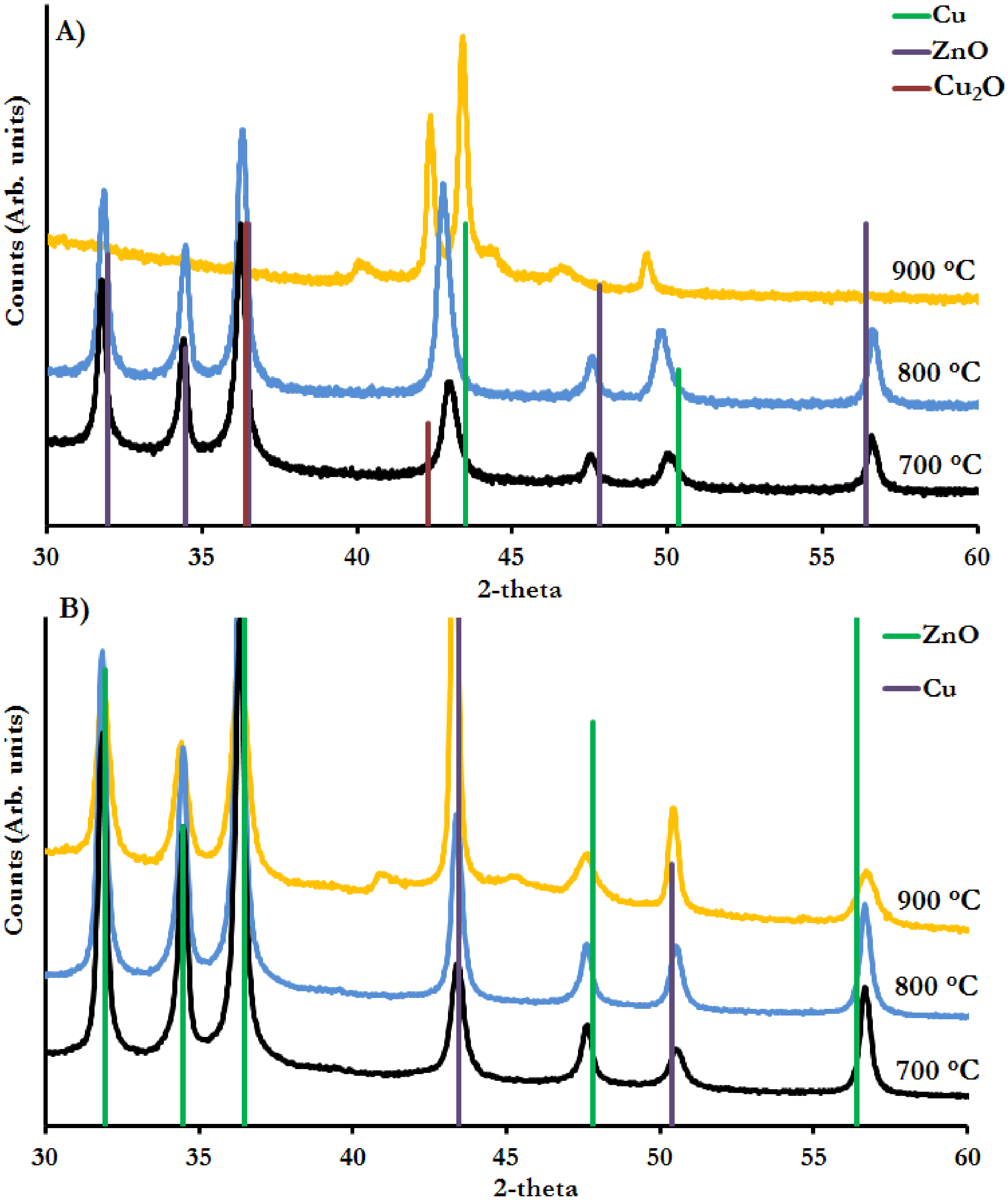

Figure 4.21 XRD patterns of samples synthesised at different temperatures; A) before and; B) after the MSR experiment

4.3.7 EFFECT OF BIOPOLYMER PERCURSOR ON ACTIVITY

The error bars for some of the graphs in the remainder of the chapter have not been included for clarity of the figures, the error is 5% for the percentage methanol conversion graphs. Figure 4.22 shows methanol conversion for samples synthesised with different biopolymers. Samples that use carrageenan and agar as the carbon source have similar activity to the gelatin synthesis of CZ75, but with a more gradual increase in conversion and also they do not reach the same 100% conversion rate. For the carrageenan sample, as well as a lower methanol conversion there was a much lower production rate for H_2 and $CO_{2,}$ Figure 4.23, and comparatively a higher CO production rate. This is because the production rates are normalised by the catalyst mass and for the carrageenan sample 20 times more mass was used to have a sample depth that was similar; this indicated the carrageenan is not as thermally stable as the other samples and therefore there is less carbon in the final product. This possibly results in bigger particles and a less porous support and these factors could combine to give the lower methanol conversion rate.

In this study there are two types of chitosan (from shrimp and crab shells) and these both have improved activity over the gelatin synthesis at lower temperatures (< 390 °C); the crab sourced chitosan has higher activity. In this case the difference could be due the difference in the degree of acetylation and/or molecular weight of this biopolymer must mean that either the formation of the nanoparticle or carbon is altered in a way to enhance the activity. However further work should be carried out to analyse the chemical composition of these samples (i.e. x-ray fluorescence spectroscopy). Investigating this further and lowering the temperature of conversion is important for making these portable and saving energy/money. This means that various biopolymers should be trialled and various sources of the same biopolymer should be tested. Starch is another potential candidate for lower temperature MSR experiments.

Further work should change biopolymers to affect change in the samples activity and try to link the structural changes to performance.

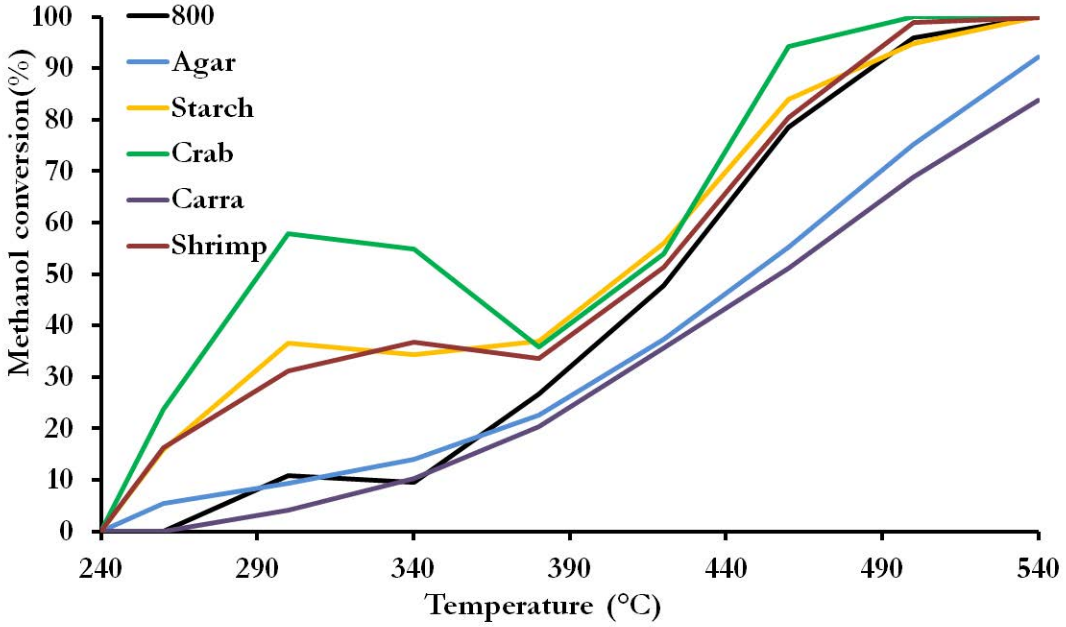

Figure 4.22 Comparison of the CZ75 synthesised with different biopolymers with the same heat treatment

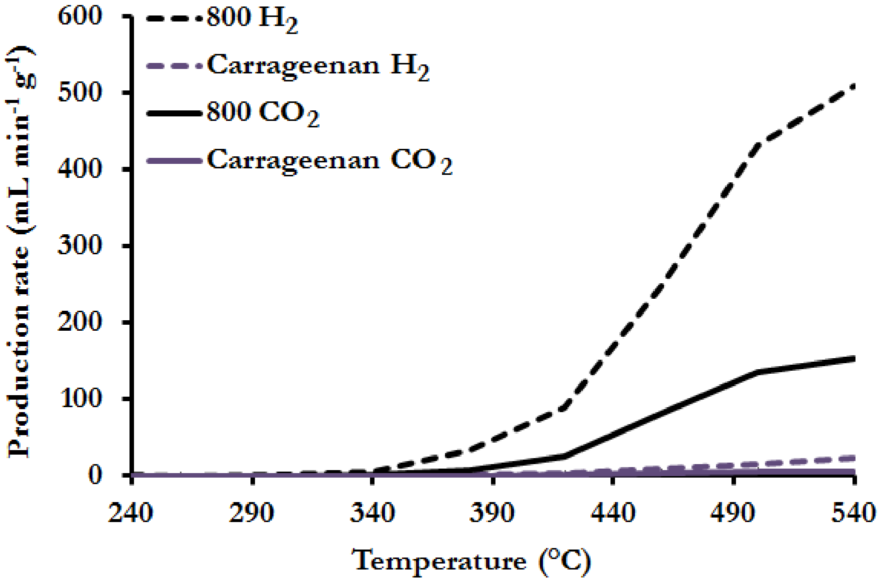

Figure 4.23 Comparison of the CZ75 and carrageenan synthesised samples

4.3.8 EFFECT OF MISCELLANEOUS FACTORS ON ACTIVITY

There were two more variables that were trialled as ways of increasing the activity of the samples. Firstly freeze drying samples has been known to increase porosity of samples, so this was attempted but from Figure 4.24 there is little difference in the $\%_{MC}$ and there is also little difference in the production rates of the gases. The second way was to double the total number of moles of metal in the sample to 0.02 mols of metal per 20 g of 10% (w/v) gelatin solution. This had the effect of initially reducing the activity of the sample but had the same final conversion rate. Hydrogen production for these samples were 509 and 725 mL min^{-1} g^{-1} for the 0.01 mols and 0.02 mols of metal samples respectively, Figure 4.25. If these were adjusted for the number of mols of metal then the 0.02 mols metal sample has lower activity, this could be due to it having larger particles.

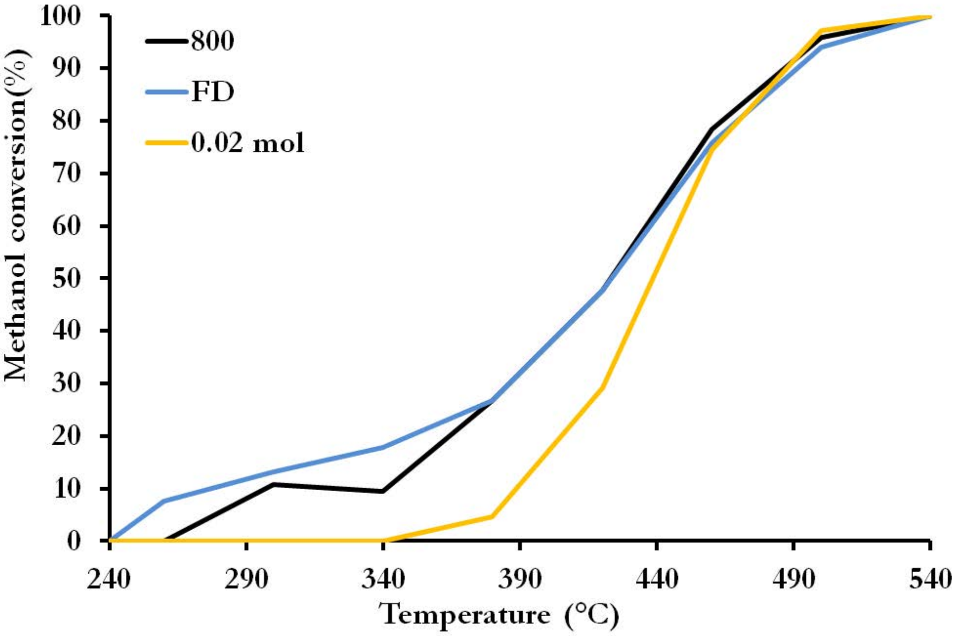

Figure 4.24 Comparison of the CZ75 synthesised with different biopolymers with the same heat treatment

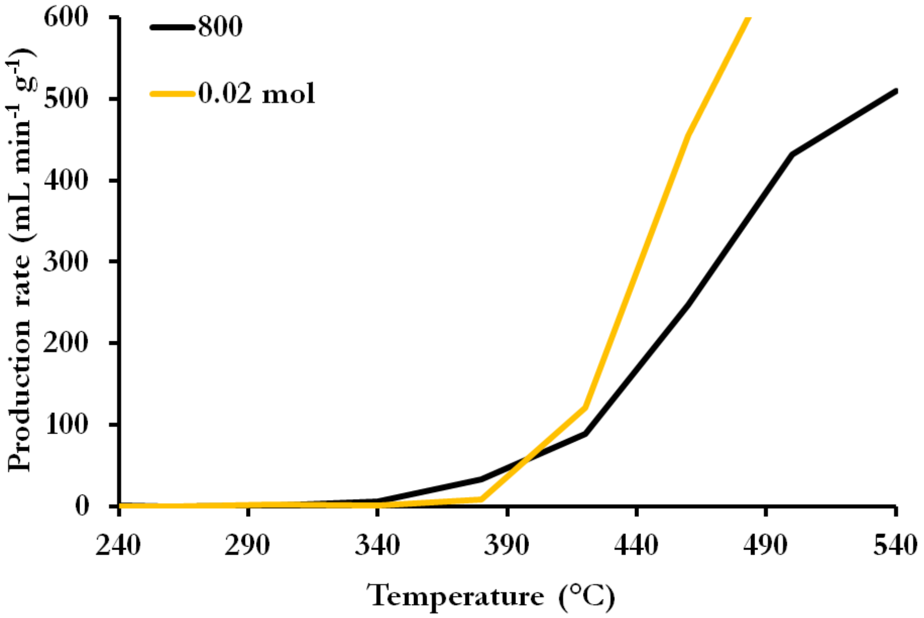

Figure 4.25 Comparison of the hydrogen production rates of CZ75 and CZ75_0.02 mol of metal

4.3.9 EFFECT OF ACID WASHING ON ACTIVITY

In previous studies on samples prepared in a similar fashion improved catalytic activity was shown by using a mild acid wash to remove some particles and open up new catalytic sites. Figure 4.26 shows the $\%_{MC}$ before and after the sample has been washed with mild acid. It shows the acid washed samples do not have all of the activity of the pre acid washed samples but they do retain a lot of it. This is despite having most of the 'active' metal removed, as was confirmed by an inductively coupled plasma - mass spectrometry experiment.

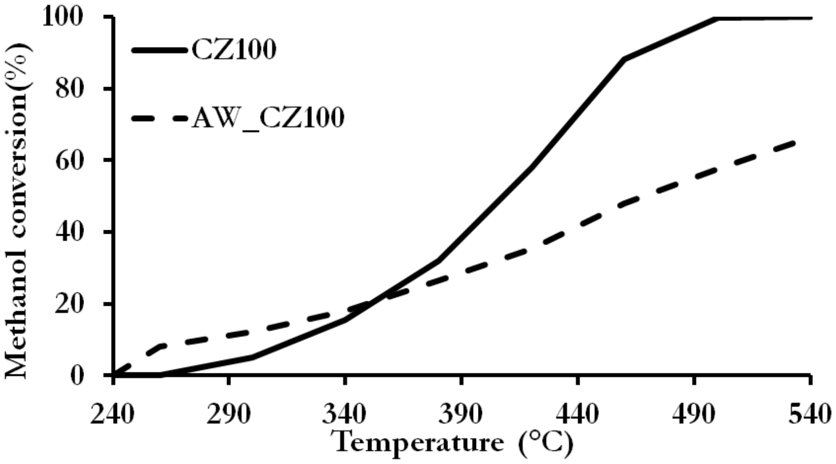

Figure 4.26 Acid washed vs non acid washed samples

The hydrogen production rate for these samples is shown in Figure 4.27 and as expected the rate is lower for the acid washed sample, however the hydrogen to carbon dioxide ratio ranges from 8-12. This means that MSR cannot be the main reaction and but instead could be water splitting or methanol decomposition followed by carbon deposition. An isothermal test revealed no increase in mass so there was not any carbon deposition. Hydrogen production is seen at low temperatures without carbon dioxide production, this indicated that the additional hydrogen may have been coming from the water splitting reaction. To test this, more of this sample was synthesised and tested with just steam passed over it, Tables 4.7 and 4.8 show the raw data for these experiments. During the stepwise temperature experiment there was no activity for water splitting before 460 °C and during the isothermal test there was limited activity for water splitting at 440 °C; however in both cases this was not enough to account for the high H_2 to CO_2 ratio. This leaves two possibilities; 1) a mistake was made during the synthesis for the second batch of sample or; 2) there was a mistake in the first experiment. There was not time to confirm which case is true.

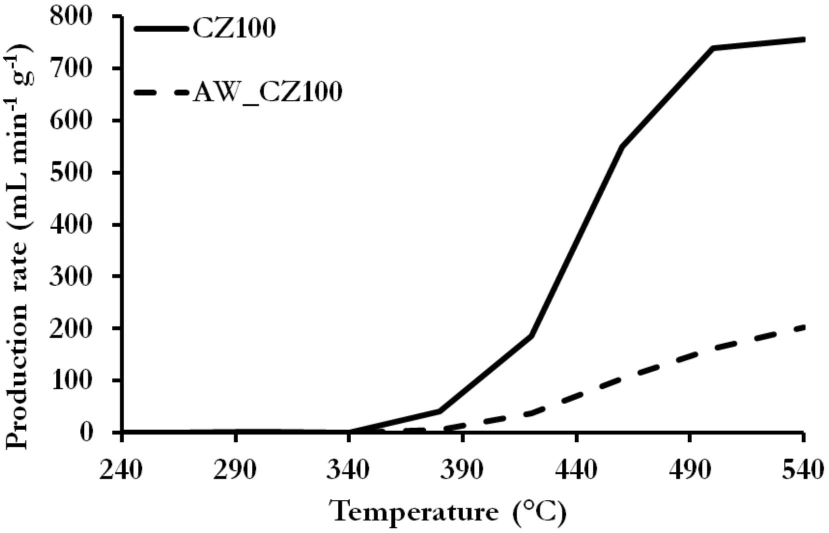

Figure 4.27 Acid washed vs non acid washed samples

Table 4.7 Raw MSR experiment data for the acid washed CZ100 sample

AW Zn			
Temp	H_2	CO_2	H_2/CO_2
240	0.060141	0	
260	0.092254	0	
300	0.094091	0	
340	0.537084	0	
380	5.923026	0.716998	8.26087
420	37.11186	6.416385	5.78392
460	103.2883	17.10869	6.037182
500	161.2908	19.85531	8.123311
540	202.5308	15.96813	12.68344

Table 4.8 Raw MSR experiment data for the acid washed CZ100 sample

Temperature (°C)	**H_2 production rate (ml min^{-1} g^{-1})**
	-
240	0
260	0
300	0
340	0
380	0
420	0
460	0.05129
500	0.15632
540	0.42918

4.3.10 EFFECT OF THE ADDITION OF ZIRCONIUM ON ACTIVITY

Zirconium has been well documented for its activity in MSR and especially tuning the selectivity for the reduction of CO, so CZ75 was prepared with some of the metal being replaced with between 2 and 25% zirconium. Figure 4.28 shows that the addition of zirconium does not change the overall $\%_{MC}$, however it does change the hydrogen production rate, Figure 4.29. A small amount of zirconium does massively increase the rate of hydrogen production but the rates of CO_2 and CO also are increased. The increased hydrogen production rate is probably due to the zirconium reducing the water gas-shift reaction; it is also seen without a large increase in the methanol conversion rate. This is partly due to the assumption there is no conversation at 240 °C, see section 3.3.4 for more clarity, and as a result the methanol conversion rate has a error associated with it. Replacing large amounts of copper and zinc with zirconium (25%) reduces overall activity, this indicates that zirconium is having the effect of promoting the reaction but is not active for MSR itself. Figure 4.30 shows the CO selectivity for these samples and it is clear the zirconium has little effect on CO production. It seems the zirconium could be used to increase activity but it would increase the price of the device, so in the long term it may not be economically viable.

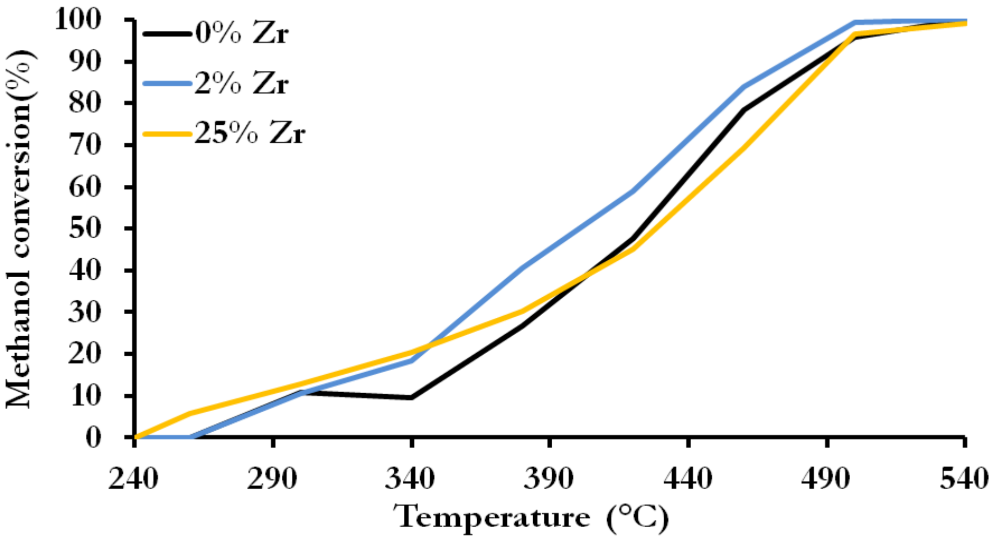

Figure 4.28 $\%_{MC}$ for Zr containing samples

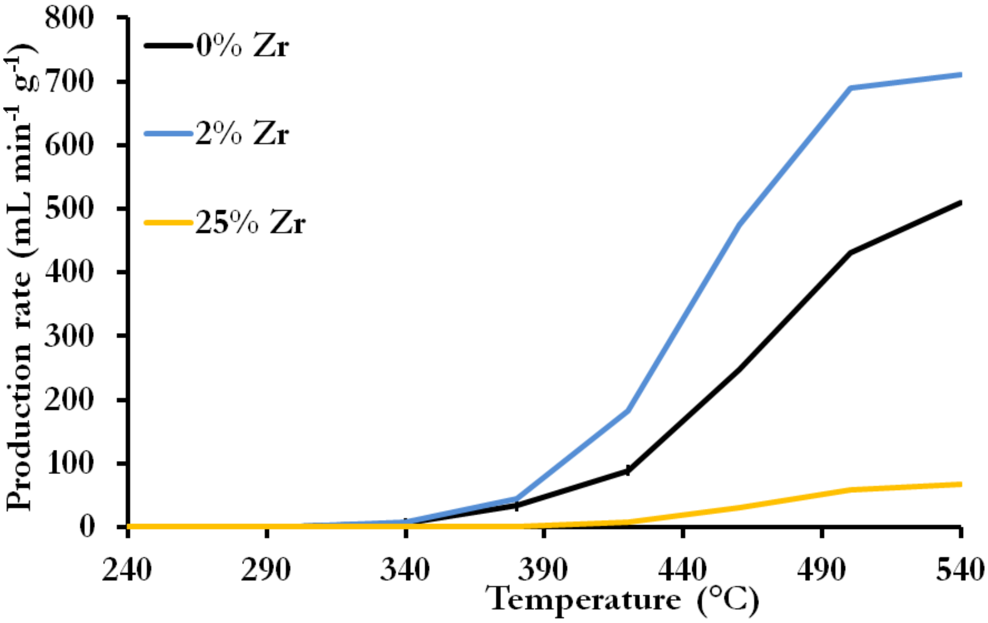

Figure 4.29 hydrogen production for Zr containing samples

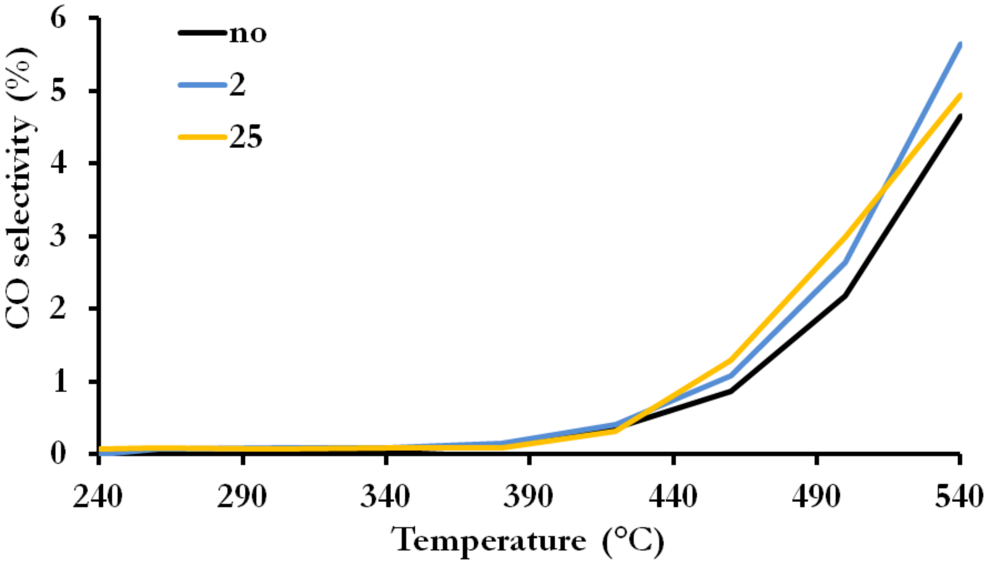

Figure 4.30 CO selectivity for Zr containing samples

4.4 CONCLUDING REMARKS

A series of Cu/Zn on porous carbon catalysts were investigated by a variety of techniques to probe their activity, stability and structure and therefore suitability for MSR. The preliminary data shown here indicates that these samples have promise as effective MSR catalysts. Currently these samples maybe useful for stationary applications but the reaction temperature must be reduced before these can be used in portable applications (i.e. cars).

The use of biopolymer in this facile sol-gel synthesis route makes this a very cheap synthesis and introduces the possibility to change the structure and activity greatly. The reason for this is probably due to the different structures of the biopolymer precursors being carried into the porous carbon in the final product, further work could look into this as understanding what lowers the activity may help to increase it.

It has been shown that the particle size is very small and further studies should include trying to change the size and investigate the effect on MSR activity. Scherrer analysis was used to estimate particle size and stability of the crystallites during the reaction, this seems to show good stability; samples should be cycled to see if they degrade further on subsequence uses.

4.5 REFERENCES

(117) *BP statistical review of world energy*, London: British Petroleum, 2016.

(118) Energy, U. D. o.; US Department of Energy: afdc.energy.gov, 2015; Vol. 2015.

(119) Roper, L. D. https://www.tesla.com/en_GB/support/model-s-specifications; Vol. 2017.

(120) Energy, U. S. D. o. https://energy.gov/sites/prod/files/2015/05/f22/fcto_targets_onboard_hydro_storage_explanation.pdf, 2015; Vol. 2017.

(121) Satyapal, S.; Petrovic, J.; Read, C.; Thomas, G.; Ordaz, G. *Catalysis Today* **2007**, *120*, 246.

(122) Pudukudy, M.; Yaakob, Z.; Mohammad, M.; Narayanan, B.; Sopian, K. *Renewable and Sustainable Energy Reviews* **2014**, *30*, 743.

(123) Dillon, A. C.; Heben, M. J. *Applied Physics A* **2001**, *72*, 133.

(124) Soulié, J. P.; Renaudin, G.; Černý, R.; Yvon, K. *Journal of Alloys and Compounds* **2002**, *346*, 200.

(125) Zamfirescu, C.; Dincer, I. *Fuel Processing Technology* **2009**, *90*, 729.

(126) Zhu, Q.-L.; Xu, Q. *Energy & Environmental Science* **2015**, *8*, 478.

(127) Chai, G. S.; Yoon, S. B.; Yu, J.-S.; Choi, J.-H.; Sung, Y.-E. *The Journal of Physical Chemistry B* **2004**, *108*, 7074.

(128) Ogden, J. M.; Steinbugler, M. M.; Kreutz, T. G. *Journal of Power Sources* **1999**, *79*, 143.

(129) Lindström, B.; Pettersson, L. J. *International Journal of Hydrogen Energy* **2001**, *26*, 923.

(130) Olah, G. A.; Goeppert, A.; Prakash, G. K. S. *The Journal of Organic Chemistry* **2009**, *74*, 487.

(131) Iwasa, N.; Mayanagi, T.; Ogawa, N.; Sakata, K.; Takezawa, N. *Catalysis Letters* **1998**, *54*, 119.

(132) Iwasa, N.; Takezawa, N. *Topics in Catalysis* **2003**, *22*, 215.

(133) Takahashi, K.; Takezawa, N.; Kobayashi, H. *Applied Catalysis* **1982**, *2*, 363.

(134) Valdes-Solis, T.; Marban, G.; Fuertes, A. *Catalysis Today* **2006**, *116*, 354.

(135) Ajamein, H.; Haghighi, M.; Shokrani, R.; Abdollahifar, M. *Journal of Molecular Catalysis A: Chemical* **2016**, *421*, 222.

(136) Sá, S.; Silva, H.; Brandão, L.; Sousa, J. M.; Mendes, A. *Applied Catalysis B: Environmental* **2010**, *99*, 43.

(137) Yong, S. T.; Ooi, C. W.; Chai, S. P.; Wu, X. S. *International Journal of Hydrogen Energy* **2013**, *38*, 9541.

(138) Bandlamudi, G. C.; Steffen, M.; Meijer, T.; Heinzel, A. In *Meeting Abstracts*; The Electrochemical Society: 2015, p 644.

(139) Iwasa, N.; Kudo, S.; Takahashi, H.; Masuda, S.; Takezawa, N. *Catalysis Letters* **1993**, *19*, 211.

(140) Iwasa, N.; Masuda, S.; Ogawa, N.; Takezawa, N. *Applied Catalysis A: General* **1995**, *125*, 145.

(141) Conant, T.; Karim, A. M.; Lebarbier, V.; Wang, Y.; Girgsdies, F.; Schlögl, R.; Datye, A. *Journal of Catalysis* **2008**, *257*, 64.

(142) Pauw, B. R. *Journal of Physics: Condensed Matter* **2013**, *25*, 383201.

(143) Sá, S.; Silva, H.; Brandão, L.; Sousa, J. M.; Mendes, A. *Applied Catalysis B: Environmental* **2010**, *99*, 43.

(144) Yao, C.-Z.; Wang, L.-C.; Liu, Y.-M.; Wu, G.-S.; Cao, Y.; Dai, W.-L.; He, H.-Y.; Fan, K.-N. *Applied Catalysis A: General* **2006**, *297*, 151.

(145) Shishido, T.; Yamamoto, Y.; Morioka, H.; Takaki, K.; Takehira, K. *Applied Catalysis A: General* **2004**, *263*, 249.
(146) Jakdetchai, O.; Takayama, N.; Nakajima, T. *Kinetics and catalysis* **2005**, *46*, 56.
(147) Günter, M. M.; Ressler, T.; Jentoft, R. E.; Bems, B. *Journal of Catalysis* **2001**, *203*, 133.

CHAPTER 5

BIOPOLYMER SOL-GEL SYNTHESIS

OF

TUNGSTEN CARBIDE

5.1 PROPERTIES OF METAL CARBIDES

Metal carbides and nitrides, especially those from the transition block, are often discussed together as they have very similar bonding characteristics, crystal structures, electric and magnetic properties. These similarities are due to the similar size and electronegativity of carbon and nitrogen. It should be noted, however, that the extra electron on the nitrogen makes the nitride of an element from one group (i.e. 6th group) more similar to the carbide of the next group (i.e. 7th group) rather than its own group. The focus of this chapter is the synthesis of tungsten carbide, however in the attempts to synthesise the carbide the nitride was also made so it is important to remember this difference.[148]

Transition metal carbides and nitrides are an attractive class of materials since they exhibit a wide range of useful physical (both functional and structural) and chemical properties. Most of the elements in this block form carbides and nitrides with the exceptions of those in the bottom right-hand corner (i.e. Ru, Rh, etc.). One of the characteristics of these materials is their extremely high melting points, meaning they can be used in very high temperature applications such as in jet engines.[149] The main use of these refractory carbides and nitrides historically though is as additives to harden materials. Carbides are normally harder than nitrides and are amongst the hardest materials known[150] and whilst they can be used on their own more commonly they are used in cemented carbides. Cemented carbides are a mixture of one or more carbide (e.g. WC, TiC) bound together in a metal (e.g. Co) and are used for producing drill bits,[151] cutting tools and other wear resistant surfaces.[152] Synthesis of these materials are facile by the means of well established furnace technology. Generally powders of the carbon and the element for which the carbide is required can be mixed and heated at elevated temperatures (approximately 1000 - 2000 °C depending on the metal) and the carbide is formed. For the uses mentioned so far particle size has been, generally, of little concern and usually the more sintered the final product is the better as this will improve its hardness. Many other physical properties of these materials make them invaluable in certain industries. For example, the electronic conductivity of tungsten nitride means it is used in resistors for integrated electronics,[153] however the area of interest for this chapter is the chemical properties.

A previous chapter talked about materials that can produce hydrogen to be used as an energy source for fuel cells. This chapter will look at materials that could potentially be used as the catalyst in a fuel cell. In addition to being a good catalyst for a number of reactions (e.g. oxygen reduction and water splitting) platinum is currently also used in fuel cells. Platinum's success is partly due to a plethora of simple synthesis routes,[154-156] these examples are all solution based, are carried out below 200 °C and allow for size and/or shape control. Such facile control over formation of nanoparticles means the already excellent catalytic activity of platinum can be further enhanced by selecting the most active crystallographic face and optimising the synthesis to increasing the accessible surface area of this face. Despite this there are a number of problems associated with using platinum such as the operation of the fuel cell requires a high overpotential to drive the reaction. Platinum is also extremely sensitive to pollutants in the fuel, such as carbon monoxide and sulphur both of which are common. The biggest problem though is the high cost of the raw material, both environmentally and economically, which in turn increases the price of any device using it and preventing it being used for mass production. This cost is due to it not being very earth abundant but this is compounded by its use in other fields (e.g. catalytic convertors and computers currently account for over 50% of the global consumption of platinum).

In 1973 Levy and Boudart[157] were the first to suggest tungsten carbide as an alternative and showed that it had catalytic activity that was similar to platinum for some reactions, e.g. hydrogen evolution reaction.[158,159] This activity though is limited to the surface of a particle and therefore surface area control is crucial to improving activity. This means traditional synthesis methods are not appropriate to form the particles sizes needed to achieve high surface area. This is highlighted by reactions carried out over tungsten carbide, when compared to platinum nanoparticles. The platinum nanoparticles tend to be much smaller than the tungsten carbide particles so therefore the increased activity could be a simple surface area effect. The fact that tungsten carbide shows this activity, albeit at lower levels is good because it is cheaper and more abundant than platinum. A survey completed by the United States Geological Survey showed that last year the tungsten was approximately 7 times cheaper and approximately 300 times more abundant.[160] Another benefit of tungsten carbide is that it is more resistant to poisoning.[161] In addition to direct use as a catalyst tungsten carbide finds use as a catalysis support/ co-catalyst[63] for areas such as for environmental remediation (i.e. nuclear waste management[62] or solar degradation) when combined with a photo-active semiconductor (e.g. TiO_2).[162]

Producing nanoparticles is difficult, as mentioned earlier, due to the high synthesis temperatures or complex synthesis routes (e.g. chemical vapour condensation).[163] As mentioned previously tungsten carbide can be synthesised from its oxide (WO_3) and carbon in a 2 step process by the reduction of the oxide to metallic tungsten and then further reaction with carbon at 1400 - 1600 °C.[164] This was a big step in reducing the synthesis temperature (down from 2000 °C) however β-W_2C and WC that were synthesised still suffered with a low specific surface area (SSA) (~30 m^2 g^{-1}). In recent years, a lot of research has focussed on tungsten carbide and these have benefits and disadvantages. For example, one technique can produce WC/W_2C on carbon with particle sizes of approximately 2 nm with competitive stability and activity when compared to commercial platinum on carbon, however it is produced through an energy intensive arc-discharge method which may hinder mass production.[165] Another example shows how tungsten carbide can be produced in minutes from tungsten and carbon in a microwave, it is a remarkable achievement however, due to high temperatures involved the particle size is large.[166]

Other researchers have looked at creating different shapes as a way of increasing SSAs and directing charge transfers by shaping the nanoparticles, e.g. at 900 °C WC nanotubes (30 - 70 nm x 1 -10 μm) have been synthesised from $W(CO)_6$ with Mg powder; this is quite an achievement as the temperature is low compared to previous studies.[167] Very small WC nanoparticles (1 - 5 nm) have been synthesised, which brings the particle size into the range of platinum nanoparticles, this was done via a multistep process which if it can be simplified will greatly increase its usefulness.[168] Although a large of synthesis routes have been developed to tackle the issue of high synthesis temperatures for the synthesis tungsten carbides, this work aims to produce a tungsten carbide/ carbon nanocomposite. This has been done before by Chen *et al.* who demonstrated how W_2C electrochemical performance and stability could be enhanced by supporting it on graphene.[169]

The main aim of this work was to synthesise WC but the precursors can have a profound effect on the final product; this is highlighted by a temperature programmed reduction of both WO_3 and β-W_2N precursors along with CH_4/H_2 atmospheres which showed that the two different precursors produced WC with very different SSAs. This reaction produced WC with SSAs of ~48 $m^2 g^{-1}$ (from WO_3) and ~100 $m^2 g^{-1}$ (from β-W_2N) highlighting that fact that the choice of precursor is as important as the reaction pathway. WN and W_2N, unlike the carbides, are difficult to synthesise as the presence of nitrogen in the tungsten lattice is thermodynamically unfavourable at ambient conditions.[170] Initially they were made by the ammonia reduction method of tungsten oxides and sulfides.[171] A wide range of CVD techniques have also been developed to produce films of W_2N.[172,173]

In an attempt to produce nanoparticulate tungsten carbide on porous carbon with high accessible surface area a biopolymer sol-gel synthesis was developed. The synthesis was based on the work of Schnepp *et al*[65] and the aim of this work was to develop a system to produce functional materials in an economically viable and environmentally friendly way. Biopolymers offer the potential to add complex structural features to materials in one step and depending on the biopolymer they can also offer a renewable source of carbon. To start, a more 'traditional' urea-metal complexation route was used to first produce tungsten carbide before the biopolymer sol-gel route was trialled. Finally this method was modified to synthesise nanocomposites.

5.2 EXPERIMENTAL

General experimental techniques, e.g. XRD, TEM, used through all chapters are described in Appendix E along with information about how the experimental techniques and how the instruments function.

5.2.1 MATERIALS

Below is a list of materials used in this chapter.

Table 5.1 List of materials used for synthesis and analysis in this chapter

Chemical	Supplier	CAS number
Gelatin, type A, porcine, G2500, 300 bloom strength	Sigma Aldrich	9000-70-8
Gelatin, type B, bovine, G9382, 225 bloom strength	Sigma Aldrich	9000-70-8
Dextran, from Leuconostoc mesenteroides, Mw ~ 25 000	Sigma Aldrich	9004-54-0
Dextran, from Leuconostoc mesenteroides, Mw ~ 70 000	Sigma Aldrich	9004-54-0
Agar, microbiology tested	Sigma Aldrich	9002-18-0
Locust bean gum, from Ceratonia siliqua seeds	Sigma Aldrich	9000-40-2
Starch, puriss. p.a., from potatoes.	Sigma Aldrich	9005-84-9
Magnesium(II) nitrate hexahydrate	Sigma Aldrich	13446-18-9
Nitric acid 70% (w/w)	Sigma Aldrich	7697-37-2
Ammonium metatungstate hydrate	Sigma Aldrich	12333-11-8
Tunngsten chloride	Sigma Aldrich	13283-01-7
Urea	Sigma Aldrich	57-13-6
Ethanol	VWR	64-17-5

5.2.2 SYNTHESIS OF TUNGSTEN CARBIDE FROM TUNGSTEN-UREA COMPLEXES (SYNTHESIS 1)

A 20% (w/v) tungsten ethoxide solution was made by dissolving tungsten(VI) chloride (20 g) in ethanol (80 mL) stirred at 50 °C (Solution A); this should be done slowly to limit the rate of release of HCl gas. Solution A (19.83 mL) was stirred at 50 °C and to this the correct amount solid urea was added to achieve the desired tungsten:urea ratio, Table 5.2. This mixture was stirred for 20 minutes to dissolve and homogenise the solution and urea, it was then dried at 70 °C until a solid was obtained. The resulting solid was placed into a crucible and heated to 800 °C (5 °C min^{-1}) in a nitrogen atmosphere, held for 240 minutes and then allowed to cool to room temperature. The final temperatures and hold times were varied. A black powder was recovered in most cases.

Table 5.2 Ratios and masses of WCl_6 and urea used to synthesise tungsten carbide

WCl_6 : Urea molar ratio	Mass of WCl_6 (g)	Volume of 20% (w/v) stock solution	Mass of Urea (g)
1 : 2	3.966	19.83	0.6
1 : 3	3.966	19.83	0.9
1 : 4	3.966	19.83	1.2
1 : 5	3.966	19.83	1.5
1 : 6	3.966	19.83	1.8
1 : 7	3.966	19.83	2.1
1 : 9	3.966	19.83	2.7
1 : 10	3.966	19.83	3.0
1 : 14	3.966	19.83	4.2

5.2.2.1 SYNTHESIS OF TUNGSTEN CARBIDE VIA A MIXED UREA/BIOPOLYMER SOL-GEL METHOD

A series of samples were prepared using an ethanolic urea/WCl_6 tungsten source in addition to the biopolymer agar. An initial ethanolic tungsten/urea solution was made from a 20% (w/v) solution of tungsten(VI) chloride and ethanol with the addition of the appropriate mass of solid urea. This solution was added to an aqueous biopolymer 5% (w/v) and stirred, with heating (70 °C), for 30 - 40 minutes to homogenise the solution. The solution was dried in an oven until a solid was obtained, this solid was then calcined in a muffle furnace under flowing nitrogen using the following heating profile - heating at 5 °C min^{-1} to 850 °C and holding at this temperature for 240 minutes. The following text is used to clarify Table 5.3 below, the first selection of samples had some of the urea replaced, this was done by substituting urea on a mass basis (i.e. 1 % by mass of the urea was replaced with the same mass of biopolymer. The other samples had the mass of biopolymer equal to that of 'X' % of urea in addition to the full amount of urea (i.e. the mass of 1 % of the urea used in the 1:14 samples was calculated and this mass of biopolymer was added without removing any urea).

Table 5.3 Mass and volumes used for samples synthesised using an ethanolic urea/tungsten

% Biopolymer added/subtracted	Volume of WCl_6	Mass of biopolymer (g)	Volume of 5% (w/v) biopolymer solution (mL)	Mass of Urea (g)
0	19.83	0.00	0.00	4.20
-1	19.83	0.04	0.84	4.16
-5	19.83	0.21	4.20	3.99
-10	19.83	0.42	8.40	3.78
+1	19.83	0.04	0.84	4.20
+5	19.83	0.21	4.20	4.20

5.2.3 SYNTHESIS OF TUNSTEN CARBIDE FROM BIOPOLYMER GELS (SYNTHESIS 2)

Initially, synthesis of tungsten carbide proved difficult, so as a result, a variety of biopolymers were trialled with various ratios of tungsten precursor to biopolymer at a range of temperatures, ramp rates and hold times. A representative spread of these variables is shown in Table 5.4, the examples shown are for the porcine gelatin, the biopolymers listed in the materials section (5.2.1) were used to produce samples under the same conditions. Most samples were produced under a nitrogen atmosphere but a few samples were synthesised under argon to investigate how this would change the reaction; these are indicated with a superscript ^{a}.

A 10% (w/v) gelatin solution was prepared by adding the biopolymer to hot and rapidly stirred distilled water (90 mL, 70 - 150 °C) until a homogeneous solution was obtained (solution A). The temperature of the water depended on the biopolymer and the beaker was covered with a watch glass to prevent water loss due to evaporation. A 10% (w/v) ammonium metatungstate solution was prepared by placing ammonium metatungstate (10g) in a 100 mL volumetric flask and filling with distilled water. Solution A (20 g) was transferred to a beaker covered with a watch glass and heated (70 - 120 °C) with rapid stirring, to this the tungsten solution (24.64 mL) (0.01

M of metal) was added. The solution was stirred for a further 20 minutes to ensure it was homogenous. This was then placed in an oven at 70 °C until a solid was obtained. The resulting solid was placed into a crucible and heated in a muffle furnace retrofitted with a metal retort to allow for atmosphere control to the required temperature and for times stated in Table 5.4. The atmosphere was flowing nitrogen/argon at 1 L min^{-1} and after the required time had elapsed, the furnace was allowed to cool to room temperature before the samples were removed. A black powder was recovered in most cases.

Table 5.4 Matrix of heating regimes, reaction conditions and concentration of metal for synthesis of tungsten carbide. ^{a} = argon

Metal concentration (Mol)	Ramp Rate (°C min^{-1})	Hold Time (min)
0.001	1	5
		60
		240
	5	5^{a}
		60
		240
	10	5^{a}
		60
		240
0.005	1	5
		60
		240
	5	5^{a}
		30
		60
		240
	10	5^{a}
		60
		240
0.01	1	5
		60
		240
	5	5^{a}
		30
		60
		240
	10	5^{a}
		60
		240
		720

5.2.4 SYNTHESIS OF TUNSTEN CARBIDE/METAL OXIDE NANOCOMPOSITES FROM BIOPOLYMER GELS (SYNTHESIS 3)

A 10% (w/v) gelatin solution was prepared by adding porcine gelatin to hot and rapidly stirred distilled water (90 mL, 70 °C) until a homogeneous solution was obtained (solution A). Separately 10% (w/v) ammonium metatungstate and magnesium nitrate solutions were prepared by placing the respective metal salts (10g) in a 100 mL volumetric flask and filling with distilled water. A mixed solution was made from these stock solutions, the stock solutions were mixed at the desired ratio, Table 5.5, to give an overall concentration of metal of 0.01 M (solution B). Solution A (20 g) was transferred to a beaker covered with a watch glass and heated (70 °C) with rapid stirring, to this solution B (0.01 M of metal) was added. The solution was stirred for a further 20 minutes to ensure it was homogeneous. This was then placed in an oven at 70 °C until a solid was obtained. The resulting solid was placed into a crucible and heated in a muffle furnace retrofitted with a metal retort to allow for atmosphere control to the required temperature and for times stated in Table 5.5. The atmosphere was flowing nitrogen/argon at 1 L min^{-1} and after the required time had elapsed, the furnace was allowed to cool to room temperature before the samples were removed. A black powder was recovered in most. Some samples were run under argon, this is indicated by a superscript ^{a} in the table below and all the samples were also synthesised using agar as the biopolymer.

Table 5.5 Molar ratio and volumes of starting metals and heating programs for a series of tungsten and magnesium nanocomposites. ^{a} = argon atmosphere.

Metal ratio Mg : W	Moles of metal	Mass of Metal (g)	Volume of stock (mL)	Heating program (temp_ramp rate_ hold)
0 : 100^{a}	0 : 0.01	0.00/2.15	0.00/21.45	900_10_5
25 : 75^{a}	0.0025:0.0075	0.64/1.61	6.40/16.09	900_10_5
50 : 50^{a}	0.005 : 0.005	1.28/1.07	12.80/10.73	900_10_5
75 :25^{a}	0.0075:0.0025	1.92/0.54	19.20/5.36	900_10_5
100 : 0^{a}	0.01 : 0	2.56/0.00	25.6/0.00	900_10_5

5.3 RESULTS AND DISCUSSION

5.3.1 SYNTHESIS OF TUNGSTEN CARBIDE FROM TUNGSTEN-UREA COMPLEXES

For the clarity of the following text, Table 5.6 shows a list of the different possible phases found and their corresponding identifying number on the ICDD database. Synthesis of tungsten carbide (WC) has been reported previously by Giordano *et al;* [158] this synthesis used tungsten(IV) chloride (WCl_4) and urea and the article shows the following trend. Low ratios of tungsten to urea (W:U) form tungsten nitride, medium W:U ratios form metallic tungsten and high ratios W:U produce tungsten carbide. A synthesis method similar to this was adopted to repeat this finding and produce a 'map' of temperatures that could be trialled with the biopolymer. An attempt to copy the paper was made using the highest W:U of 1:7, however this was unsuccessful as the XRD pattern of the product from this experiment, Figure D1 (appendix), shows tungsten dioxide (WO_2) and metallic tungsten (W) were produced. Since the precursor WCl_4 is expensive, the method from the paper is vague and the experiment did not produce the carbide as expected, this synthesis route was changed. Tungsten(VI) chloride (WCl_6) is approximately a sixth of the price of the 4^+ metal chloride (£2 g^{-1} vs. £12 g^{-1}) and soluble in ethanol so it is a suitable substitute. An added benefit of WCl_6 is that it is a greener precursor as WCl_4 is produced from it so by using the 6^+ metal salt an extra preparation step has been skipped.

Table 5.6 List of tungsten phase and PDF numbers found during the urea synthesis route

Material name	Molecular formula	PDF number
Tungsten	W	00-001-1203
Tungsten dioxide	WO_2	00-032-1393
Tungsten trioxide	WO_3	04-007-2322
Tungsten nitride	WN	04-015-0316
Tungsten hemi-nitride	W_2N	00-025-1257
Tungsten carbide	WC	00-003-1096
Tungsten hemi-carbide	W_2C	00-002-1134
Tungsten sub-carbide	WC_{1-x}	00-022-1316
Tungsten oxy-carbide	$W_2(C, O)$	00-059-0959
Tungsten oxy-nitride	$W_{0.62}(N, O)$	00-065-1254

Before the results are discussed it should be noted that the samples produced at lower temperature and some of those with lower W:U ratios had x-ray diffraction (XRD) patterns with very broad peaks. This means there is difficultly in identifying certain phases as oxygen, nitrogen and carbon are similar in size and are soluble in MX (where X = C, N) often without a large structural change. To illustrate this WC_{1-x}, WN, W_2N, $W_2(C,O)$ and $W_{0.62}(N,O)$ are all cubic and Figure 5.1 shows how the reference patterns are quite similar; as a result identification from XRD alone is difficult. Further work is required to definitely prove identities of the phases, i.e. elemental analysis or Raman. As a result of all this these peaks will be labelled as WN in future XRD patterns but the reader should be aware that this is just for the clarity of the figures, i.e. rather than including all of the possible phases.

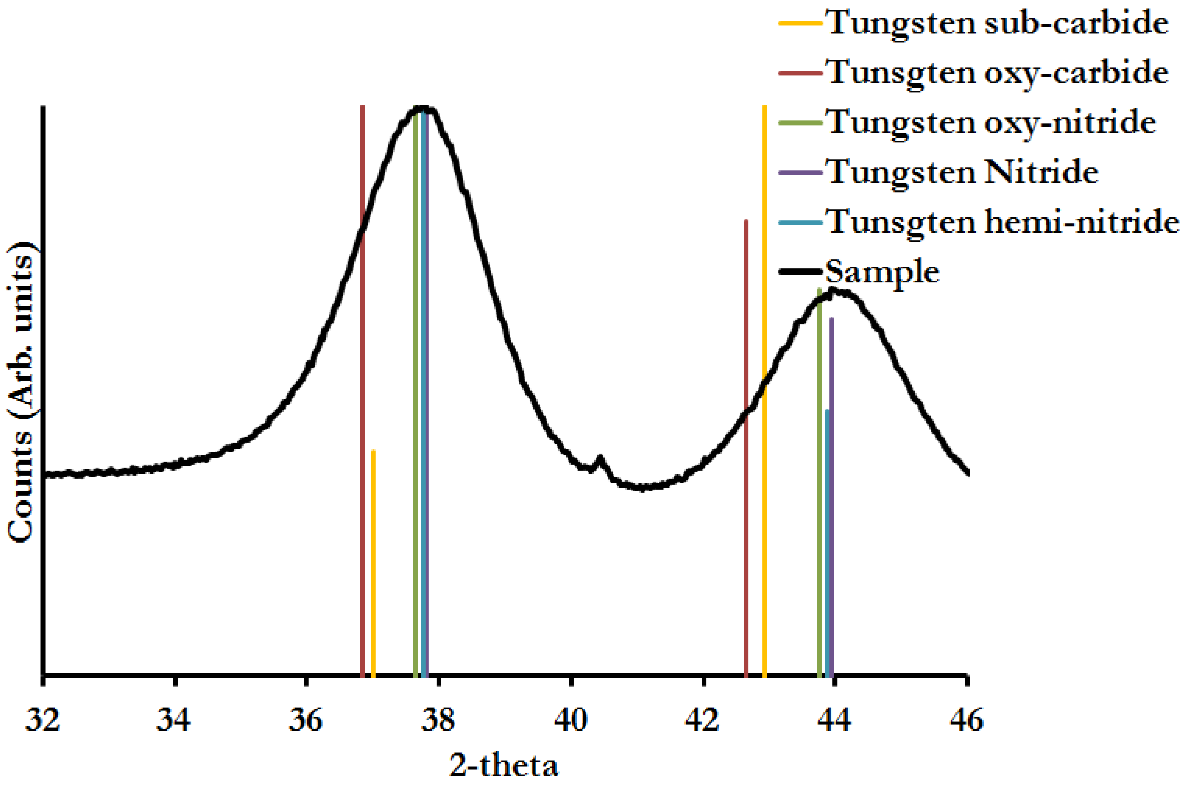

Figure 5.1 A sample XRD from the phase map showing how the broad peaks overlap with several reference patterns

Samples were prepared at different temperatures using a range of W:U ratios, the XRD patterns were analysed (Figures D2 - D40, appendix) and used to produce a basic phase map, Figure 5.2 Crosses on the phase map correspond to samples produced and the lines connecting them show areas where the XRD patterns contained the same phases; this is not an exhaustive phase map but it was helpful in showing trends for the other syntheses.

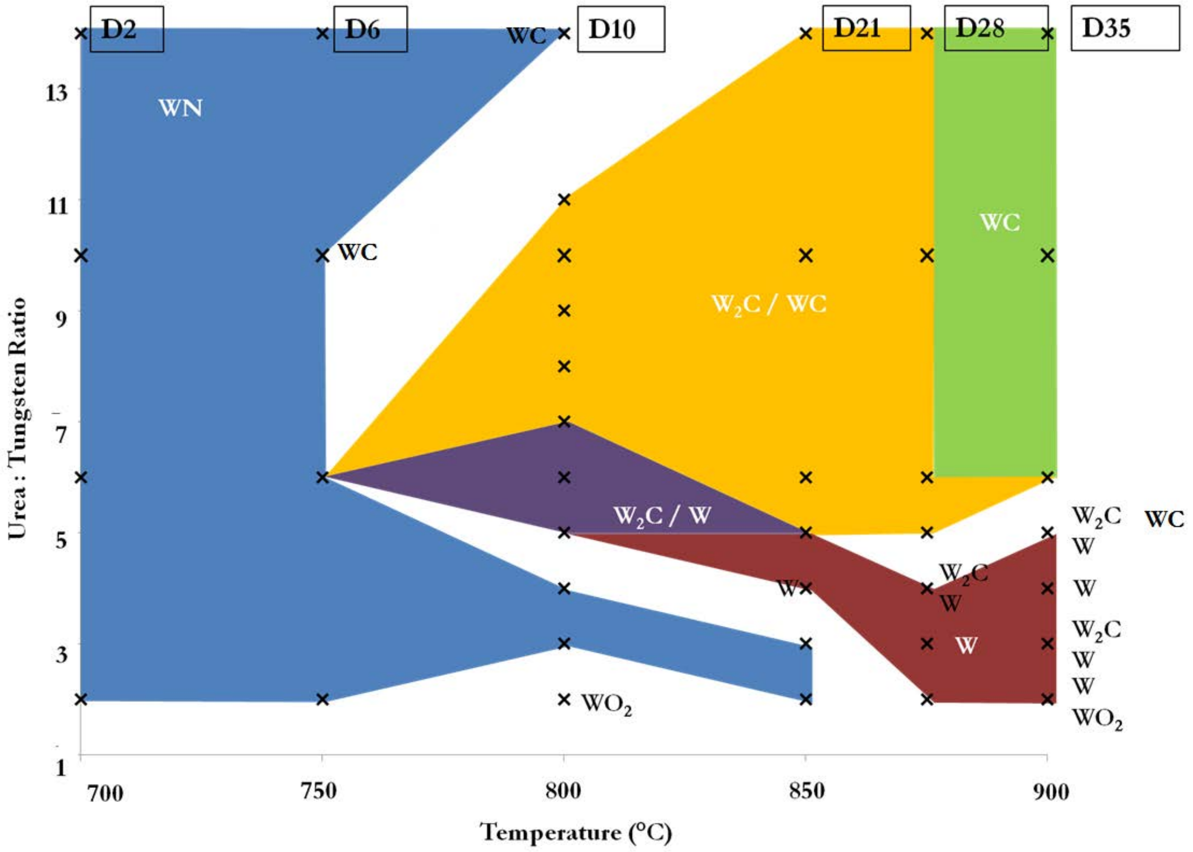

Figure 5.2 XRD phase map of temperature versus tungsten to urea ratio. Ramp rate and holding times at max temperature are 5 °C min^{-1} and 240 minutes respectively. Numbers in the boxes at the top of the figure indicates the number of the corresponding XRD in the appendix

The main molar ratios used for this study were 1:2, 1:6, 1:10 and 1:14 W: U the others were included to further investigate the bottom right-hand corner of the phase map (high temperature and low urea concentration. Phase boundaries were identified by XRD patterns with the same phases in and further samples are needed to fill in the white areas. The wide range of temperatures and molar ratios were used to investigate if the WCl_6/urea system was similar to the WCl_4/urea system and there are a number of similarities. If formation of tungsten carbide follows the same synthesis route as iron carbide then the carbide is formed through the nitride at higher temperatures: this would lead to WN formation at lower temperatures. From the XRD patterns that make up the phase map it suggests that this may be the case as at lower temperatures (i.e. below 750 °C) broad peaks that could be WN are see across all W:U ratios; it is also seen at higher temperatures but only with low W:U ratios. This can be rationalised by the urea decomposition route.[174] As urea decomposes it forms many nitrogen containing intermediates, these help to produce tungsten nitride phase, this decomposition starts at approximately 150 °C and continues to approximately 600 °C. At high temperatures but lower W:U ratios all of the urea has fully combusted and therefore it is not possible to form the carbide. An alternative explanation could be that at these higher temperatures one of the mixed phases (i.e. $W_2(C,O)$ or $W_{0.62}(N,O)$) or WC_{1-x} is being formed. The later can be rationalised by the same logic, the carbide has started to form but there isn't enough organic precursor to complete the transformation. The possible formation of the oxy-nitride could be due to the longer synthesis times and the imperfect nitrogen atmosphere, but this isn't consistent with other areas of the phase map.

An interesting point is that the higher ratios at the same temperature show XRD patterns with much broader peaks, Figure 5.3, this suggests smaller particles and this was estimated using the Scherrer equation, Figure D42 and D43, appendix. There is approximately a 20 nm difference in particle size which equates to approximately a 3.4 times increase in surface area (assuming a sphere) meaning if the carbide can be isolated then this could be a means to increase surface area. However there is also a shift in peak position as well indicating a change unit cell size, this could be due to carbon diffusing into the structure, but further work is required to confirm this (Raman, elemental analysis).

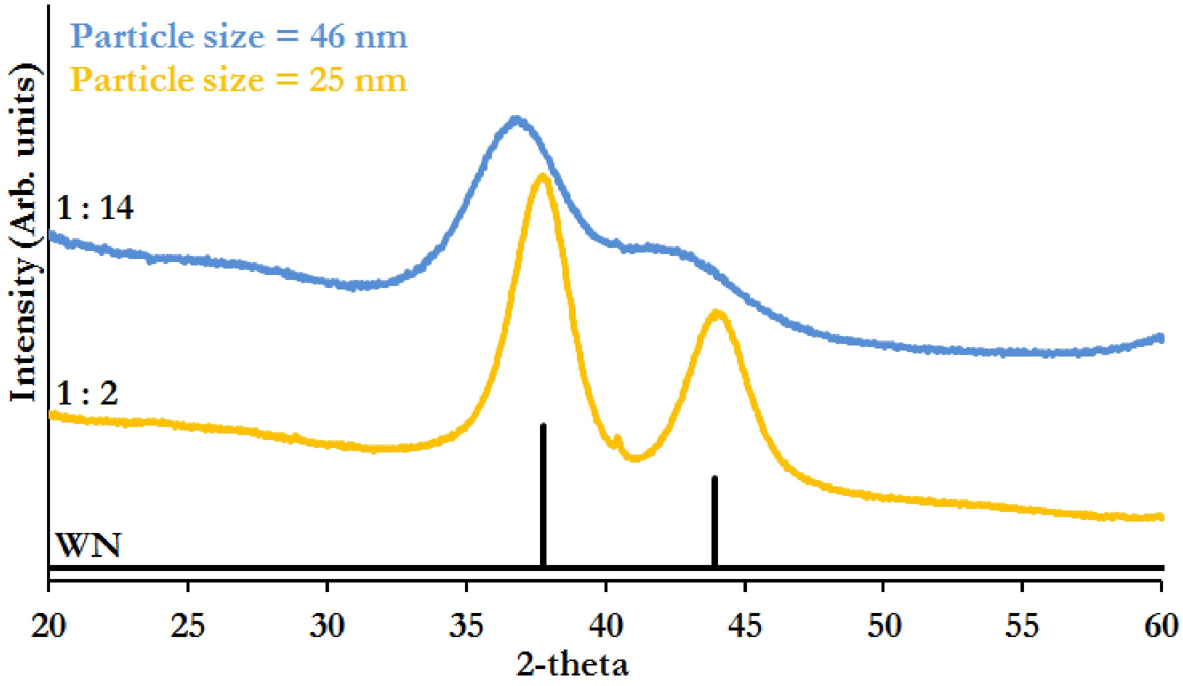

Figure 5.3 XRD pattern of samples synthesised at 750 °C (5 °C min^{-1}) under flowing nitrogen for 240 minutes from tungsten(VI) chloride and urea. Unmarked peak at approximately 40 ° is tungsten

At slightly higher temperatures and W:U ratios tungsten is formed. One possibility for this could be that after the nitride is formed the nitrogen starts to leave the structure before the carbon enters to form the carbide and it is the intermediate that has been isolated in these samples. To confirm this an in-situ synchrotron experiment could be carried out.

Almost all of the samples above 750 °C and a W:U ratio of 1:6 or higher have XRD patterns that show either WC or W_2C. Most of the samples show a mixture of phases which highlights how similar the synthesis conditions are for these compounds. Figure 5.4 shows the XRD patterns for samples in this area synthesised at 850 °C with increasing ratios. As the amount of urea increases there is greater peak intensity for WC and decreasing intensity for W_2C. A W:U ratio of 1:6 produces W_2C and WC but the main phase is W_2C. Increasing the W:U ratio to 1:10 and then to 1:14 the WC peak intensity increases and becomes the main phase. This indicates the W_2C is more stable and that the synthesis of WC is only possible with the increased amount of carbon which allows more to diffuse into the lattice, this is similar to the mechanism that was proposed for the formation of iron carbide from iron nitride.[67]

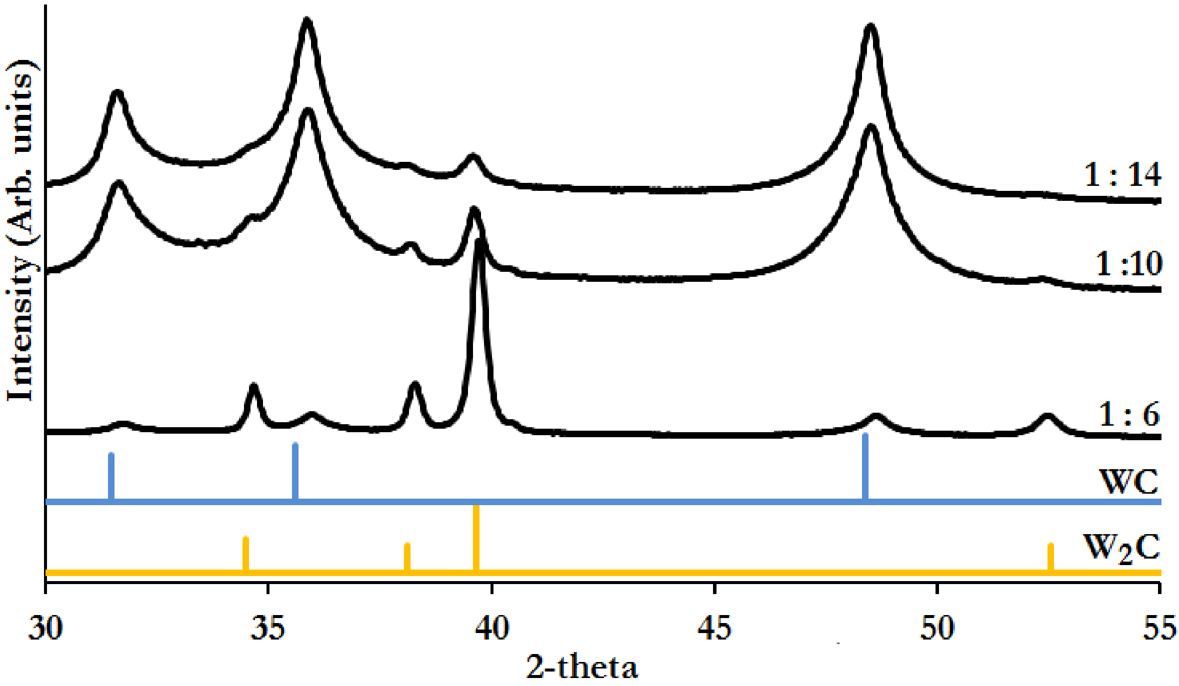

Figure 5.4 XRD pattern of samples synthesised at 850 °C (5 °C min^{-1}) under flowing nitrogen for 240 minutes from tungsten(VI) chloride and urea

In the phase map WC is seen in the XRD patterns between 750 and 850 °C at moderate to high levels of urea. Future work should be done in this area as this could provide information about how the carbides are formed, but these initial experiments seem to support existing literature that WC is thermodynamically more stable at lower temperatures.[175] The only two XRD patterns to apparently show WC at 900 °C are from the sample made with the highest amounts of urea in the precursor, the peaks are still quite broad so it is possible that a second phase could be 'hidden' under these peaks. As WC was successfully synthesised at 900 °C this temperature was selected to be used for the biopolymer synthesis.

Before changing the methodology to the biopolymer sol-gel (BSG) method a hybrid urea/biopolymer synthesis was tried; for this work agar was used. For samples with either additional (+1%) or substituted (-1%) biopolymer content the XRD pattern, Figure 5.5, shows that the formation of WC is favoured over W_2C and the particle size is smaller, this is indicated by peak broadening. The mass of added biopolymer was calculated on a mass basis (i.e. 1% by mass of the urea was replaced with the same mass of biopolymer. Other samples had extra mass of biopolymer added (i.e. the mass of 1 % of the urea used in the 1:14 samples was calculated and this mass of biopolymer was added without removing any urea). Using the formula mass of agar($C_{12}H_{18}O_9$) and urea(NH_2CONH_2) the percentage carbon was calculated as 47% and 20% respectively). This means for the for the '-1%' sample had 0.0084 g of carbon from the urea replaced with 0.0197 g of carbon from agar, this corresponds to the 1% increase in carbon mass overall; for the '+1%' sample this is a increase of 2% in the carbon. The additional carbon found in a biopolymer compared to urea means there is more excess carbon to drive the formation of WC over W_2C. Smaller particle size is due to the enhanced thermal stability of the biopolymer which stops sintering of the particles until higher temperatures.

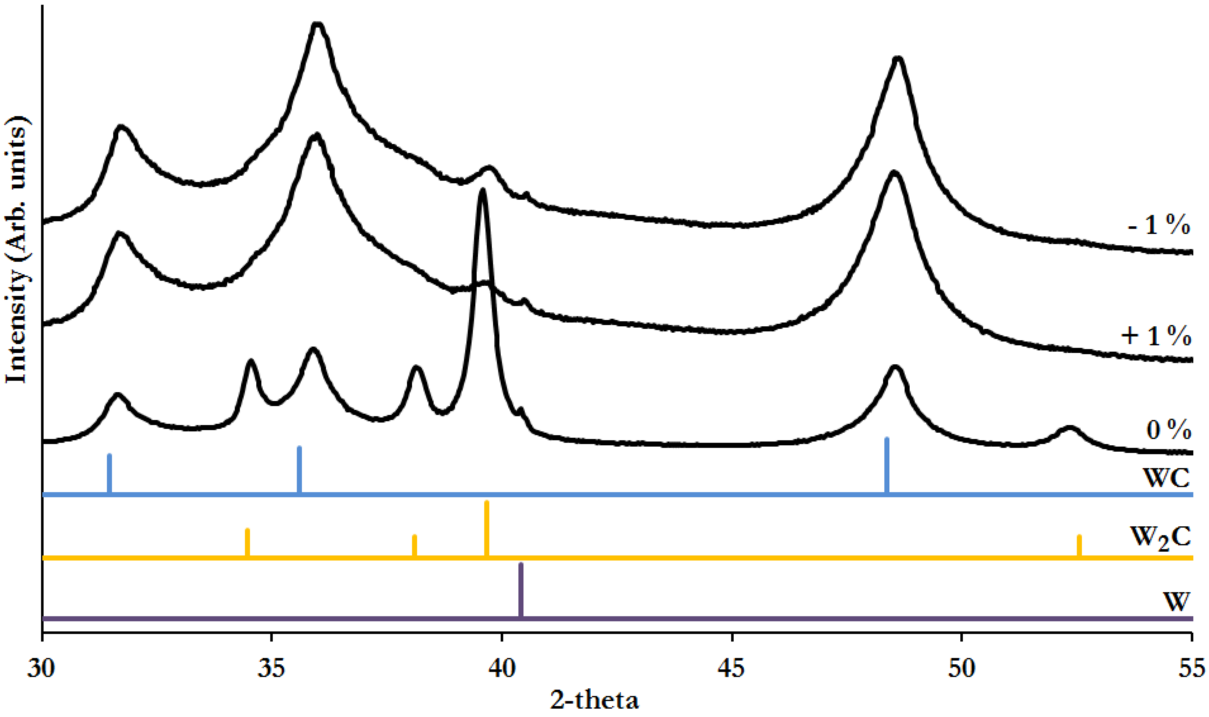

Figure 5.5 XRD patterns for samples synthesised from a urea/agar/WCl_6 sol-gel method at 850 °C (5 °C min^{-1}) for 240 minutes under flowing nitrogen

Figure 5.6 shows the XRD patterns for samples synthesised using 1, 5 and 10 percent mass substituted biopolymer. As more biopolymer is substituted for urea two broad peaks, as seen earlier, are observed and this could be WN due to the compositional change of the biopolymer being added; as agar has no nitrogen the formation of WN is slower. Alternatively these peaks could be from WC_{1-x}, future work could try other temperatures to investigate this. A small amount of W_2C is also seen, if this is evidence that the biopolymer is slowing down the reaction and W_2C is the end product a longer reaction time would show more W_2C.

The XRD patterns in Figure 5.7 possibly provide some evidence of this as W_2C is possibly present in the 5 percent substituted biopolymer sample but not in the additional 5 percent biopolymer sample; it should be noted that due to such broad peaks it is difficult to assert this from the XRD patterns alone. The sample with the most organic material has slowed the reaction and prevented the formation of the carbide. These indicators should be considered in further work and biopolymer to metal ratios should be varied.

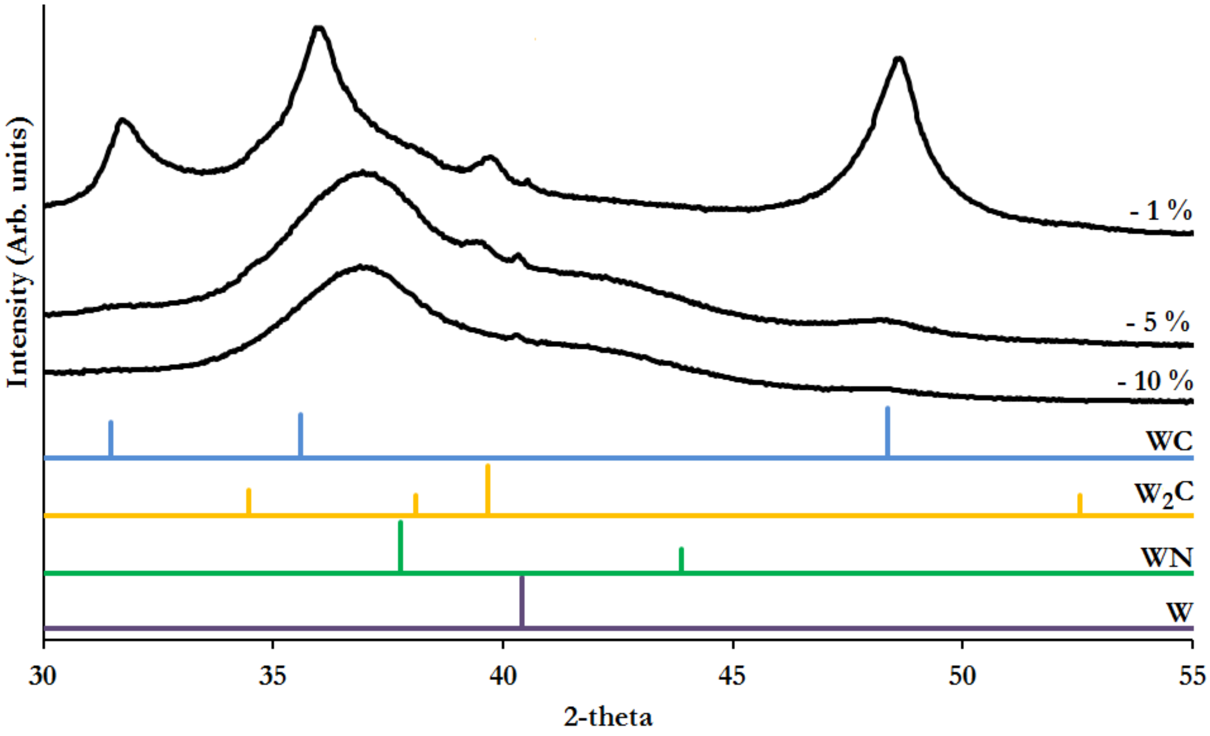

Figure 5.6 XRD patterns for samples synthesised from a urea/agar/WCl_6 sol-gel method at 850 °C (5 °C min^{-1}) for 240 minutes under flowing nitrogen

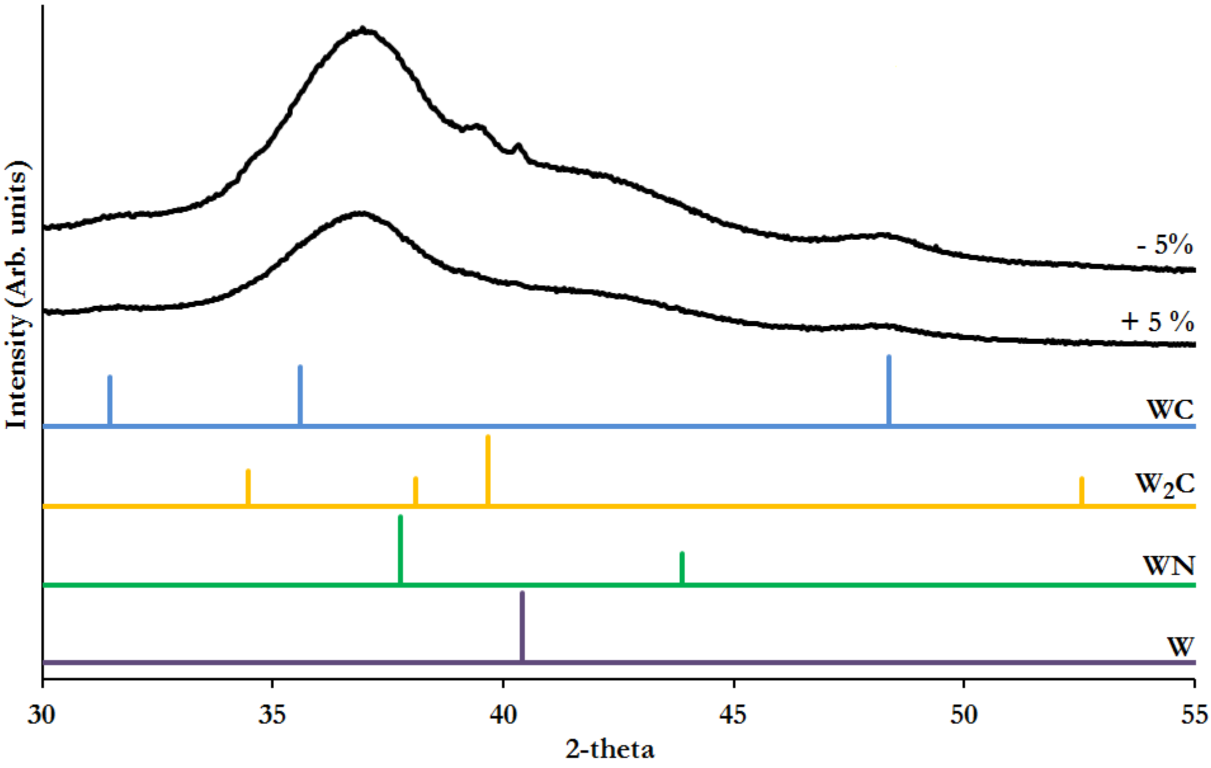

Figure 5.7 XRD patterns for samples synthesised from a urea/agar/WCl_6 sol-gel method at 850 °C (5 °C min^{-1}) for 240 minutes under flowing nitrogen

Finally the hold times for the furnace were varied. As the hold time increases it mean there is more time for the phases to change from the nitride to the carbide possibly through several mixed phases, although this cannot be shown with the current data. The XRD patterns in Figure 5.8 seem to show that WN is converted to a mixture of WC and W_2C and as the hold time is increased W_2C becomes the predominant phase, this seems to indicate that this is the more stable phase at these temperatures.

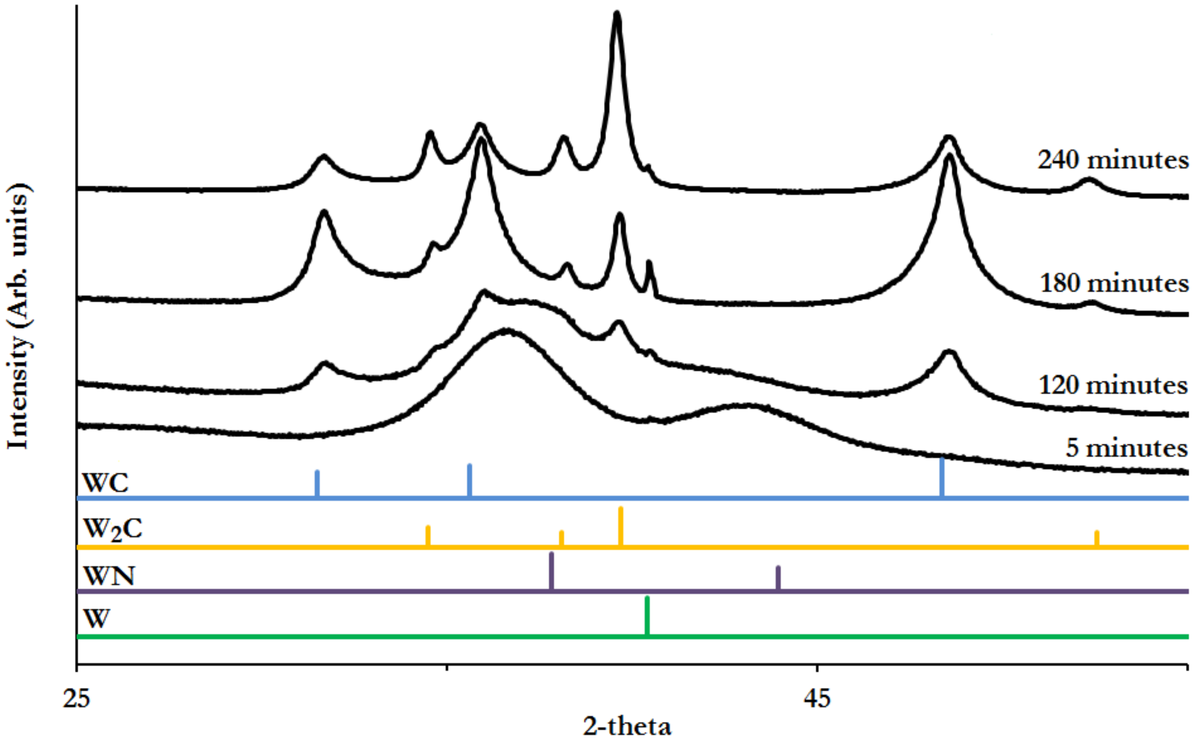

Figure 5.8 XRD patterns for samples synthesised from a urea WCl_6 sol-gel method at 850 °C (5 °C min^{-1}) under flowing nitrogen, the hold times were varied between 5 - 240 minutes

5.3.1 SYNTHESIS 2

For this synthesis method the tungsten source was changed to be water soluble so that the metal ions could bind easily to the aqueous biopolymers. A 'phase map' was made using gelatin as the biopolymer source, these samples were calcined at 900 °C as this showed the most promise of producing tungsten carbide from the urea methodology. Also the tungsten to carbon source (i.e. biopolymer) ratio was varied as the urea method showed that this ratio had an effect of the material formed; three ratios were used 0.001, 0.005 and 0.01 M total molar concentration of metal to a constant 20 g of a 10% (w/v) solution of the biopolymer. To get an overview of this system both hold time (5, 60 and 240 minutes) and ramp rates (1, 5 and 10 °C min^{-1}) were varied. The structure of gelatin can vary depending on its source and extraction method so before starting these experiments a number of gelatins were trialled to see if this would have an effect on the samples synthesised. From this experiment there are minimal differences in the XRD patterns, Figure 5.9. For all of the different types of gelatin, two broad peaks are seen in the XRD pattern which could be tungsten nitride or any of the other phases indicated in Figure 5.1, this shows that changing the gelatin source has minimal effect on the formation of the crystalline phases. Electron microscopy of these samples was not carried out but if tungsten carbide can be synthesised as a pure phase, then this experiment should be repeated to investigate if different gelatins provide different carbon structures around the carbide particles.

For the lowest concentration, 0.001 mol of tungsten per 20 g of gelatin solution 10% (w/v), the XRD patterns were similar for all heating programs Figure 5.10 shows an example of one of these samples and it is not possible to identify any phases from these XRD patterns. It could be the start of the tungsten nitride peaks, but it could also be a mixture of amorphous phases due to the low metal content.

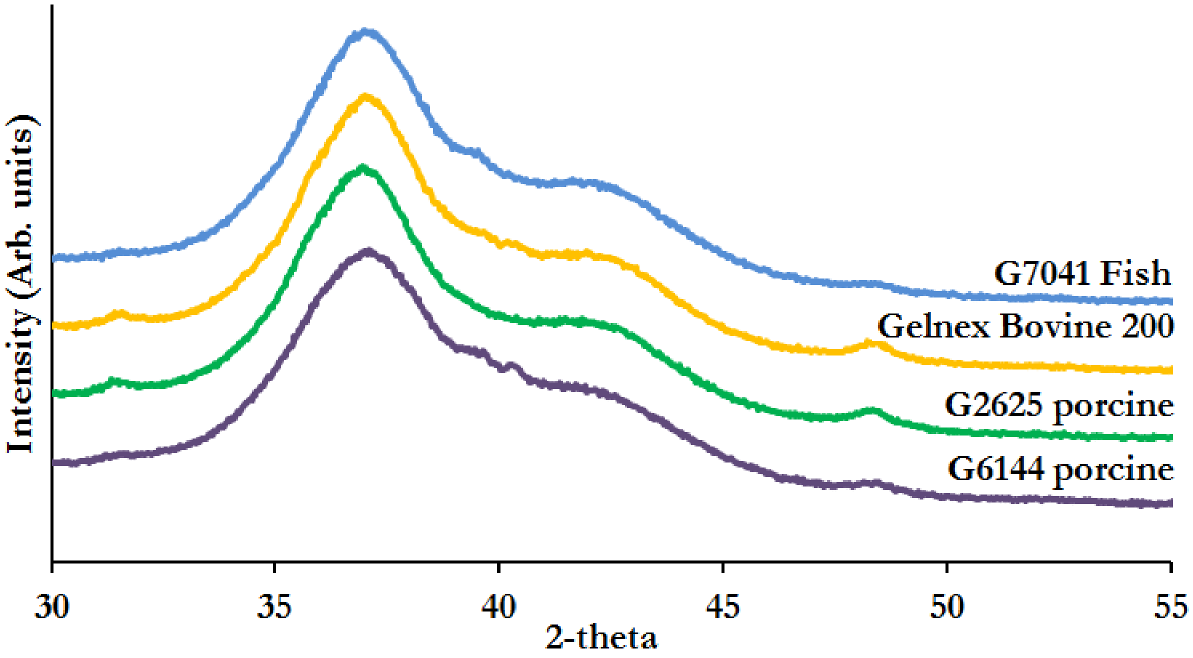

Figure 5.9 XRD patterns comparing the effect of different type of gelatin on the crystalline phases samples prepared at 850 °C (5 °C min^{-1}) for 240 minutes under flowing nitrogen. Code starting 'G' refers to the code from Sigma Aldrich

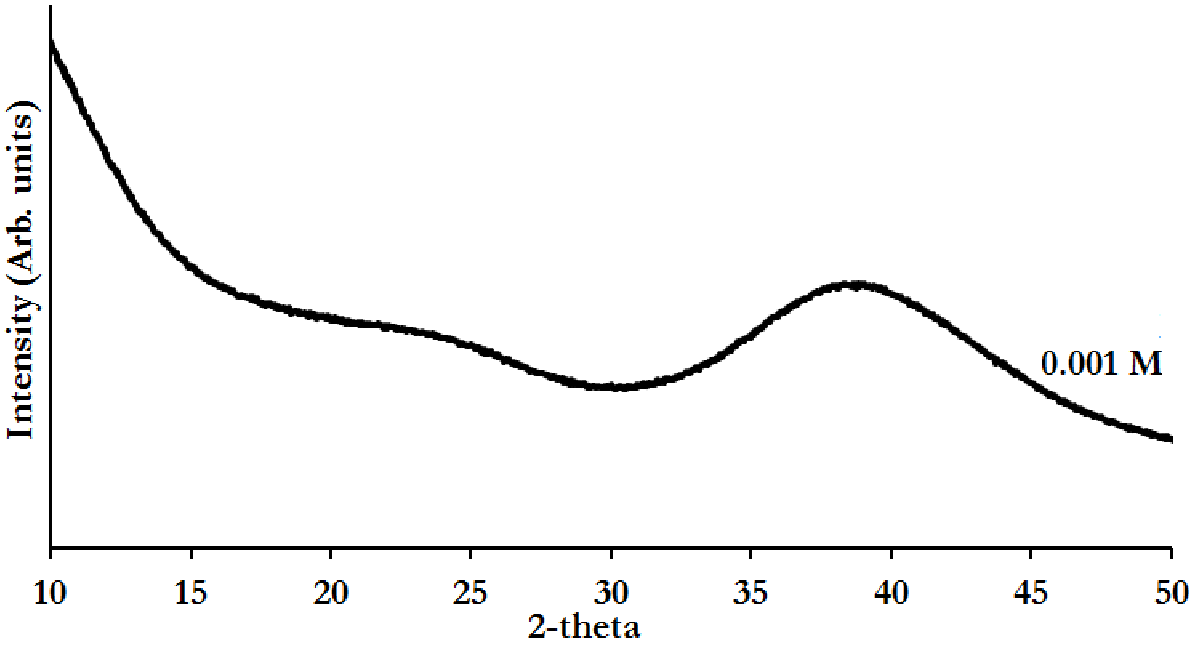

Figure 5.10 XRD pattern for a sample synthesised using 0.001 mol of tungsten per 20 g of gelatin solution 10% (w/v) synthesised at 900 °C (5 °C min^{-1}) for 240 minutes under flowing nitrogen

Table 5.7 showing the phases identified in the XRD patterns for samples synthesised using 0.005 mol of tungsten per 20 g of gelatin solution 10% (w/v) at 900 °C under flowing nitrogen

Ramp rate / Hold time	1 °C min^{-1}	5 °C min^{-1}	10 °C min^{-1}
5 minutes	WN	WN	WN
60 minutes	WN	WN	WN / WC
240 minutes	WN	WN	W / WN / WO_2

Table 5.8 showing the phases indentified in the XRD patterns for samples synthesised using 0.01 mol of tungsten per 20 g of gelatin solution 10% (w/v) at 900 °C under flowing nitrogen

Ramp rate / Hold time	1 °C min^{-1}	5 °C min^{-1}	10 °C min^{-1}
5 minutes	WN/WC/W_2C	WN/WC/W_2C/W	WN/W_2C
60 minutes	WN/WC/W_2C/W	WN/WC/W_2C/WO_3	W/WC/W_2C/WO_2
240 minutes	W/WC	W/WC/WO_3	W/WC/WO_3

The phases identified from the XRD patterns of the other two concentrations, 0.005 and 0.01 mol of tungsten per 20 g of gelatin solution 10% (w/v), are summarised in Tables 5.7 and 5.8, all of the XRD patterns can be found in the appendix, Figures D42 - D61, however some of these are duplicated in the text below to compare specific examples. The main phase seen in the XRD patterns for samples synthesised using 0.005 M of tungsten per 20 g of gelatin solution 10% (w/v) are possibly tungsten nitride but again due the broadness of the peak it is difficult to accurately determine this, Figure 5.11. The peak broadening suggests that the crystallites are nanoparticulate and this can be estimated by the Scherrer equation as shown in the appendix, Figures D62 and D63, as approximately 25 nm for each sample. This concentration also has trends that follow ramp rates and hold times. In line with the previous data longer hold time and slower ramp rates (i.e. longer reaction times) the XRD patterns start to show evidence of the tungsten carbides as well as the 2 broad peaks.

The highest concentrations are also susceptible to changes in the heating rate. Figure 5.12, shows an example of this. These samples were held at the maximum temperature for 5 minutes with varying heating rates this was to ensure that the final maximum temperature was the same before the furnace started to cool. In addition to the two broad peaks in these XRD patterns there appears to be smaller peaks that could correspond to WC, W_2C and W. This indicates that longer synthesis times are need with the biopolymer sol-gel route.

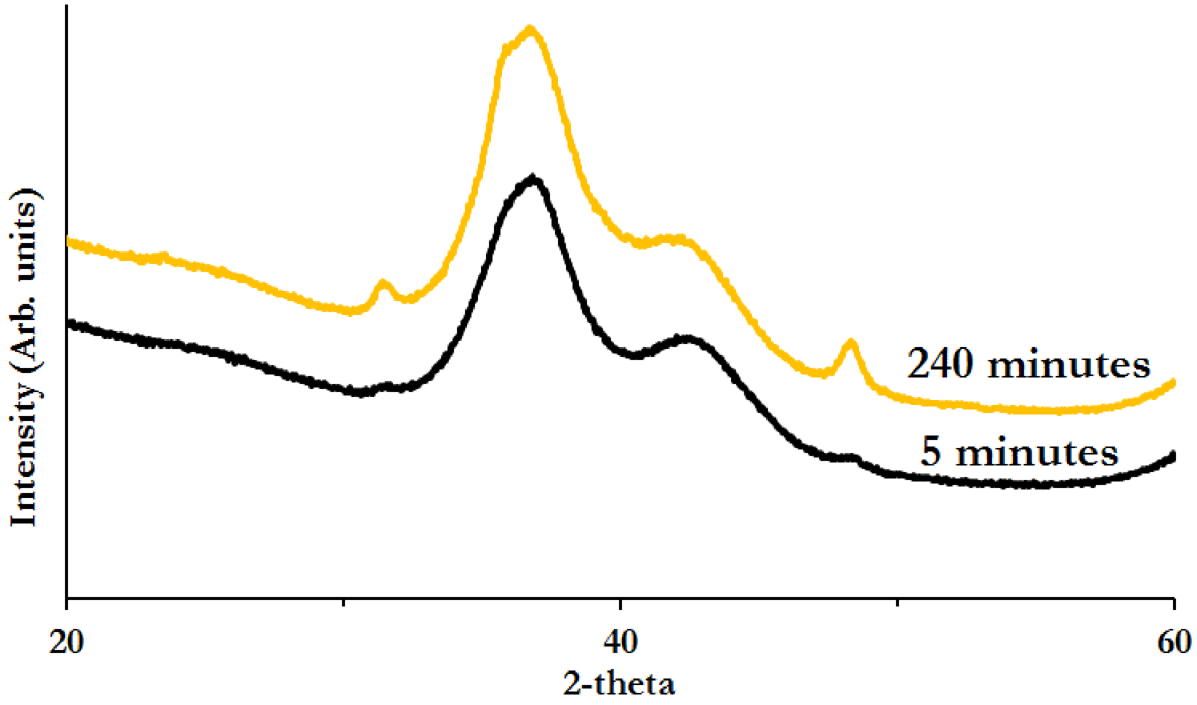

Figure 5.11 XRD patterns comparing the same concentration of W with varying hold times calcined at 900 °C (5 °C min^{-1}) under flowing nitrogen

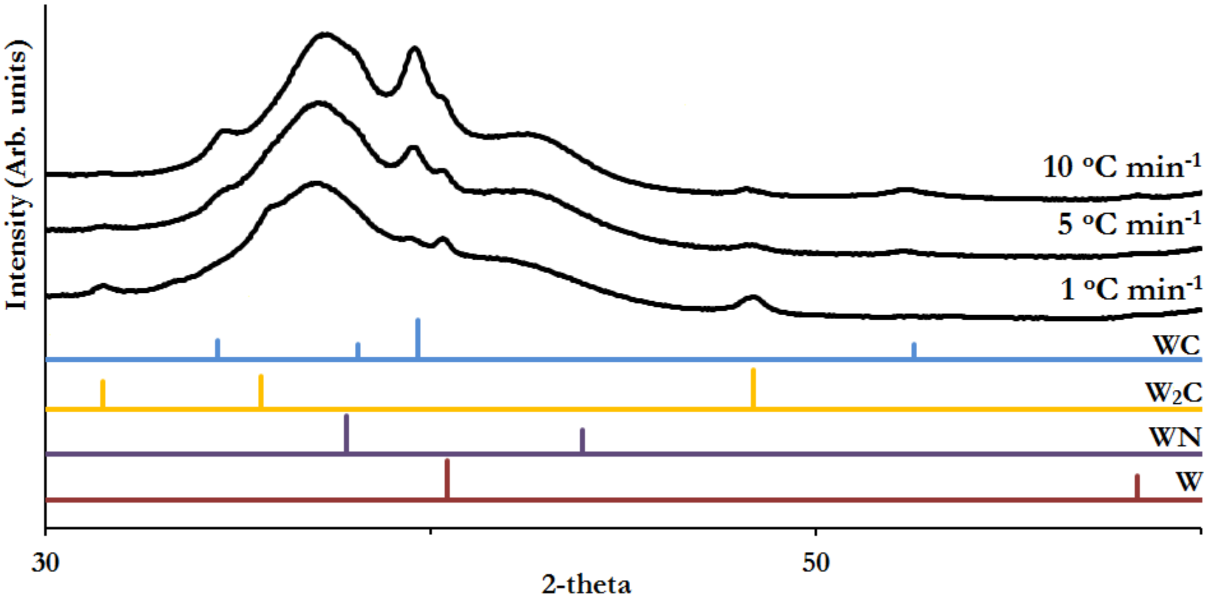

Figure 5.12 XRD patterns comparing heating rates of agar and tungsten samples calcined at 900 °C under flowing nitrogen with a 5 minute hold time to ensure 900 °C was reach for all samples before cooling started.

Increasing the hold times at 900 °C had the effect of increasing the number of phases present and also the XRD peaks are sharper, indicating sintering to form larger particles. Longer hold times, especially when combined with slower heating rates results in more W being formed but also WO_3, Figure 5.13. The reason for the formation of WO_3 at longer hold times is unknown but could be from the tungsten precursor reacting with oxygen in the residue left behind from the decomposition of the biopolymer to form the oxide, and this oxide having enhanced stability over the nitride/ carbide. That is unlikely as there was evidence that tungsten oxide forms and is converted into nitride.

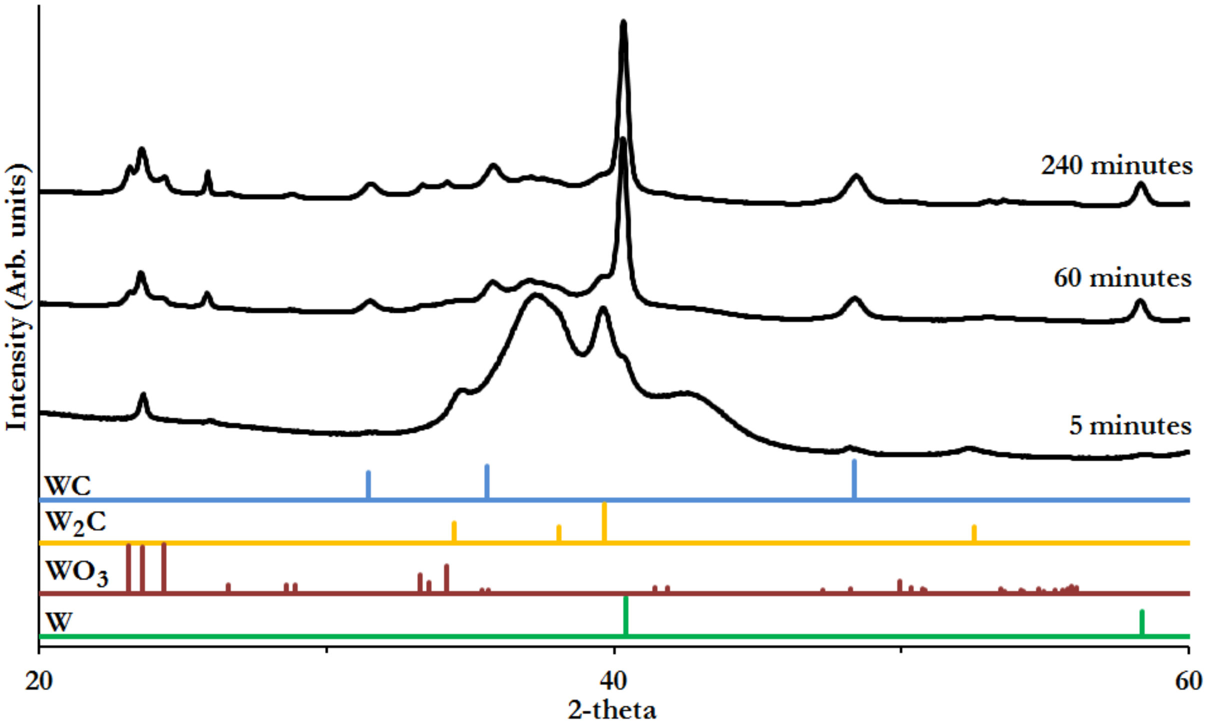

Figure 5.13 XRD patterns of gelatin plus 0.01M W heated to 900 °C (5 °C min^{-1}) for varying hold times under flowing nitrogen

The main results from the above are that tungsten nitride seems to be the preferred product, at least initially, however it is possible to synthesise tungsten carbide with a biopolymer sol-gel method. There is a lot of nitrogen in this synthesis, it is in the atmosphere, in the biopolymer and the tungsten precursor, reducing this/increasing the carbon content should help to produce the carbide. This is different from the urea synthesis where having more nitrogen is a benefit. In the urea system, urea decomposes into nitrogen compounds and these burn off to leave carbon behind so by having more nitrogen, more carbon is left behind. For the biopolymer synthesis CO_x compounds are burnt off first leaving behind a nitrogen enriched residue as most of the nitrogen is part of the gelatin backbone; this is compared to the urea route which binds through the carbonyl group and the nitrogen compounds burn off first. Therefore a nitrogen free biopolymer substitute was used to determine if this would help the synthesis of tungsten carbide.

A range of agar plus ammonium metatungstate samples were produced in a similar fashion to the gelatin matrix shown above. The hold times of 5 and 60 minutes at ramp rates of 5 and 10 °C min^{-1} were chosen for this experiment. The lowest concentration and heating rate as well as the longest hold time were omitted from this experiment because they either did not form an identifiable phase or ran the risk of producing WO_3. Figure 5.14 shows XRD patterns with much sharper peaks indicating larger crystallites, these patterns also show only W_2C and W. This seems to support the hypothesis that there was too much nitrogen in the reaction mixture/ not enough carbon. Secondly is the sharper peaks may indicate the agar is not as thermally stable as gelatin, meaning it loses its structure at lower temperatures and allows sintering to occur more readily. Figure 5.14 also shows that the slower heating rate increases the amount of W_2C formed relative to W, this suggests the W_2C is forming from metallic tungsten by diffusion of carbon into the matrix. Decreasing the concentration of metal shows increased formation of tungsten nitride and W_2C relative to tungsten, Figure 5.15.

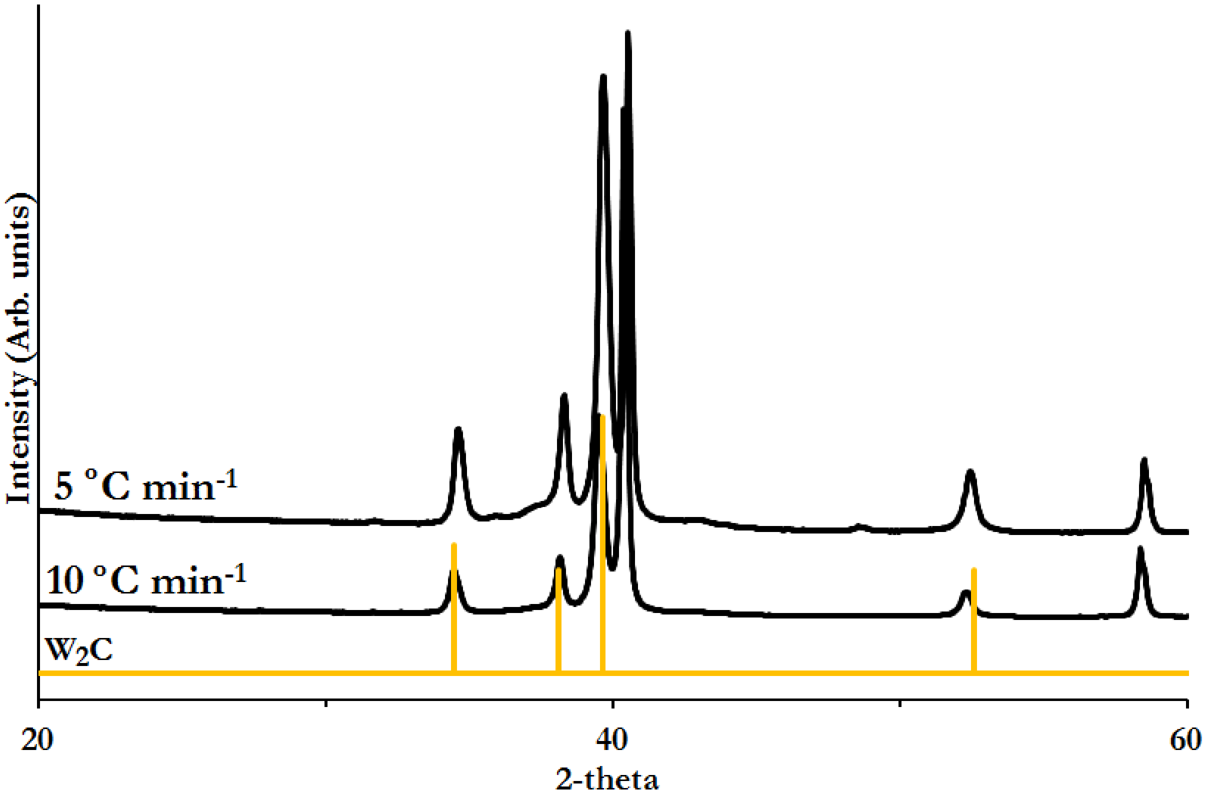

Figure 5.14 XRD patterns comparing heating rates for agar plus tungsten samples synthesised under flowing nitrogen and 900 °C for 240 minutes. Un-marked peak is tungsten

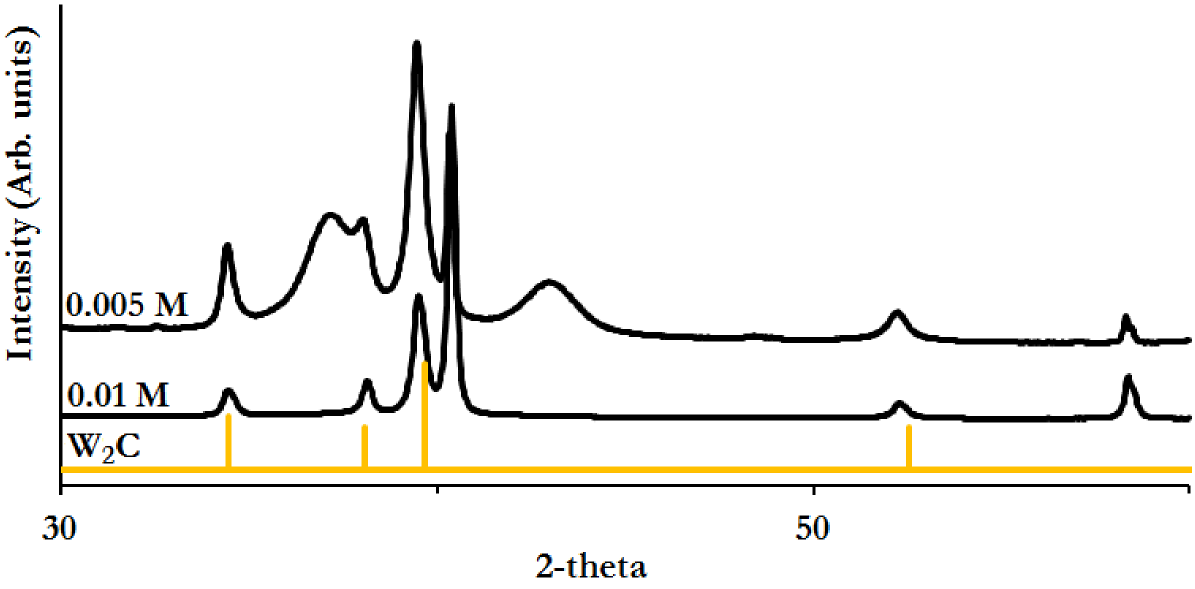

Figure 5.15 XRD patterns comparing concentration effects for agar plus tungsten W synthesised under flowing nitrogen and 900 °C (5 °C min^{-1}) for 240 minutes. Sharper peak at ~41 ° is W. The broad peaks are unidentified.

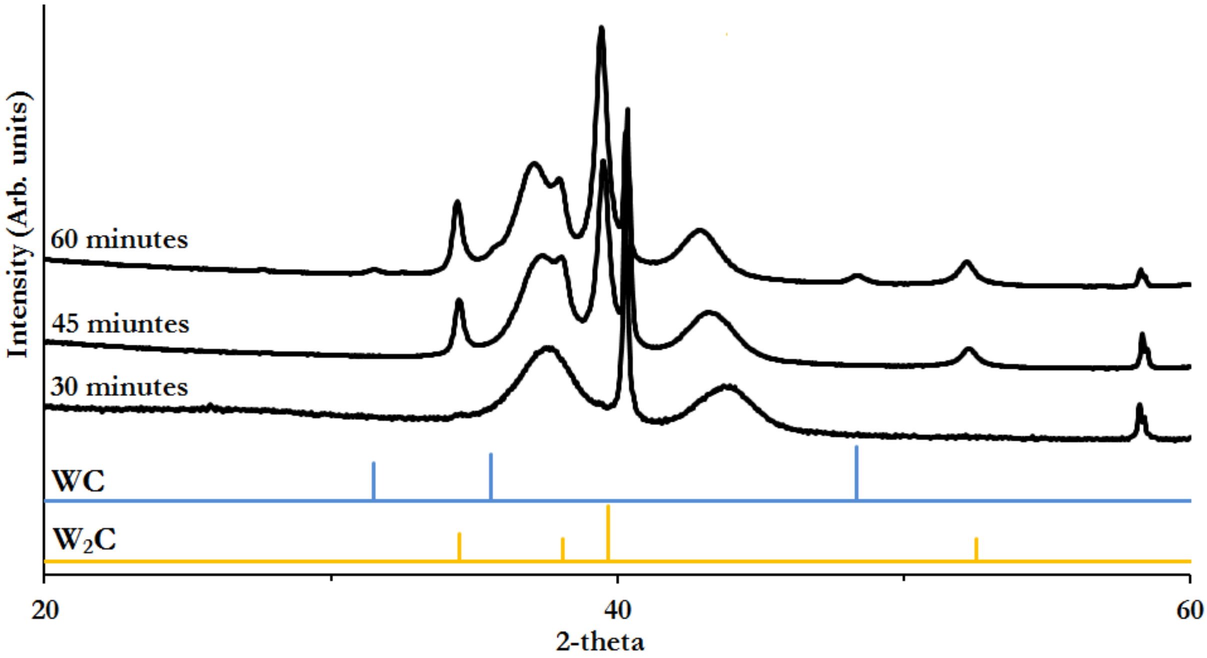

Figure 5.16 XRD patterns comparing the effect of hold time on agar plus tungsten samples at 900 °C (5 °C min^{-1}) under flowing nitrogen

Increasing the hold time has the same effect as described for the gelatin synthesis; Figure 5.16 shows XRD patterns with increasing holding time at 900 °C; the amount of W_2C seems to increase.

Another strategy for reducing the amount of nitrogen in the synthesis was to replace the nitrogen atmosphere with argon. The XRD of these samples, Figure 5.17, showed the main phase was still WN although some of the faster ramp rates also showed peaks that could be from WC and W_2C. However this was not a significant improvement to the final product, meaning that the nitrogen atmosphere is probably not the source of the nitrogen in WN; so nitrogen gas was used for future experiments as it is more earth abundant and cheaper.

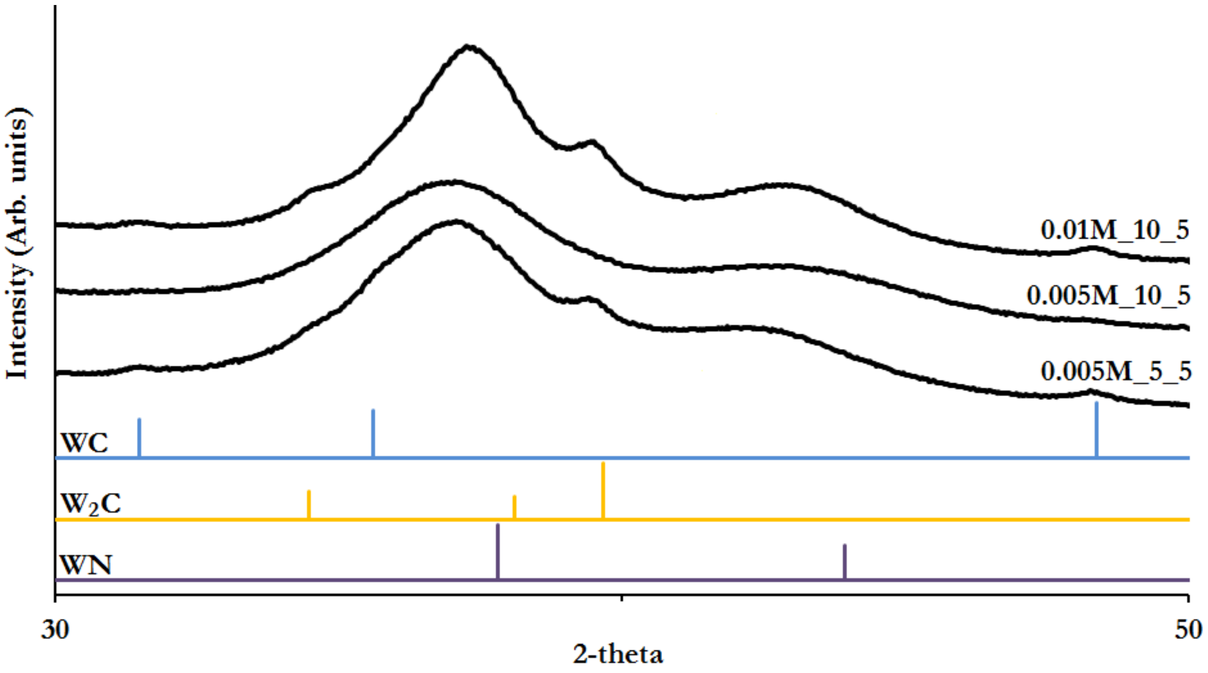

Figure 5.17 XRD patterns comparing heating concentrations and heating ramps to 900 °C (5 °C min^{-1}) under flowing argon

During a research trip to the National Institute for Materials Science in Japan it was possible to attempt this synthesis under a vacuum. Tungsten carbide has been synthesised under vacuum by chemical vapour condensation,[163] this is obviously a very different type of synthesis but it was thought that if the sample was calcined from these precursors under vacuum then any gases released would be drawn away before reacting with the tungsten/carbon. These samples were heated at 10 °C min^{-1} to 900 °C for 60 minutes at 2 different concentrations (0.005 and 0.01 M of tungsten). In these experiments both samples produced a mixture of phases including WC, W_2C and WN, Figure 5.18. Both these samples have a greater peak intensity for the carbide than the samples prepared under nitrogen meaning a vacuum may help the formation of the carbide. However the reason for this is unknown and as these are the only two samples prepared this way, further work would be needed to investigate this, however this is not an environmentally favourable synthesis route so no additional work was carried out. This test did provide insight to tungsten nitride formation, however, as there was no nitrogen in the biopolymer or the atmosphere the only source of nitrogen could have been from the tungsten salt (ammonium metatungstate). Ammonium metatungstate was continued to be used as there are no water alternatives and most biopolymer are not soluble in ethanol; another problem with ethanol as a solvent is that is it not as 'green' as water so this is the preferred solvent.

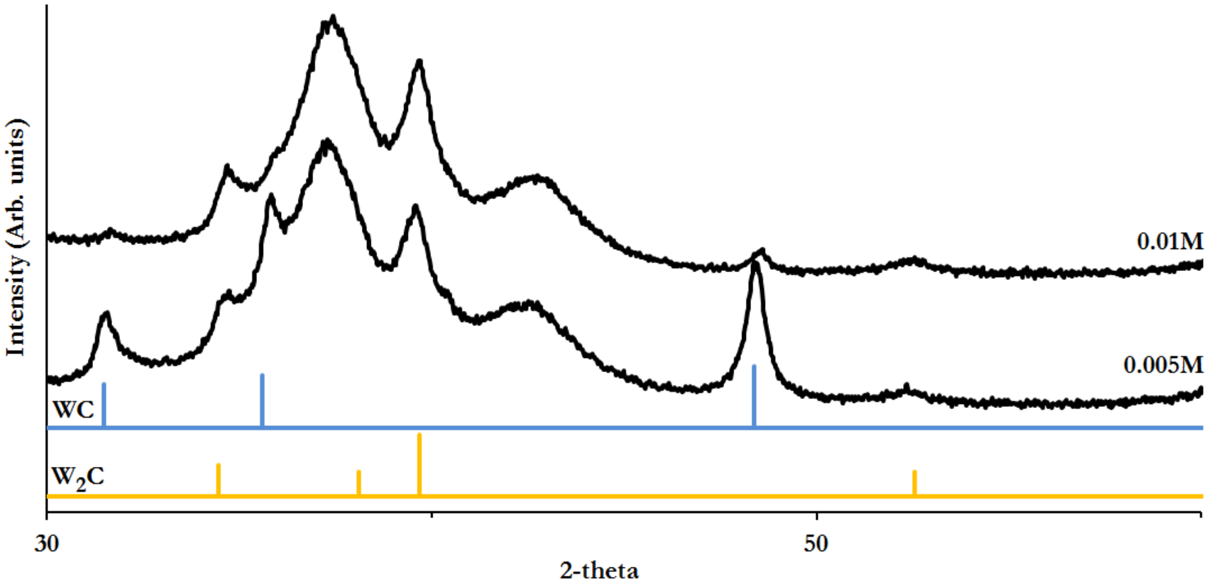

Figure 5.18 XRD patterns of agar plus tungsten samples synthesised in a vacuum at 900 °C (10 °C min^{-1}) with a 60 minute hold time

Agar plus ammonium metatungstate does not form a foam, unlike the gelatin system, this may mean there is no porous carbon to support the tungsten containing particles. In the mechanism chapter nitric acid was added to samples to cause them to foam so an experiment was carried out on agar plus ammonium metatungstate samples with nitric acid. These samples did foam slightly on drying and Figure 5.19 shows the XRD patterns of these samples. In additional to the creation of a foam the nitric acid also had another effect, it changed the phases that were isolated. Small volumes of nitric acid promoted the formation of WC and suppress metallic tungsten whilst moderate and high volumes of nitric acid suppressed formation of W_2C/WC and metallic tungsten was the main phase. This could be due the acid attacking the biopolymers structure helping to release the carbon to react with the tungsten; however too much acid causes the biopolymer to burn off too quickly and that is why more tungsten metal is seen. This maybe a good way of fine tuning the purity of samples but however this is not a good way of increasing the porosity of the carbon for agar as it is has too much of an effect on the inorganic phases.

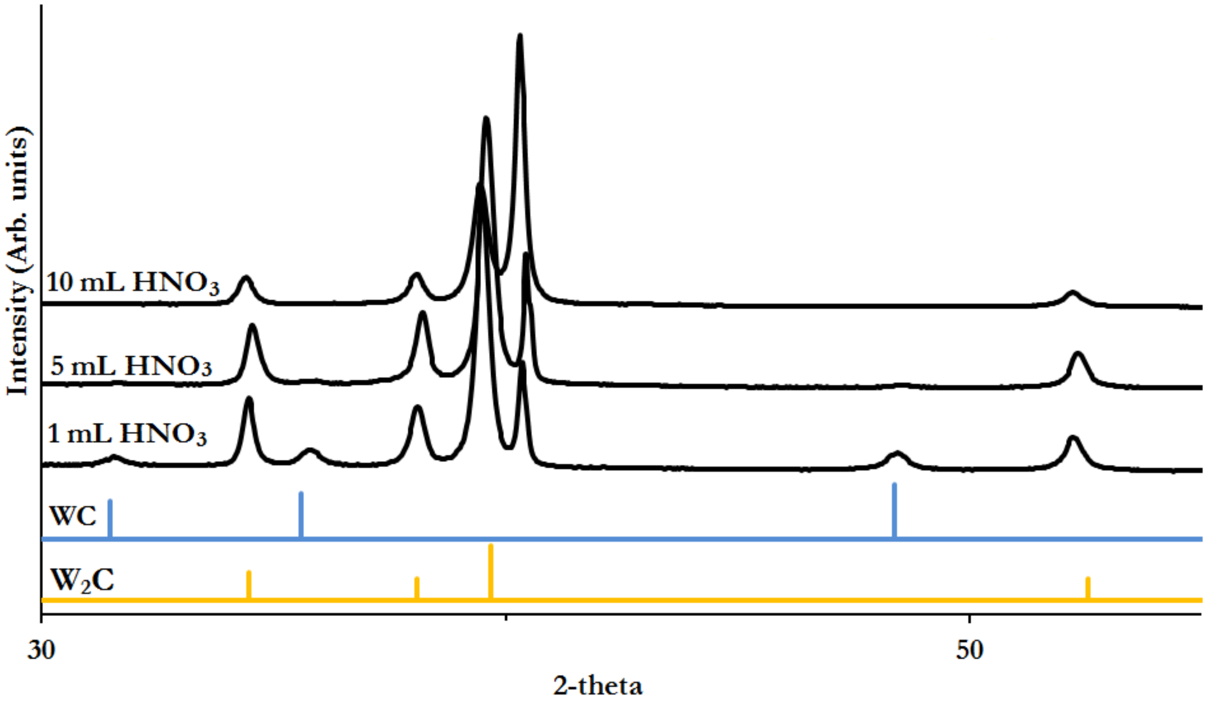

Figure 5.19 XRD patterns comparing the effect of nitric acid on agar plus tungsten samples calcined at 900 °C (5 °C min^{-1}) under flowing nitrogen

The final experiment that was carried out was to vary the amount of biopolymer used for sample preparation. This is similar to varying the molar concentration of the metal precursor however but due to the large molecular weights of the biopolymers any change should be more noticeable. Also, metallic tungsten was seen in a number of samples and this could be due to there being excess metal ions in solution after metal binding has occurred. Figure 5.20 shows XRD patterns of samples prepared from 3.5 and 2 g of dextran (MW 25, 000) calcined at 850 °C under flowing nitrogen. Increasing the mass of biopolymer used per sample has increased the amount of tungsten nitride and decreased the amount of tungsten; this implies that the metal ions have reacted with the additional biopolymer.

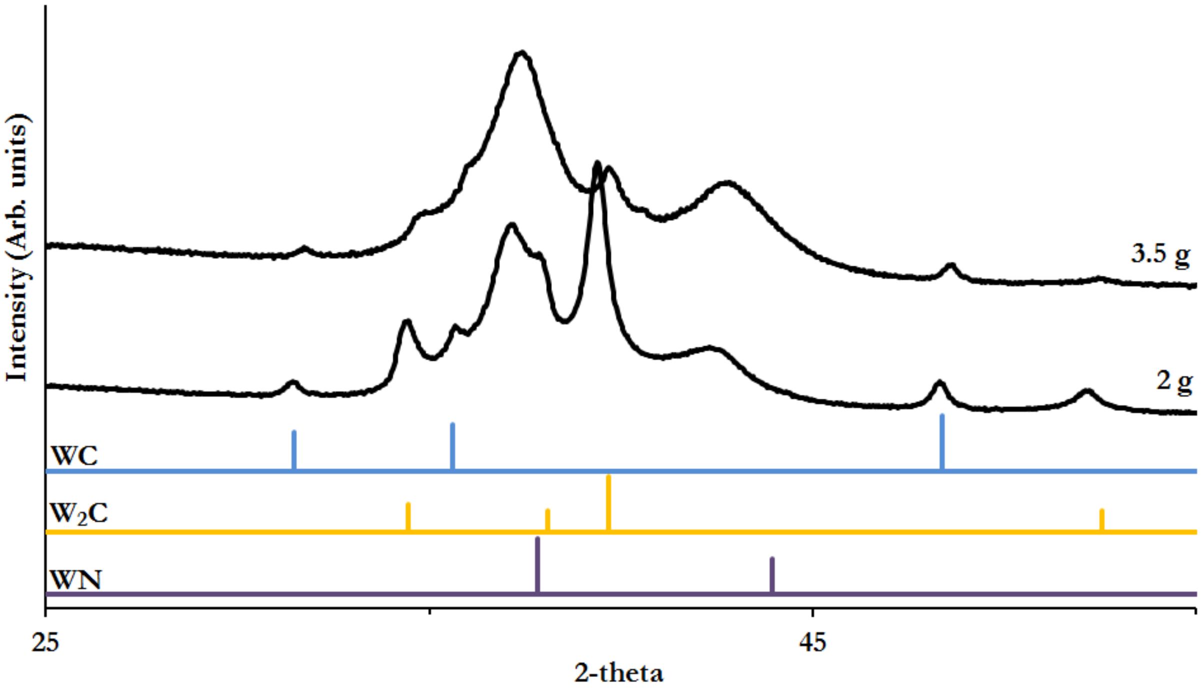

Figure 5.20 XRD patterns comparing increases in the mass of biopolymer used calcined at 900 °C (5 °C min^{-1}) for 240 minutes under flowing nitrogen

5.3.3 SYNTHESIS OF TUNSTEN CARBIDE/METAL OXIDE NANOCOMPOSITES FROM BIOPOLYMER GELS

It has been shown that biopolymer sol-gel synthesis can be used to produce nanocomposites of tungsten nitride, magnesium oxide and carbon.[65] This synthesis was carried out to investigate if it is possible to produce tungsten carbide in place of tungsten nitride. Gelatin was used initially so it could be compared to the previous gelatin work and several variables were tested including changing the atmosphere in the furnace and the biopolymer.

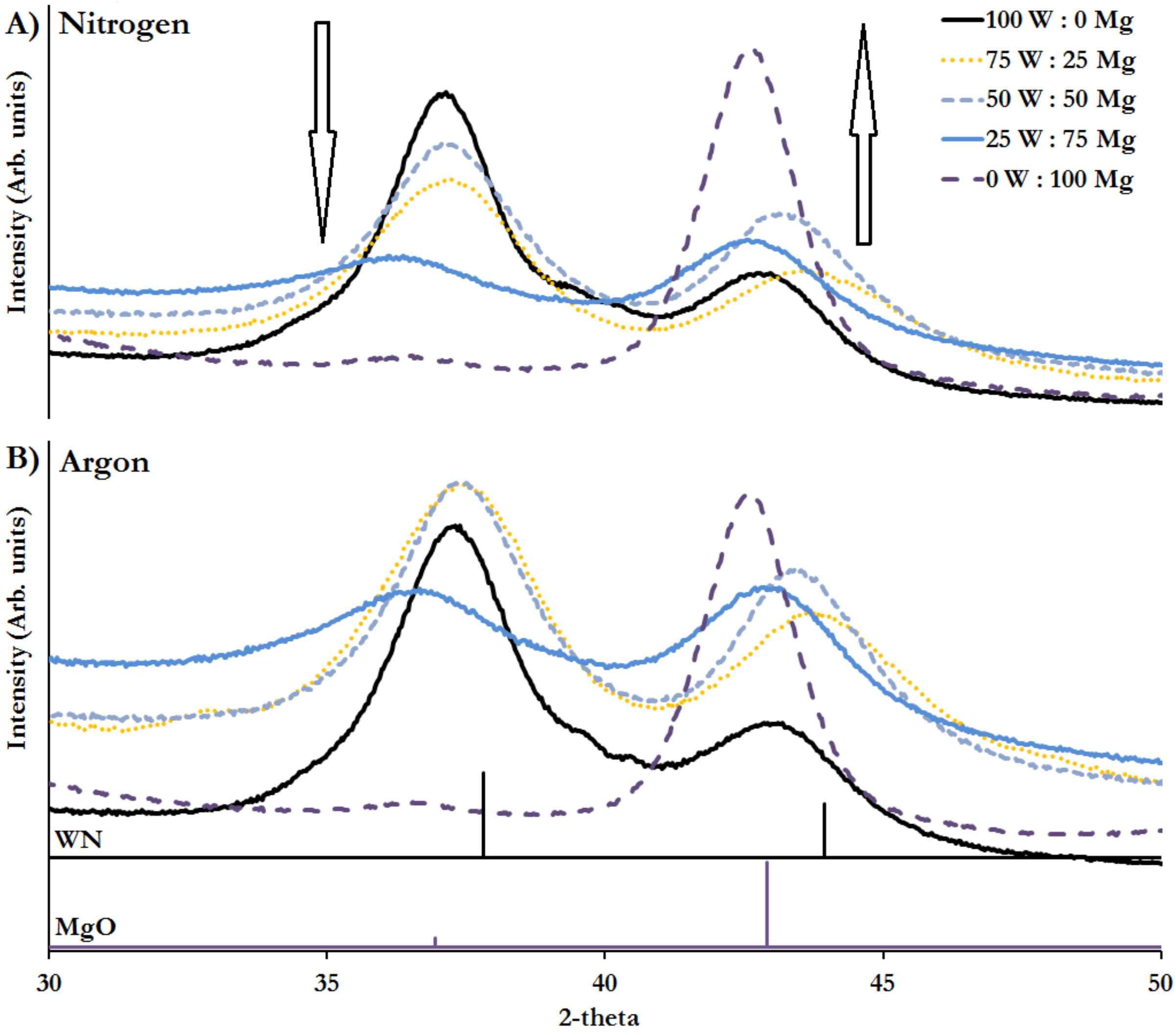

Figure 5.21 XRD patterns for a series of nanocomposites synthesised from gelatin plus ammonium metatungstate and magnesium nitrate synthesised; A) under flowing nitrogen; B) or flowing argon at 900 °C (5 °C min^{-1})

Figure 5.21 shows XRD patterns from a series of nanocomposites produced from gelatin ammonium metatungstate and magnesium nitrate where the initial concentration of metal ions was 0.01 mol of tungsten and magnesium per 20 g of gelatin solution 10% (w/v) in varying ratios. The XRD patterns show that all samples under both argon and nitrogen atmosphere form tungsten nitride (WN) and magnesium oxide (MgO, PDF #00-004-0329); this again indicates the atmosphere has very little effect on the reaction pathway. A restricted 2-theta range is shown for clarity as the main peaks for WN and MgO lie close to one another making it difficult to say what is happening. The highest intensity peak for each pattern is the 2-theta value of the lower intensity peak from the other pattern (i.e. the first peak is WN bigger than the second peak and the opposite is true for MgO) so the ratio of the two peaks can be used to provide information. For samples synthesised in a nitrogen atmosphere as the magnesium ratio increases, and tungsten ratio decreases, the peak intensity at a 2-theta of approximately 37 ° decrease showing that less WN is being formed. This change mirrors the other peak and the ratio change of the metals. The exception is the 50 W : 50 Mg sample which shows higher than expected intensities but this could be due to a synergy in the particle growth rate at this ratio but further study would be needed to ascertain this.

Samples synthesised under an argon atmosphere, Figure 5.21, show the same basic trend but in this series 75 % and 25 % W (i.e. 25 % and 75 % Mg) samples have similar XRD patterns especially for the first peak. This could indicate tungsten nitride formation is enhanced compared to magnesium oxide under argon but this is inconclusive. Tungsten carbide was not isolated in these samples but there are small shoulders on the first peak (~37 °), at these 2-theta values WC and W_2C have peaks. Whilst these phases are clearly not in this XRD these shoulders hint that samples synthesised at conditions close to this may yield the carbide.

XRD patterns of samples produced from agar and the same metal salt as before showed many peaks, Figure 5.22A and Appendix D63 and D64, for all W:Mg ratios with the exception 100% Mg. Due to the number of peaks and mixture of phases it is not possible to correctly identify all the peaks but part of the mixture is tungsten oxide and mixed tungsten/ magnesium oxides. 100 molar% Mg sample, Figure 5.22B, produced pure MgO. Agar did not produce tungsten carbide however other biopolymers should be screened to test if they can as the agar system shows changing the biopolymer has a big effect on tungsten phases.

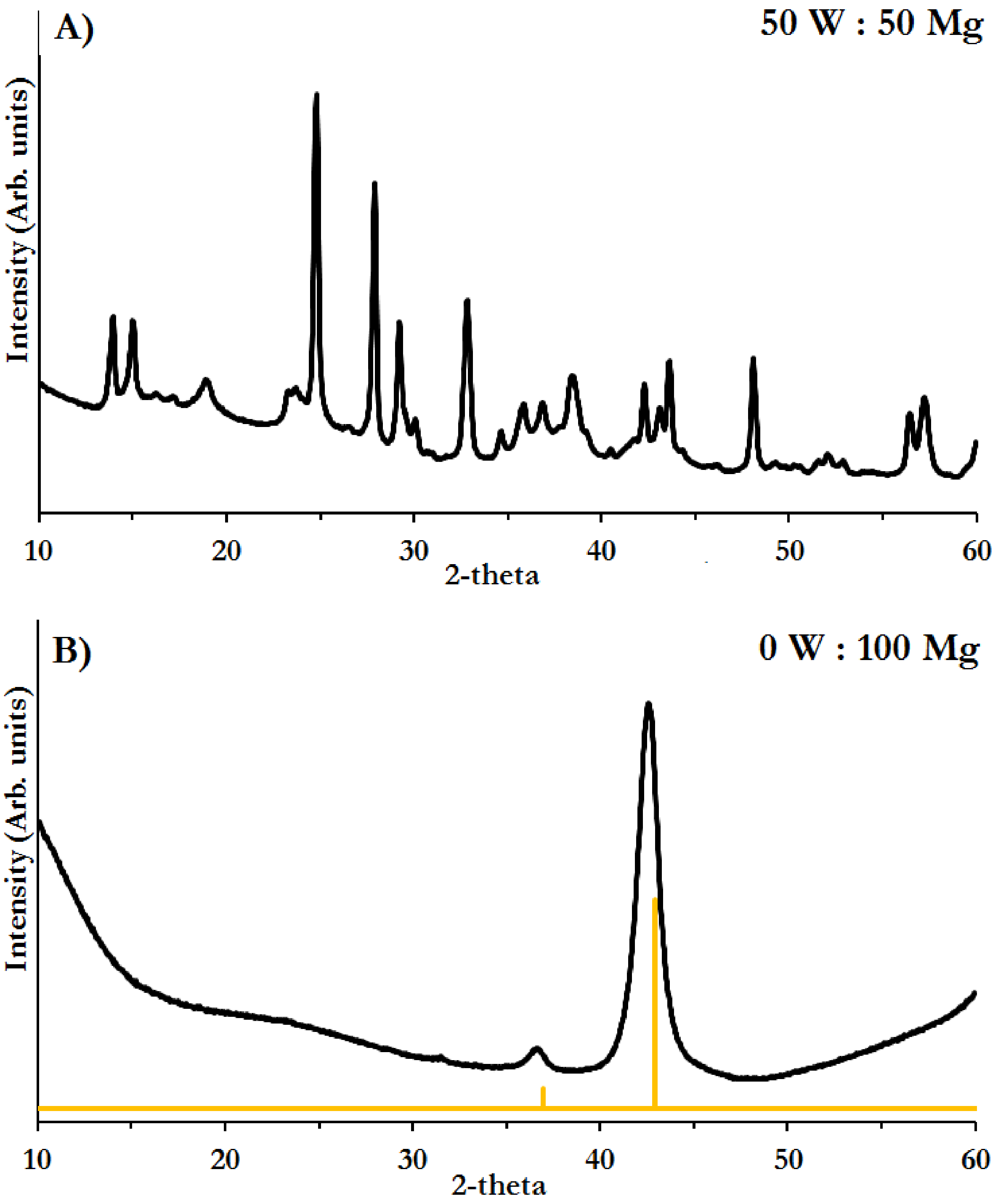

Figure 5.22 XRD patterns nanocomposites synthesis from agar plus A) ammonium metatungstate and magnesium nitrate; B) magnesium nitrate under flowing nitrogen at 900 °C (5 °C min^{-1})

5.4 CONCLUDING REMARKS

In this chapter the synthesis of WC/C and W_2C/C nanocomposites has been attempted via several methods. Both the urea and biopolymer systems have been explored and the areas in which tungsten carbide maybe isolated as a single phase have been identified.

For the urea synthesis the importance of high urea to tungsten ratios and high temperatures for tungsten carbide has been demonstrated. The high ratios means there is enough carbon left behind to convert the tungsten nitride to tungsten carbide after all of the nitrogen containing compounds are burnt off. It has also been shown that the particle size can be controlled but the introduction of small amounts of biopolymer.

In the biopolymer synthesis a simple water based sol-gel method was used to produce tungsten nitride and tungsten carbide. This has proven difficult and the phase pure tungsten carbide has not been achieved; however the fact this synthesis method does produce the carbide is a positive result for the field of carbide/nitride synthesis. Through these experiments it was discovered that control over the synthesis temperature and nitrogen concentration is important; too hot or too much nitrogen and the carbide cannot be isolated. Further work should be carried out to further investigate different biopolymers at different temperatures to fine tune this aspect. Creating a homogeneous inert atmosphere is also important as any oxygen in the atmosphere will cause the formation of the oxide during long synthesis times; however whether argon or nitrogen is used has minimal effect on the synthesis. The ratio of biopolymer to metal precursor needs to be fine-tuned to stop the formation of tungsten metal.

Finally, tungsten/magnesium nanocomposites were synthesised from agar and gelatin. The gelatin samples produced MgO/WN composites whilst the agar samples produced a mixture of tungsten and tungsten/magnesium mixed phases. Once tungsten carbide can be synthesised by the gelatin sol-gel methodology it should be repeated with this synthesis combined with BET/SEM to investigate the surface area and topology.

In line with previous literature, this preliminary study has synthesised WC at 900 °C and it was also seen in mixed phase samples at lower temperatures; further work should be done with optimising the reaction mixture to investigate if it could be isolated as a single phase at lower temperatures. The particle size is approximately 25 nm for some samples, once more work has been carried out on the reaction mixtures the thermal treatments can be optimised to control particle size; currently these particles are larger than what currently exists in the literature. The main benefits of this synthesis route are the choice of earth abundant precursors and the one pot 'low' temperature synthesis, all work should focus on this to maximise this advantage over other techniques.

Further work should also include electrochemical testing (hydrogen evolution reaction) once the carbide can be isolated as a single phase.

5.5 REFERENCE

(148) Toth, L. E. *Transition metal carbides and nitrides*; Academic Press, 1971.

(149) Pejryd, L.; Wigren, J.; Greving, D. J.; Shadley, J. R.; Rybicki, E. F. *Journal of Thermal Spray Technology* **1995**, *4*, 268.

(150) Kiani, S.; Yang, J. M.; Kodambaka, S. *Journal of the American Ceramic Society* **2015**, *98*, 2313.

(151) Fischer, U. K. R.; Hartzell, E. T.; Akerman, J. G. H.; Google Patents: 4743515 A: 1988.

(152) Jindal, P. C.; Santhanam, A. T.; Schleinkofer, U.; Shuster, A. F. *International Journal of Refractory Metals and Hard Materials* **1999**, *17*, 163.

(153) Chan, L.; Google Patents: 5870121 A: Ti/titanium nitride and ti/tungsten nitride thin film resistors for thermal ink jet technology, 1999.

(154) Ahmadi, T. S.; Wang, Z. L.; Green, T. C.; Henglein, A.; El-Sayed, M. A. *Science* **1996**, *272*, 1924.

(155) Wang, C.; Daimon, H.; Onodera, T.; Koda, T.; Sun, S. *Angewandte Chemie International Edition* **2008**, *47*, 3588.

(156) Navaee, A.; Salimi, A.; Soltanian, S.; Servati, P. *Journal of Power Sources* **2015**, *277*, 268.

(157) Levy, R.; Boudart, M. *Science* **1973**, *181*, 547.

(158) Giordano, C.; Erpen, C.; Yao, W.; Antonietti, M. *Nano letters* **2008**, *8*, 4659.

(159) Giordano, C.; Erpen, C.; Yao, W.; Milke, B.; Antonietti, M. *Chemistry of Materials* **2009**, *21*, 5136.

(160) USGS Commodity Statistics and Information Vol. 2015.

(161) Weidman, M. C.; Esposito, D. V.; Hsu, I. J.; Chen, J. G. *Journal of the Electrochemical Society* **2010**, *157*, F179.

(162) Ryu, J.; Choi, W. *Environmental Science & Technology* **2008**, *42*, 294.

(163) Kim, J. C.; Kim, B. K. *Scripta Materialia* **2004**, *50*, 969.

(164) Sherif, F.; Vreugdenhil, W.; Oyama, S. *Blackie Academic & Professional, New York* **1996**, 414.

(165) Guo, J.; Mao, Z.; Yan, X.; Su, R.; Guan, P.; Xu, B.; Zhang, X.; Qin, G.; Pennycook, S. J. *Nano Energy* **2016**, *28*, 261.

(166) Vallance, S. R.; Kitchen, H. J.; Ritter, C.; Kingman, S.; Dimitrakis, G.; Gregory, D. H. *Green Chemistry* **2012**, *14*, 2184.

(167) Pol, S. V.; Pol, V. G.; Gedanken, A. *Advanced Materials* **2006**, *18*, 2023.

(168) Hunt, S. T.; Nimmanwudipong, T.; Román ‐ Leshkov, Y. *Angewandte Chemie International Edition* **2014**, *53*, 5131.

(169) Chen, W. F.; Schneider, J. M.; Sasaki, K.; Wang, C. H.; Schneider, J.; Iyer, S.; Iyer, S.; Zhu, Y.; Muckerman, J. T.; Fujita, E. *ChemSusChem* **2014**, *7*, 2414.

(170) Wang, S.; Yu, X.; Lin, Z.; Zhang, R.; He, D.; Qin, J.; Zhu, J.; Han, J.; Wang, L.; Mao, H.-k. *Chemistry of Materials* **2012**, *24*, 3023.

(171) Ko, A.-R.; Han, S.-B.; Lee, Y.-W.; Park, K.-W. *Physical Chemistry Chemical Physics* **2011**, *13*, 12705.

(172) Kafizas, A.; Carmalt, C. J.; Parkin, I. P. *Coordination Chemistry Reviews* **2013**, *257*, 2073.

(173) Lee, C. W.; Kim, Y. T.; Min, S. K. *Applied physics letters* **1993**, *62*, 3312.

(174) Podsiadło, S. *Thermochimica acta* **1995**, *256*, 367.

(175) Zhong, Y.; Xia, X.; Shi, F.; Zhan, J.; Tu, J.; Fan, H. J. *Advanced Science* **2016**, 1.

CHAPTER 6

CONCLUDING REMARKS

This thesis has detailed a brief history of the 'sol-gel' technique and how it has evolved to incorporate biopolymers with their vast array of chemical and structural properties.

Chapter 2 focussed on gelatin plus metal nitrate foaming reaction. It was found that the foaming is caused by gelatin stabilising bubbles in the resin as the final evaporation of water occurred. Nitrate ions that attack the gelatin as the solution concentrates affects the ability of the biopolymer to stabilise these bubbles, changing the final pore structure. This also works in conjunction with low pH and low temperatures to radically change that pore structure. As a result the system is more flexible and more able to stabilise the bubbles. In this area further work should include using the BJH theorem, FID SEM or tomography to invest the pore structure throughout the pore carbon and confirm its usefulness as a catalyst/ filter.

From various experiments, especially SANS, it was proposed that the introduction of the metal ions change conventional triple-helical junction zones of gelatin to a network crosslinked by M^+ ions. These data combined with visual observations confirms this and has been demonstrated with combinations of metals. The cloudy precipitates/ rubbery solids are an example of the Hofmeister effect, where both the iron and magnesium ions combine in such a way to ‘salt out’ gelatin. Further investigation of this effect should be carried out to reveal any trends as this could provide a control mechanism for design and synthesis before samples are synthesised, by using the viscoelastic properties. This could lead to particle and pores size being selected to allow a host of different catalytic activity being targeted in rapid succession. Further studies using these techniques and others (i.e. freeze drying samples) will allow a system to create truly designer carbon with nano particles of choice for a wide range of applications.

Chapter 3 took the mechanistic study a step further by adding another variable that could be used to control the final materials. This chapter detailed the preliminary work that used the energy and time savings of microwaves to make this reaction more green. A wide range of composites were synthesised, including metal oxide/carbide/carbon, metal carbide and metal oxides from biopolymers or biomass. Reliability, energy and scaling issues were detailed and, where possible, suggestions for improvements were made or discussed. A flow reactor was suggested as a possible way to combat the problems of overheat and scaling, it is thought this is a novel solution for high temperature microwave work.

Another area of research that should be investigated is the formation of meta-stable phases, for example this work highlights the formation of iron carbide proceeding through a different route than that observed in a furnace and a $FeN_{0.0324}$ intermediate phase is seen. It is possible that other meta-stable phases can be found with interesting properties. The samples produced during this study are not all pure products so future work should try to isolate these; this would be a simple task of varying parameters such as the metal to biopolymer precursor. Finally this simple method, with large energy and time savings, has shown promise in the synthesis of metal carbide composites and should expand microwave processing by exploiting the morphological diversity offered by a wide range of natural and synthetic precursors.

Chapter 4 detailed the first attempt to quantify the ability of these materials as catalysts A series of Cu/Zn on porous carbon catalysts were investigated by a variety of techniques to probe their activity, stability and structure and therefore suitability for MSR. The preliminary data shown here indicates that these samples have promise as effective MSR catalysts although this currently occurs at temperatures higher than used in the current literature, it is thought though this could be reduced through optimisation of the catalysis. Currently these samples may be useful for stationary applications but the reaction temperature must be reduced before these can be used in portable applications (i.e. cars).

The use of biopolymer in this facile sol-gel synthesis route makes this a very cheap synthesis and introduces the possibility to change the structure and activity greatly. The reason for this is probably due to the different structures of the biopolymer precursors being carried into the porous carbon in the final product, further work could look into this as understanding what lowers the activity may help to increase it.

It has been shown that the particle size is very small and further studies should include trying to change the size and investigate the effect on MSR activity. Scherrer analysis was used to estimate particle size and stability of the crystallites during the reaction, this seems to show good stability; samples should be cycled to see if they degrade further on subsequence uses.

Chapter 5 described the synthesis of WC/C and W_2C/C nanocomposites as well as possible WN phases. This work should be considered as preliminary and much more study is required to adequately describe this research, however due to the facile synthesis this should be studied further as there is potential to have a low temperature route to phase pure WC, W_2C and nanocomposites involving these phases. Through study of the 'traditional' urea sol-gel route alongside the biopolymer sol-gel route valuable knowledge was gather about the differences and similarities of these techniques, i.e. for the urea synthesis the importance of high urea to tungsten ratios and high temperatures for tungsten carbide was been demonstrated. The high ratios means there is enough carbon left behind to convert the tungsten nitride to tungsten carbide after all of the nitrogen containing compounds are burnt off. It has also been shown that the particle size can be controlled with the introduction of small amounts of biopolymer.

Further work should be carried out to investigate different biopolymers at different temperatures to fine tune this reaction. Creating a homogeneous inert atmosphere is also important as any oxygen in the atmosphere will cause the formation of the oxide during long synthesis times; however whether argon or nitrogen is used has minimal effect on the synthesis.

The ratio of biopolymer to metal precursor needs to be fine-tuned to stop the formation of tungsten metal. Finally further work should also include electrochemical testing (hydrogen evolution reaction and oxygen reduction reactions, life-cycling) once the carbide can be isolated as a single phase in multiple samples.

As a final statement for this thesis, the work detailed within it provides new information on the biopolymer sol-gel reactions and how porous materials can be formed/controlled and green heat treatments were investigated and potential applications were targeted.

APPENDIX A

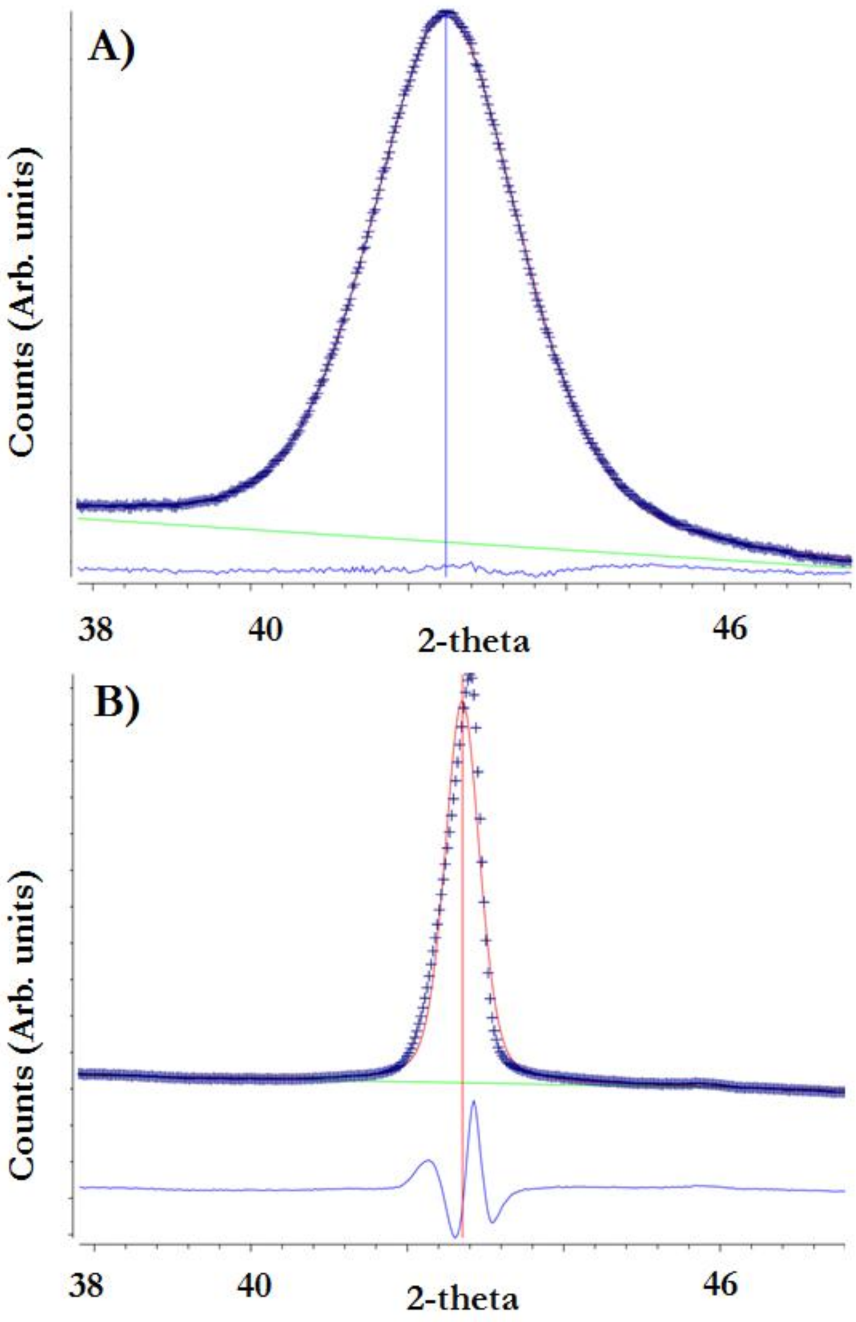

Figure A1 Screen shot an example fit for Scherrer analysis using the CMPR software. A) MgGel plus HCl and B) MgGel plus HNO_3

APPENDIX B

On the following pages is the data provided by Memmert and Carbolite on the power consumption of their ovens and furnaces respectfully. Below is an email from Carbolite

---

From: [redacted]

Sent: 04 August 2016 09:59

To: Ashleigh Danks (Studying PhD School of Chemistry FT)

Subject: CWF 11/13 efficiency

Hi Ashley,

The information I have been able to gather is as follows:

- Heat up with the output power set to 100% to 800°C is approximately 50 minutes. For this we have to assume the furnace is using the full 3.1 kW, but of course this is not the energy lost as the chamber is still heating.
- At 815°C the furnace needs to use 0.911 kW to maintain temperature, so this is the energy lost into the room.

I hope this gives you what you need.

If I can be of further help please let me know.

Best Regards,

[redacted]

[redacted] | www.carbolite-gero.com

Below is the data sheet provided by Memmert on their UF55 oven

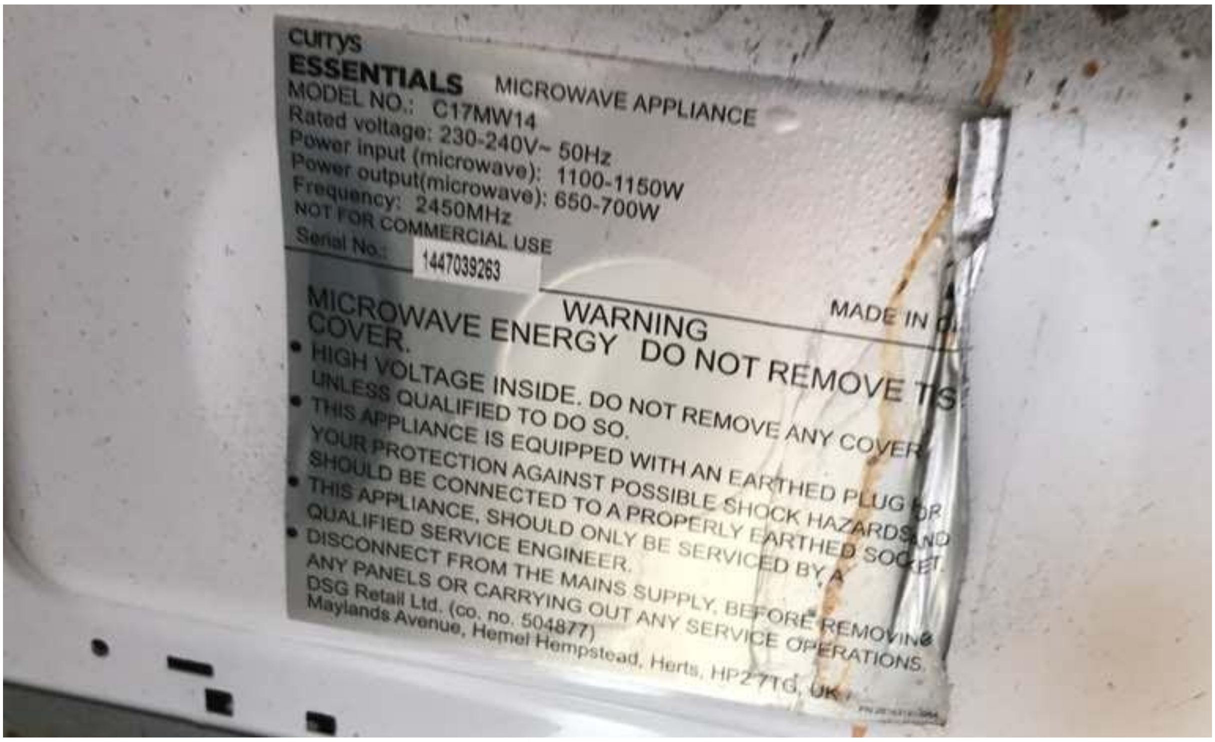

currys
ESSENTIALS MICROWAVE APPLIANCE
MODEL NO.: C17MW14
Rated voltage: 230-240V~ 50Hz
Power input (microwave): 1100-1150W
Power output(microwave): 650-700W
Frequency: 2450MHz
NOT FOR COMMERCIAL USE
Serial No.: 1447039263
MADE IN

WARNING
MICROWAVE ENERGY DO NOT REMOVE T
COVER.
- HIGH VOLTAGE INSIDE. DO NOT REMOVE ANY COVER UNLESS QUALIFIED TO DO SO.
- THIS APPLIANCE IS EQUIPPED WITH AN EARTHED PLUG OR YOUR PROTECTION AGAINST POSSIBLE SHOCK HAZARDS AND SHOULD BE CONNECTED TO A PROPERLY EARTHED SOCKET.
- THIS APPLIANCE, SHOULD ONLY BE SERVICED BY A QUALIFIED SERVICE ENGINEER.
- DISCONNECT FROM THE MAINS SUPPLY, BEFORE REMOVING ANY PANELS OR CARRYING OUT ANY SERVICE OPERATIONS.

DSG Retail Ltd. (co. no. 504877)
Maylands Avenue, Hemel Hempstead, Herts, HP2 7TG, UK

Figure B1 Power information on the microwave used

APPENDIX C

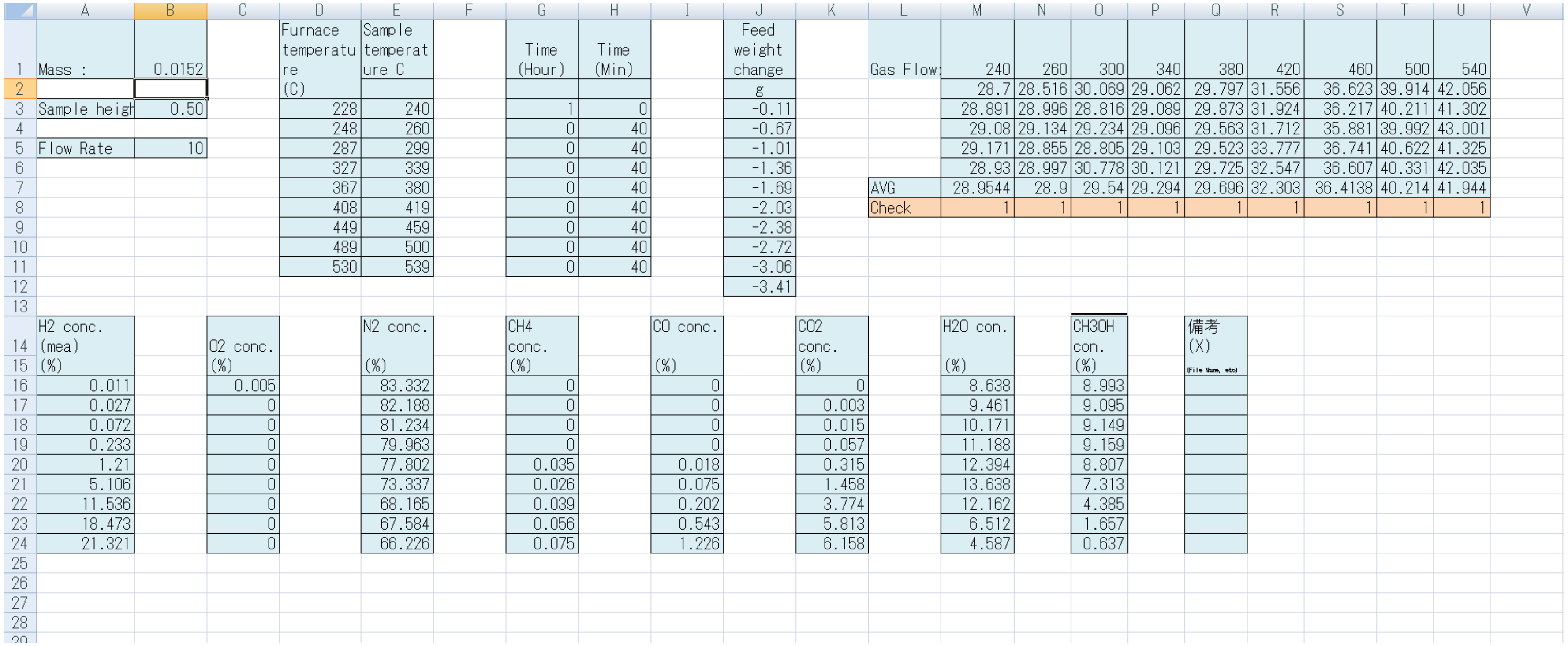

	A	B	C	D	E	F	G	H	I	J
1	Mass :	0.0152		Furnace temperature	Sample temperature C		Time (Hour)	Time (Min)		Feed weight change
2				(C)						g
3	Sample heigh	0.50		228	240		1	0		-0.11
4				248	260		0	40		-0.67
5	Flow Rate	10		287	299		0	40		-1.01
6				327	339		0	40		-1.36
7				367	380		0	40		-1.69
8				408	419		0	40		-2.03
9				449	459		0	40		-2.38
10				489	500		0	40		-2.72
11				530	539		0	40		-3.06
12										-3.41

	L	M	N	O	P	Q	R	S	T	U
1	Gas Flow:	240	260	300	340	380	420	460	500	540
2		28.7	28.516	30.069	29.062	29.797	31.556	36.623	39.914	42.056
3		28.891	28.996	28.816	29.089	29.873	31.924	36.217	40.211	41.302
4		29.08	29.134	29.234	29.096	29.563	31.712	35.881	39.992	43.001
5		29.171	28.855	28.805	29.103	29.523	33.777	36.741	40.622	41.325
6		28.93	28.997	30.778	30.121	29.725	32.547	36.607	40.331	42.035
7	AVG	28.9544	28.9	29.54	29.294	29.696	32.303	36.4138	40.214	41.944
8	Check	1	1	1	1	1	1	1	1	1

	A	C	E	G	I	K	M	O	Q
14–15	H2 conc. (mea) (%)	O2 conc. (%)	N2 conc. (%)	CH4 conc. (%)	CO conc. (%)	CO2 conc. (%)	H2O con. (%)	CH3OH con. (%)	備考 (X) (File Num, etc)
16	0.011	0.005	83.332	0	0	0	8.638	8.993	
17	0.027	0	82.188	0	0	0.003	9.461	9.095	
18	0.072	0	81.234	0	0	0.015	10.171	9.149	
19	0.233	0	79.963	0	0	0.057	11.188	9.159	
20	1.21	0	77.802	0.035	0.018	0.315	12.394	8.807	
21	5.106	0	73.337	0.026	0.075	1.458	13.638	7.313	
22	11.536	0	68.165	0.039	0.202	3.774	12.162	4.385	
23	18.473	0	67.584	0.056	0.543	5.813	6.512	1.657	
24	21.321	0	66.226	0.075	1.226	6.158	4.587	0.637	

Figure C1 Screenshot of Microsoft excel data input page

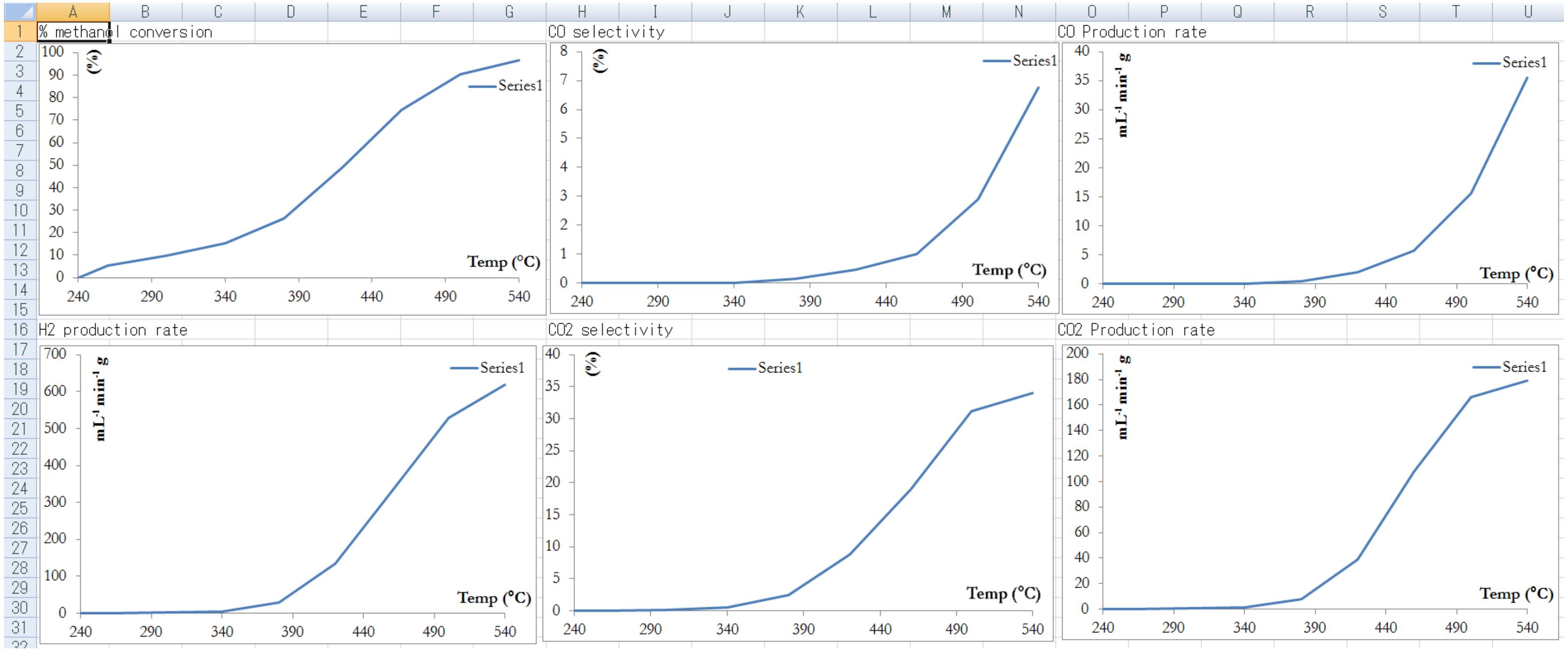

Figure C2 Screenshot of Microsoft excel output graphs page

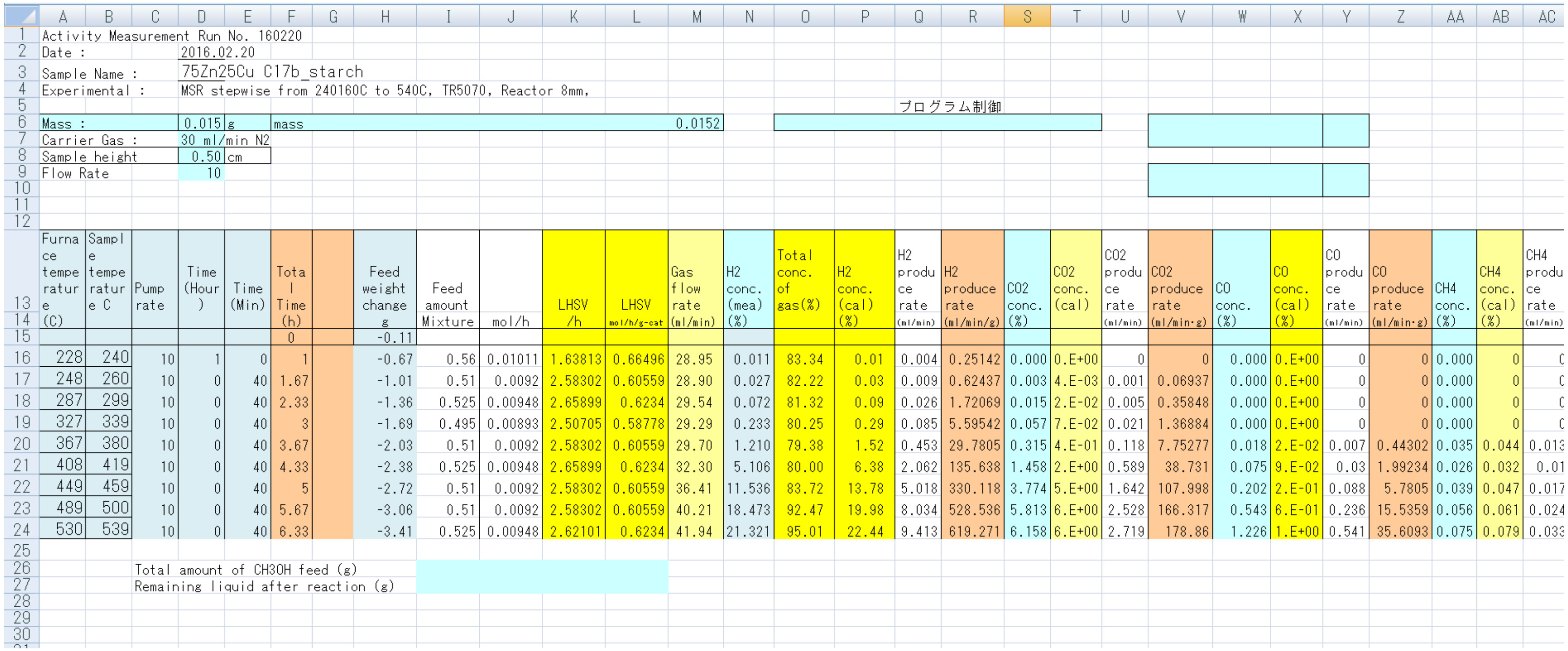

Activity Measurement Run No. 160220
Date : 2016.02.20
Sample Name : 75Zn25Cu C17b_starch
Experimental : MSR stepwise from 240160C to 540C, TR5070, Reactor 8mm,
プログラム制御
Mass : 0.015 g mass 0.0152
Carrier Gas : 30 ml/min N2
Sample height 0.50 cm
Flow Rate 10

Furnace temperature (C)	Sample temperature C	Pump rate	Time (Hour)	Time (Min)	Total Time (h)		Feed weight change g	Feed amount Mixture	mol/h	LHSV /h	LHSV mol/h/g-cat	Gas flow rate (ml/min)	H2 conc. (mea) (%)	Total conc. of gas(%)	H2 conc. (cal) (%)	H2 produce rate (ml/min)	H2 produce rate (ml/min/g)	CO2 conc. (%)	CO2 conc. (cal)	CO2 produce rate (ml/min)	CO2 produce rate (ml/min·g)	CO conc. (%)	CO conc. (cal) (%)	CO produce rate (ml/min)	CO produce rate (ml/min·g)	CH4 conc. (%)	CH4 conc. (cal) (%)	CH4 produce rate (ml/min)
					0		-0.11																					
228	240	10	1	0	1		-0.67	0.56	0.01011	1.63813	0.66496	28.95	0.011	83.34	0.01	0.004	0.25142	0.000	0.E+00	0	0	0.000	0.E+00	0	0	0.000	0	0
248	260	10	0	40	1.67		-1.01	0.51	0.0092	2.58302	0.60559	28.90	0.027	82.22	0.03	0.009	0.62437	0.003	4.E-03	0.001	0.06937	0.000	0.E+00	0	0	0.000	0	0
287	299	10	0	40	2.33		-1.36	0.525	0.00948	2.65899	0.6234	29.54	0.072	81.32	0.09	0.026	1.72069	0.015	2.E-02	0.005	0.35848	0.000	0.E+00	0	0	0.000	0	0
327	339	10	0	40	3		-1.69	0.495	0.00893	2.50705	0.58778	29.29	0.233	80.25	0.29	0.085	5.59542	0.057	7.E-02	0.021	1.36884	0.000	0.E+00	0	0	0.000	0	0
367	380	10	0	40	3.67		-2.03	0.51	0.0092	2.58302	0.60559	29.70	1.210	79.38	1.52	0.453	29.7805	0.315	4.E-01	0.118	7.75277	0.018	2.E-02	0.007	0.44302	0.035	0.044	0.013
408	419	10	0	40	4.33		-2.38	0.525	0.00948	2.65899	0.6234	32.30	5.106	80.00	6.38	2.062	135.638	1.458	2.E+00	0.589	38.731	0.075	9.E-02	0.03	1.99234	0.026	0.032	0.01
449	459	10	0	40	5		-2.72	0.51	0.0092	2.58302	0.60559	36.41	11.536	83.72	13.78	5.018	330.118	3.774	5.E+00	1.642	107.998	0.202	2.E-01	0.088	5.7805	0.039	0.047	0.017
489	500	10	0	40	5.67		-3.06	0.51	0.0092	2.58302	0.60559	40.21	18.473	92.47	19.98	8.034	528.536	5.813	6.E+00	2.528	166.317	0.543	6.E-01	0.236	15.5359	0.056	0.061	0.024
530	539	10	0	40	6.33		-3.41	0.525	0.00948	2.62101	0.6234	41.94	21.321	95.01	22.44	9.413	619.271	6.158	6.E+00	2.719	178.86	1.226	1.E+00	0.541	35.6093	0.075	0.079	0.033

Total amount of CH3OH feed (g)
Remaining liquid after reaction (g)

Figure C3 Screenshot of Microsoft excel data manipulation page 1

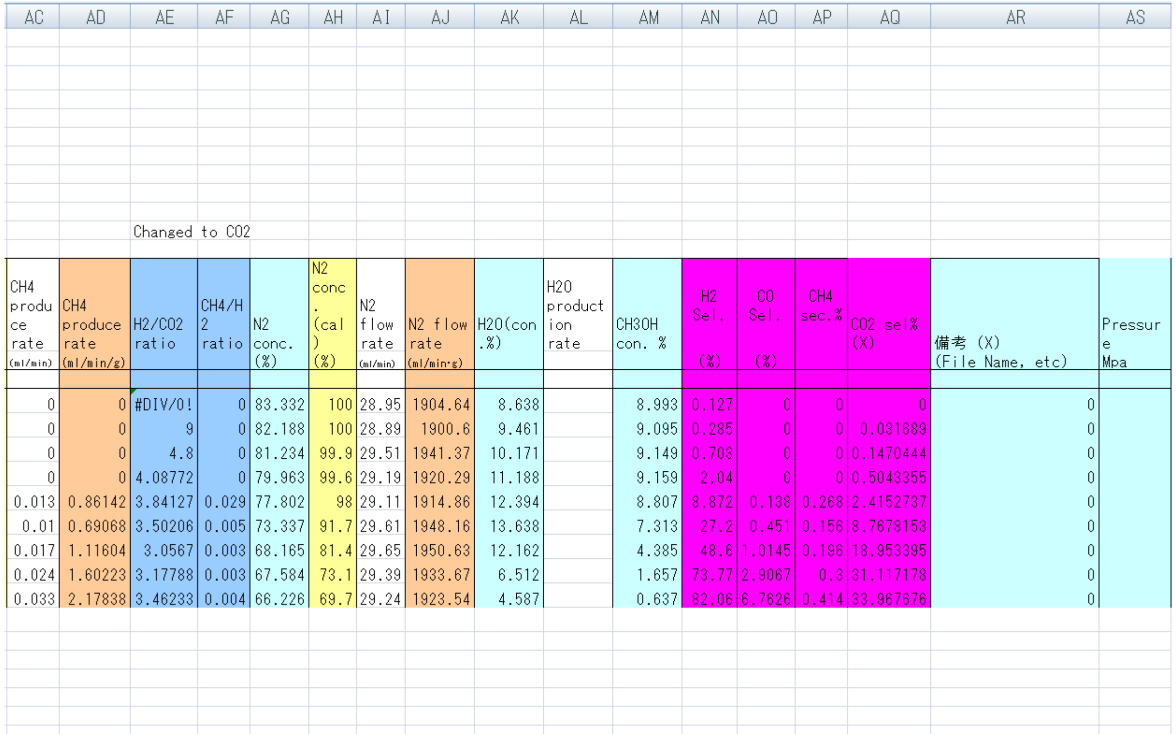

Changed to CO2

AC	AD	AE	AF	AG	AH	AI	AJ	AK	AL	AM	AN	AO	AP	AQ	AR	AS
CH4 produce rate (ml/min)	CH4 produce rate (ml/min/g)	H2/CO2 ratio	CH4/H2 ratio	N2 conc. (%)	N2 conc. (cal) (%)	N2 flow rate (ml/min)	N2 flow rate (ml/min·g)	H2O(con.%)	H2O production rate	CH3OH con. %	H2 Sel. (%)	CO Sel. (%)	CH4 sec.%	CO2 sel% (X)	備考 (X) (File Name, etc)	Pressure Mpa
0	0	#DIV/0!	0	83.332	100	28.95	1904.64	8.638		8.993	0.127	0	0	0	0	
0	0	9	0	82.188	100	28.89	1900.6	9.461		9.095	0.285	0	0	0.031689	0	
0	0	4.8	0	81.234	99.9	29.51	1941.37	10.171		9.149	0.703	0	0	0.1470444	0	
0	0	4.08772	0	79.963	99.6	29.19	1920.29	11.188		9.159	2.04	0	0	0.5043355	0	
0.013	0.86142	3.84127	0.029	77.802	98	29.11	1914.86	12.394		8.807	8.872	0.138	0.268	2.4152737	0	
0.01	0.69068	3.50206	0.005	73.337	91.7	29.61	1948.16	13.638		7.313	27.2	0.451	0.156	8.7678153	0	
0.017	1.11604	3.0567	0.003	68.165	81.4	29.65	1950.63	12.162		4.385	48.6	1.0145	0.196	18.953395	0	
0.024	1.60223	3.17788	0.003	67.584	73.1	29.39	1933.67	6.512		1.657	73.77	2.9067	0.3	31.117178	0	
0.033	2.17838	3.46233	0.004	66.226	69.7	29.24	1923.54	4.587		0.637	82.06	6.7626	0.414	33.967676	0	

Figure C4 Screenshot of Microsoft excel data manipulation page 2

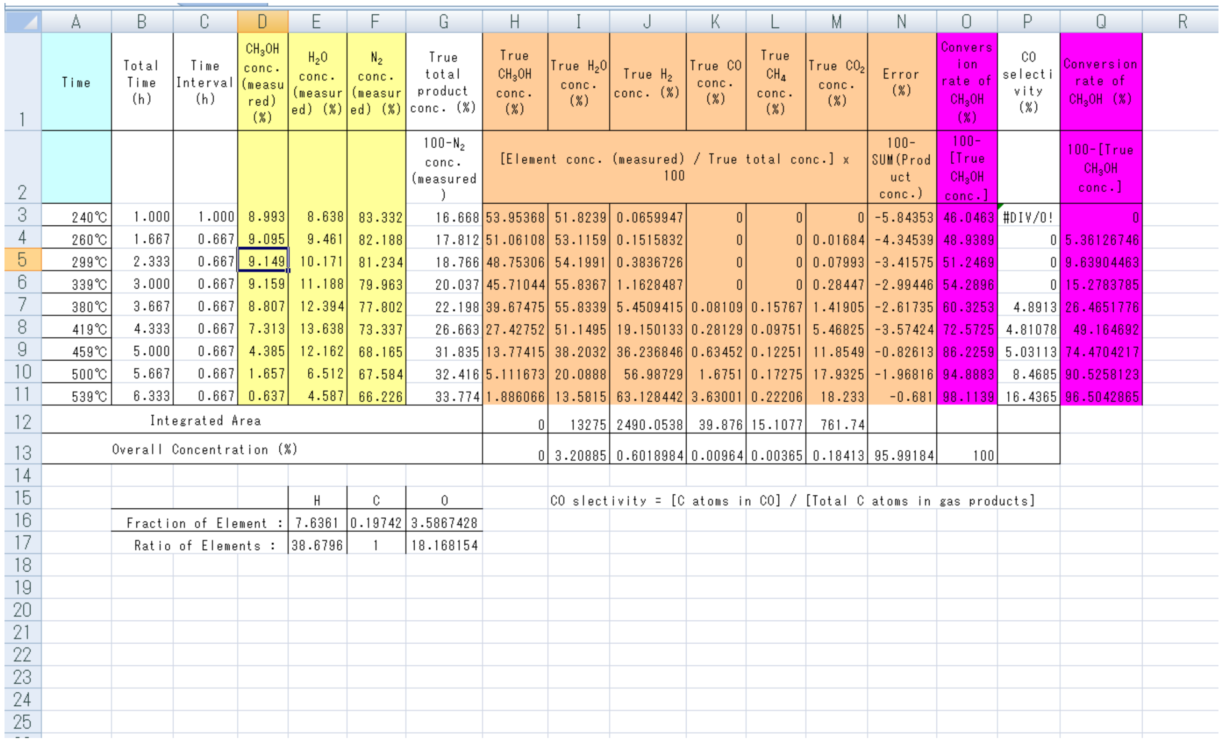

Time	Total Time (h)	Time Interval (h)	CH_3OH conc. (measured) (%)	H_2O conc. (measured) (%)	N_2 conc. (measured) (%)	True total product conc. (%)	True CH_3OH conc. (%)	True H_2O conc. (%)	True H_2 conc. (%)	True CO conc. (%)	True CH_4 conc. (%)	True CO_2 conc. (%)	Error (%)	Conversion rate of CH_3OH (%)	CO selectivity (%)	Conversion rate of CH_3OH (%)
						100-N_2 conc. (measured)	[Element conc. (measured) / True total conc.] x 100						100-SUM(Product conc.)	100-[True CH_3OH conc.]		100-[True CH_3OH conc.]
240℃	1.000	1.000	8.993	8.638	83.332	16.668	53.95368	51.8239	0.0659947	0	0	0	-5.84353	46.0463	#DIV/0!	0
260℃	1.667	0.667	9.095	9.461	82.188	17.812	51.06108	53.1159	0.1515832	0	0	0.01684	-4.34539	48.9389	0	5.36126746
299℃	2.333	0.667	9.149	10.171	81.234	18.766	48.75306	54.1991	0.3836726	0	0	0.07993	-3.41575	51.2469	0	9.63904463
339℃	3.000	0.667	9.159	11.188	79.963	20.037	45.71044	55.8367	1.1628487	0	0	0.28447	-2.99446	54.2896	0	15.2783785
380℃	3.667	0.667	8.807	12.394	77.802	22.198	39.67475	55.8339	5.4509415	0.08109	0.15767	1.41905	-2.61735	60.3253	4.8913	26.4651776
419℃	4.333	0.667	7.313	13.638	73.337	26.663	27.42752	51.1495	19.150133	0.28129	0.09751	5.46825	-3.57424	72.5725	4.81078	49.164692
459℃	5.000	0.667	4.385	12.162	68.165	31.835	13.77415	38.2032	36.236846	0.63452	0.12251	11.8549	-0.82613	86.2259	5.03113	74.4704217
500℃	5.667	0.667	1.657	6.512	67.584	32.416	5.111673	20.0888	56.98729	1.6751	0.17275	17.9325	-1.96816	94.8883	8.4685	90.5258123
539℃	6.333	0.667	0.637	4.587	66.226	33.774	1.886066	13.5815	63.128442	3.63001	0.22206	18.233	-0.681	98.1139	16.4365	96.5042865
Integrated Area							0	13275	2490.0538	39.876	15.1077	761.74				
Overall Concentration (%)							0	3.20885	0.6018984	0.00964	0.00365	0.18413	95.99184	100		

	H	C	O
Fraction of Element :	7.6361	0.19742	3.5867428
Ratio of Elements :	38.6796	1	18.168154

CO slectivity = [C atoms in CO] / [Total C atoms in gas products]

Figure C5 Screenshot of Microsoft excel data manipulation page for calculating methanol conversion rate

APPENDIX D

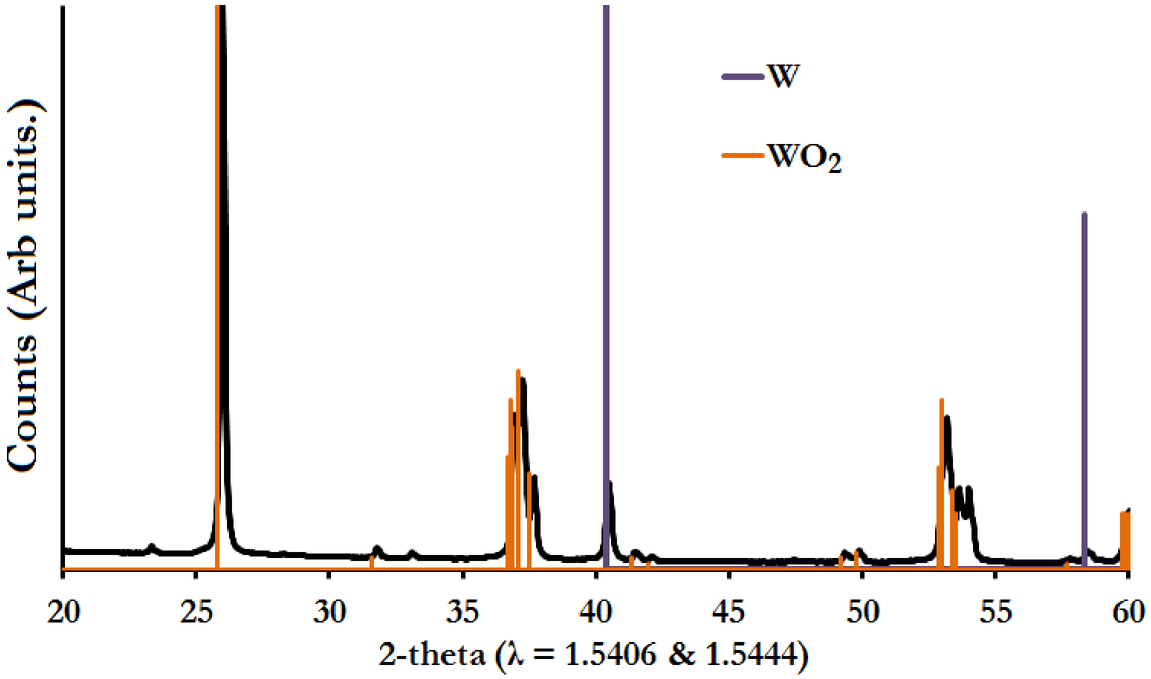

Figure D1 XRD pattern of a sample synthesis from WCl_4 and urea at a 1 : 7 ratio

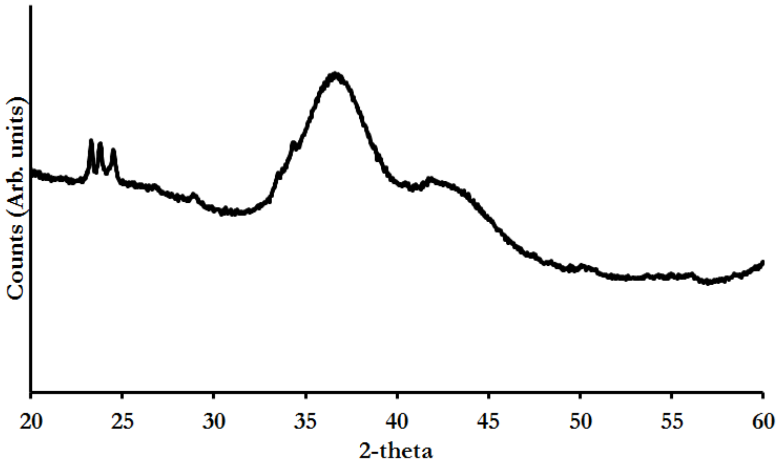

Figure D2 XRD pattern for samples synthesised using 0.01 mol of tungsten and a tungsten to urea ratio of 1:14 at 700 °C for phase map. Main phase is WN

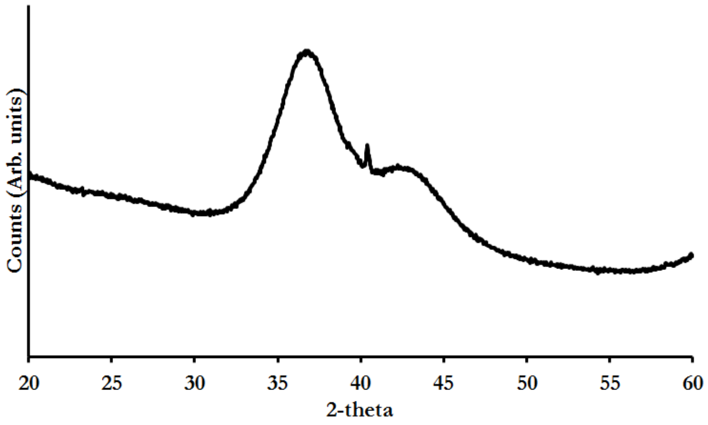

Figure D3 XRD pattern for samples synthesised using 0.01 mol of tungsten and a tungsten to urea ratio of 1:10 at 700 °C for phase map. Main phase is WN

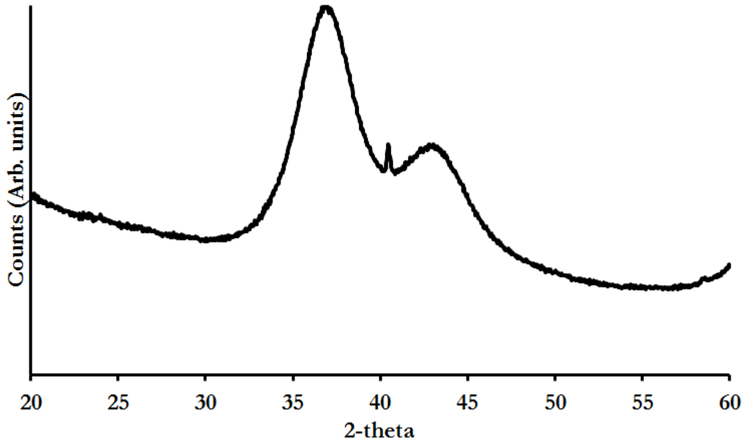

Figure D4 XRD pattern for samples synthesised using 0.01 mol of tungsten and a tungsten to urea ratio of 1:6 at 700 °C for phase map. Main phase is WN

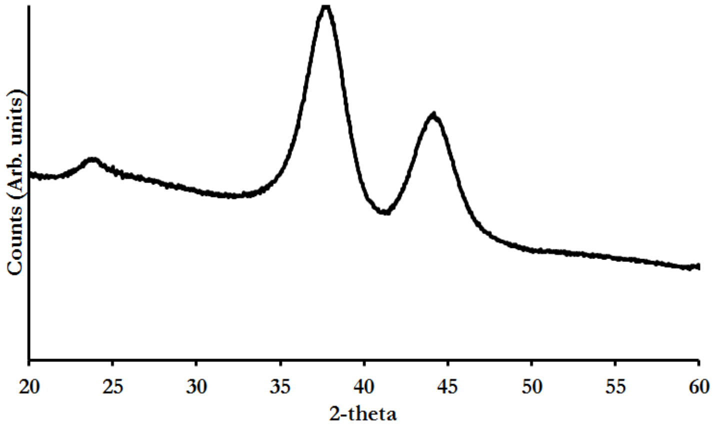

Figure D5 XRD pattern for samples synthesised using 0.01 mol of tungsten and a tungsten to urea ratio of 1:2 at 700 °C for phase map. Main phase is WN

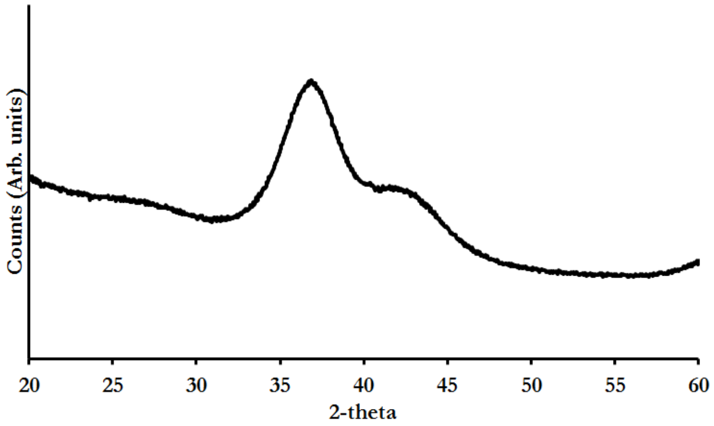

Figure D6 XRD pattern for samples synthesised using 0.01 mol of tungsten and a tungsten to urea ratio of 1:14 at 750 °C for phase map. Main phase is WN

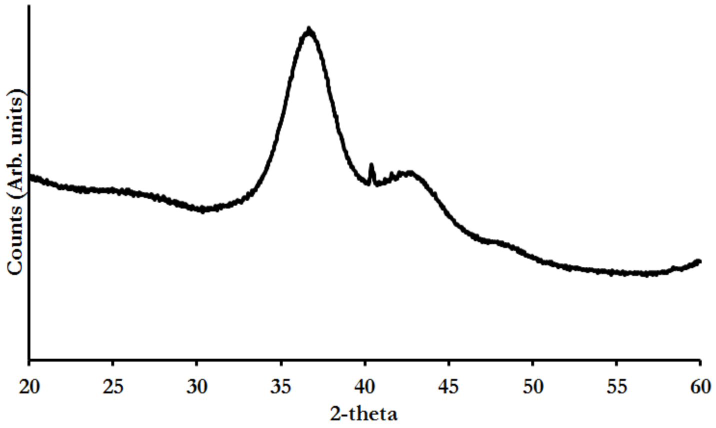

Figure D7 XRD pattern for samples synthesised using 0.01 mol of tungsten and a tungsten to urea ratio of 1:10 at 750 °C for phase map. Main phase is WN

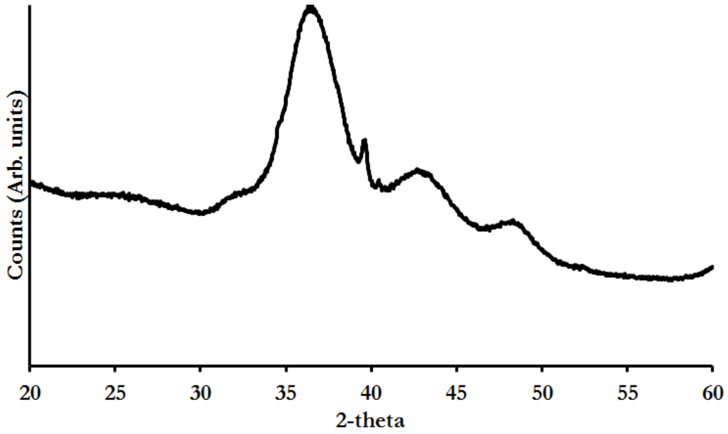

Figure D8 XRD pattern for samples synthesised using 0.01 mol of tungsten and a tungsten to urea ratio of 1:6 at 750 °C for phase map. Main phases are WN and WC

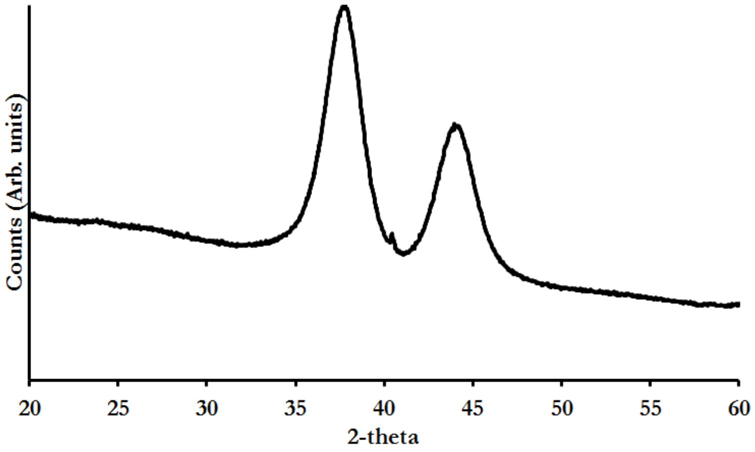

Figure D9 XRD pattern for samples synthesised using 0.01 mol of tungsten and a tungsten to urea ratio of 1:2 at 750 °C for phase map. Main phase is WN

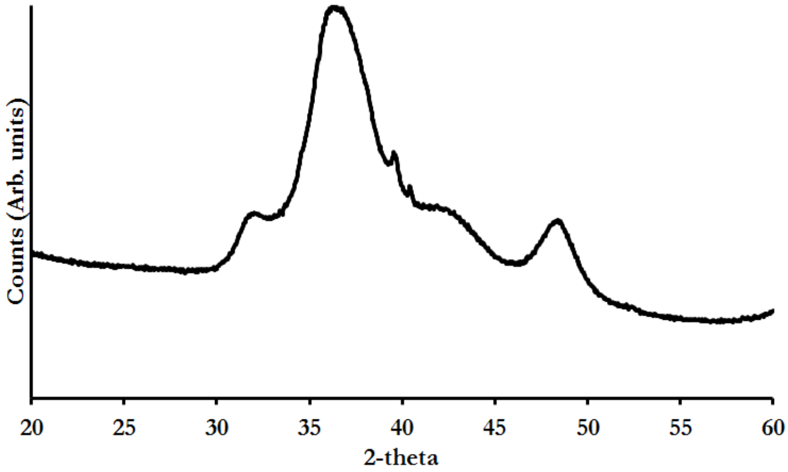

Figure D10 XRD pattern for samples synthesised using 0.01 mol of tungsten and a tungsten to urea ratio of 1:14 at 800 °C for phase map. Main phases are WN and WC

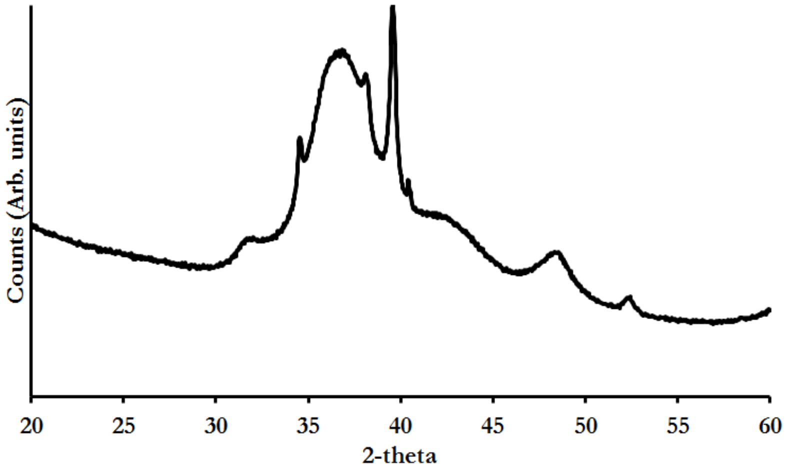

Figure D11 XRD pattern for samples synthesised using 0.01 mol of tungsten and a tungsten to urea ratio of 1:11 at 800 °C for phase map. Main phases are WN and WC

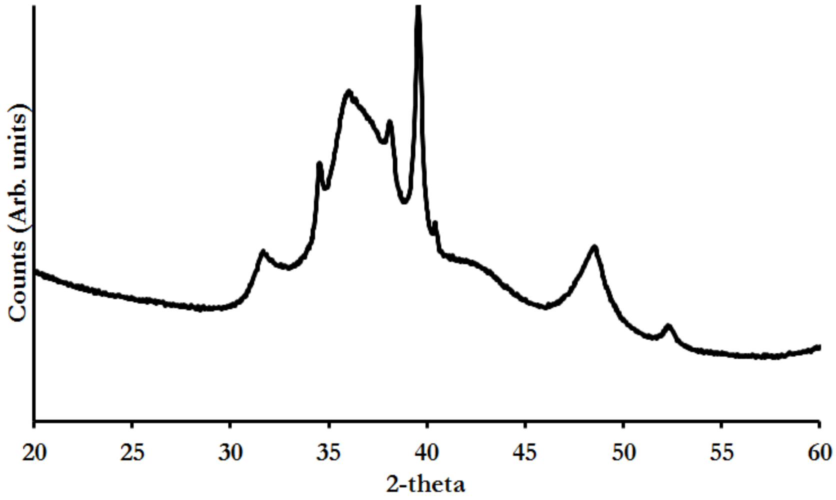

Figure D12 XRD pattern for samples synthesised using 0.01 mol of tungsten and a tungsten to urea ratio of 1:10 at 800 °C for phase map

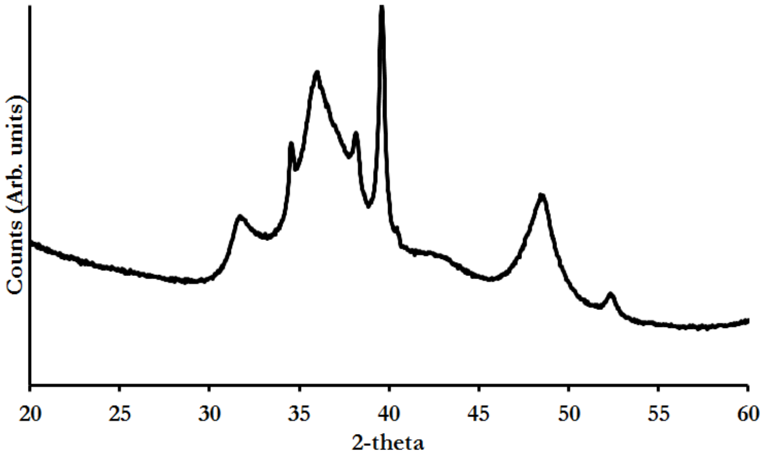

Figure D13 XRD pattern for samples synthesised using 0.01 mol of tungsten and a tungsten to urea ratio of 1:9 at 800 °C for phase map

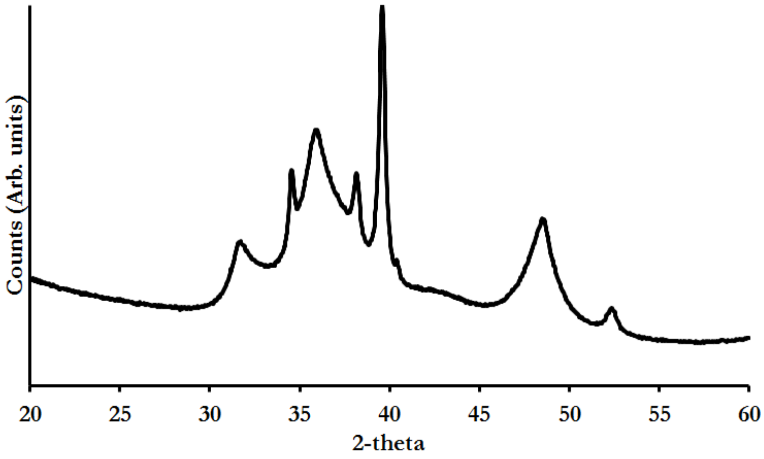

Figure D14 XRD pattern for samples synthesised using 0.01 mol of tungsten and a tungsten to urea ratio of 1:8 at 800 °C for phase map

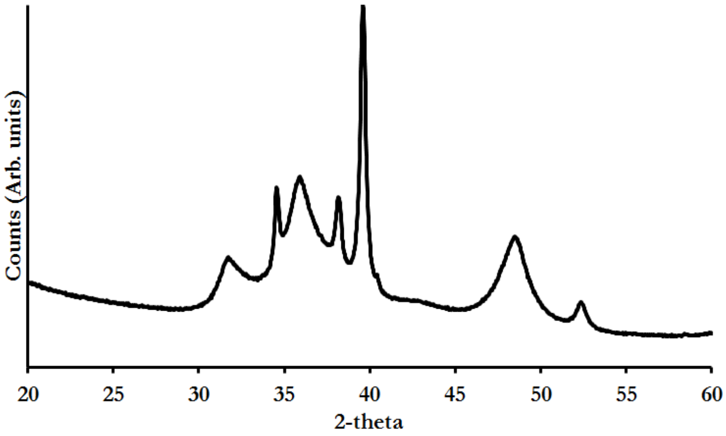

Figure D15 XRD pattern for samples synthesised using 0.01 mol of tungsten and a tungsten to urea ratio of 1:7 at 800 °C for phase map

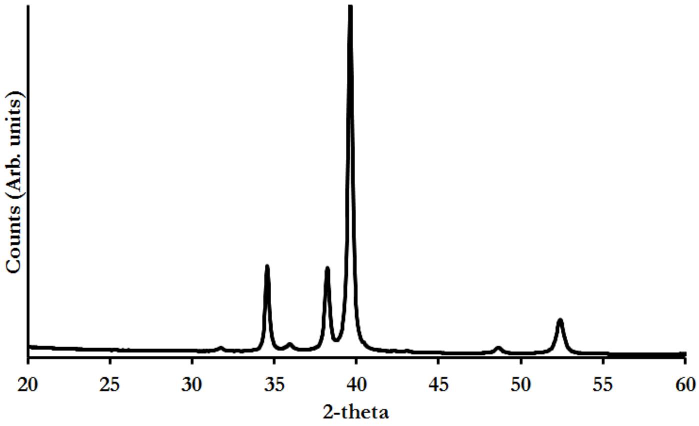

Figure D16 XRD pattern for samples synthesised using 0.01 mol of tungsten and a tungsten to urea ratio of 1:6 at 800 °C for phase map

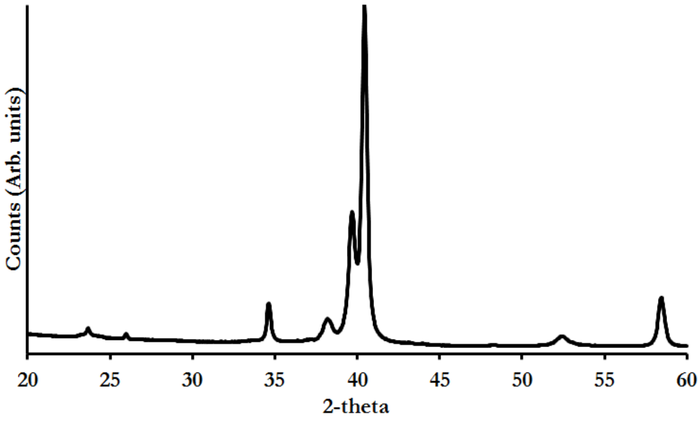

Figure D17 XRD pattern for samples synthesised using 0.01 mol of tungsten and a tungsten to urea ratio of 1:5 at 800 °C for phase map

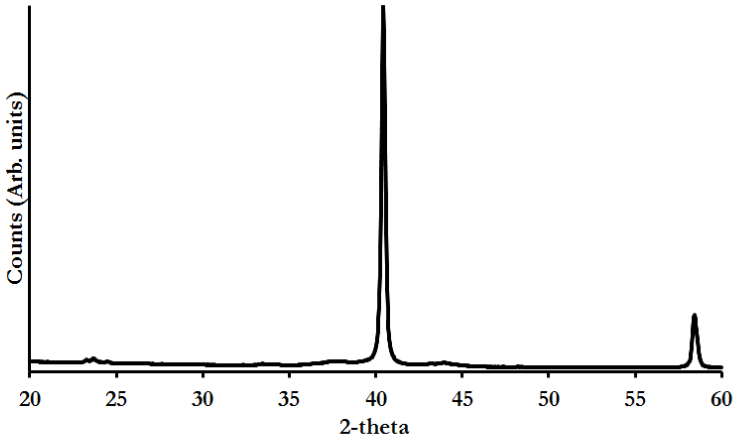

Figure D18 XRD pattern for samples synthesised using 0.01 mol of tungsten and a tungsten to urea ratio of 1:4 at 800 °C for phase map

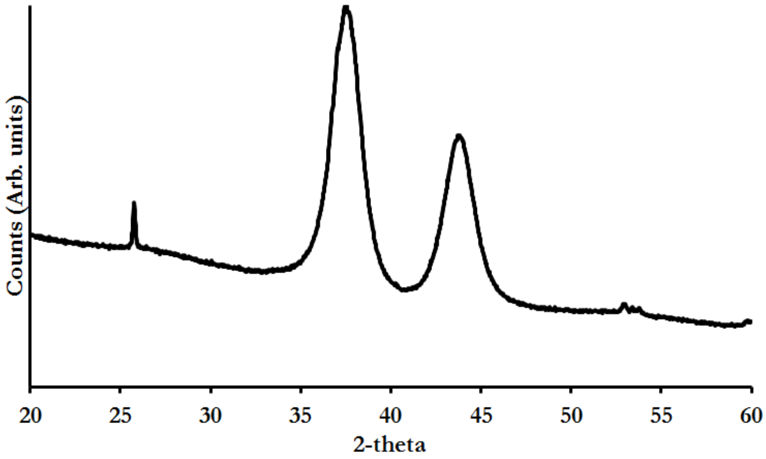

Figure D19 XRD pattern for samples synthesised using 0.01 mol of tungsten and a tungsten to urea ratio of 1:3 at 800 °C for phase map

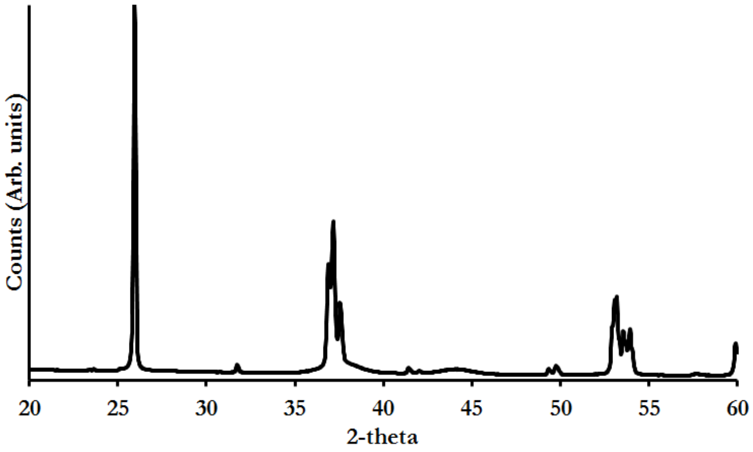

Figure D20 XRD pattern for samples synthesised using 0.01 mol of tungsten and a tungsten to urea ratio of 1:2 at 800 °C for phase map

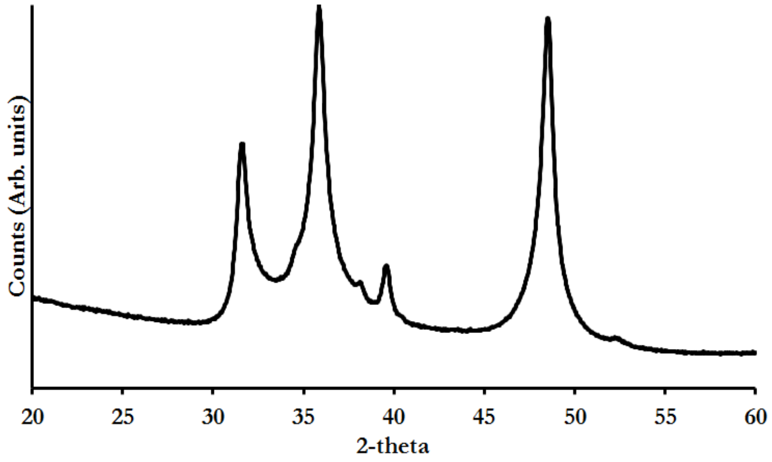

Figure D21 XRD pattern for samples synthesised using 0.01 mol of tungsten and a tungsten to urea ratio of 1:14 at 850 °C for phase map

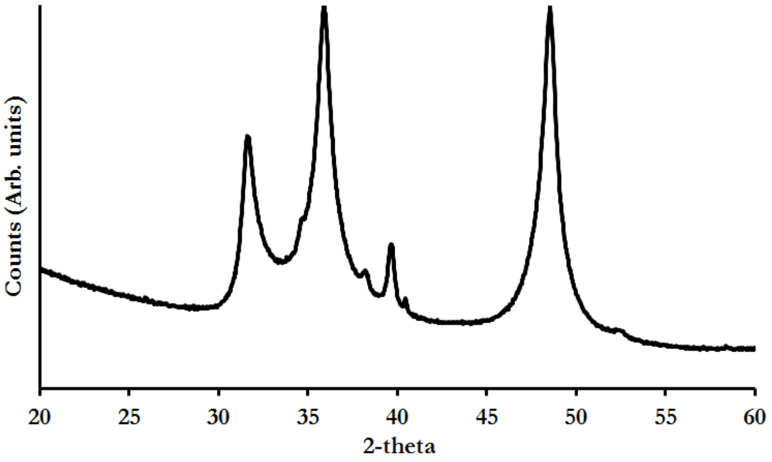

Figure D22 XRD pattern for samples synthesised using 0.01 mol of tungsten and a tungsten to urea ratio of 1:10 at 850 °C for phase map

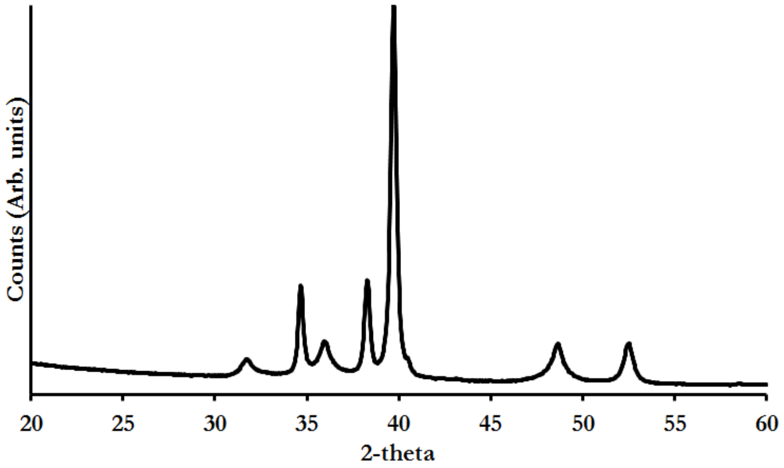

Figure D23 XRD pattern for samples synthesised using 0.01 mol of tungsten and a tungsten to urea ratio of 1:6 at 850 °C for phase map

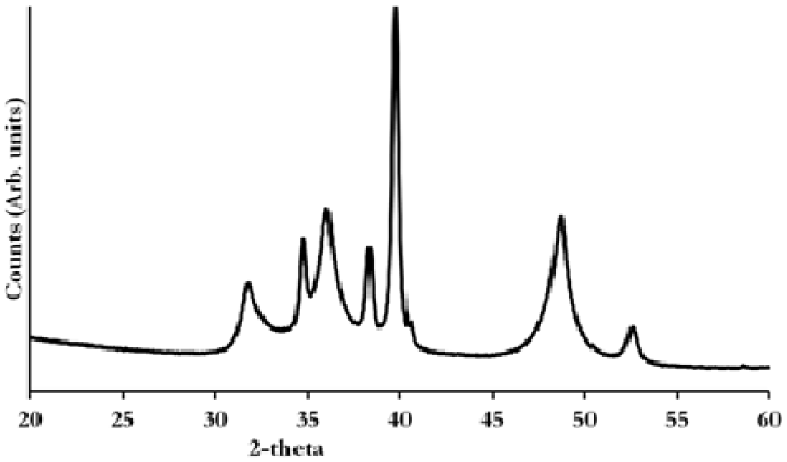

Figure D24 XRD pattern for samples synthesised using 0.01 mol of tungsten and a tungsten to urea ratio of 1:5 at 850 °C for phase map

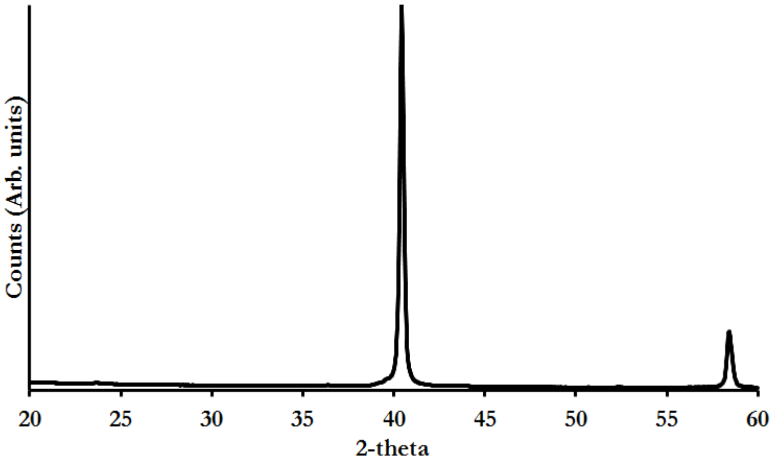

Figure D25 XRD pattern for samples synthesised using 0.01 mol of tungsten and a tungsten to urea ratio of 1:4 at 850 °C for phase map

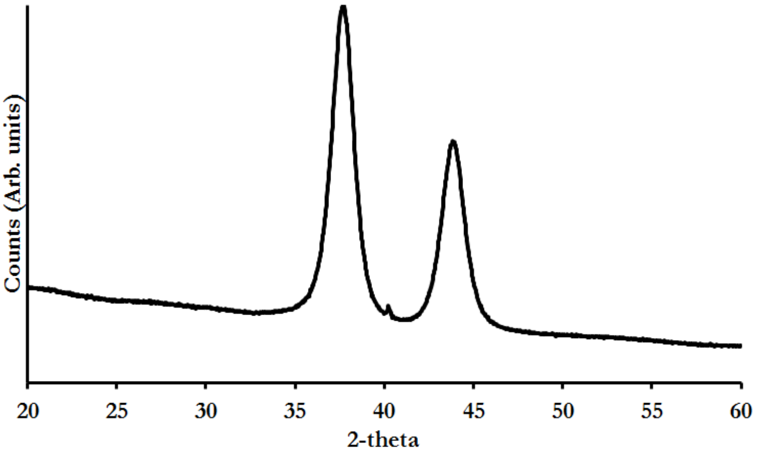

Figure D26 XRD pattern for samples synthesised using 0.01 mol of tungsten and a tungsten to urea ratio of 1:3 at 850 °C for phase map

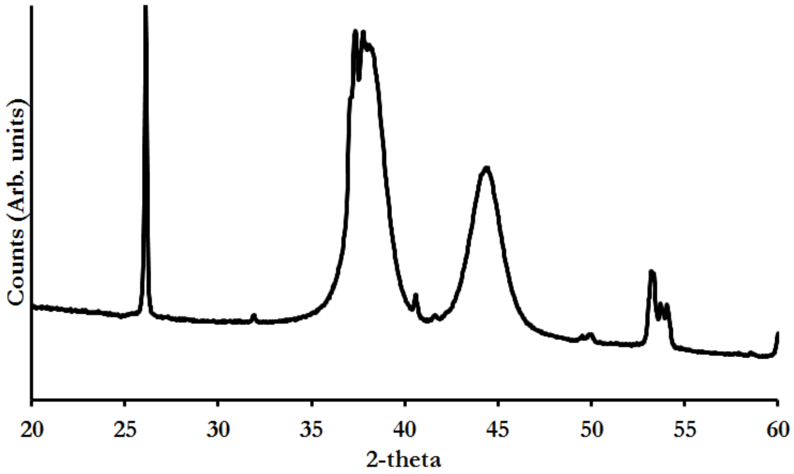

Figure D27 XRD pattern for samples synthesised using 0.01 mol of tungsten and a tungsten to urea ratio of 1:2 at 850 °C for phase map

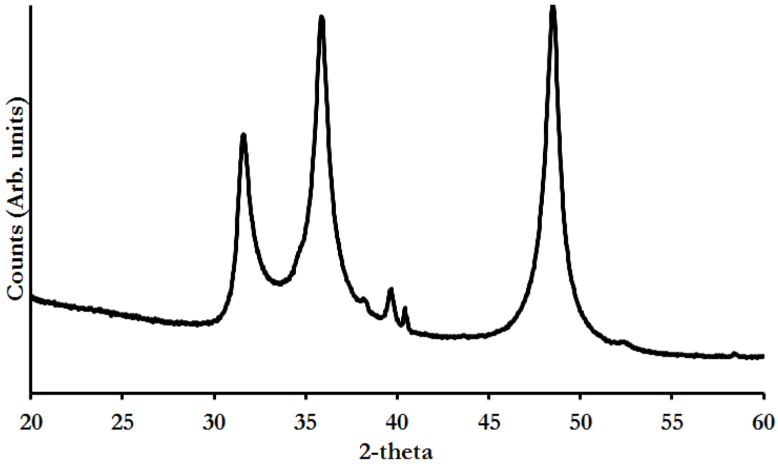

Figure D28 XRD pattern for samples synthesised using 0.01 mol of tungsten and a tungsten to urea ratio of 1:14 at 875 °C for phase map

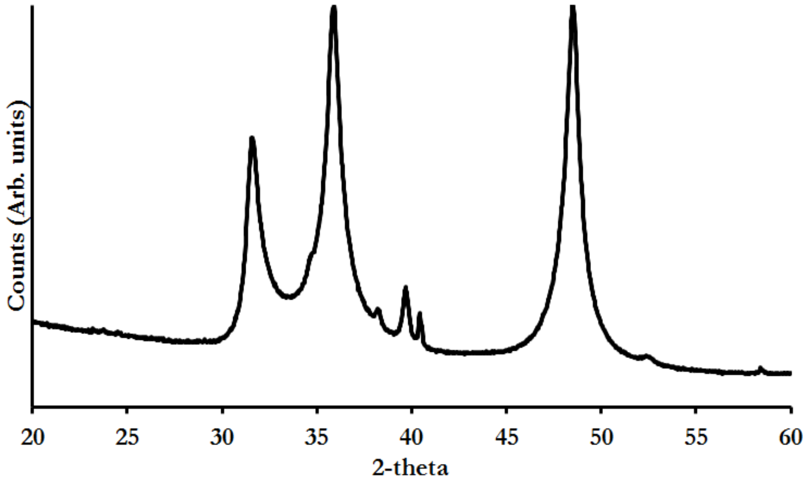

Figure D29 XRD pattern for samples synthesised using 0.01 mol of tungsten and a tungsten to urea ratio of 1:10 at 875 °C for phase map

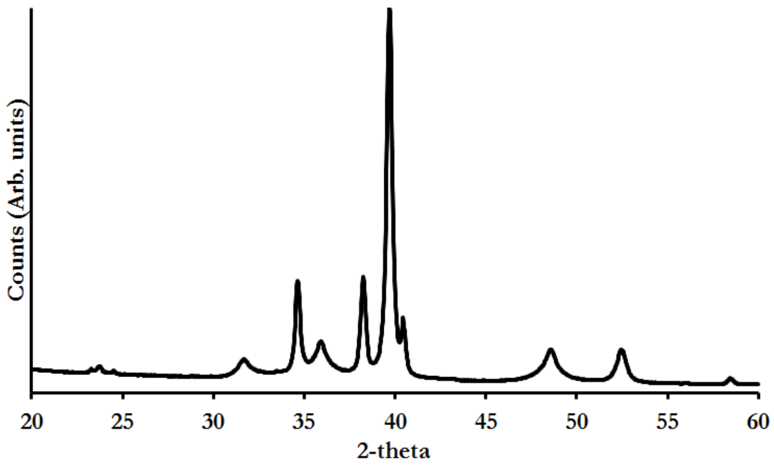

Figure D30 XRD pattern for samples synthesised using 0.01 mol of tungsten and a tungsten to urea ratio of 1:6 at 875 °C for phase map

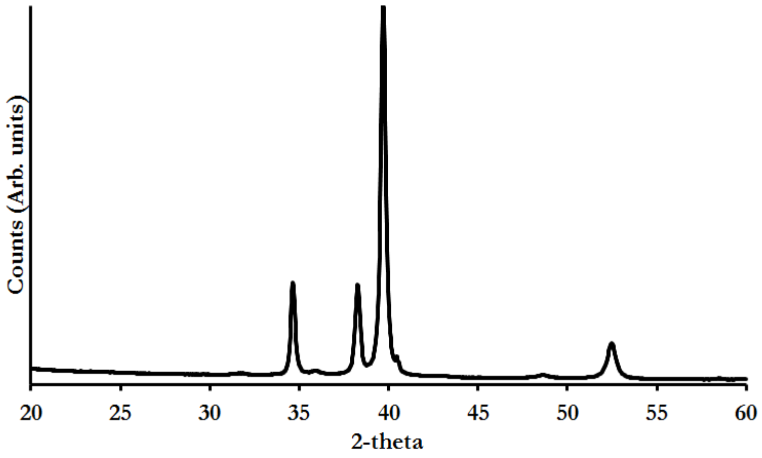

Figure D31 XRD pattern for samples synthesised using 0.01 mol of tungsten and a tungsten to urea ratio of 1:5 at 875 °C for phase map

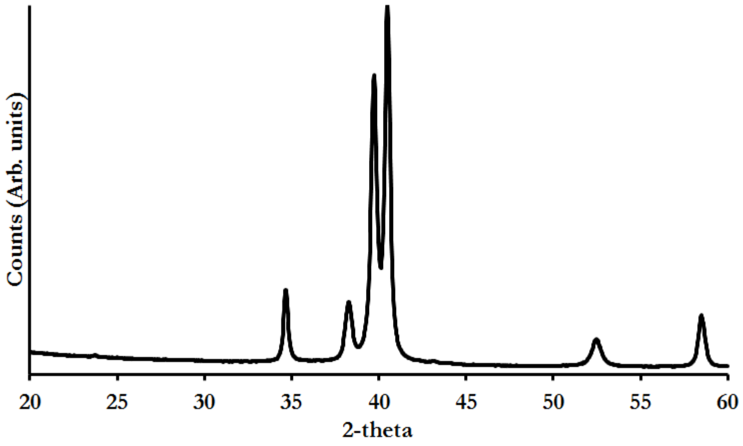

Figure D32 XRD pattern for samples synthesised using 0.01 mol of tungsten and a tungsten to urea ratio of 1:4 at 875 °C for phase map

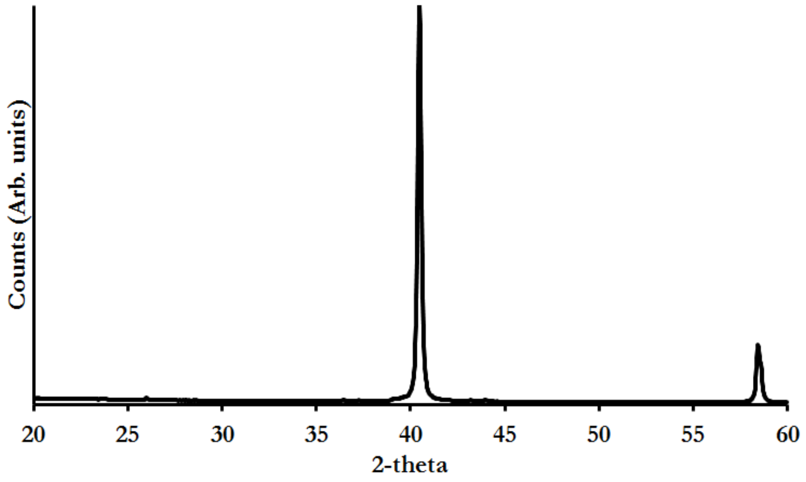

Figure D33 XRD pattern for samples synthesised using 0.01 mol of tungsten and a tungsten to urea ratio of 1:3 at 875 °C for phase map

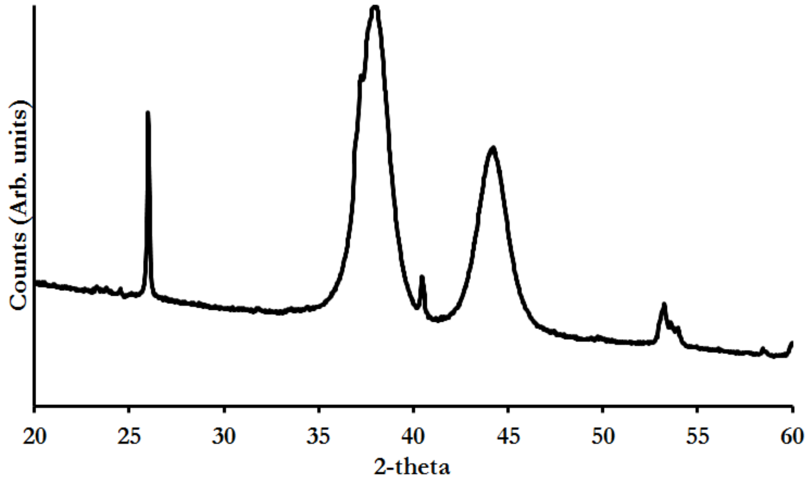

Figure D34 XRD pattern for samples synthesised using 0.01 mol of tungsten and a tungsten to urea ratio of 1:2 at 875 °C for phase map

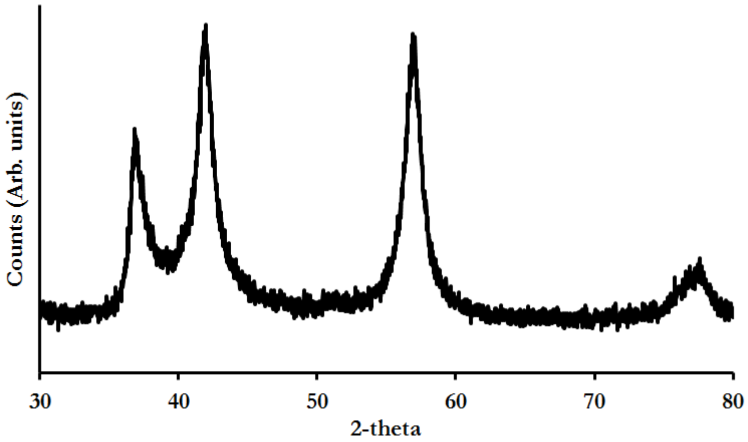

Figure D35 XRD pattern for samples synthesised using 0.01 mol of tungsten and a tungsten to urea ratio of 1:14 at 900 °C for phase map. This XRD was produced from the Bruker D2 Phaser, see experimental

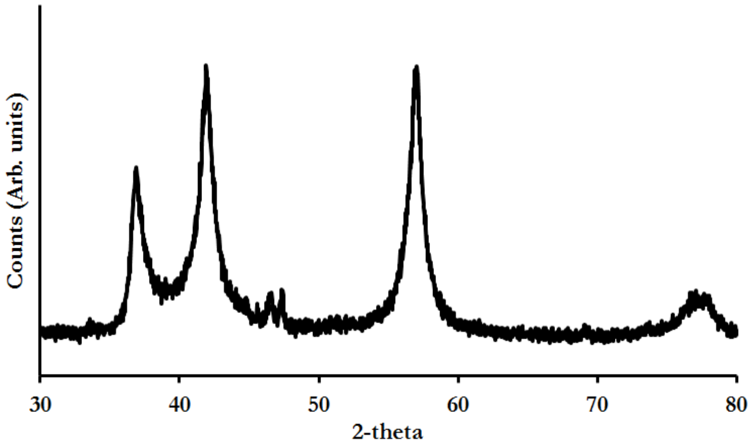

Figure D36 XRD pattern for samples synthesised using 0.01 mol of tungsten and a tungsten to urea ratio of 1:10 at 900 °C for phase map. This XRD was produced from the Bruker D2 Phaser, see experimental

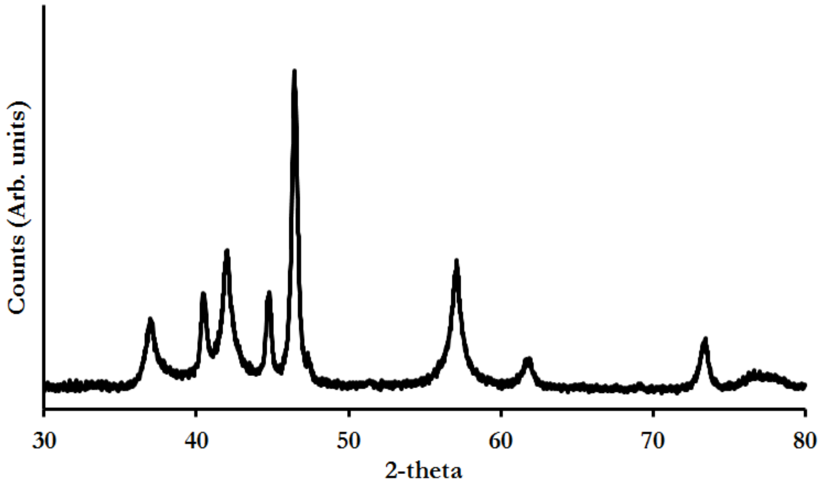

Figure D37 XRD pattern for samples synthesised using 0.01 mol of tungsten and a tungsten to urea ratio of 1:6 at 900 °C for phase map. This XRD was produced from the Bruker D2 Phaser, see experimental

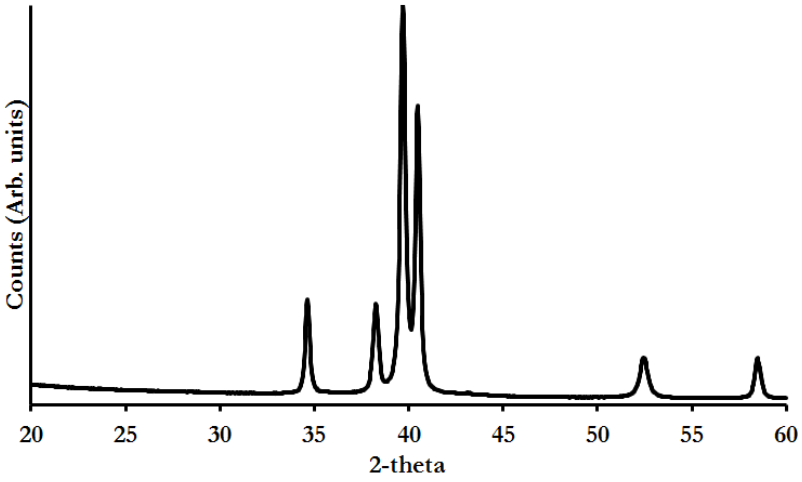

Figure D38 XRD pattern for samples synthesised using 0.01 mol of tungsten and a tungsten to urea ratio of 1:5 at 900 °C for phase map

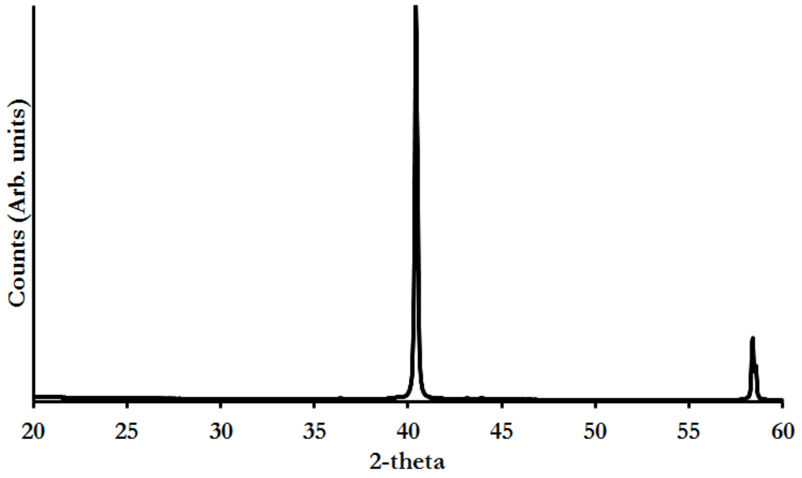

Figure D39 XRD pattern for samples synthesised using 0.01 mol of tungsten and a tungsten to urea ratio of 1:4 at 900 °C for phase map

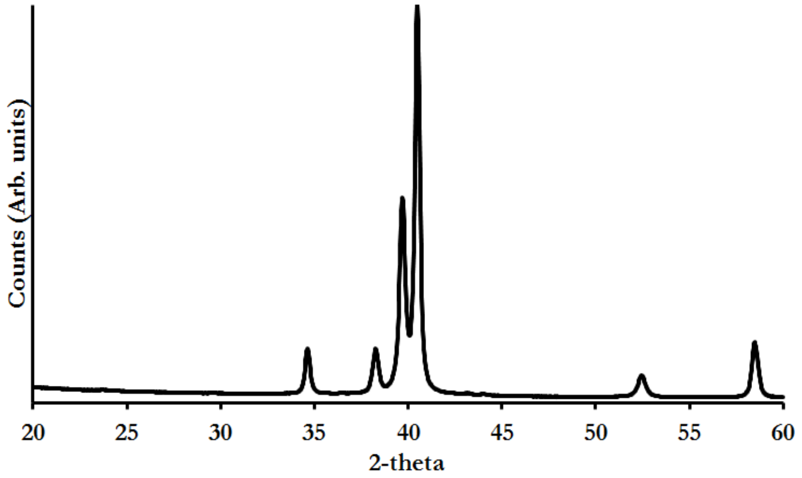

Figure D40 XRD pattern for samples synthesised using 0.01 mol of tungsten and a tungsten to urea ratio of 1:3 at 900 °C for phase map

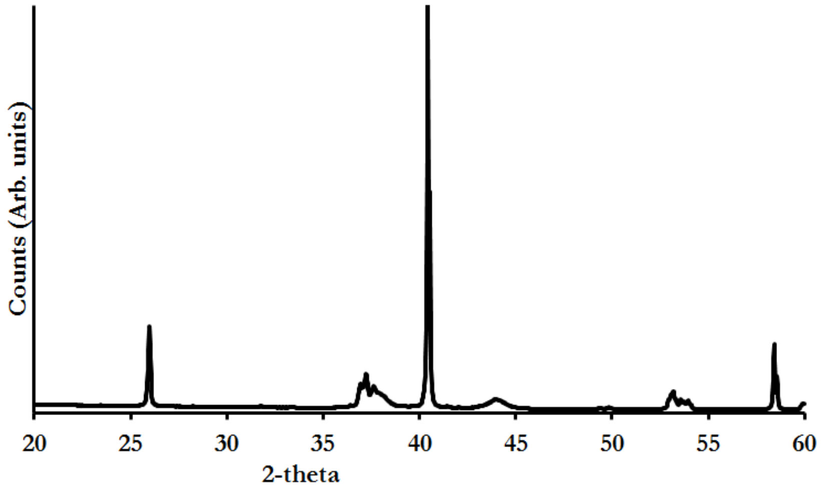

Figure D41 XRD pattern for samples synthesised using 0.01 mol of tungsten and a tungsten to urea ratio of 1:2 at 900 °C for phase map

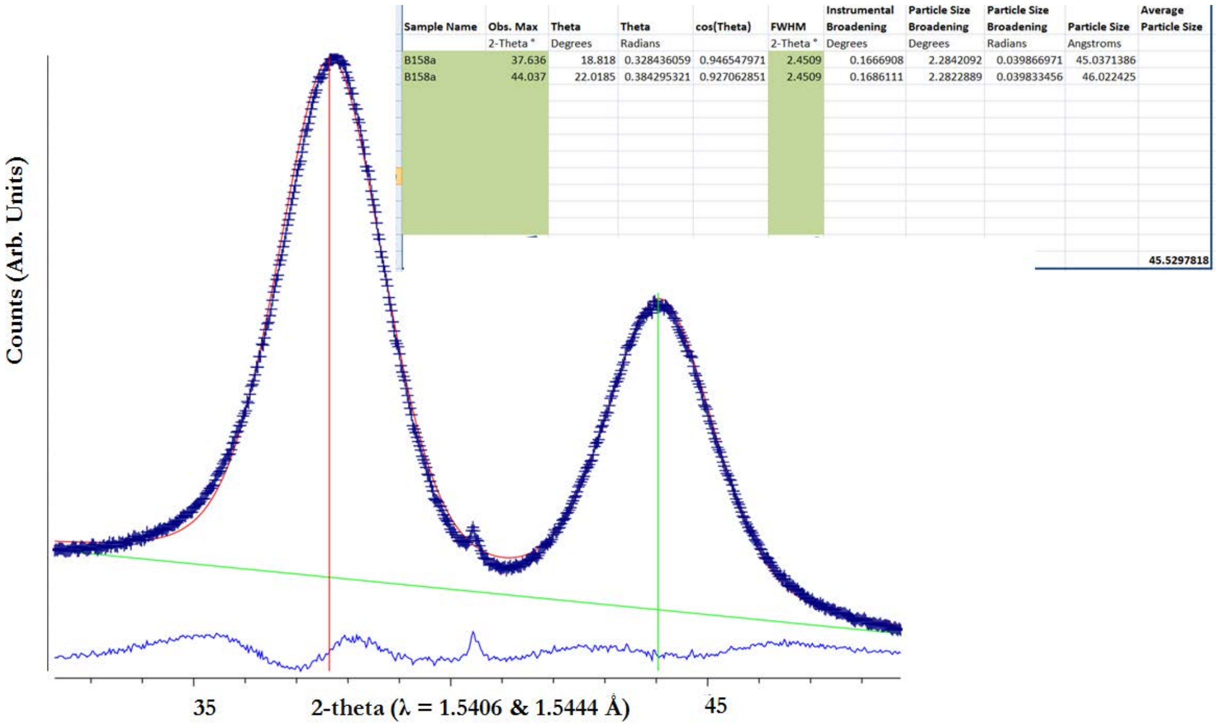

Sample Name	Obs. Max	Theta	Theta	cos(Theta)	FWHM	Instrumental Broadening	Particle Size Broadening	Particle Size Broadening	Particle Size	Average Particle Size
	2-Theta °	Degrees	Radians		2-Theta °	Degrees	Degrees	Radians	Angstroms	
B158a	37.636	18.818	0.328436059	0.946547971	2.4509	0.1666908	2.2842092	0.039866971	45.0371386	
B158a	44.037	22.0185	0.384295321	0.927062851	2.4509	0.1686111	2.2822889	0.039833456	46.022425	
										45.5297818

Figure D42 Fit and calculation for Scherrer analysis for tungsten + urea synthesised sample

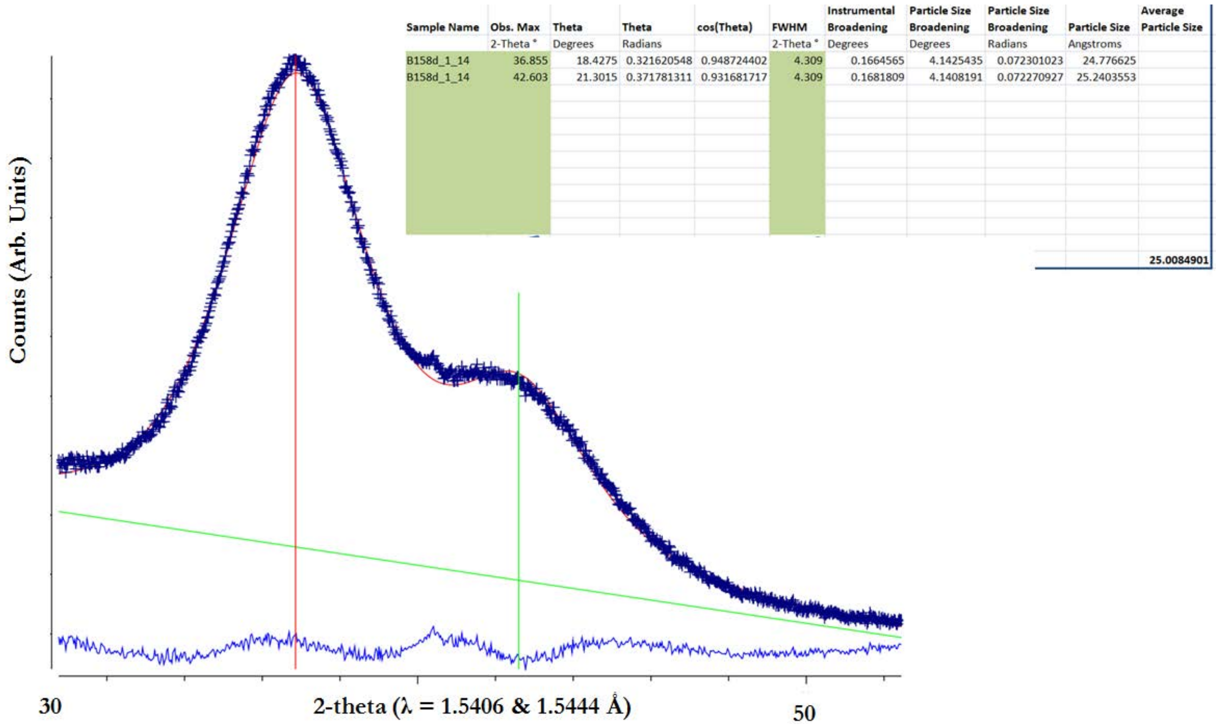

Sample Name	Obs. Max	Theta	Theta	cos(Theta)	FWHM	Instrumental Broadening	Particle Size Broadening	Particle Size Broadening	Particle Size	Average Particle Size
	2-Theta °	Degrees	Radians		2-Theta °	Degrees	Degrees	Radians	Angstroms	
B158d_1_14	36.855	18.4275	0.321620548	0.948724402	4.309	0.1664565	4.1425435	0.072301023	24.776625	
B158d_1_14	42.603	21.3015	0.371781311	0.931681717	4.309	0.1681809	4.1408191	0.072270927	25.2403553	
										25.0084901

Figure D43 Fit and calculation for Scherrer analysis for tungsten + urea synthesised sample

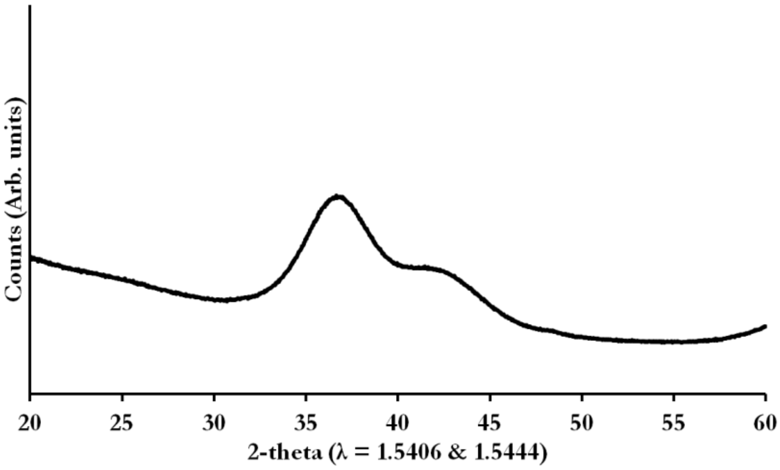

Figure D44 XRD pattern for samples synthesised using 0.005 mol of tungsten per 20 g of gelatin solution 10% (w/v). Furnace treatment - Max temp. 900 °C, heat rate 1 °C min^{-1}, hold time 5 mins

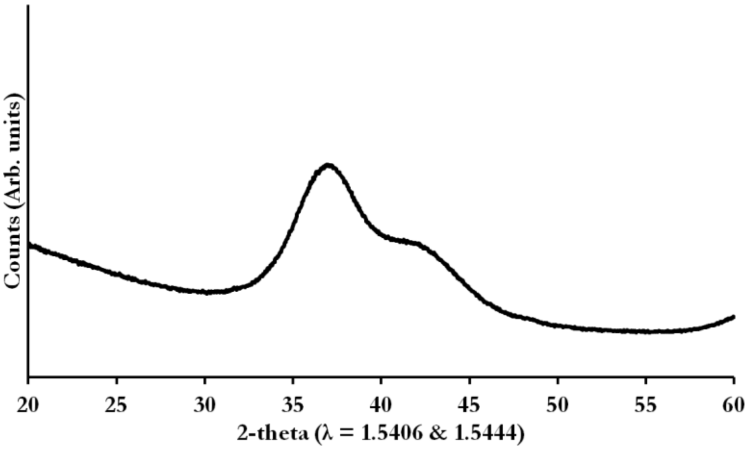

Figure D45 XRD pattern for samples synthesised using 0.005 mol of tungsten per 20 g of gelatin solution 10% (w/v). Furnace treatment - Max temp. 900 °C, heat rate 1 °C min^{-1}, hold time 60 mins

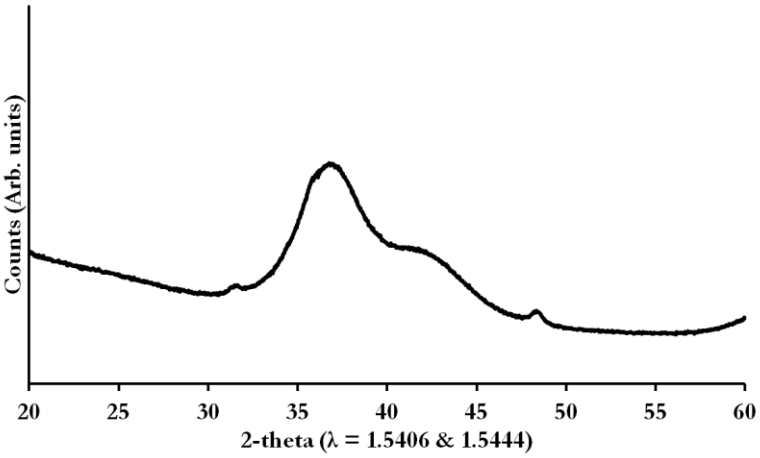

Figure D46 XRD pattern for samples synthesised using 0.005 mol of tungsten per 20 g of gelatin solution 10% (w/v). Furnace treatment - Max temp. 900 °C, heat rate 1 °C min^{-1}, hold time 240 mins

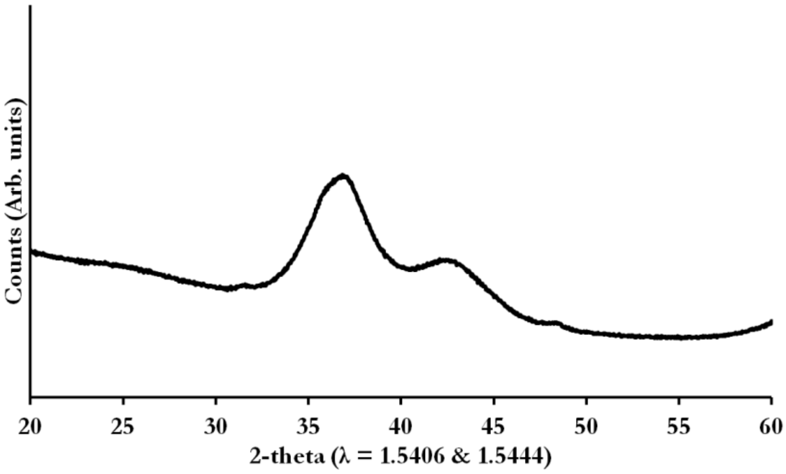

Figure D47 XRD pattern for samples synthesised using 0.005 mol of tungsten per 20 g of gelatin solution 10% (w/v). Furnace treatment - Max temp. 900 °C, heat rate 5 °C min^{-1}, hold time 5 mins

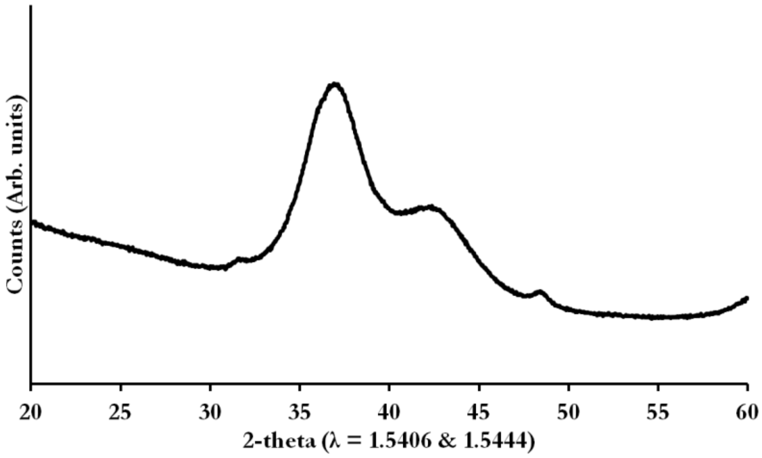

Figure D48 XRD pattern for samples synthesised using 0.005 mol of tungsten per 20 g of gelatin solution 10% (w/v). Furnace treatment - Max temp. 900 °C, heat rate 5 °C min^{-1}, hold time 60 mins

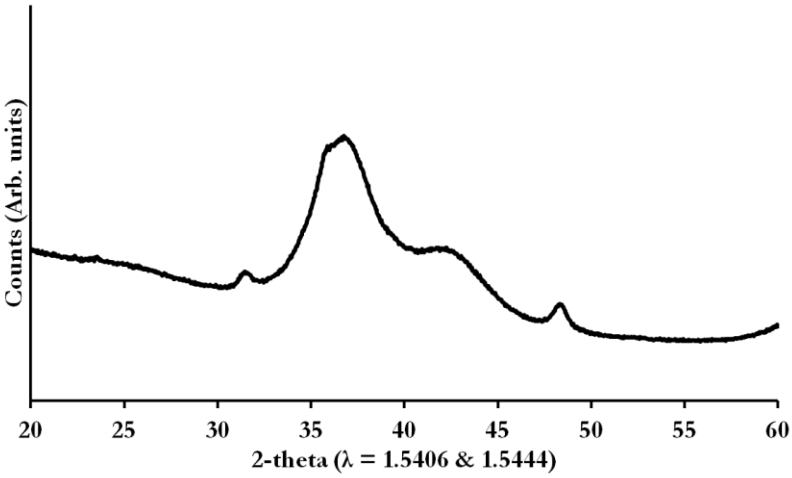

Figure D49 XRD pattern for samples synthesised using 0.005 mol of tungsten per 20 g of gelatin solution 10% (w/v). Furnace treatment - Max temp. 900 °C, heat rate 5 °C min^{-1}, hold time 240 mins

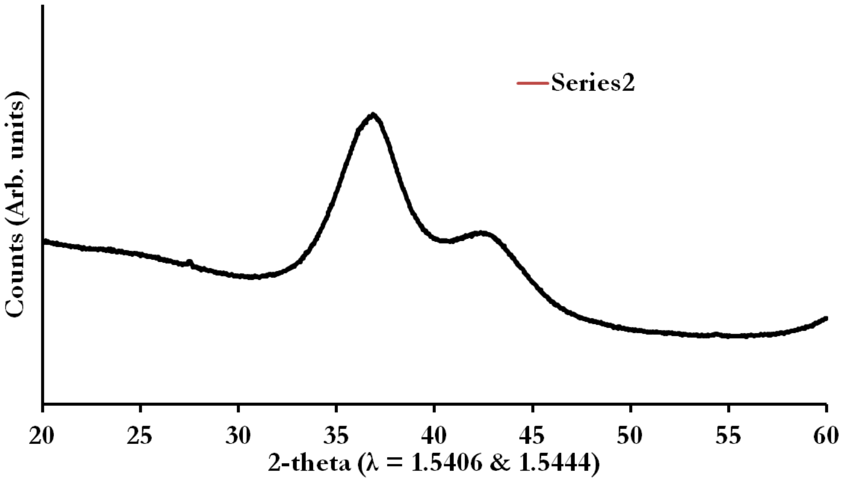

Figure D50 XRD pattern for samples synthesised using 0.005 mol of tungsten per 20 g of gelatin solution 10% (w/v). Furnace treatment - Max temp. 900 °C, heat rate 10 °C min^{-1}, hold time 5 mins

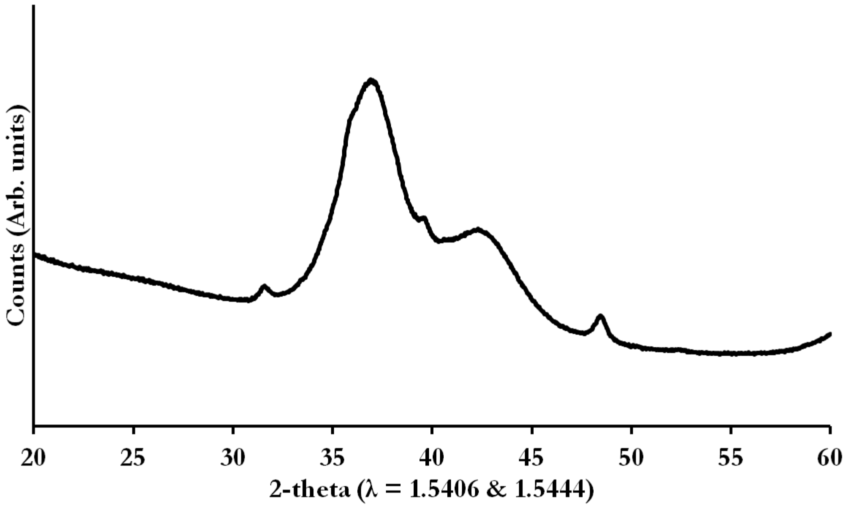

Figure D51 XRD pattern for samples synthesised using 0.005 mol of tungsten per 20 g of gelatin solution 10% (w/v). Furnace treatment - Max temp. 900 °C, heat rate 10 °C min^{-1}, hold time 60 mins

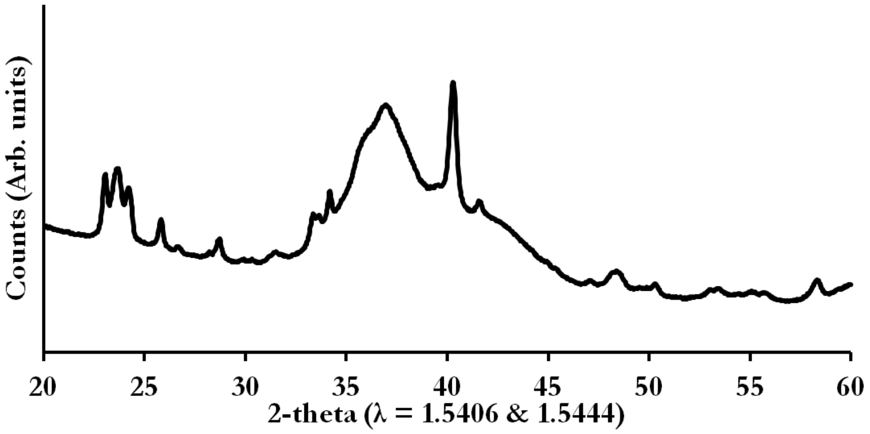

Figure D52 XRD pattern for samples synthesised using 0.005 mol of tungsten per 20 g of gelatin solution 10% (w/v). Furnace treatment - Max temp. 900 °C, heat rate 10 °C min^{-1}, hold time 240 mins

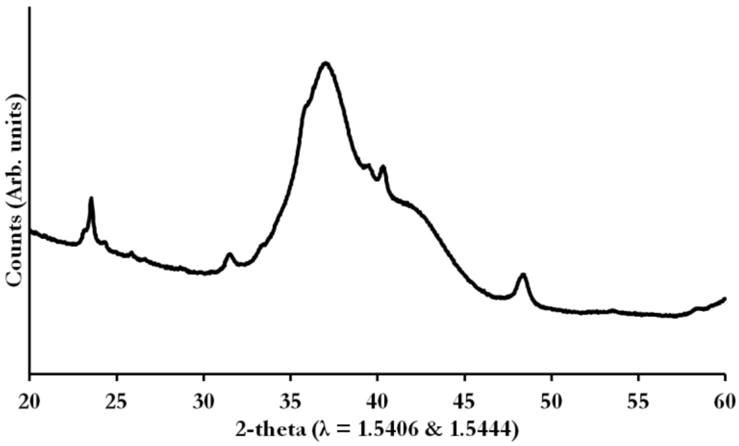

Figure D53 XRD pattern for samples synthesised using 0.005 mol of tungsten per 20 g of gelatin solution 10% (w/v). Furnace treatment - Max temp. 900 °C, heat rate 1 °C min^{-1}, hold time 5 mins

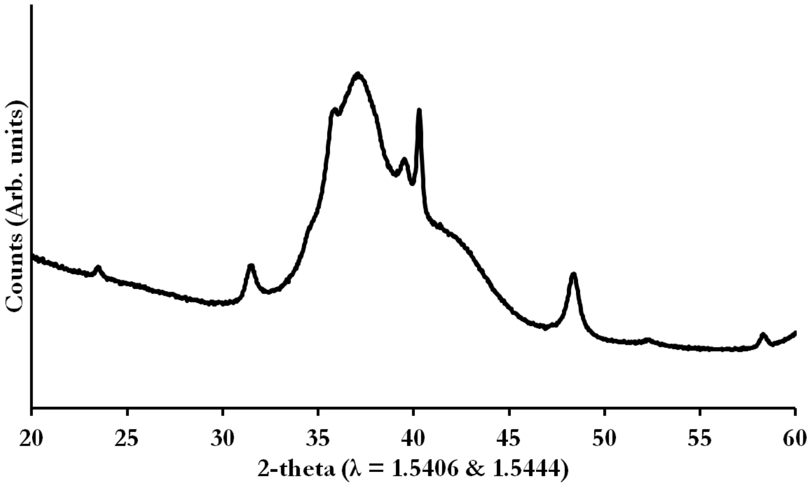

Figure D54 XRD pattern for samples synthesised using 0.005 mol of tungsten per 20 g of gelatin solution 10% (w/v). Furnace treatment - Max temp. 900 °C, heat rate 1 °C min^{-1}, hold time 60 mins

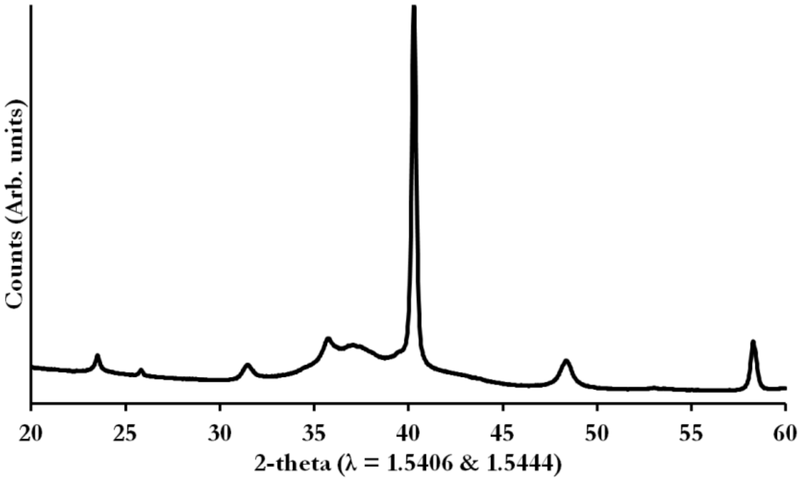

Figure D55 XRD pattern for samples synthesised using 0.005 mol of tungsten per 20 g of gelatin solution 10% (w/v). Furnace treatment - Max temp. 900 °C, heat rate 1 °C min^{-1}, hold time 240 mins

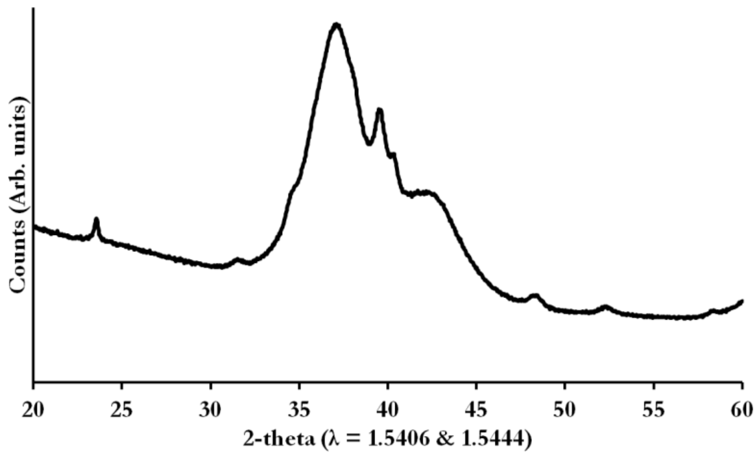

Figure D56 XRD pattern for samples synthesised using 0.005 mol of tungsten per 20 g of gelatin solution 10% (w/v). Furnace treatment - Max temp. 900 °C, heat rate 5 °C min^{-1}, hold time 5 mins

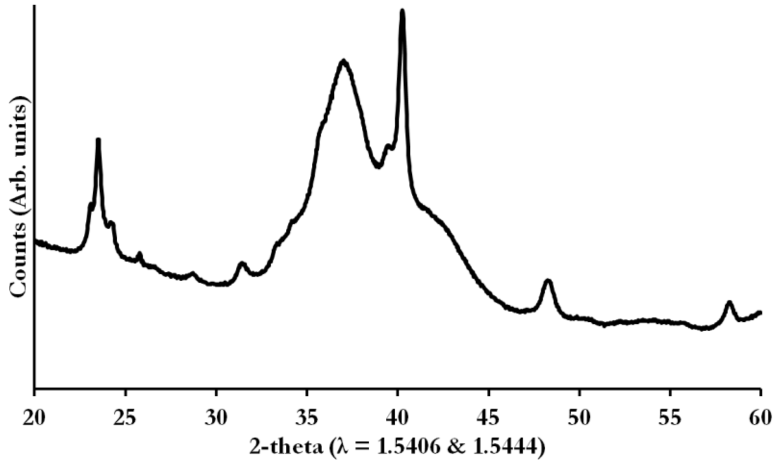

Figure D57 XRD pattern for samples synthesised using 0.005 mol of tungsten per 20 g of gelatin solution 10% (w/v). Furnace treatment - Max temp. 900 °C, heat rate 5 °C min^{-1}, hold time 60 mins

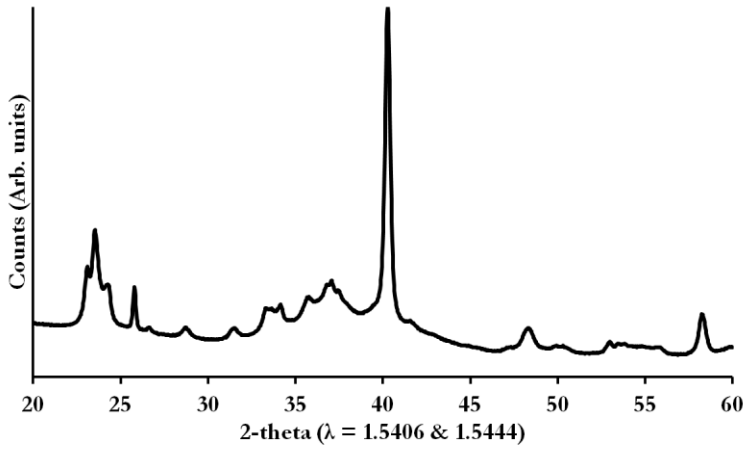

Figure D58 XRD pattern for samples synthesised using 0.005 mol of tungsten per 20 g of gelatin solution 10% (w/v). Furnace treatment - Max temp. 900 °C, heat rate 5 °C min^{-1}, hold time 240 mins

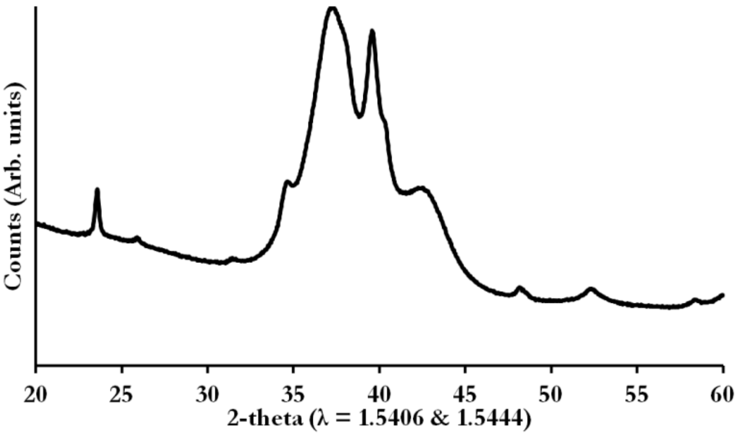

Figure D59 XRD pattern for samples synthesised using 0.005 mol of tungsten per 20 g of gelatin solution 10% (w/v). Furnace treatment - Max temp. 900 °C, heat rate 10 °C min^{-1}, hold time 5 mins

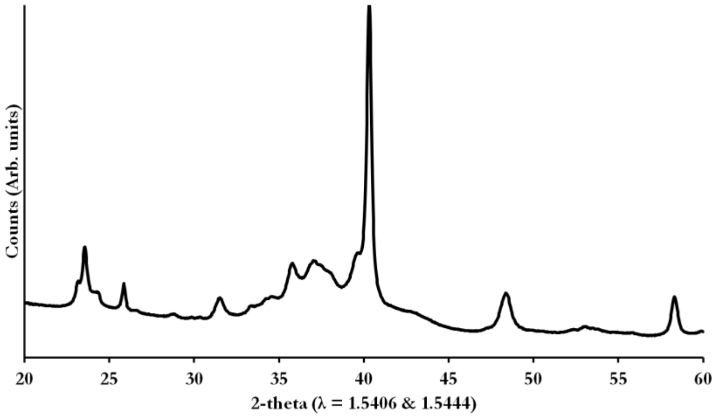

Figure D60 XRD pattern for samples synthesised using 0.005 mol of tungsten per 20 g of gelatin solution 10% (w/v). Furnace treatment - Max temp. 900 °C, heat rate 10 °C min^{-1}, hold time 60 mins

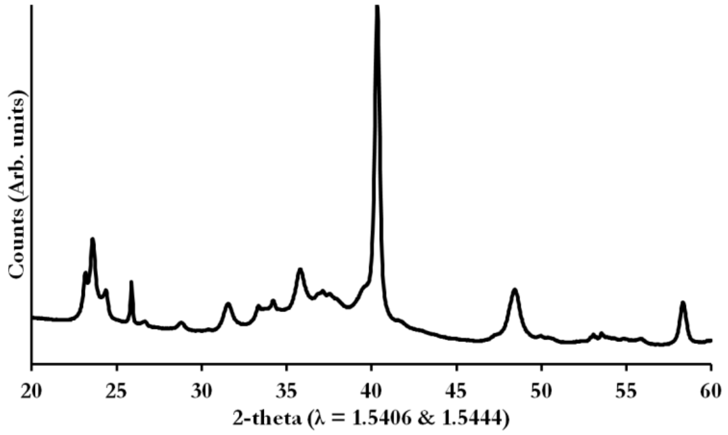

Figure D61 XRD pattern for samples synthesised using 0.005 mol of tungsten per 20 g of gelatin solution 10% (w/v). Furnace treatment - Max temp. 900 °C, heat rate 10 °C min^{-1}, hold time 240 mins

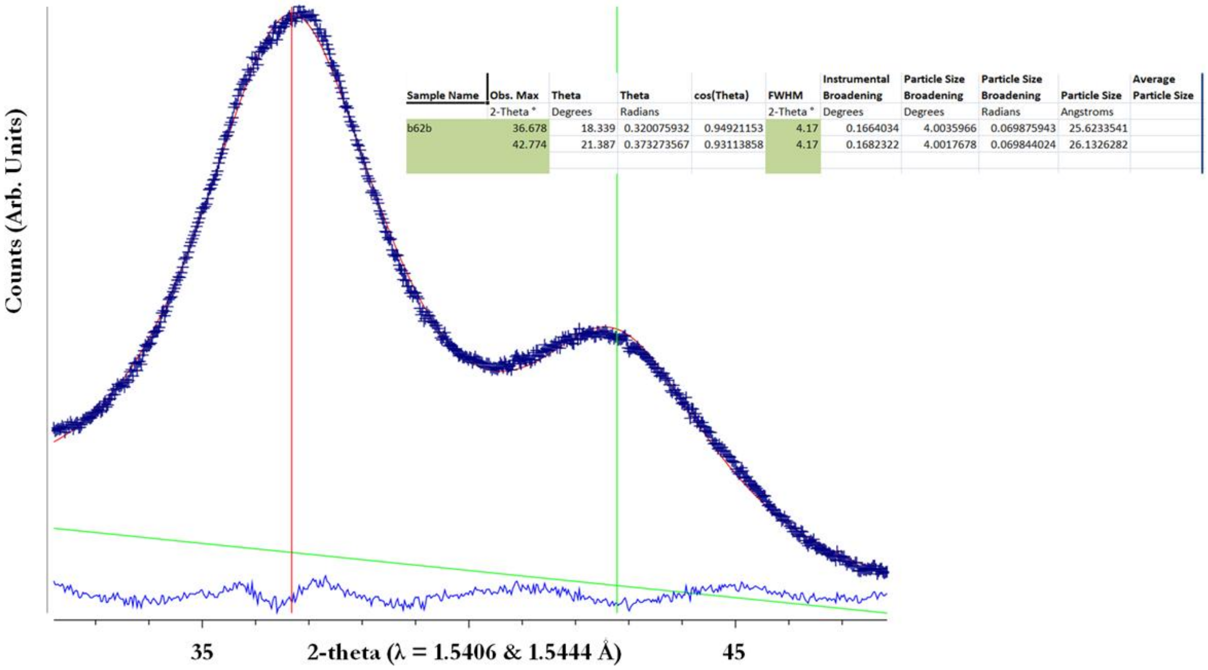

Sample Name	Obs. Max	Theta	Theta	cos(Theta)	FWHM	Instrumental Broadening	Particle Size Broadening	Particle Size Broadening	Particle Size	Average Particle Size
	2-Theta °	Degrees	Radians		2-Theta °	Degrees	Degrees	Radians	Angstroms	
b62b	36.678	18.339	0.320075932	0.94921153	4.17	0.1664034	4.0035966	0.069875943	25.6233541	
	42.774	21.387	0.373273567	0.93113858	4.17	0.1682322	4.0017678	0.069844024	26.1326282	

Figure D62 Fit and calculation for Scherrer analysis for tungsten + gelatin synthesised sample

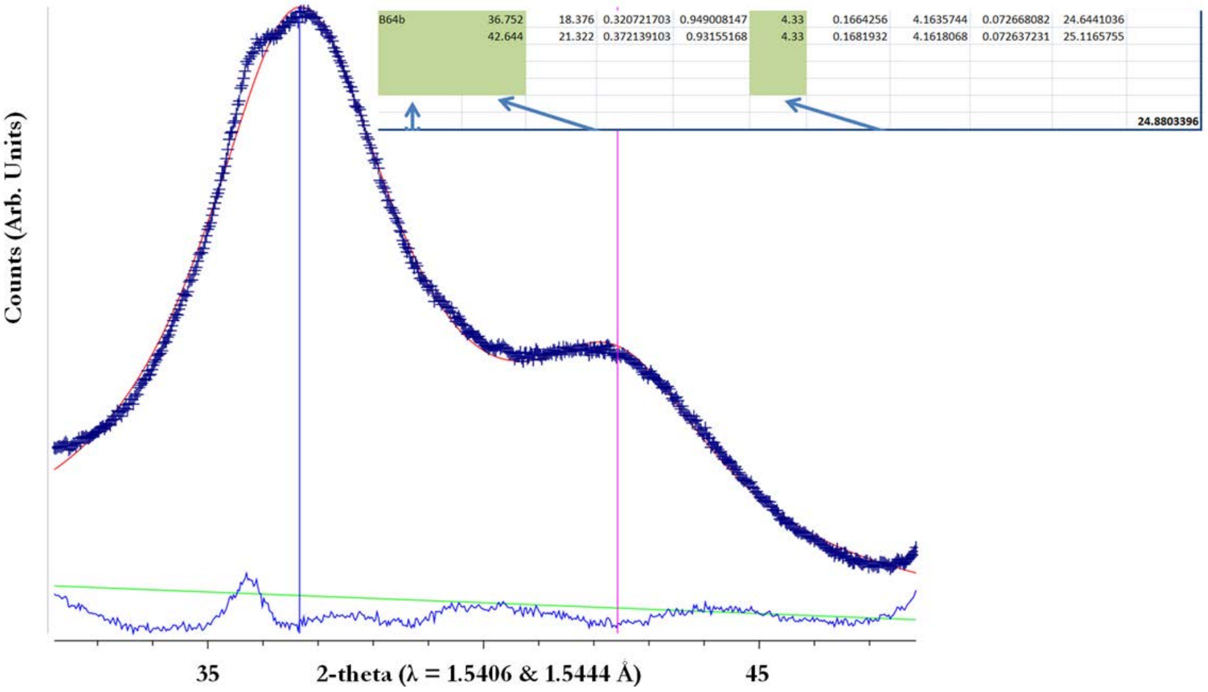

B64b	36.752	18.376	0.320721703	0.949008147	4.33	0.1664256	4.1635744	0.072668082	24.6441036	
	42.644	21.322	0.372139103	0.93155168	4.33	0.1681932	4.1618068	0.072637231	25.1165755	
										24.8803396

Figure D63 Fit and calculation for Scherrer analysis for tungsten + gelatin synthesised sample

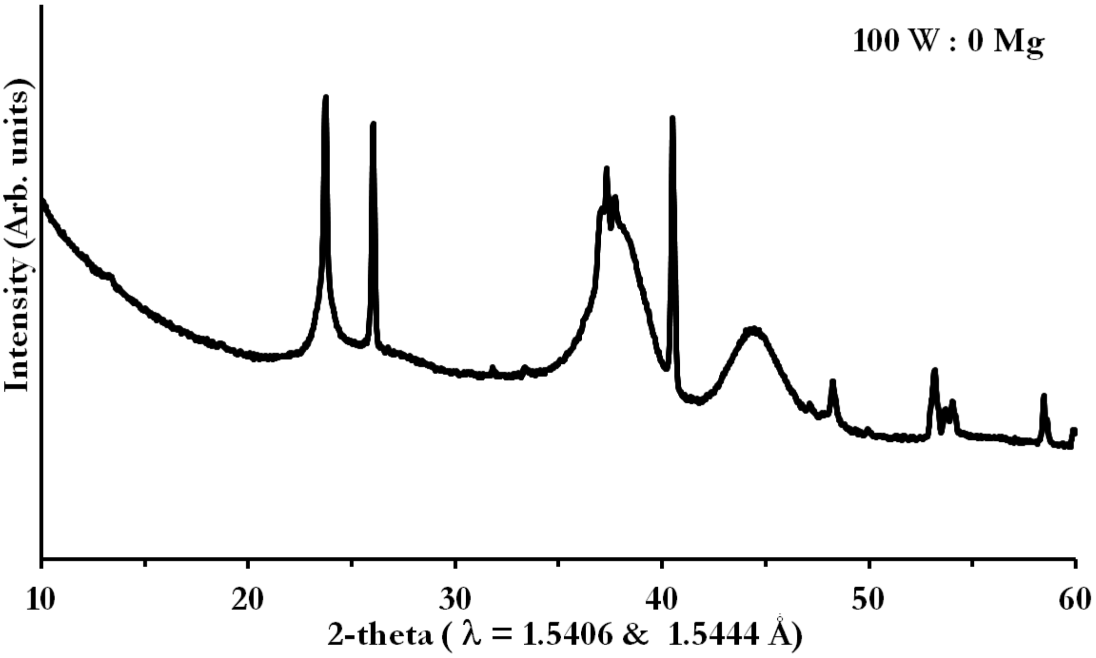

Figure D64 XRD pattern for sample synthesised from agar and ammonium metatungstate

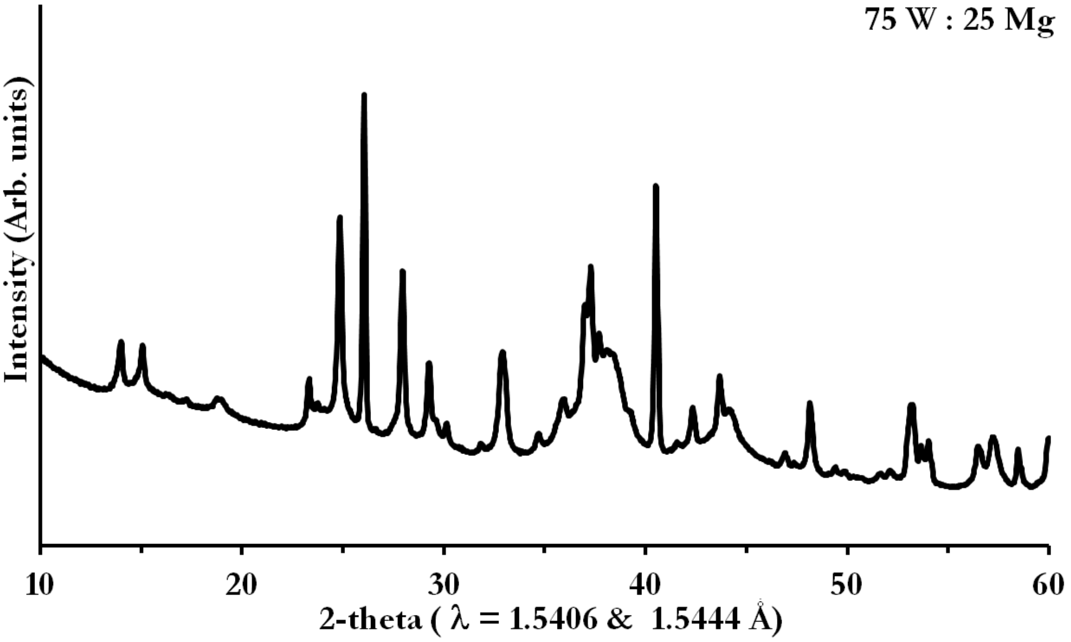

Figure D65 XRD pattern for sample synthesised from agar and ammonium metatungstate

APPENDIX E

EXPERIMENTAL TECHNIQUES

E1.1 GENERAL DISCUSSION

This chapter details the theory behind the main analytical techniques used throughout this thesis, how they were put into practice and finally the instruments that were used for these experiments.

E1.2 NITROGEN POROSIMETRY MEASUREMENTS

E1.2.1 BASIC OPERATION

Samples were first dried under high vacuum at 120 °C overnight; the weight was recorded before and afterwards. A glass filler rod was used to minimise the volume in the tube and placed on the instrument. The computer then ran a pre-programmed sequence to calculate the minimum and maximum pressures before using 40 points for the adsorption and desorption isotherms for relative pressure of 0.01 to 1. This occurs whilst the tube is submersed in liquid nitrogen.

As the tubes are calibrated with set amounts of nitrogen the instrument can calculate the amount of additional nitrogen needed to reach each partial pressure; the excess being adsorbed onto the sample.

E1.2.2 BRUNAUER EMMETT TELLER (BET) THEORY

BET theory is used to calculate the specific surface area of materials by using the adsorption of gases onto the sample. A number of gases can be used but primarily it is nitrogen and these experiments are therefore usually carried out at 77 K (liquid nitrogen cooled).

Equation E5.1 shows the relationship of pressure and volume of gas adsorbed, where p and p_o are pressure relating to the equilibrium and the saturation of the gas, v is the amount of adsorbed gas, v_m is the amount of gas in the monolayer and c is the BET constant. For values of p/p_o between 0.05 and 0.35 a straight line can be plotted (with p/p_o on the x-axis) and the yintercept and gradient of the slope can be used to calculate the amount of gas in the monolayer. Finally the BET surface is calculated from the total volume of gas and the mass of the sample.

$$\frac{1}{v\left[\left(\frac{p_o}{p}\right)-1\right]} = \frac{c-1}{v_m c}\left(\frac{p}{p_o}\right) + \frac{1}{v_m c} \qquad \textbf{Equation E1.1}$$

E1.2.3 INSTRUMENT

The instrument used was the Quantachrome Nova-E at 77 K using nitrogen as the absorbent.

E1.3 POWDER X-RAY DIFFRACTION (XRD)

E1.3.1 BASIC THEORY

Crystal lattices contain regular repeating arrangements of atoms and the smallest possible section that can reproduce this is called the unit cell. The dimensions of the unit cell can be described by sides of a, b and c separated by angles α, β and γ, Figure E1.1, and it is possible to generate 7 unique crystal systems with atoms on the corners of the unit cell. There can also be atoms in other positions giving 14 different lattices (Bravais lattices); combing these with the other symmetry operations in three dimension (i.e. mirror planes, translations, etc.), of which there are 32 possibilities, produces 230 different combinations called space groups. All crystals have internal symmetry relating to one of these space groups.[176]

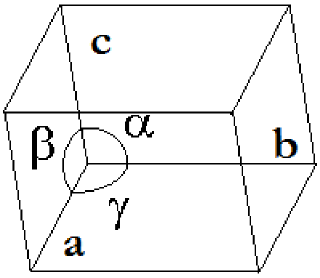

Figure E1.1 Unit cell parameters

There are planes of atoms that run throughout the crystal, these are called lattice planes, and are labelled with Miller indices. Planes that run parallel to each other allow for diffraction to occur and thus identification. When X-rays come into contact with these planes they diffract and there is diffraction off many layers, these diffracted X-rays mostly cancel each other out. However when the planes are suitably spaced and the angle of incidence is correct there is constructive interference between the diffracted X-rays that are separated by a multiple of the wavelength; this satisfies Braggs law, Equation E1.2, and increased intensity is seen in the diffracted X-rays. These spikes in intensity occur at particular 2-theta values for the Miller indices and this 'fingerprint' can be used to indentify materials.

Powder diffraction works by assuming the crystals are showing all possible diffracted beams at once generating a cone of X-rays. Moving the detector to collect data at all the angles means that the detector moves through this cone giving peaks in the diffraction pattern.

$$n\lambda = 2d \sin 2\theta \qquad \textbf{Equation E1.2}$$

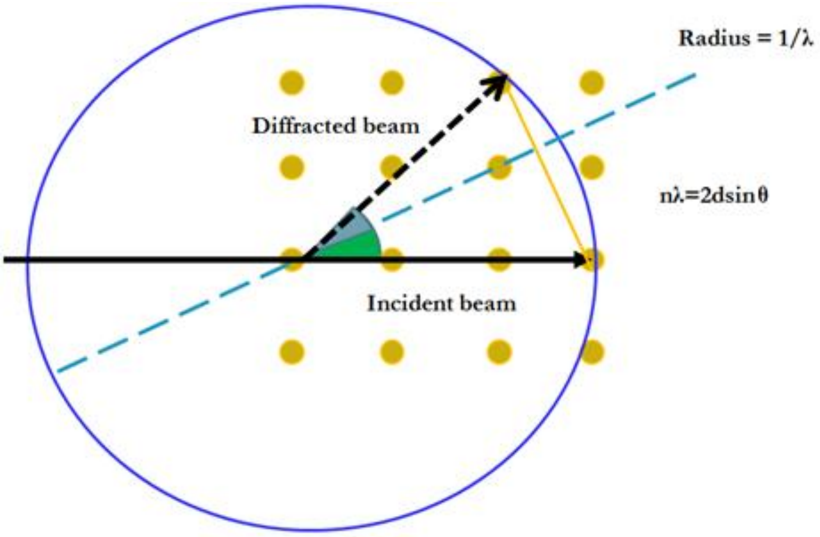

Figure E1.2 Braggs law schematic

E1.3.2 X-RAY SOURCE/OPTICS

An electron beam is generated (by thermionic emission, see 6.5.1) and accelerated toward a water cooled anode by a potential difference of approximately 40 kV. Most commonly used anode materials are copper, cobalt or molybdenum although silver targets can also be used. When the electrons impact the anode they rapidly decelerate causing several electronic transitions to occur. The effect of this is a continuum of electromagnetic radiation called Bremsstrahlung and characteristic emission lines are particular to that element. Copper has 3 such lines, Kβ (λ=1.392 Å) and Kα_1 (λ=1.5406 Å) and Kα_2 (λ=1.5444 Å). If all of these wavelengths were used the analysis of the diffraction pattern would be difficult as each insistence of the Bragg condition being met would result in 3 peaks, so as a result Kβ is always removed. This is achieved through a nickel filter which allows most of the Kα through whilst the Kβ is absorbed. The Kα lines are very close to each other so these cannot be removed in the same manner, instead a monochromator is used. Monochromators are single crystals of a material (such as germanium or silicon) that have an orientation to reflect only the desired wavelength onto the sample. It should be noted that a monochromator is not necessary (the Panalytical Empyrean does not have one) as the extra peaks can be accounted for in the analysis programs. Removing unwanted wavelengths in either manner reducing the intensity, this is why an un-monochromated X-ray source was used.[177]

E1.3.3 DETECTION

There are two types of detectors used commonly in laboratory diffractometers, the older type is a scintillation counter and operates by converting the X-rays into visible light which are converted again by photomultiplier tube to an electrical impulse. The input energy of the X-rays is proportional to the output energy of the light photons. The newer detector type, and the one used on the Panalytical Empyrean, is a position sensitive detector. These are based on charge coupled devices (CCD) and these use a p-type semiconductor in an array of small electrodes, a current is placed through these electrodes and the response time of the electrons can be used to determine their original position across a range of angles: this greatly increases the speed of data collection.[177]

E1.3.4 SAMPLE PREPARATION

Samples were prepared by being ground with a pestle and mortar until a fine homogenous particle size was achieved. Samples were either placed in the sample cup provided by Panalytical or on a silicon wafer and flattened with a glass slide.

E1.3.5 DATA ANALYSIS

The data for most samples was used to identify the crystalline phase present. This was done by converting the file type to .raw and then EVA's search and match feature was used. For some samples the peak widths were used in the Scherrer calculation, this analysis was carried out using the CMPR software from Argonne National Laboratories.[178] The Scherrer equation is shown below:- K is the shape factor (a typical value of 0.95 was used, indicating spherical particles with no strain); λ is the wavelength of the x-rays; B is the peak broadening from the particles (in radians); and cosθ is Braggs angle (in degrees). It was assumed these particles were not strained although in reality probably do exhibit some stress/strain, however for an estimation of particle size this is sufficient.

$$\tau = \frac{K\lambda}{B\cos\theta}$$

To calculate particle broadening a corundum standard was first scanned (as described in E2.5.7) and the 'fit' module was used to calculate the full width at half maximum (FWHM). This was used to plot a FWHM against 2-theta graph with a line of best fit (y=mx+c) and this was used in the Scherrer equation using the spreadsheet shown in Figure E1.3.

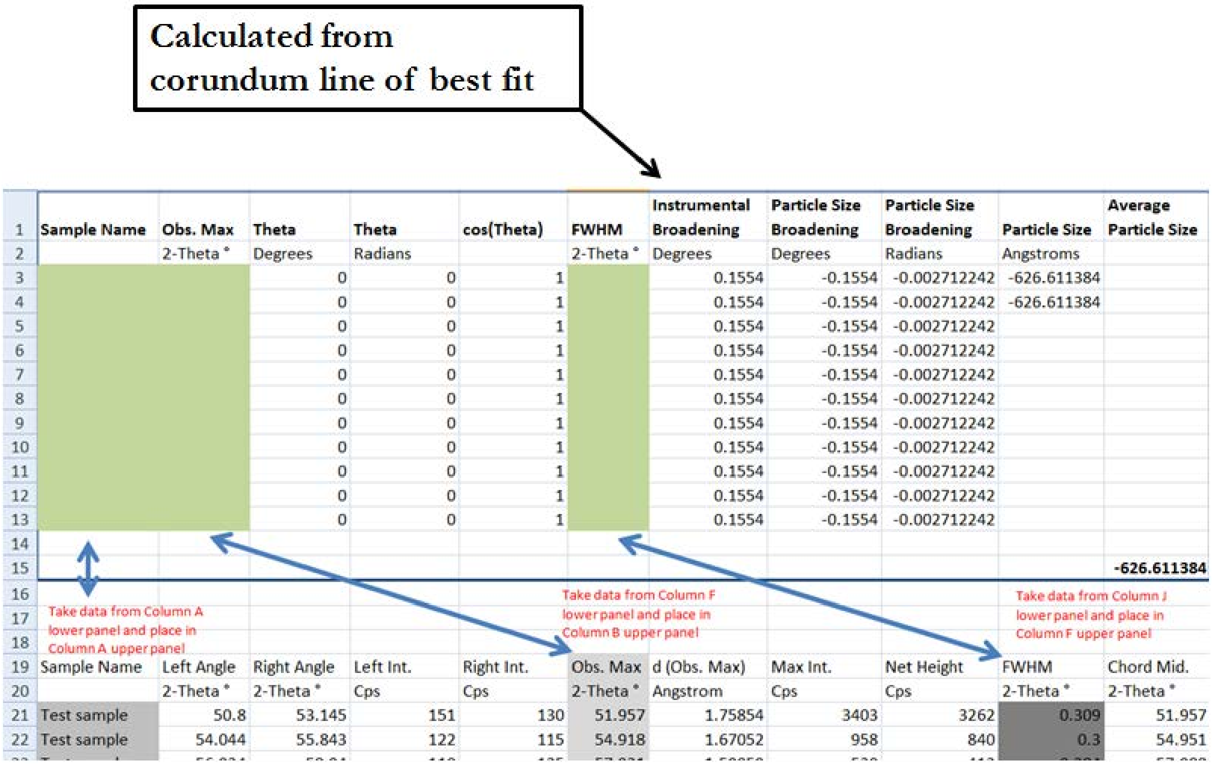

Calculated from corundum line of best fit

1	Sample Name	Obs. Max	Theta	Theta	cos(Theta)	FWHM	Instrumental Broadening	Particle Size Broadening	Particle Size Broadening	Particle Size	Average Particle Size
2		2-Theta °	Degrees	Radians		2-Theta °	Degrees	Degrees	Radians	Angstroms	
3			0	0	1		0.1554	-0.1554	-0.002712242	-626.611384	
4			0	0	1		0.1554	-0.1554	-0.002712242	-626.611384	
5			0	0	1		0.1554	-0.1554	-0.002712242		
6			0	0	1		0.1554	-0.1554	-0.002712242		
7			0	0	1		0.1554	-0.1554	-0.002712242		
8			0	0	1		0.1554	-0.1554	-0.002712242		
9			0	0	1		0.1554	-0.1554	-0.002712242		
10			0	0	1		0.1554	-0.1554	-0.002712242		
11			0	0	1		0.1554	-0.1554	-0.002712242		
12			0	0	1		0.1554	-0.1554	-0.002712242		
13			0	0	1		0.1554	-0.1554	-0.002712242		
14											
15											-626.611384
16						Take data from Column F lower panel and place in Column B upper panel				Take data from Column J lower panel and place in Column F upper panel	
17	Take data from Column A lower panel and place in Column A upper panel										
18											
19	Sample Name	Left Angle	Right Angle	Left Int.	Right Int.	Obs. Max	d (Obs. Max)	Max Int.	Net Height	FWHM	Chord Mid.
20		2-Theta °	2-Theta °	Cps	Cps	2-Theta °	Angstrom	Cps	Cps	2-Theta °	2-Theta °
21	Test sample	50.8	53.145	151	130	51.957	1.75854	3403	3262	0.309	51.957
22	Test sample	54.044	55.843	122	115	54.918	1.67052	958	840	0.3	54.951

Figure E1.3 Screenshot of Excel file used to calculate particle size using the Scherrer equation

E1.3.6 INSTRUMENT

Samples were scanned using a Panalytical Empyrean diffractometer in flat plate reflection geometry equipped with a Pixcel-2D position sensitive detector from 10 ° to 80 ° 2-theta. A nickel filter was used to remove the Cu Kβ and Cu Kα radiation was used without being monochromated.

The D2 Phaser from Bruker was used for some samples as the Panalytical was down for an extended time. The details of this instrument are as follows:- cobalt radiation with a Lynx eye scintillation counter.

E1.4 TRANSITION ELECTRON MICROSCOPY (TEM)

TEM is able to image the interior of materials and it does this by using the small de Broglie wavelength[179] of the electrons. The wavelength of an electron is similar to interatomic distances, which allow it to be diffracted through these spaces and is detected on the other side, allowing for imaging. Figure E1.4 shows the basic layout of a TEM.

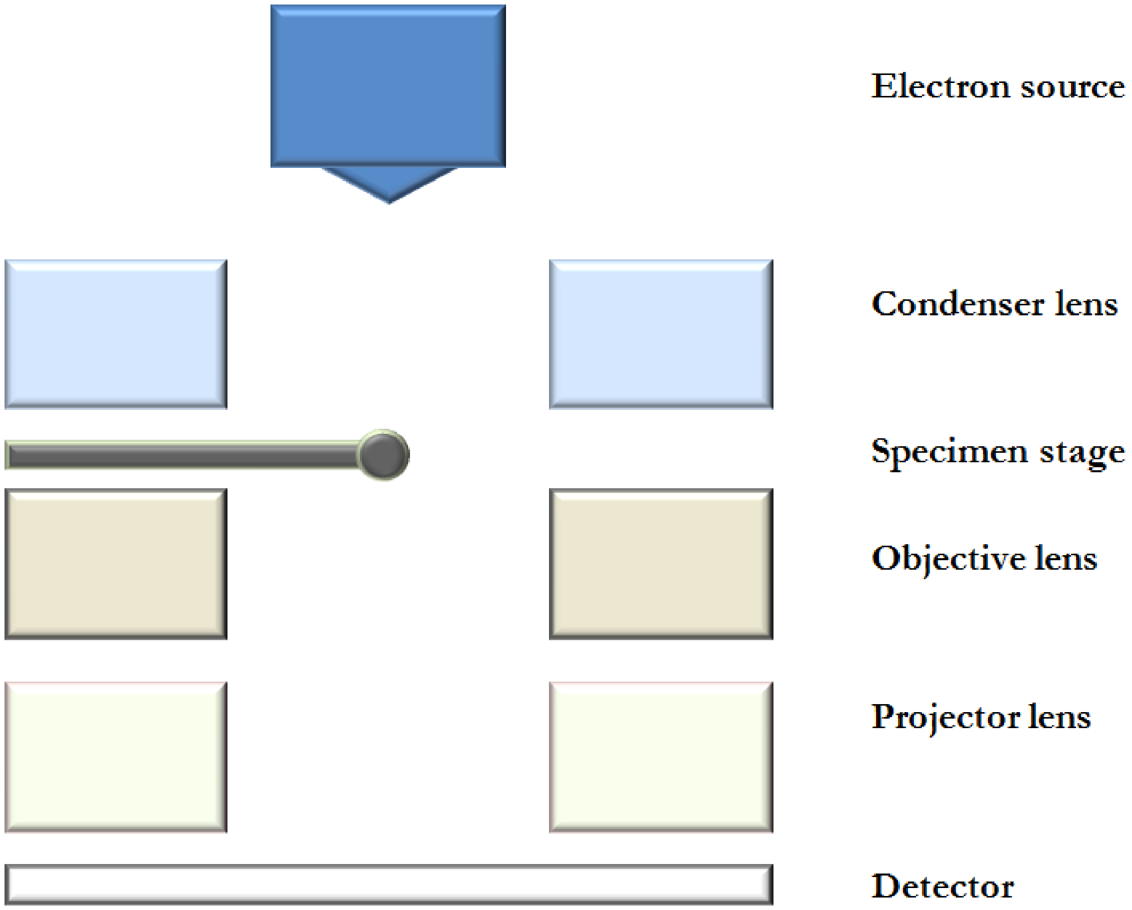

Figure E1.4 Schematic representation of a TEM

E1.4.1 ELECTRON SOURCE

Electrons are generated at the top of the column by filament with a large current (100-300 kV) passing through it; this causes the electrons to be ejected either by thermionic emission or field electron emission (FEE). The former is by far the more common, and is a consequence of the filament being heated to the point that electrons have enough kinetic energy to be ejected from the surface. FEE is when the removal of electrons is due to a strong electrostatic field. In either case the filament is usually tungsten although LaB_6 has also been used for FEE.

Beam formation occurs due to the presence of an anode, held at a positive voltage relative to the filament so electrons are attracted to it. A Wehnelt cap, which is held at a negative voltage to the filament, is usually employed to assist this process; the negative voltage of the Wehnelt focuses the beam by acting as a convergent lens controlling the beam as it travels downward due the pull of the anode, Figure E1.5.[180]

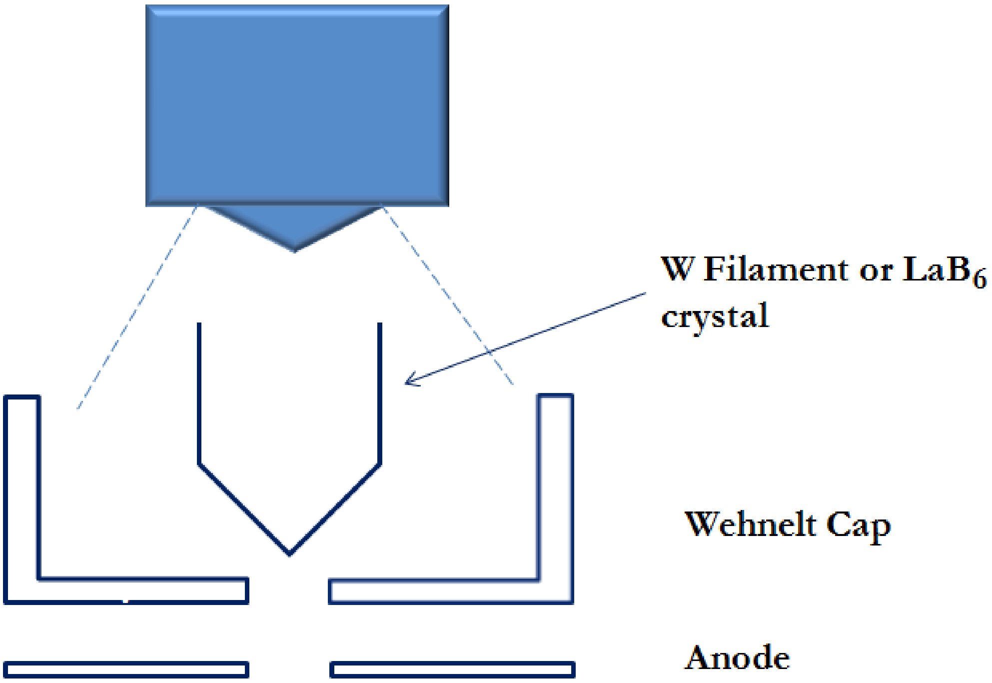

Figure E1.5 Schematic of the electron source of a TEM, showing the Wehnelt plate and anode

E1.4.2 OPTICS

The electron beam needs to be focussed in order to image the sample; there are at least three stages of lensing and these are condensing, objective and projector lensing. The projector lens opens the beam so that it can be imaged via a phosphorescent screen or charge coupled device (CCD). The magnification of the image is a product of the distance between the objective lens and the projector lens and the condenser lens is responsible for primary beam formation; use of magnetic and electrostatic fields allow for the beam to be collimated and directed to the desired area on the sample. The lens are made of either 4 or 6 electromagnets, called quadru-/hexa-poles, which allow the electrons to be directed and focused, additionally there is usually an option for correcting the astigmatism (another quadrupole).

E1.4.3 DETECTION

Detection of the diffracted electrons can be done in a number of ways and most modern TEMs have the option of both of the following. The first and most common detector type is a phosphor screen for visual inspection by the operator; there usually are binoculars to aid this process. An example of one such device is Y_2O_4:Eu screen, the electrons cause emission of photons which the operator can view.[181] The other commonly used imaging device is a CCD and the operation of this is described above.

E1.4.4 SAMPLE PREPARATION

Samples must be extremely thin, typically <100 nm thick, for electrons to be able to penetrate, this can mean laborious sample thinning. However for the samples used here, sample preparation involved dispersing samples (~100mg) in ethanol (~7ml) and dropping several drops on a carbon coated copper mesh, 100 μm sized apertures.

E1.4.5 ENERGY DISPERSIVE X-RAY SPECTROSCOPY (EDX)

It is also possible to run EDX on most TEM's; this technique is good at indentifying which elements are present in your sample. Practically this involves focussing either an X-ray beam, or as in this case, a high energy beam of electrons onto the sample. This causes inner electrons to be ejected leaving a hole which is filled by an outer electron which causes a release of energy in the form of an X-ray. Due to the characteristic nature of the X-ray spectrum of all atoms, the energy of this X-ray can be measured and associated with a particular element and energy level. Recently there has been a shift to use silicon drift detectors (SDD) for detecting the X-rays. The signal received from the detector is due to the energy and location of the X-rays hitting the detector.

E1.4.6 INSTRUMENT

The TEM used was a JEOL 2100, using a tungsten filament and CCD to capture the images.

E1.5 SCANNING ELECTRON MICROSCOPY (SEM)

There a number of aspects of SEM that are similar to TEM, firstly the electron beam is generated in the same way however the accelerating voltage is much lower at 0.2 to 40 kV. The optics are also similar but with the addition of scanning coils which deflect the beam in regular patterns to produce an image of the sample.

E1.5.1 INTERACTION OF ELECTRONS WITH THE SAMPLE / DETECTION/ PREPERATION

When the electron beam hits the sample there are a number of possible outcomes, Figure E1.6. Structural and chemical information can be extracted from most of these interactions. The tear drop shape is similar in all samples but the penetration depth can vary from 100 nm to a few microns. The information that can be extracted is as follows: -

Auger electrons - provide surface atomic composition

Characteristic electrons (EDX) - bulk atomic composition

Cathodoluminescence - electronic states

Secondary electrons (SE) - morphology

Backscattered electrons (BSE) - chemical composition (i.e. atomic number)

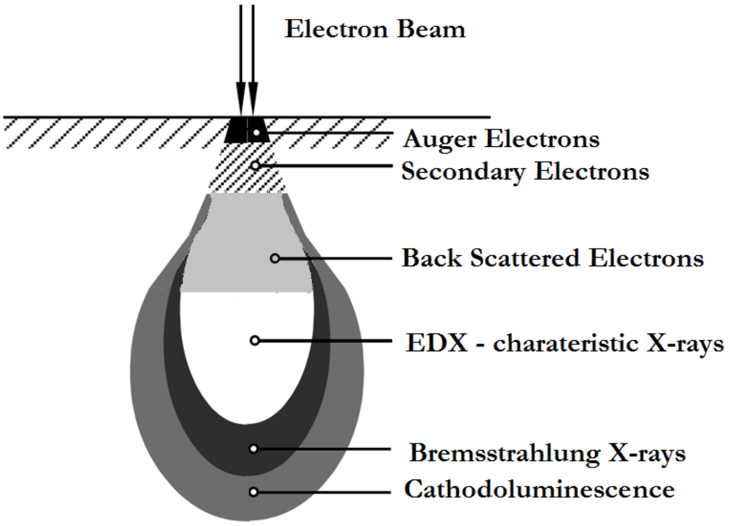

Figure E1.6 electron interactions for SEM

The last two are the most important for this work as they allow for the pore structure to be investigated for samples and backscattered electrons allow us to see the distribution of elements throughout the sample.

Secondary electrons are detected using a scintillator and photomultiplier system developed by Everhart and Thornley.[182] These are usually placed one side of the sample at an angle as to maximise the collection of SE. BSE are collected using a scintillator place directly above the sample, surrounding the beam.

Samples were ground using a pestle and mortar and then mounted on a double sided sticky carbon tape, before being coated in gold.

E1.5.2 INSTRUMENT

Images were captured using a Phillps XL-30 ESEM.

E1.6 REFERENCES

(176) Jenkins, R.; Snyder, R. *Introduction to X-ray powder diffractometry*; John Wiley & Sons, 1996; Vol. 138.

(177) Dinnebier, R. E. *Powder diffraction: theory and practice*; Royal Society of Chemistry, 2008.

(178) Toby, B. H. *Journal of Applied Crystallography* **2005**, *38*, 1040.

(179) Belyaeva, T.; Serkin, V. *The European Physical Journal D* **2012**, *66*, 1.

(180) Davidson, S. M. *Institute of Physics Conference Series* **1982**, 39.

(181) Wakefield, G.; Holland, E.; Dobson, P. J.; Hutchison, J. L. *Advanced Materials* **2001**, *13*, 1557.

(182) Everhart, T. E.; Thornley, R. *Journal of scientific instruments* **1960**, *37*, 246.

APPENDIX F

The follow pages contain published papers relating to Chapter 1 and Chapter 2.